Inaugural – Dissertation

zur

Erlangung der Doktorwürde

der

Gesamtfakultät für Mathematik, Ingenieur- und Naturwissenschaften

der

Ruprecht-Karls-Universität

Heidelberg

Vorgelegt von M.Sc. Felix Hainer

Tag der mündlichen Prüfung: 27.07.2023

Rationalization of excited-state tuning through ultrafast transient absorption and vibrational coherence spectroscopy

Gutachter: Dr. Tiago Buckup
Prof. Dr. Andreas Dreuw

Abstract

Photophysical and-chemical processes make use of light as strongly quantized energy source, rendering mechanisms possible, which involve excited states that are thermally unavailable. This puts them at the heart of many exciting and promising technologies from photovoltaics to photocatalysis and photodynamic therapy. In this work, several strategies to tuning these excited states are rationalized by ultrafast transient absorption and impulsive vibrational spectroscopy, applied to two different classes of samples. Firstly, the excited-state dynamics of two iron(II) complexes are investigated for the tuning effect of solvent choice and ligand design. They toggle on and off the involvement of metal-centered (MC) excited states acting as loss channels for desired metal-to-ligand charge transfer (MLCT) states. Impulsive vibrational spectroscopy is established as suitable method for identifying MLCT-MC transitions in $[Fe(bpy)(CN)_4]^{2-}$, a well-known reference sample. The method is then applied to an iron(II)N-heterocyclic carbene complex and identifies an ultrafast MLCT-MC branching in this promising dye-sensitizer candidate. Secondly, the photophysics and -chemistry of triphenylamine is thoroughly investigated for the influences of solvent, the oxygen content therein and enforced planarity. In n-hexane, triphenylamine is converted to N-phenylcarbazole, with oxygen playing an intricate double role. The conversion is stopped completely by planarization due to the cancellation of p-orbital preorientation. In chloroform, ultrafast electron transfer to the solvent dominates the photochemistry, producing the radical cation leading to chromophore dimerization.

Kurzzusammenfassung

Photophysikliaschen und –chemische Prozesse nutzen Licht als quantisierte Energiequelle. Dadurch laufen Mechanismen ab, die elektronisch angerete Zustände beinhalten, welche auf thermischem Wege unzugänglich sind. Das macht diese Prozesse zum zentralen Bestandteil vielversprechender Technologien wie Photovoltaik, Photokatalyse und photodynamischer Therapie. In der vorliegenden Arbeit werden verschiedene Strategien zu Anpassung angeregter Zustände in zwei Probenklassen mittels ultraschneller transienter Absorptionspektroskopie und impulsiver Schwingungsspektroskopie nachvollzogen. Erstens werden die angeregten Zustandsdynamiken zweier Eisen(II)-Komplexe auf den Einfluss von Lösungsmittel und Ligandendesign untersucht. Mittels dieser lassen sich metallzentrierte (MC) angeregte Zustände als Verlustkanal für die gewünschten Metall-zu-Ligand Ladungs-Übertragungszustände (MLCT) zu und abschalten. Impulsive Schwingingsspektrokopie wird am Beispiel von $[Fe(bpy)(CN)_4]^{2-}$ als geeinete Methode zu Identifizierung von MC-MLCT Übergängen etabliert. In der Folge wird die Methode auf einen Eisen(II)-N-heterozyklischen Carbenekomplex angewandt, wo sie eine ultraschnelle MLCT-MC Verzweigung nachweist. Zweitens wird die Photophysik und –chemie von Triphenylamin gründlich auf die Einflüsse des Lösungsmittels sowie dessen Sauerstoffgehalt und der erzwungenen Planarisierung untersucht. In n-Hexan wird Triphenylamin zu N-Phenylcarbazol umgesetzt, wobei Sauerstoff eine komplexe Doppelrolle zukommt. Der Umsatz wird durch die Planarisierung komplett unterbunden, da sie eine notwendige Vororientierung der p-Orbitale verhindert. In Chloroform kommt es zu einem ultraschnellen Elektronentransfer an das Lösungsmittel. Das gebildete Radikalkation bildet anschließend das Chromophordimer.

Publications and Conference Contributions:

Vibrational Coherence Spectroscopy Identifies Ultrafast Branching in an Iron(II) Sensitizer. Hainer, F.; Alagna, N.; Reddy Marri, A.; Penfold, T.J.; Gros, P.C.; Haacke, S.; and Buckup, T.; Journal of Physical Chemistry Letters, **2021**, 12, 8560-8565

Femtosecond Electronic and Vibrational Spectroscopy of the Excited States in Fe(II)-NHC Complexes. Hainer, F.; Alagna, N.; Liu, L.; Darari, M.; Gros, P.C.; Penfold, T.J., Buckup, T.; and Haacke, S.; International Conference on Photochemistry, 2021, Virtual Conference

Excited-State Dynamics of Triphenylamine. Hainer, F.; Jocic, A.; Kivala, M.; Buckup, T.; 2nd Symposium on Material for Organic Electronics: Synthesis, Spectroscopy and Theory, 2022, Heidelberg, Germany

Femtosecond Vibrational Spectroscopy of Fe(II)-NHC Complexes. Hainer, F.; Darari, M.; Gros, P.C.; Penfold, T.J.; Haacke, S.; and Buckup, T.; 28th PhotoIUPAC, 2022, Amsterdam, Netherlands

Table of Contents

1 Introduction 1

2 Theory 5

  2.1 Central concepts of photophysics 7

    2.1.1 Potential Energy Surfaces and non-radiative transitions 7

    2.1.2 Radiative transitions and selection rules 8

    2.1.3 The Franck-Condon principle 9

    2.1.4 Tuning of excited-state dynamics 11

  2.2 Excited state tuning by solvent choice 13

  2.3 Excited state tuning by chemical modification 17

    2.3.1 Ligand field transitions and metal centered states 17

    2.3.2 Metal to ligand charge transfer states 19

    2.3.3 Excited state tuning by ligand choice 20

3 Methods 25

  3.1 Perturbative description of nonlinear spectroscopy[56, 57] 27

  3.2 Transient absorption spectroscopy 31

    3.2.1 Analysis of TA datasets 32

  3.3 Impulsive vibrational coherence spectroscopy 37

    3.3.1 Analysis of IVS data 40

4 Experimental Setups 45

  4.1 Transient Absorption, (Pump-)Impulsive Vibrational Spectroscopy 45

    4.1.1 Setup 45

    4.1.2 White light generation 47

    4.1.3 VIS Pump, Push & Probe 48

    4.1.4 Prism compressor 49

  4.2 Transient Absorption, UV Pump 51

    4.2.1 Setup 51

    4.2.2 White light probe spectra 53

  4.3 Sample preparation 55

    4.3.1 General sample preparation 55

    4.3.2 Degassing procedure 55

    4.3.3 Irradiation series 56

5 Exploring MC and MLCT states of Fe(II) complexes 57

  5.1 Photophysics and solvatochromism of $[Fe(bpy)(CN)_4]^{2-}$ 57

  5.2 Characterization of excited-state dynamics of $[Fe(bpy)(CN)_4]^{2-}$ in Methanol 61

5.3 Characterization of excited-state dynamics of $[Fe(bpy)(CN)_4]^{2-}$ in DMSO 67
5.4 Photophysics of $[Fe(cpbmi)_2]^{2+}$ investigated for the role of metal centered states[86] 73
6 Photophysics and -chemistry of triphenylamines 83
6.1 Photochemical reactivity of TPA in hexane 87
6.2 Photophysics of DTPA in hexane 105
6.3 Photochemical reactivity of TPA and DTPA in chloroform 113
7 Conclusion & Outlook 121
7.1 Identification of elusive MLCT-loss channels in Fe(II) complexes 121
7.2 Manipulation of TPA photophysics and –chemistry by oxygen and solvent choice 123
8 References 125
9 Acknowledgements 135

1 Introduction

Classical chemistry has undoubtedly gathered myriads of ways to prepare desirable molecular structures. Along the way it has abstracted trends, rules and explained exceptions and bundled them together in a bouquet of specialized fields to guide and predict chemical reactions. For the process of breaking and making of bonds, it always requires the necessary energy (albeit just a barrier) to be provided by reagents of high chemical energy (for the case of spontaneous reactions) and/or heat. In the face of global warming and the ongoing energy crisis both strategies have proven themselves as inefficient regarding the evermore expensive resource energy. Obviously, the usage of reagents of high chemical energy (such as oxidizing or reducing agents) merely shifts energy costs up the supply chain. In fact, many of these high energy reagents or their precursors are already produced electrochemically, because they are thermally inaccessible. Heat on the other hand is a very available, yet extraordinarily untargeted form of energy. It is distributed statistically over all degrees of freedom, not only on the reagent molecules, but on the solvent's too. In photochemistry, the energy is applied in quanta, the photons, to individual molecules. A photon of typical visible wavelength (λ=600 nm) carries ~2.0 eV of energy (in the order of magnitude of binding energies), corresponding to a thermal energy of ~24000 K. From this rough estimate it becomes evident, that this amount of energy cannot purely be stored in translation, rotation, and vibration, as is the case with thermal energy. Instead, while thermal chemistry is limited to the electronic ground state, photoexcited molecules take on electronically excited states, in which their physical and chemical properties may be altered drastically, leading to entirely new (reactive) pathways (Figure 1.1). These may include elongation or breakage of bonds, formation of entirely new bonds or electron transfer, to name just the examples investigated in this work. This versatility and the chance to utilize light as energy source are why photophysical and -chemical

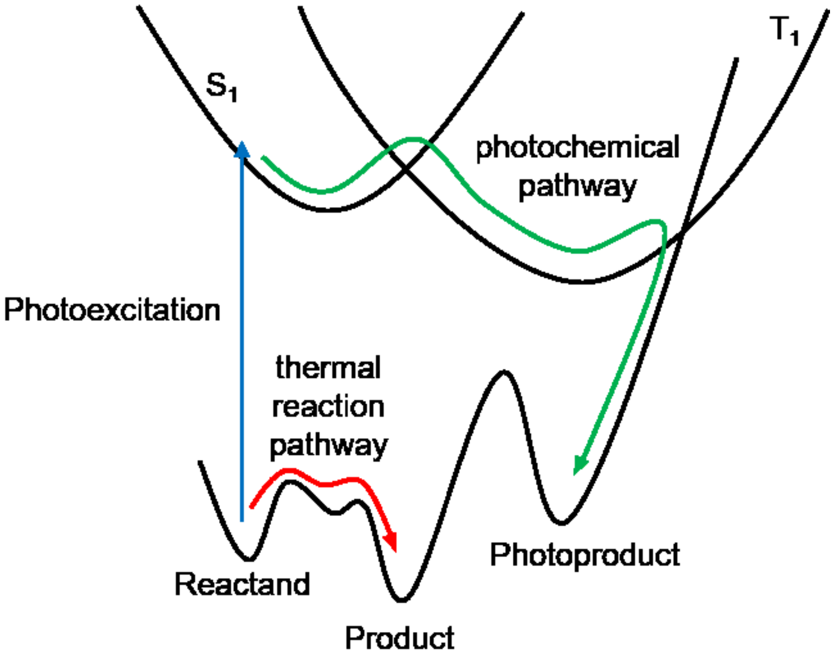

Figure 1.1: Scheme of ground and excited-state potential energy surfaces depicting the qualitative difference between thermally activated chemistry (red arrow) and photochemistry (green arrow).

processes are at the heart of many promising technologies stretching from solar energy harvesting (photovoltaic), to photocatalysis and precisely timed and localized medical applications.[1]

For each application, devices are meticulously designed to guide and direct the energy provided by the incoming light as efficiently as possible to the designated purpose. This also applies to the molecular systems that first absorb the incoming light. It is critical, that their excited-state potential energy surfaces (PES) are suited to funnel the molecules into specific states and geometries to form photoproducts or pass the energy on to external acceptors. Understanding the influence of different tuning strategies is key to the rational design of suitable chromophores. Preparation and characterization of the photoinduced excited states is therefore a prerequisite to the advancement of the abovementioned technologies.

Every waking minute, we are exposed to myriads of light-matter interactions and the excited-state dynamics they induce, from flower petals and leaves to sunscreens, solar cells, pens, highlighters, posters, good-night books and glow-in-the-dark pacifiers. However, only exceptional cases of these excited-state dynamics are radiative of nature, show macroscopic responses and occur on perceivable timescales, so that they can be followed by eye (as is the case with the glow-in-the-dark pacifier). The vast majority of light-induced excited-state dynamics remain hidden to the bare eye due to the unperceivable timescales and unordered fashion in which they occur. In the field of spectroscopy, numerous techniques have been developed to relate transmitted, scattered or reflected light to physical properties of the samples under investigation in equilibrium (ground state). However, with continuous irradiation, even coupled to fast acquisition times of, e.g., 1 ms it is not feasible to monitor excited-state properties behind photophysical or -chemical processes that last, e.g., 1 ns. Firstly, the dynamics will not start simultaneously in the molecules, but will rather be triggered at random by the constant flow of light. Therefore, one would record a mixture of all excited and ground states, averaged over 1 ms exposure time. It is therefore not possible to gain information about the sequence of excited states from these steady-state experiments. Secondly, it is intuitive, that states with long lifetimes contribute more to such a temporally averaged signal than short-lived ones do. While excited states in principle do contribute to the recorded signal, the ground-state contribution easily exceeds any short-lived excited-state contributions by orders of magnitude. The field of time-resolved spectroscopy addresses both these issues by using ultrashort laser pulses to both trigger and probe excited-state dynamics. By triggering excited-state dynamics simultaneously, i.e., faster than the dynamics of interest, the excited-state contributions of the individual molecules add up to a macroscopic signal. Usage of ultrashort laser pulses as probe reduces the exposure time down to femto- or even attoseconds. Both triggering and probing the excited-state dynamics therefore limit the achievable temporal resolution. Different techniques have been developed to probe distinct excited-state properties. In this work, transient absorption and impulsive vibrational spectroscopy are applied to rationalize three strategies for shaping the excited-state potential energy surfaces in two classes of samples.

The first class of samples are iron(II)complexes which are promising candidates to replace the toxic and expensive ruthenium(II)complexes in light-harvesting applications. Unlike their heavier homologues, which are established as dye sensitizers in solar cells,[2, 3] photochemotherapeutics[1, 4, 5] and molecular motors,[6] iron(II)complexes suffer from ultrafast deactivation of the highly desirable, bright metal-to-ligand charge-transfer states (MLCT). Instead, they tend to relax into high-spin metal centered (MC) states, sometimes referred to as ligand field- or d-d states, on the femtosecond timescale.[7, 8] A direct approach to expulse these MC states from the photophysics is to introduce strongly σ-donating ligands, increasing the ligand field splitting energy which needs to be overcome for their formation. In this regard, transient absorption (TA) and impulsive vibrational spectroscopy (IVS) are employed to $[Fe(bpy)(CN)_4]^{2-}$ and comparisons to $[Fe(bpy)_3]^{2+}$ and $[Fe(CN)_6]^{4-}$ known from literature are drawn to characterize, how the ligand design shapes the PES and channels the photophysics. As a second strategy for the tuning of excited-state energies, the choice of solvent is examined in $[Fe(bpy)(CN)_4]^{2-}$, which is dissolved in methanol and DMSO to compare Lewis acidic and non-acidic solvents. This direct comparison of the same molecular system in two different solvents allows to establish IVS as sensitive to MLCT – MC transitions. The technique is then applied to $[Fe(cpbmi)_2]^{2+}$, a promising dye sensitizer candidate, to clarify the involvement of spectrally elusive MC states in its photophysics. The cpbmi ligand is specifically designed as a combination of an isonicotinic acid and two N-heterocyclic carbene units. Both features have distinct purposes in tuning the excited-state landscape to optimize MLCT lifetime. The isonicotinic acid, as a pyridine derivate, allows formation of MLCT states in the first place. The N-heterocyclic carbene units on the other hand impose a strong ligand field to the central Fe^{2+} ion, meant to suppress MC loss channels.

The second class of samples are triphenylamine (TPA) and derived molecules, whose reversible oxidizability have gained them attention due to their applicability as hole-conductors in organic electronics. They are reported to have rich photophysics and – chemistry, which is reproduced and expanded on in this work. The multitude of partaking excited states is manipulated using the presence and absence of oxygen, structural modifications to enforce a planar geometry and by the choice of solvent.

The excited-state dynamics of TPA in n-hexane involve two distinct triplet states particularly susceptible to molecular oxygen in the solution. Direct comparison of experiments with and without dissolved oxygen allows clear characterization of its influence on the individual states. Chemical modification of the chromophore's molecular structure intuitively affects for the associated ground and excited-state properties.

In this work, a TPA and a derivate with dimethylmethylene-bridges between the ortho positions of neighboring phenyl rings (DTPA) are investigated. These bridges do not actively contribute to the conjugated π-system, primarily responsible for the optically bright π-π* transitions. Instead, they enforce a planar geometry of the phenyl rings, improving the π-conjugation through the central nitrogen atom. Contrasting the transient absorption of TPA and DTPA enables identification of the exact point, where the excited-state dynamics diverge. Lastly, TPA and DTPA are investigated in chloroform. In contrast to n-hexane, this is a highly electron affine solvent, opening an entirely new photochemical relaxation pathway via electron transfer leading to dimer formation of both chromophores.

This work is structured as follows:

- In chapter 2 the required theoretical background for the characterization of excited states is presented and two major tuning strategies are introduced.
- In chapter 3 the time-resolved spectroscopic methods employed in this work are described theoretically.
- In chapter 4 the experimental implementation of the presented methods is documented.
- Chapter 5 presents the work on the characterization of the excited states of iron(II) complexes as metal-centered or metal-to-ligand charge transfer states.
- In chapter 6 the exploration of the photophysics and –chemistry of TPA and DTPA with respect to solvent and oxygen content is given.
- A summarizing conclusion and outlook on possible future expansions of this work is shown in chapter 7.

2 Theory

Photophysics and photochemistry are characterized by a photoexcitation, transferring population from the electronic ground state, to electronically excited states, followed by relaxation through (several) geometric and electronic configurations, governed by the corresponding potential energy surfaces (PES, Figure 2.1). If the population relaxes back to the initial (local) minimum on the ground-state PES, i.e., the chromophore is recovered, this is categorized as photophysics. In photochemistry, on the other hand, the initial chromophore forms a photoproduct as result of the excited-state cascade. The changes subjected to the chromophore may vary from cleavage of chemical structures to isomerization, although the distinction to photophysics becomes blurred on the latter end of the scale. A prominent example of a fringe case are the molecular motors devised by 2016 Nobel Laureate Ben Feringa: These overcrowded alkene-based motors can be isolated in different states of their light- and heat driven rotation around the C=C double bond, and their specific characteristics differ significantly. However, as the concept of a motor suggests, the process is cyclic, so that the initial isomer can indeed be recovered quantitatively.

There are many possible routes a photoexcited chromophore may take in relaxing back to its initial or to a photoproduct's ground state. Typically, implementation into an efficient application requires a well-defined relaxation route. The iron(II)complexes examined in this work for example are desired to feature long lived MLCT states, as this constitutes an initial charge separation. Oftentimes it is also required to prevent the formation of photoproducts to inhibit photodamage on the sensitizing unit. As photophysical and photochemical processes typically occur on the femtosecond to microsecond timescale, they are typically too fast to allow for manipulation of the ongoing relaxation process. Exceptions are summarized under the term coherent

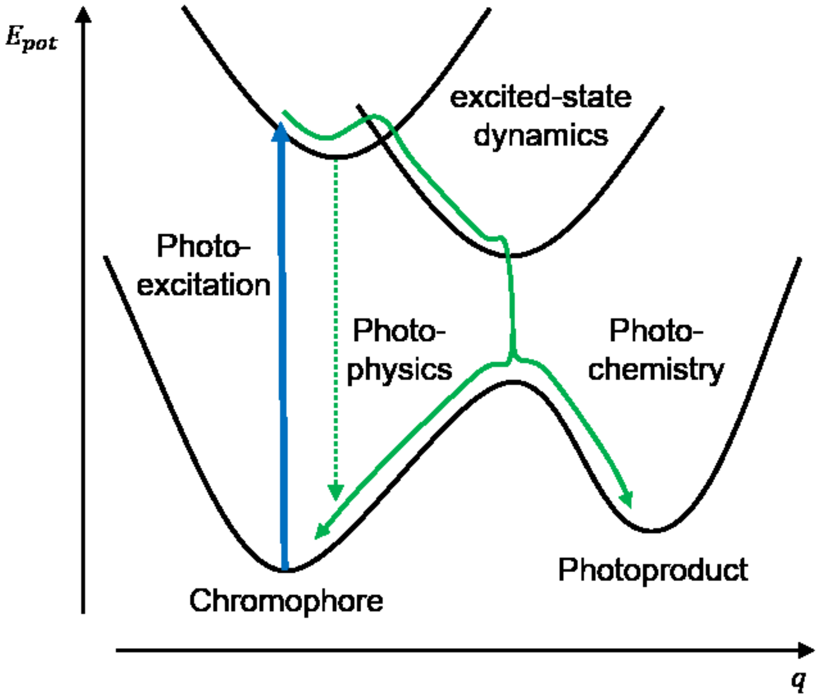

Figure 2.1: Schematic representation of ground- and excited-state potential energy surfaces governing excited-state dynamics and the resulting photophysics or photochemistry.

control: meticulously timed and shaped series of laser pulses control the photoexcited population to favor certain outcomes of the relaxation process. Due to the inefficient energy conversion of (pulsed) Lasers, coherent control has so far been an exclusively academic field. By far the most efficient approach to the design of desired photophysical and –chemical properties, is to regard them as predetermined by the chemical structure and environment of the chromophore. From this approach follows the necessity to understand how structure and environment influence the excited states at play, to purposefully design those. It is the main goal of this work to understand these relations between structure and photophysical and photochemical properties of several examples of the sample classes introduced above. To do so, the reader will be introduced to the most relevant concepts required to describe and understand photophysics and photochemistry in section 2.1. Sections 2.2 and 2.3 are then dedicated to particular strategies to influence the individual states.

2.1 Central concepts of photophysics

2.1.1 **Potential Energy Surfaces and non-radiative transitions**

The Born-Oppenheimer approximation states that the total wave function describing a molecule in a specific state can be constructed using a product Ansatz of an electronic and a nuclear wave function. This is justified considering, that typically electrons move significantly faster than the much heavier nuclei and hence adapt to their changes rapidly. The positions of the nuclei, which constitute a molecular geometry, can be considered parametrically in the electronic wave function. Hence, an electronic state of a molecule is characterized by a multi-electron wave function $|\Psi_{el}\rangle$, which is an eigenvector solving the electronic part of the Schrödinger equation for a given molecular geometry. The multi-electron wave function $|\Psi_{el}\rangle$ itself is comprised of one-electron wave functions $|\psi_{el}\rangle$, the so-called molecular orbitals (MOs). Electronic states $|\Psi_{el}\rangle$ differ in the contribution from the individual MOs. The eigenvalue corresponding to an electronic eigenvector $|\Psi_{el}\rangle$ at a specific geometry is the potential energy. Mapping out the potential energy as a function of the geometry hence yields the potential energy surface. Since any nonlinear n-atom molecule has 3n-6 internal coordinates (i.e., normal modes) defining its geometry, these surfaces are 3n-6-dimensional, making them hypersurfaces, strictly speaking. However, for the discussion of a given problem, typically only a cut through the PES along one or two relevant internal coordinates is depicted.

A (local) minimum on such a PES corresponds to a (meta-) stable geometry, which may resemble a specific isomer. The depth of said minimum (i.e., energy of smallest barrier) characterizes the stability of the geometry and the curvature of the PES along a given normal mode defines its vibrational frequency.

Since there are multiple eigenvectors solving the molecular Schrödinger equation, there are also multiple electronic states and associated PES. These generally have varying shapes and can approach and intersect each other at specific geometries.

Transitioning from one electronic state to another is hence effortlessly possible at said intersections. If the spin state is retained through such a transition, this process is called internal conversion (IC), if it changes, this is called intersystem crossing (ISC). Since these transitions pass through intersections of PES of different states, no energy difference needs to be overcome once the geometry is reached.

It is also possible to construct a PES considering more than one molecule. Chemical reactions can be regarded as a population transfer from a (local) minimum to another on one, either on the same, or another PES. Classical, thermally activated chemistry is hereby limited to an evolution on the ground state – i.e., the state of lowest potential energy at the given geometry. The thermal energy is hereby required to overcome the barrier on a PES to allow for evolution towards the product geometry. Even though the state of lowest potential energy may change during the reaction, the molecular system will always evolve on the lowest PES.

The great advantage of photophysics and photochemistry is, that excited states are accessed, opening entirely new routes on which the system can evolve. Therefore, transitions between states are possible, even at geometries where their PES do not intersect. The energy difference then needs to be overcome by absorption or emission of a photon introducing new possibilities and constraints, which are addressed in the next paragraph.

2.1.2 **Radiative transitions and selection rules**

Light mediated transitions between the initial state $|\Psi_i\rangle$ and final state $|\Psi_f\rangle$ can, to a first approximation, be described quantum mechanically using the transition dipole matrix element $\vec{M}_{if}$ given in Eq. 2.1.

$$\vec{M}_{if} = \langle \Psi_i | \vec{\mu} | \Psi_f \rangle \qquad \text{Eq. 2.1}$$

The probability for a radiative transition is the square of this matrix element. Close inspection of its symmetry properties can therefore give qualitative information about relative intensities of absorption and emission bands. Considering the Born-Oppenheimer approximation in section 2.1.1, the total wave function $|\Psi_i\rangle$ can be constructed using a product Ansatz (Eq. 2.2) from the electronic $|\Phi_i\rangle$ and the nuclear wave function $|\eta_i\rangle$:

$$|\Psi_i\rangle = |\Phi_i\rangle * |\eta_i\rangle \qquad \text{Eq. 2.2}$$

The total electronic wave function $|\Phi_i\rangle$ in turn is constructed of a product of an angular momentum term $|\varphi_i\rangle$ and a spin term $|\sigma_i\rangle$ (Eq. 2.3).

$$|\Phi_i\rangle = |\varphi_i\rangle * |\sigma_i\rangle \qquad \text{Eq. 2.3}$$

Since the dipole moment operator $\vec{\mu}$ does not act on the electron spin function $|\sigma_j\rangle$ nor the nuclear wave function $|\eta_i\rangle$ the matrix element simplifies to the expression given in Eq. 2.4:

$$\vec{M}_{if} = \langle \varphi_i | \vec{\mu} | \varphi_f \rangle * \langle \sigma_i | \sigma_f \rangle * \langle \eta_i | \eta_f \rangle \qquad \text{Eq. 2.4}$$

Each of the three terms contributing to $\vec{M}_{if}$ as a factor can either favor radiative transitions by being large or forbid the transition by being zero.

Let us first regard $\langle \varphi_i | \vec{\mu} | \varphi_f \rangle$. As this bra-ket notation represents a symmetric integral ($\int_{-\infty}^{+\infty} d\vec{r}$) over a product of three functions, the element $\langle \varphi_i | \vec{\mu} | \varphi_f \rangle$ is zero, if the product is antisymmetric, i.e. if it has odd parity. In centrosymmetric molecules, such as the (approximately) octahedral coordination complexes in this work, the electronic states inherit the point symmetry and are hence either of odd or even parity. The dipole moment operator itself ($\vec{\mu} = q * \vec{r}$) is always of odd parity. It follows, that, in centrosymmetric molecules, the initial and final state, $|\varphi_i\rangle$ and $|\varphi_f\rangle$, must be of opposing parity for the transition to be allowed. Prominently, transitions between d-orbitals are hence symmetry forbidden, leading to their low intensity, especially compared to charge-transfer transitions. This selection rule is named Laporte-rule after German American physicist Otto Laporte.

The second term of Eq. 2.4 $\langle \sigma_i | \sigma_f \rangle$ is the overlap integral between the initial and final spin state. By definition, spin functions are orthonormal, i.e., this integral equals one if the two spin states are equal or zero, if they are not. Hence, radiative transitions between states of differing spin are strictly forbidden. Therefore, photoexcitation occurs to a state of the same spin as the ground state (typically singlet), and that fluorescence, the radiative deactivation of an excited state, is only possible between states of the same spin. Intersystem crossing to a state of higher spin inhibits fluorescence to the ground state and consequently enables longer excited-state lifetimes.

The last factor in Eq. 2.4, $\langle\eta_i|\eta_f\rangle$, is the overlap of the initial and final nuclear wave function and will be considered in the following section.

2.1.3 **The Franck-Condon principle**

Section 2.1.1 introduced PES as the electrons' potential energy, on which the nuclei, i.e., the molecular geometry, evolve with the derived consequences for configurational stability and vibrational frequencies. The factor $\langle\eta_i|\eta_f\rangle$ in Eq. 2.4 describing the transition dipole matrix element $\vec{M}_{if}$ now requires a (qualitative) analysis of the nuclear wave function to discuss the role of the geometry for radiative transitions.

The PES minima, corresponding to stable geometric configurations, are wells, in which the nuclei oscillate. These minima and the region around them can be described as a 3n-6-dimensional (harmonic) oscillator with approximately parabolic potential. Solutions to the corresponding Schrödinger equation are the nuclear wave functions $|\eta_i\rangle$. One-dimensional cuts through two PES with corresponding nuclear wave functions are depicted in Figure 2.2. The transition probability and hence intensity of the corresponding absorption / emission band is proportional to the absolute square $|\langle\eta_i|\eta_f\rangle|^2$. These properties are called Franck-Condon factors, named after James Franck who proposed vibrational excitation occurs along with electronic excitation and Edward Condon, who expanded the idea by quantification based on harmonic

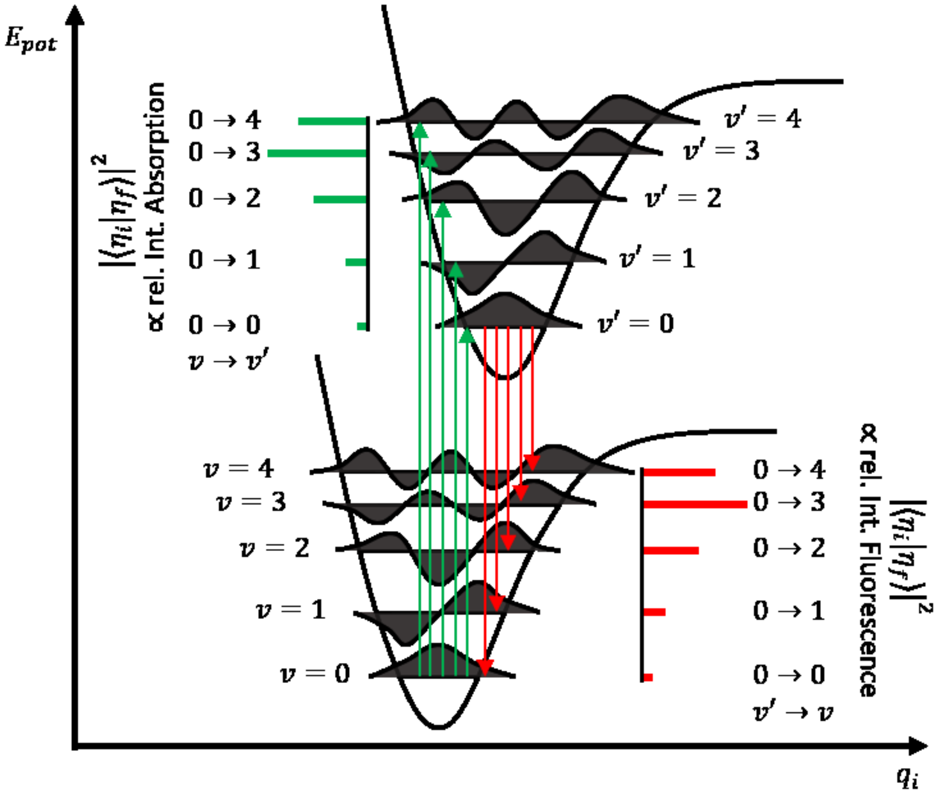

Figure 2.2: Energy diagram elucidating the Franck-Condon factors for absorption (green) and fluorescence (red). Each overlap $\langle\eta_i|\eta_f\rangle$ depends on a nuclear wave function in the electronic ground and excited state.

oscillator eigenstates.[9, 10] Since electrons move much faster than the significantly heavier nuclei, a change of the electronic state occurs quasi instantly with respect to the molecular geometry. For the duration of the optical transition, the molecular geometry is virtually frozen. Hence, the absorption or emission of a photon can be represented as vertical lines in a graph plotting the energy E_{pot} over a normal mode q_i, as is shown in Figure 2.2.

Let us first consider the absorption of a photon. At room temperature, almost exclusively the lowest vibrational level of the electronic ground state is populated. Hence, the ground-state equilibrium geometry is the entry point on the excited-state PES. This point, or region, defined by the square of the vibrational ground-state wave function $|\eta_{v=0}|^2$, is therefore called the Franck-Condon region in all excited states. Absorption of a photon leads to a vertical electronic transition to different vibrational levels within these specific regions. The subsequent evolution of the generated wave packet is strongly influenced by the exact configuration reached after excitation. As different electronic states correspond to different bonding properties, the equilibrium geometry of excited states is not necessarily that of the ground state. Hence the potential wells of electronic ground and excited states are typically shifted along some internal coordinates with respect to one another. Consequently, after photoexcitation molecules are generally in a geometric disequilibrium, represented by a vibrationally excited state. Transitions to these excited vibrational states are doubly favored in this process: firstly, they allow for larger displacement from the equilibrium geometry, due to the (approximately) parabolic potential. Secondly, higher vibrational levels have increasingly larger relative probability density on the edges of the potential, which agrees with the correspondence principle. As a result, the transitions probabilities to the final vibrational states $\eta_{v'}$, given by their Franck-Condon factors $|\langle\eta_{v=0}|\eta_{v'}\rangle|^2$, are typically distributed as shown in Figure 2.2.

After photoexcitation, the molecular geometry relaxes from the Franck-Condon region along the local gradient, either into a (local) minimum on the PES, or the PES may even have a dissociative course, resulting in photocleavage. If a binding excited state was populated, the question of the subsequent return to the chromophore or photoproduct ground state arises. Here radiationless and radiative deactivation channels are competing. As rule of thumb, excited states that are efficiently populated by photoexcitation (because they are spin- and Laporte allowed) are principally also suited for fluorescence. However, spontaneous fluorescence is a statistically occurring process and may be easily outcompeted by effective radiationless transitions, such as IC or even ISC in certain circumstances. If a bright state is long lived enough for fluorescence to be a meaningful deactivation channel, the molecules typically had sufficient time to relax to the vibrational ground state within the electronic excited state. These states are in literature also sometimes referred to as Thexi states (thermally equilibrated excited states),[11, 12] and the process of vibrational relaxation as vibrational cooling. For fluorescence, this means, that the vertical energy difference to the electronic ground state decreases, compared to the initial absorption energy. Hence, fluorescence displays a characteristic red-shift with respect to absorption, and the Franck-Condon factors dictating the relative amplitude of the vibronic transitions are $|\langle\eta_{v'=0}|\eta_{v}\rangle|^2$.

At room temperature, and especially in solution, the individual vibronic transitions are not clearly resolved. Doppler broadening and a statistic distribution of solvent interactions altering the energy difference obscure the separate bands. Nevertheless, the concept of the Franck-Condon region is central to understanding and purposefully tuning excited dynamics, as described in the next section.

2.1.4 **Tuning of excited-state dynamics**

With the central concepts required to describe photophysics established, the tuning of photophysics and –chemistry through manipulation of the participating states will now be discussed. Tuning the photophysics of a given sample into a specific direction is typically done by the introduction or removal of barriers in an unwanted or wanted pathway on the partaking PESs, respectively. This way, the route of least resistance can be changed, stirring the excited-state population into a favorable direction. Popular strategies include extending excited-state lifetime to allow for efficient luminescence or charge transfer, or the ultrafast radiationless deactivation towards a photoproduct for potent photoswitches. Figure 2.3 shows three main vectors, along which barriers may be introduced.

The initial situation in all panels of Figure 2.3 shows a very effective radiationless relaxation of the S_1 to the ground state S_0 via a mediating excited state T_1. The combination of lower energy and shifted equilibrium geometry results in the S_1-T_1-intersection being close to the S_1 equilibrium geometry, allowing for a rapid ISC. Similarly, there is also no energy barrier between the T_1-S_0-intersection and the T_1 equilibrium geometry. As result, both the S_1 and the T_1 lifetime are expected to be short. The tuning of the triplet state in both cases a and b result in a significantly altered situation: In a, the energy of the T_1 is greatly increased, which also introduces a barrier ΔE between the S_1 equilibrium geometry and the S_1-T_1-intersection. Depending on the exact position of the Franck-Condon region on the S_1, molecules might not have sufficient vibrational energy to overcome said barrier. Even if the barrier was overcome, molecules could easily reverse the ISC from the T_1 to the S_1, as there is

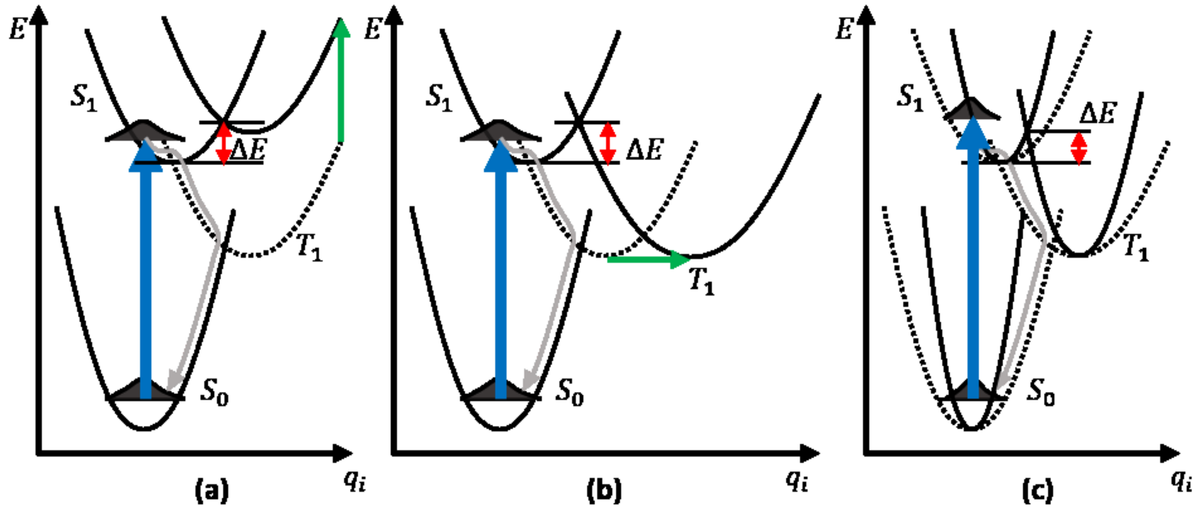

Figure 2.3: Ultrafast radiationless deactivation (grey arrow) in initial arrangement of states (dotted lines) circumvented by excited-state barriers (red) introduced by tuning (a) excited-state energy, (b) geometry and (c) shape.

almost no energy barrier there. This would make for a very efficient fluorescence dye, for example.

In b on the other hand, the energy of the T_1 is not changed, but the equilibrium geometry is shifted significantly along q_i. Notably, this also introduces a large energy barrier between the S_1 minimum and its intersection with the T_1 PES. However, it also shifts the T_1 minimum away from the intersection with the S_0. While, similarly to a the S_1 is hence prolonged, in b the T_1 lifetime is drastically extended and not cut short.

In Figure 2.3c the equilibrium geometries and energy minima of the participating states are retained as in the initial condition of a and b. However, the slopes of the PES cut along q_i are much steeper, which might be accomplished by introduction of bulky substituents limiting spatial freedom deformation modes. In effect, the radiative S_0-S_1 transition is blue-shifted significantly, leading to a larger portion of vibrational energy within the S_1. Noticeably, the vibrational energy exceeds the S_1-T_1barrier, so that the T_1 may be populated effectively. Given a temporal resolution shorter than the vibrational frequency of q_i in the S_1, time-resolved spectroscopy could be able to identify bursts of T_1 formation as the wave packet launched along q_i repeatedly traverses the S_1-T_1 intersection. In this variant of the same three states, the S_1 might show two distinct lifetimes. Firstly, a short one, corresponding to the S_1-T_1 transition from the vibrationally excited S_1, lying well above the S_1-T_1 barrier. Secondly, the lifetime of the vibrationally equilibrated S_1, lying below the S_1-T_1 barrier, which might correspond to a slow, radiationless transition to the T_1, or be limited by the radiative decay to the ground state (fluorescence). The branching ratio between the two relaxation channels would depend on the vibrational redistribution, i.e., how fast vibrational energy of the mode q_i is transferred to other modes.

These three qualitative examples stress, how complex the tuning of photophysical properties can be: Even if, as is depicted in Figure 2.3a and b, individual states could be addressed by some tuning mechanism, intersections with and hence transitions to several other states are affected, changing the course of the relaxation pathway.

The effects of inducing or clearing out barriers or changing the Franck-Condon region for the resulting dynamics have been discussed. There are many strategies to cause these changes in the PESs. Three of them have been applied in this work and will be introduced in the following sections.

2.2 Excited state tuning by solvent choice

As explained in Section 2.1.1, electronic states $|\Psi_{el}\rangle$ differ in the population of molecular orbitals $|\psi_{el}\rangle$. A differing electron configuration implies a differing charge distribution and hence a different permanent molecular dipole moment. In fact, it is precisely this change in charge distribution (change in MO population) that enables optical transitions according to the transition dipole moment (Eq. 2.5):

$$\vec{M}_{if} \propto \langle \Psi_{el,i} | \vec{\mu} | \Psi_{el,f} \rangle \qquad \text{Eq. 2.5}$$

This implies that the charge distribution of the molecule changes abruptly with an optical transition. In dissolved samples, the solvent sphere, which at the moment of photoexcitation is optimized for the ground-state charge distribution, can also affect the excited-state dynamics.

Firstly, the question arises, how the solvent affects the stability of excited-state molecules. While a nonpolar solvent may be very well suited to support a nonpolar chromophore, this might not be the case for a charge separated excited state and vice versa. Hereby the interactions between solvent and solute may be purely electrostatic, but also more intricate like Lewis acid and base interplay or explicit formation of hydrogen bonds. The lifetime of excited states typically does not allow for aggregation of “insoluble” excited-state molecules, but the energy difference between a ground and an excited state may indeed be affected by solvent choice.

Figure 2.4a displays two cases: In the first, the ground state is stabilized by the solvent, but the excited state is not. This results in a large energy difference that needs to be overcome by the absorbed light. In the second case, the solvent stabilizes the excited state much better, but supports the ground state more weakly. Both effects decrease the energy difference between the ground and the excited state, leading to a red-shifted absorption band in the latter case. This change in absorption, and hence perceived color, with the choice of solvent is termed solvatochromism and can affect excited-state dynamics. Intuitively, solvatochromism allows the manipulation of the relative energetic position of the excited state partaking in the optically bright transition.

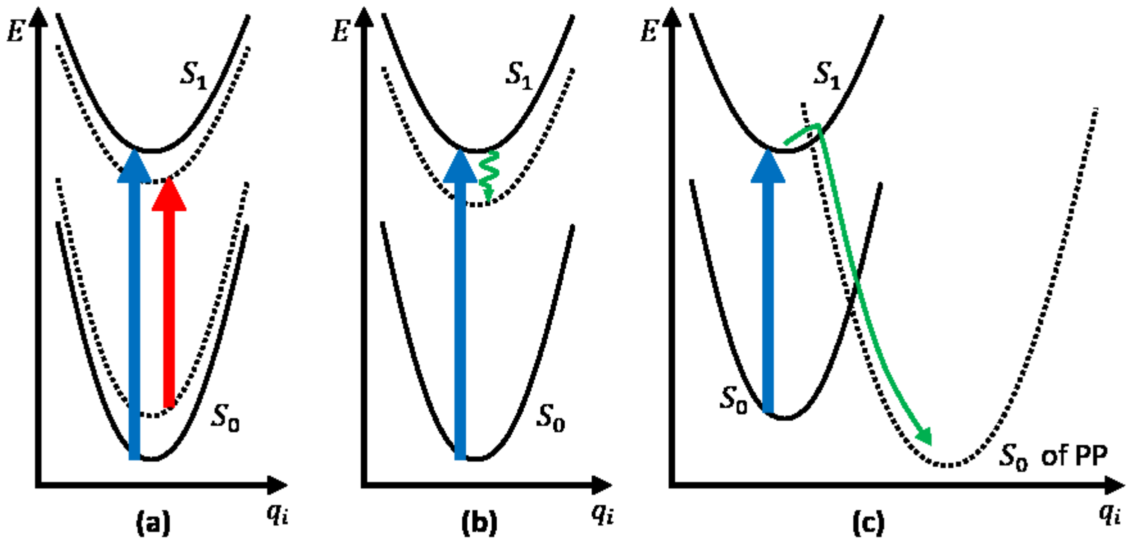

Figure 2.4: Solvent effects on optical transitions and excited-state dynamics: (a) Solvatochromism, (b) dynamic stokes shift (c) solvent as reactant forming a photoproduct (PP).

This may be exploited to introduce or remove barriers between the initially populated state (in this case S_1) and other excited states. More generally, however, energy differences between all electronic states differing significantly in charge distribution can be affected by the solvent choice. The chance of manipulation is consequently not limited to the state populated by photoexcitation, as the classical understanding of solvatochromism would suggest.

Expanding on the static understanding of the solvent-solute interactions explaining solvatochromism, the solvent sphere will also respond to the photoexcitation and hence charge redistribution, dynamically. While the solvent sphere is optimized for the ground-state charge distribution at the instance of photoexcitation, it will also adapt to the altered charge distribution by rearrangement into more favorable solvent-solute interactions. Consequently, the newly populated excited state is stabilized dynamically after photoexcitation has occurred. This process is termed dynamic stokes shift. It is depicted in Figure 2.4b may be observed using time-resolved absorption or fluorescence spectroscopy. Since the energy of the populated state is lowered during the solvent adaptions, it manifests similarly to vibrational cooling, by red-shifted (stimulated) emission and blue-shifted absorption bands.

Lastly, solvents might be directly involved in the excited-state dynamics and change their outcome by participating in the photochemistry. While this might seem like the description of unlikely exceptional cases, it is worth considering two facts that make an involvement of the solvent more likely.

The obvious consideration is the sheer availability of solvent to the irradiated chromophore. The lifetimes of excited states limit the capabilities of molecules to diffuse and find suitable reaction partners, which is why most photochemical reactions are intramolecular. However, if the solvent can serve as a reaction partner, diffusion is no longer a limiting factor and favorable orientation may even be supported by the deliberate design of reaction sites. This easily facilitates reactant interactions within typical excited-state lifetimes, opening up the route to intermolecular photoreactions.

The other consideration is, that, as described earlier, photoexcited molecules carry amounts of energy that are not comparable with conventional chemistry. Hence, solvents considered stable, passive, or inert under thermal conditions, do not necessarily hold these qualities considering a chromophore under irradiation.

In the simplified electron configuration representation of electronic states in Figure 2.5, the ground state of an n-electron molecule can be regarded as the electronic configuration, with all the $n/2$ orbitals of lowest energy doubly occupied. An electronically excited state diverges from this by formally removing at least one electron from such an orbital and transferring it to a formerly unoccupied one. On one hand, electronically excited molecules can therefore serve as potent oxidizing agents by taking an electron from their surroundings to fill the empty orbital of low energy. On the other hand, they can also more easily transfer their electron promoted to a high-energy orbital to their surroundings, effectively acting as a reducing agent. Solvents that are prone to redox-reactions may therefore easily be affected, effectively

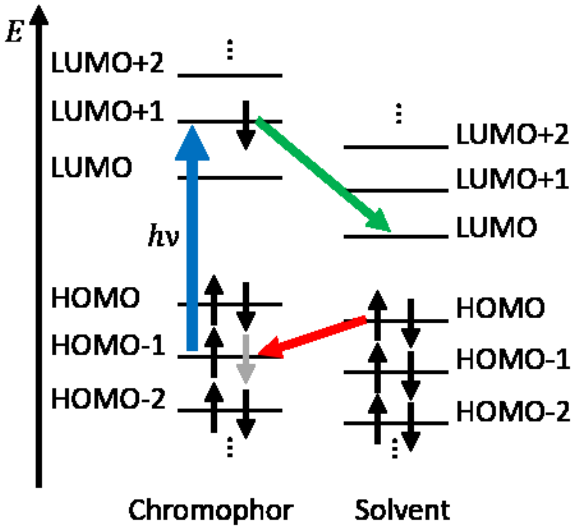

Figure 2.5: Chromophore and Solvent represented in MO electron configurations. After photoexcitation (blue arrow) both reduction (green arrow) and oxidation (red) of solvent become feasible.

quenching the “original” excited-state dynamics. This “detour” is purposefully exploited in the field of photocatalysis, where to this date, principally inorganic semiconductor nanoparticles like TiO_2 are employed in aqueous solution. In these cases, the MO structure is replaced by a band structure, yet the working principle remains the same.

Lastly, although it is not strictly part of the solvent, molecular oxygen, which under ambient conditions is inevitably contained in the solvent, is worth an additional examination. Molecular oxygen is a potent oxidizing agent with triplet ground state. Because most molecules have singlet ground state, oxidation reactions are impeded due to spin-state mismatch. However, many excited-state dynamics involve intersystem crossings from the initially populated excited singlet state to a triplet state, in which they are then vulnerable towards oxygen. Possible oxygen-related quenching mechanisms include triplet fusion and oxidation.[13, 14]

After this thorough examination of the chromophore’s surroundings, the next section will address excited state tuning by modifications on the chromophore itself.

2.3 Excited state tuning by chemical modification

The most intuitive approach to changing excited-state properties and consequently photo-physical or –chemical behavior is the chemical modification of the chromophore. This can include the introduction of electron rich or withdrawing groups to affect HOMO or LUMO energies, or blockage of otherwise susceptible positions to avert photodamage. More elaborate approaches may be linkage to another molecular subunit to enable energy transfer towards a reaction center, or dimerization of the original chromophore to enable intramolecular singlet fission. The multitude of chemical reactions, functionalizations and molecular engineering schemes open a vast field of possible modifications. Simple cause-and-effect connections can, however, often not be given, because the chemical composition affects many characteristics, which on their part also influence the photophysical and –chemical properties. To minimize at least molecular geometry as one significant strand of these multiple influences, this section will focus on transition metal complexes. They are one of the two classes of samples investigated in this work and ligand substitution is possible while keeping the molecular geometry mostly unchanged. In the first two sections, two important classes of excited states in the photophysics of transition metal complexes will be established and the third section will focus on the tuning of these states.

2.3.1 Ligand field transitions and metal centered states

Transition metal complexes consist of a transition metal atom, a cation in most cases, and ligands coordinating to it via free electron pairs forming bonds that can be described as of dative or covalent character. These ligands create an electric field, which affects the atomic orbitals of the central atom. While orbitals of closed shells are contracted and contribute little to molecular properties, orbitals of valence shells can be greatly affected by the presence of the ligands. In vacuo, the nth row transition metals in general adopt electron configurations of ns^2 (n-1)d^m because the ns-orbitals are of lower energy than the (n-1)d-orbitals. Figure 2.6 displays energy diagrams of valence orbitals of Fe^{2+}, which is the most important case in this work. In Figure 2.6a, the 4s-orbital is doubly populated, as it lies below the 3d-orbitals. A first consequence of the electrostatic ligand field is, that the ns-orbitals, which are more diffuse than the contracted (n-1)d-orbitals, are shifted up in energy. Consequently, in transition metal complexes, the central atom has two more d-electrons than it would have in vacuo. Let us therefore first consider the introduction of a theoretical spherically symmetric ligand field to the Fe^{2+} ion (Figure 2.6b). This ligand field shifts both the 4s and 3d-orbitals up in energy, although the 4s-orbitals are affected more strongly due to their wider expansion. Now all six valence electrons are distributed over the 5 d-orbitals. In realistic ligand fields, which are not spherically symmetric, the d-orbitals are not affected equally because they are not spherically symmetric, either. While the average d-orbital energy is also shifted upwards in energy, actual ligand fields also lead to a splitting into subgroups, depending on the symmetry of the complex (Figure 2.6c). In fact, in most cases it is the number of d-electrons at the central atom that dictates the symmetry of the ligands in such manner, that it allows for maximum stabilization of the populated d-orbitals. In the d^6 case of Fe^{2+}, localization of the negative charges at the corners of an octahedron causes the d-orbitals to split into two subgroups, the t_{2g} and the e_g manifold. The d-orbitals of the e_g-manifold, $d_{x^2-y^2}$ and d_{z^2}, point directly towards

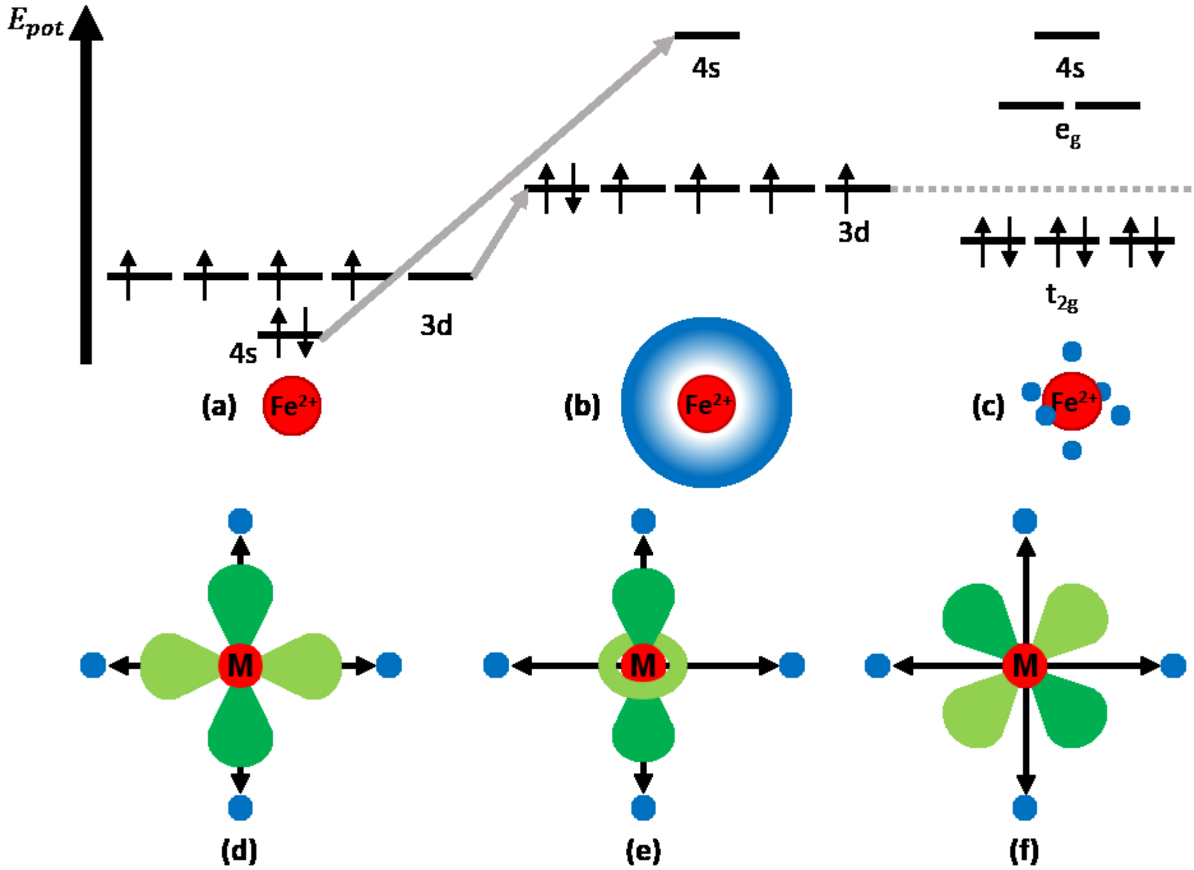

Figure 2.6: Top: Energy diagrams of valence orbitals of a Fe^{2+} cation (a) in vacuo, (b) in a spherically symmetric field and (c) in an octahedral ligand field. Dotted line represents average d-orbital energy to visualize ligand field stabilization. Bottom: Shape and orientation of d-orbitals in an octahedral ligand field: (d) $d_{x^2-y^2}$, (e) d_{z^2}, (f) d_{xy}, d_{xz} and d_{yz}.

the ligands, so that they are more strongly affected by the octahedral ligand field, than by a spherical one of the same net strength (Figure 2.6d+e). The d_{xy}, d_{xz} and d_{yz} orbitals in the t_{2g}-manifold on the other hand point in between ligands and are therefore less affected than in a spherical symmetric field (Figure 2.6f). Consequently, the e_g lies above and the t_{2g} below the energy of d-orbitals in the theoretical spherical field of equal net strength. In the case of the Fe^{2+} cation (d^6), all three orbitals of the t_{2g} manifold are therefore doubly populated resulting in maximum ligand field stabilization, zero net spin and a singlet ground state. Because this configuration generates the lowest possible net spin, it is called a low-spin configuration. If the ligand field splitting is small, it might become energetically favorable to populate the orbitals of the e_g-manifold before pairing the spins of electrons in the t_{2g} manifold. This strategy of distributing electrons into the d-orbitals accords to Hund's rule and results in a maximization of the net spin. Resulting configurations are termed high-spin configurations. In the present d^6-case of Fe^{2+} the maximum possible net spin is 2, corresponding to a quintuplet state. However, for octahedral coordination geometries, the sheer presence of six ligands typically results in sufficient ligand field strength to account for low-spin ground-state configurations.

Nonetheless, it is the central characteristic of photophysics, that it is not restricted to the ground state. Therefore, it is still interesting to consider the properties and energies of states, formally formed by transferring an electron within the d-orbital manifold. These states are called metal-centered (MC) states because the ligands do formally not contribute to them. As described in Section 2.1.2, radiative transitions between states of differing spin are forbidden, so direct photoexcitation from a low-spin ground to a high-spin excited state are optically forbidden. This is especially true for the approximately octahedral Fe^{2+} complexes investigated in this work, since their point symmetry means, that also the Laporte rule forbids d-d transitions. The ligand field- or d-d-transitions leading to MC states therefore have marginal molar absorption coefficients ε in the order of 10^{-3}-1 $lmol^{-1}cm^{-1}$.[15] Yet still MC states play an important role in many transition metal complex photophysics, as they can be populated via other mechanisms than direct optical excitation. Long-lived high-spin MC states for example are investigated under the term light induced excited-state spin trapping (LIESST)[16-18] as basis of memory storage devices. In applications based on the harvesting of light energy and charge separation however, MC states are unproductive because both the excited electron and the generated hole are located at the metal center. There they form undesired loss channels for another class of states satisfying the initial charge separation, which are discussed in the next section.

2.3.2 Metal to ligand charge transfer states

Excited states are termed charge transfer states when an electron is transferred from one site of the molecular chromophore to another. Since a hole is generated at the first site and an excess electron is brought to the second, this constitutes a charge separation on the molecular scale. In transition metal complexes, the different sites may be a metal center or a ligand, opening up four sub species of charge transfer states[19] named after the direction of the underlying electron transfer: metal-to-ligand (MLCT),[20] ligand-to-metal (LMCT),[21] ligand-to-ligand (LLCT),[22] and, in complexes incorporating multiple metal centers, metal-to-metal charge transfer states (MMCT).[23] Because the transitions leading to these charge transfer states are not generally spin- or even Laporte forbidden, they are much more bright (optically active) with absorption coefficients ε ranging from 10^2-10^5 mol^{-1}.[15] By far the most prominent examples of charge transfer states in transition metal complexes are MLCT states in $[Ru(bpy)_3]^{2+}$ and related compounds. They have bright transitions in the visible spectral range leading to ^{1}MLCT states, in which the Ru^{2+} center is formally oxidized to Ru^{3+} and a 2,2'-bipyridine ligand is reduced to 2,2'-bipyridine$^{\bullet-}$. The ^{1}MLCT state relaxes via ISC to a ^{3}MLCT state living for hundreds of nanoseconds. This is highly desirable for applications that rely on proceeding this initial charge separation because it allows for efficient collection of the excess electron located on the complex's periphery. It is for these particular properties, that ruthenium(II)polypyridyl complexes are employed in a wide variety of applications, such as dye-sensitized solar cells[2, 3], molecular motors[6], photodynamic therapy[1, 4, 5, 24] or water oxidation.[25, 26] Unfortunately, ruthenium is toxic and one of the rarest elements on earth, leading to high material costs. Much research effort is, therefore, directed towards bestowing the same superior photophysical properties to the more commonly available first row transition metals.[27-36] Among those, especially iron stands out, as it is ruthenium's lighter homologue and one of the most abundant elements in the earth crust. However, ruthenium, as a second-row transition metal, has 4d-orbitals which expand further towards the ligands than the 3d-orbitals of iron. As a result, the ligand field splitting of 3d-orbitals is generally smaller

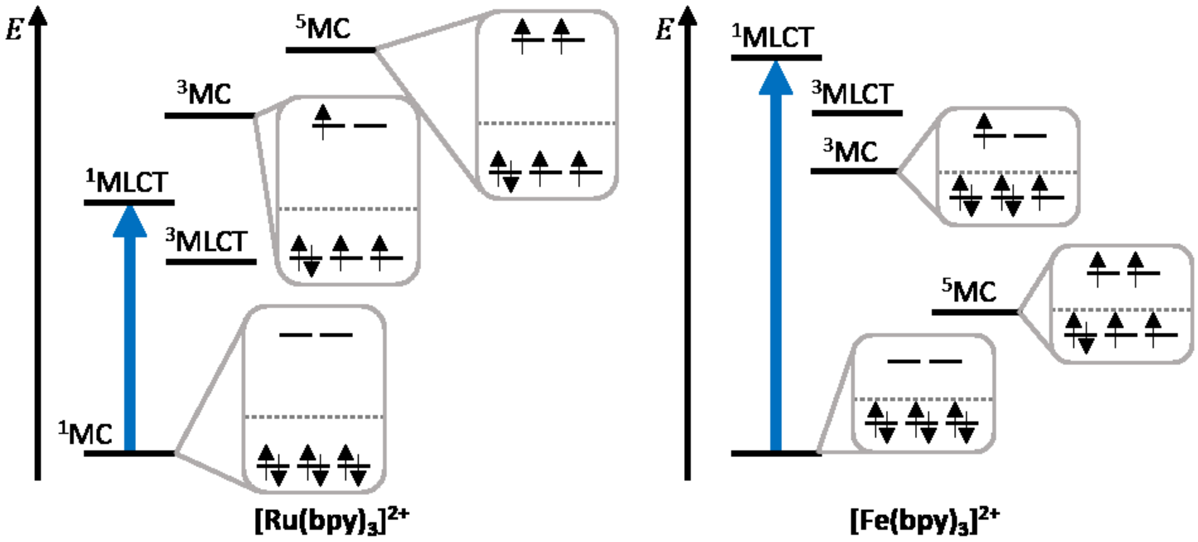

Figure 2.7: Energy diagrams of electronic states (and the corresponding d-electron configurations) of $[Ru(bpy)_3]^{2+}$ *and* $[Fe(bpy)_3]^{2+}$*. Dotted lines in electron configurations represent average d-orbital energy to visualize ligand field stabilization.*

than that of 4d-orbitals. In addition, the larger volume of the 4d and 5d-orbitals also reduces the coulomb energy fine for doubly populating a single d-orbital, which further stabilizes low-spin configurations compared to lighter homologues. Consequently, the MC states of first row transition metal complexes are lower in energy than their second-row counterparts. This is depicted for the paradigmatic $[Ru(bpy)_3]^{2+}$ and its iron counterpart in Figure 2.7, where the smaller ligand field splitting in iron leads to MC states energetically below the MLCT manifold. As result, $[Fe(bpy)_3]^{2+}$ suffers from ultrafast MLCT deactivation by ISC and IC to high-spin MC states.[7, 8] The next section will present strategies to compensate this difference in ligand field splitting to improve MLCT lifetimes in iron-based sensitizers.

2.3.3 **Excited state tuning by ligand choice**

General trends for the ligand field strength for both metal ions and ligands are summarized in the spectrochemical series.[37] There, the metal ions or ligands are sorted by increasing ligand field strength. The series for metal ions shows two clear trends: Firstly, the ligand field splitting increases with increasing oxidation number. This is due to the larger electric field posed by the metal ion, which attracts the ligands further towards the splitting d-orbitals. Secondly, the ligand field increases down a group. This is due to the 4d- and 5d-orbitals increasingly larger expansion towards the ligands which intensifies their interaction. Additionally, the larger volume of the 4d and 5d-orbitals reduces the spin pairing energy. As discussed above, this is the reason for the stark difference in the ligand fields of $[Fe(bpy)_3]^{2+}$ and $[Ru(bpy)_3]^{2+}$ which leads to efficient MLCT deactivation via low lying MC states. The activation barrier for the IC from the ^{1}MLCT to the ^{3}MC in $[Fe(bpy)_3]^{2+}$ was estimated by varying temperature transient absorption to be merely 0.04 eV, which is negligible compared to the 2.35 eV excitation energy.[38] This very small barrier results not only from the low energy of the ^{3}MC but also its shifted Fe-L equilibrium bond length, which result in a situation similar to that sketched in Figure 2.3a. This opens up two ligand-based routes to introduce a larger barrier towards MLCT deactivation: Ligands producing a larger ligand field splitting will upshift the MC energy in general which can produce a larger barrier

(Figure 2.3a) or change the order of excited states altogether. Next, chelating ligands with a sturdy backbone can be employed to make the potential wells steeper along the vibrational mode q_i mediating the IC (Figure 2.3c). The nature of this mode is explored in detail in section 5.

Inspection of the bpy ligand in $[Fe(bpy)_3]^{2+}$ reveals that it is a chelating as well as a strong field generating ligand already, emphasizing the difficulty of finding more strongly donating ligands. Consulting the excerpt of the spectrochemical series of the ligands given here,[37] one finds that ligands with empty π orbitals are especially strong donors.

$$I^- < Br^- < S^{2-} < \mathit{S}CN^- < Cl^- < N_3^- \approx F^- < OH^- < ox \approx O^{2-} < H_2O < \mathit{N}CS^- < py \approx NH_3 < en$$
$$< bpy \approx phen < NO_2- < CN^- < PR_3 < CO$$

At the metal center the d-orbitals of the e_g and the t_{2g} manifold have σ- and π symmetry concerning the Fe-L axis, respectively (see Figure 2.8b). Accordingly, strongly σ donating ligands destabilize exclusively the e_g and π acceptors stabilize the t_{2g} manifold. This constitutes σ bonding and π backbonding, with both contributions leading to a larger ligand field splitting. Furthermore, not all three bpy units can just be exchanged for stronger ligands, but at least one ligand must be capable of accepting an electron to enable bright MLCT states. One stronger ligand than bpy with an established chemistry with iron ions is the cyanide ion CN^-. To iron(II) it coordinates with the softer, more diffuse C side. The two p_z orbitals at both the carbon and the nitrogen form a bonding σ orbital, while the p_x and p_y form π bonds orthogonal to each other. Since the C-N axis is also the Fe-L axis, the symmetry of the MOs is the same towards the coordination bond, allowing for strong σ donor capacities and π backbonding via the empty antibonding combinations of the p_x and p_y orbitals.

While the bpy ligand is also a good π acceptor, the σ donor capacity of the CN^- ligand exceeds that of the bpy ligand due to the greater overlap with the σ MO which is significantly larger on the C side (Figure 2.8b). This stronger σ donor strength destabilizes the e_g manifold, which are necessarily a part of d^6 high-spin MC states. Therefore, a ligand exchange of CN^- for bpy shifts MC states upwards in energy with

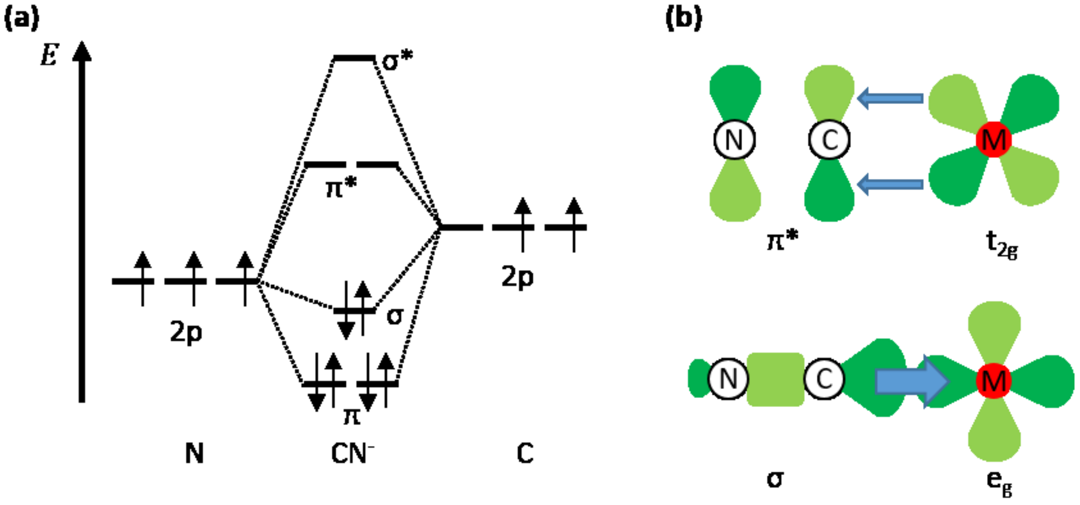

Figure 2.8: Electronic properties of cyanide-ligand. (a): Abbreviated MO scheme of cyanide (only 2p-orbitals shown for clarity). (b): Orbital overlap of transition metal HOMO and cyanide LUMO and vice versa.

respect to both the ground state and MLCT states. $[Fe(bpy)(CN)_4]^{2-}$ is therefore a much investigated example of iron(II)complexes with considerable MLCT lifetimes.[39-42] The cyanide ligands introduce a solvent dependence of the excited-state dynamics, which is discussed and exploited in section 5 of this work to establish pump-IVS as a method sensitive to MLCT MC transitions.

The use of strongly σ donating cyanide ions as ligands follows exclusively the first route of introducing barriers in the MLCT-MC transition. The route of introducing chelating ligands to hinder geometric rearrangements associated with MLCT-MC transitions was ignored there. Next, another ligand type is introduced combining both approaches: chelating N-heterocyclic carbenes (NHCs).

Carbenes are chemical compounds containing carbon atoms with two substituents and two unshared valence electrons. They are generally highly reactive but can be stabilized by coordinating to metal centers. While there are several general types of carbenes, the only relevant group for this work are N-heterocyclic carbenes or Arduengo carbenes due to the pioneering works of Anthony J. Arduengo.[43-45] They consist of the carbenoid atoms bonded to two nitrogen in a heterocyclic compound – oftentimes imidazole. C-deprotonation of imidazolium salts leaves the carbon atom with a doubly populated sp^2 orbital pointing outwards in the plane of the imidazole ring and a formally empty p-orbital.

N-heterocyclic carbenes owe their surprising stability largely to the stabilization of the empty p-orbital at the carbon atom via the mesomeric support of the nitrogen atoms (Figure 2.9a+b). Because of the smaller electronegativity, the sp^2 orbital at the carbon atom expands further out than that of comparable N-based donors, such as bpy. This gives rise to NHC's superior σ donor abilities, as depicted in Figure 2.9c. Similar to bpy and cyanide, NHCs too have an empty p-orbital at the σ-coordinating atom whose π symmetry towards the M-L bond makes it available for π-backdonation from the populated t_{2g} manifold (Figure 2.9d). While the M-NHC bond is dominated by the σ donation, this π backdonation accounts for 10-20% of the bonding character.[46] It is therefore mostly their σ donating character that causes the strong ligand field which destabilizes high-spin MC states. Since the π* orbital at the ligand is of higher energy in NHCs than in bpys, they are not fit as electron accepting ligands in MLCT states

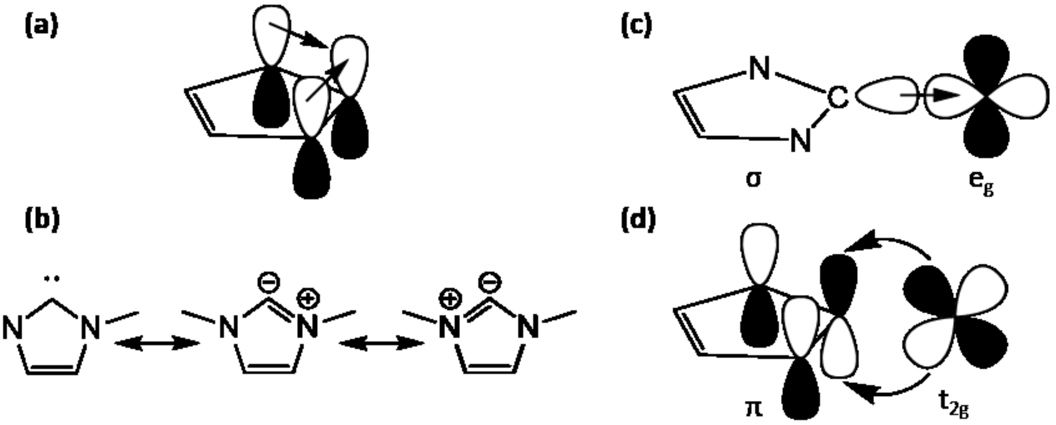

Figure 2.9: Mesomeric stabilization of empty p-orbital of carbene by neighboring nitrogen atoms in (a) MO and (b) Lewis structure representation. (c) σ donation and (d) π backdonation between NHC and d^6 transition metal.

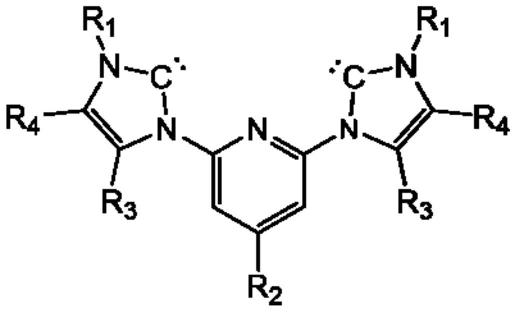

Figure 2.10: Series of C-N-C chelating ligands based on pyridine and imidazole-derived NHCs.

with transitions in the visible spectral range. The ligand design therefore requires incorporation of an electron accepting unit, such as a pyridyl moiety. The imidazole ring offers several possibilities to connect to a larger scaffold, but the nitrogen atom offers a favorable orientation towards other coordination sites. This leads to a series of symmetric C-N-C coordinating chelating ligands, featuring a central pyridyl unit coordinating via the nitrogen atom and two imidazole-based NHCs, see Figure 2.10. This scaffold results in a chelating ligand physically coupling the three coordination sites, introducing larger rigidity as resistance towards geometric rearrangements associated with changes in electronic state nature. The introduction of such NHC ligands propelled iron(II)complexes as replacement of the expensive ruthenium counterparts into reach, sparking large research interest. Many of the possible variations of this and closely related scaffolds have been investigated for MLCT lifetimes and involvement of MC states.[27, 47-53] It was observed, that the MLCT lifetimes had indeed been extended significantly, from the hundreds of femtoseconds to several picoseconds. Furthermore, the exceedingly long lived ^{5}MC state is no longer populated, suggesting the introduction of strong σ donors successfully shifts high-spin MC states out of the MLCT relaxation pathway. However, a recent study on one such derivate shows decisive proof of the involvement of the ^{3}MC state in the early deactivation of the photo-excited ^{1}MLCT state.[47] In this work, a closely related derivate is investigated, where R_3=R_4=H and R_1=CH_3 for minimal steric hindrance. Additionally, R_4 is chosen to be COOH, an electron withdrawing group, which lowers the MOs localized on pyridine, including the π* orbital participating in the MLCT states. Furthermore, the carboxyl group enables binding to titanium dioxide nanoparticles acting as semiconductor in dye-sensitized solar cells (DSSCs).[48]

3 Methods

This chapter is concerned with the theoretical description of the experimental methods applied in this work. In a general introduction, the central challenges for probing excited-state dynamics are discussed highlighting the necessity of time resolved experiments and reliable reference data. In section 3.1, the time-dependent perturbative description of the polarization through resonant light-matter interactions in the form of double-sided Feynman diagrams is introduced. In sections 3.2 and 3.3, transient absorption (TA) and impulsive vibrational spectroscopy (IVS), the two main techniques employed in this work, are examined using the established tools and their specific analysis procedures are presented.

If the electronically excited states of a given sample are to be investigated, it is evidently necessary, to prepare at least a significant portion of said sample in these excited states and to probe them before they relax back into the ground state. From this, two fundamental requirements for the experimental observation of excited state dynamics derive.

Firstly, it is necessary to trigger these dynamics in a sufficient number of atoms, molecules, or particles simultaneously to obtain a macroscopically measurable response. Secondly, both triggering and probing of these processes must occur with temporal resolution below the timescales on which they evolve, which are femto-, pico-, nano- and microseconds. Time-resolved spectroscopy addresses both challenges by making use of ultrashort laser pulses to trigger, manipulate and probe excited-state dynamics within the sample. While powers of, e.g., 50 µW might seem negligible compared to everyday light sources, it is worth considering that these 50 µJ/s are not distributed evenly within one second. Instead, in a typical experiment, 500 pulses of approximately 20 fs duration arrive at the sample within a second. Dividing 50 µJ by 10 ps effective irradiation time gives peak power of 5 MW, clearly capable of preparing non-equilibrium states in a significant number of molecules simultaneously. This non-equilibrated ensemble can then be probed by a second laser pulse (UV-VIS, IR, THz), to interrogate its electronic state, molecular vibrational properties, or lattice vibrations, respectively.

For the accurate interpretation of UV-VIS or IR ground-state spectra, there are textbooks, large reference libraries of readily collected ground-state spectra and easily accessible prediction programs allowing for reliable identification of characteristic band shapes, positions, and intensities. Furthermore, often other, lengthy, spectroscopic, or spectrometric methods are consulted, such as nuclear magnetic resonance spectroscopy (NMR) or mass spectrometry (MS) in the identification of otherwise unclear species. Certainly, many principles established for ground-state spectra can be transferred to the excited-state realm, and setups supporting time-resolved methods become ever more commercially available. In some cases, excited states of molecules can be mimicked in the ground state by electrochemical manipulations.[54, 55] Nonetheless, there is currently no comprehensive collection of spectroscopic data of excited states, and stabilizing and isolating them to allow for the application of further methods impossible in the vast majority of cases. Therefore, quantum chemical calculations of excited-state properties are a powerful partner for time-resolved spectroscopy. The prediction of energies and probabilities of specific transitions, as well as structural changes associated with them are extremely helpful for developing and corroborating models explaining the photophysics and photochemistry of novel samples.

3.1 Perturbative description of nonlinear spectroscopy[56, 57]

If excited-state dynamics are to be investigated experimentally, it is essential to prepare these excited states and to probe their evolution on the relevant time scales. The field of nonlinear time-resolved spectroscopy, comprising among others transient absorption, impulsive vibrational spectroscopy and degenerate four-wave-mixing is dedicated to this goal. The term nonlinear thereby indicates, that the obtained signal depends on higher order polarizations induced in the sample by a series of laser pulses. The theoretical description of nonlinear time-resolved spectroscopy therefore requires both quantum mechanical treatment of the investigated sample, as well as faithful accounting of all light-matter interactions. In this section, the density matrix is introduced as a useful representation of the sample's quantum state and a brief introduction into the diagrammatic perturbation theory is given, to establish double sided Feynman diagrams as a powerful, yet comprehensible way to infer signal properties.

The following sections are dedicated to the discussion of transient absorption and impulsive vibrational spectroscopy and make use of double-sided Feynman diagrams. Subsections are included describing the numerical signal processing in the data analysis.

The quantum state of systems is typically represented by a wave function ψ, a solution to the Schrödinger equation. Since the Schrödinger equation is an eigenvalue equation, the wave function is also often represented in linear algebraic terms by a ket-eigenvector $|\psi\rangle$. However, this only allows to represent the system in pure states, and macroscopic signal, as collected in TA and IVS, can only be obtained from a large ensemble of systems. Rather than a pure state, one prepares and probes a statistical mixture of states with these methods. To account for this, the density matrix operator $\hat{\rho}$ is introduced. As the name suggests, it expands the concept of the ket-eigenvector by the outer product with a bra-eigenvector to a matrix $\hat{\rho} = |\psi_i\rangle\langle\psi_j|$. In this matrix, every combination of i and j (every matrix element) refers to a state the individual systems can take on. Within this framework, populations are represented by the density matrix $|\psi_i\rangle\langle\psi_i|$, and coherences as $|\psi_i\rangle\langle\psi_j|$ with $i \neq j$. This specific density matrix refers to a coherent superposition of the eigenstates ψ_i and ψ_j. Let us now consider, how populations and coherences are prepared by external electric fields in the form of laser pulses. Qualitatively, an external field can interact with the system in two ways: absorption and the inverse process stimulated emission. Absorption leads to a quantum state of higher energy, stimulated emission brings the system to a state of lower energy. The formalism of the density matrix also allows to classify these light-matter interactions as interactions with the ket-side $|\psi_i\rangle$ or the bra side $\langle\psi_i|$. Consider a two-level system with eigenstates $|0\rangle$ and $|1\rangle$. As is typically the case, the system is in the ground state $|0\rangle\langle 0|$ before interactions with the laser pulses occur. Absorption of the electric field with frequency $\omega_{01} = \frac{E_1 - E_0}{\hbar}$ on the ket-side leads to the coherent superposition $|1\rangle\langle 0|$, whereas absorption on the bra-side leads to $|0\rangle\langle 1|$.

Note, that neither interaction produces a population, but coherences, which are the complex conjugate of each other. Only after a second interaction with an external electric field, the system can adopt a population – either in the ground state, or in the

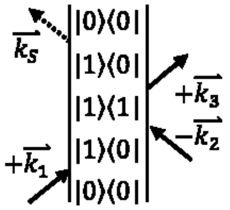

Figure 3.1: Exemplary double-sided Feynman diagram. Sequence of events from bottom to top. Absorption on ket- and bra side ($+\overrightarrow{k_1}, -\overrightarrow{k_2}$, respectively) creates an excited-state population $|1\rangle\langle 1|$. Stimulated emission on the bra side ($+\overrightarrow{k_3}$) creates a coherence $|1\rangle\langle 0|$, which emits the signal.

excited state. A second interaction of the external electric field with the same side (ket or bra) can therefore induce stimulated emission and produce the ground-state population $|0\rangle\langle 0|$. Two-quantum coherences ($|2\rangle\langle 0|$) are possible as well, although not in the two-level system regarded here. If the two interactions occur on different sides, the excited-state population $|1\rangle\langle 1|$ is created. A compact way of representing the complex sequences leading to the signal generation of a given nonlinear spectroscopic technique are double sided Feynman diagrams (Figure 3.1). They consist of two vertical lines, representing the ket-side (left) and the bra-side (right) of the density matrix, and arrows inclined inside or outside representing absorption or stimulated emission, respectively. The arrows are ordered from bottom to top, so that the sequence of events depicted in the diagram progresses upwards. Conventionally, the system starts in the ground-state population $|0\rangle\langle 0|$, and after a series of interactions (absorption, stimulated emission), the signal is emitted by convention from the ket-side forming a population ($|n\rangle\langle n|$). After every interaction, the adopted density matrix $|i\rangle\langle j|$ is denoted. Typically, the initial and final state ($|0\rangle\langle 0|$, $|n\rangle\langle n|$, respectively) are not denoted, as they are clear to the familiarized reader. In between interactions, the density matrix evolves unperturbed in time, i.e., populations relax and coherences dephase. The great benefit of double-sided Feynman diagrams is that they are a compact, yet accurate representation of the correlation function relating the external electric fields and characteristic sample properties to the emitted signal. From this diagrammatic representation, it is possible to directly infer the frequency, wave vector and sign of the signal, without explicitly writing down the lengthy correlation function itself.

Every interaction with the external field characterized by a frequency ω_i and a wave vector $\overrightarrow{k_i}$ adds a contribution to the signal's frequency ω_S and its wave vector $\overrightarrow{k_S}$, i.e., its spatial direction. Absorption and stimulated emission on the ket-side contribute positively and negatively to ω_S and $\overrightarrow{k_S}$, respectively. Due to the complex conjugate nature, the sign of the contributions from interactions on the density matrix's bra-side are reversed. It can be summarized, that interactions represented by arrows inclined to the right contribute positively, and those inclined to the left contribute negatively. Let us apply this procedure to determine the frequency (Eq. 3.1) and wave vector (Eq. 3.2) of the signal characterized by the diagram shown in Figure 3.1.

$$\omega_S = \omega_1 - \omega_2 + \omega_3 \qquad \text{Eq. 3.1}$$

$$\overrightarrow{k_S} = \overrightarrow{k_1} - \overrightarrow{k_2} + \overrightarrow{k_3} \qquad \text{Eq. 3.2}$$

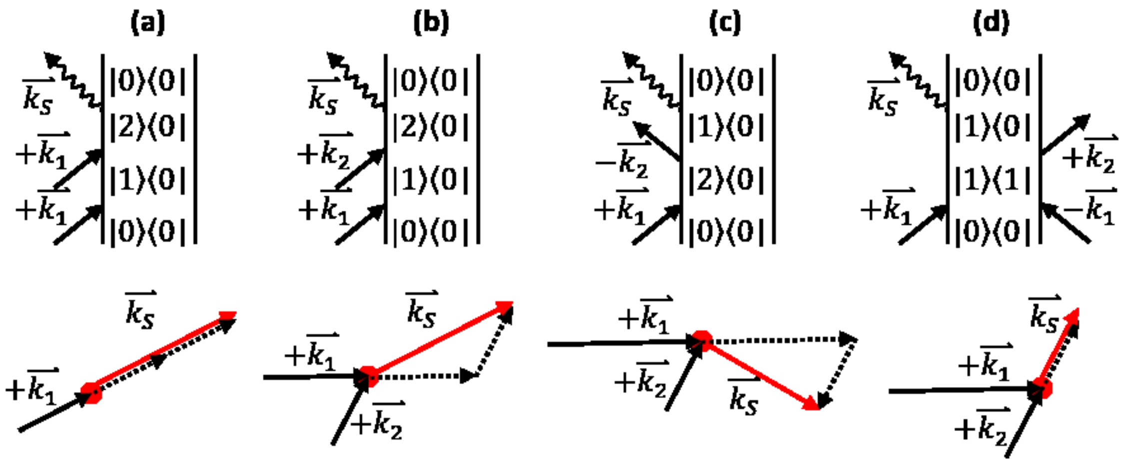

Figure 3.2: Double-sided Feynman diagrams representing (a) second harmonic generation, (b) sum frequency generation, (c) difference frequency generation and (d) stimulated emission as contribution to transient absorption spectroscopy.

Furthermore, the signal can be attributed a sign based on the double-sided Feynman diagram representing its generation. The sign of a signal contribution is defined as $(-1)^m$, with m being the number of interactions on the bra side (absorption or stimulated emission). The double-sided Feynman diagram shown in Figure 3.1 leads to positive signal, which, according to convention – is an additional photon reaching the detector.

The expressions for the signal frequency and wave vector given in Eq. 3.1 and Eq. 3.2 are the general form. However, not all interactions leading to signal emission necessarily occur with distinct laser pulses. Instead, multiple interactions with the electric field of a single pulse take place, so that they contribute several times. Second harmonic generation as well as sum- and difference-frequency generation as they occur in non-linear optical media are suitable examples to illustrate the differences (Figure 3.2a, b & c, respectively). For typical second harmonic generation, there is only a single incident beam $(\omega_1, \overrightarrow{k_1})$, therefore the resulting signal is emitted in the same direction with twice the frequency (second harmonic, $\omega_S = 2\omega_1$, $\overrightarrow{k_S} = 2\overrightarrow{k_1}$). For sum frequency generation, the resulting beam of the sum of the incident frequencies $(\omega_S = \omega_1 + \omega_2)$ is emitted along $\overrightarrow{k_S} = \overrightarrow{k_1} + \overrightarrow{k_2}$ in between the two transmitted beams. Note, that second harmonic generation is a special case of sum frequency generation, where $\omega_1 = \omega_2$ and it is therefore also possible to generate the second harmonic with an angle between two incident beams $(\overrightarrow{k_1} \neq \overrightarrow{k_2})$. This offers the advantage of a spatially separated second harmonic beam. However, in practice it is often much simpler and more efficient to generate the second harmonic form a single incident beam and to remove the transmitted fundamental by a band selective filter or mirror. For difference frequency generation, the signal $(\omega_S = \omega_1 - \omega_2)$ is even emitted outside the angle spanned between the two transmitted beams. For the case demonstrated in Figure 3.2d, let us reconsider the double-sided Feynman diagram shown in Figure 3.1, but assume, that the two interactions creating the population occur with the same incident pulse $(\omega_1, \overrightarrow{k_1})$. A second pulse $(\omega_2, \overrightarrow{k_2})$ then interrogates this population, creating the coherence $|1\rangle\langle 0|$ which emits the signal. Because ω_1 and $\overrightarrow{k_1}$ act on both the bra and the ket-side, their contributions cancel out, and the signal is of the same frequency and wave vector as the second pulse ($\omega_S = \omega_2$, $\overrightarrow{k_S} = \overrightarrow{k_2}$). Note, that all diagrams shown in Figure 3.2 have positive sign, as can be expected from processes generating photons.

The signal generated, and thus the information that can be retrieved about the sample, is indistinguishable when using two (Figure 3.2d) or three distinct pulses (Figure 3.1). Yet, the direction of the signal, relative to the incident beams, can be changed by conscious design of the experiment. Usage of three linearly independent beams will result in the signal being emitted in a fourth distinct direction, as given in Eq. 3.2. When only two beams are employed, the same signal is emitted along the second pulse, termed probe. While it may seem arbitrary to distinguish between the two cases, the difference in signal direction has further implications.

Let us first consider the case, where the signal is spatially separated from the probe. Evidently, this is experimentally more challenging (overlapping and timing three pulses instead of two). Furthermore, it also requires samples with large susceptibilities, leading to strong emitted electric fields, as the following discussion will show. The detected intensity is proportional to the square of the electric field emitted by the sample E_s (Eq. 3.3).

$$I_{det} \propto E_s^2 \qquad \text{Eq. 3.3}$$

Since the signal intensity exclusively depends on the electric field of the signal, this is termed a homodyne detection technique. Typically, E_s is quite weak compared to the electric fields of the Laser pulses.

Let us now reconsider the two-pulse experiment. Emission of the signal along the probe beam means, that they cannot be separated spatially. The probe beam is inevitably directed into the detector with the signal. The detector therefore records intensity comprising of the electric field of the signal and the probe (Eq. 3.4).

$$I_{det} \propto \left(E_s + E_{pr}\right)^2 \qquad \text{Eq. 3.4}$$

$$I_{det} \propto E_s^2 + 2E_sE_{pr} + E_{pr}^2$$

Since the signal is much weaker than the probe generating it, it is necessary to subtract the spectrum of the transmitted probe. This is achieved by collecting a reference spectrum without the first pulse generating an excited-state population. While it is necessary, the data acquisition rate and signal-to-noise ratio suffer from this procedure. After subtraction of the reference probe spectrum $I_{pr} \propto E_{pr}^2$, the retrieved signal is not only proportional to the square of the electric field of the signal (E_s^2), but also to the product $E_S E_{Pr}$. Since the electric field of the probe is much stronger than that of the signal ($E_{Pr} \gg E_S$), it follows that this constitutes a significant amplification of the signal with respect to the homodyne detected technique ($E_sE_{pr} \gg E_s^2$). Due to the other electric field (E_{Pr}), this is called a heterodyne detection technique. The most common example of a heterodyne detection technique is transient absorption, which is introduced in more detail in the following section.

3.2 Transient absorption spectroscopy

Transient absorption spectroscopy (TA) is one of the simplest implementation of time-resolved spectroscopy.[58] It is a two-pulse experiment in which an intense first pulse (pump) prepares a population within sample system in a non-equilibrium state, which is interrogated by a weaker pulse, the probe. The delay between the two pulses is introduced by varying the path length of one of them using a pair of mirrors on a translatable platform, the so-called delay stage. TA is a heterodyne detection technique, meaning the signal is generated in the direction of and amplified by the probe pulse. From this arises the necessity to subtract the probe reference spectrum in the absence of the dynamic changes induced by the pump to single out the signal. This is achieved by directing the pump through a chopper, synchronized with the repetition rate of the laser, so that it blocks every second pump pulse. A schematic setup as well as the pulse sequence are shown in Figure 3.3. The probe transmits through a pumped and unpumped sample alternatingly before being detected, allowing for calculation of the difference in absorption. Given the definition of absorption as the logarithmic depletion of intensity – the TA-signal is computed according to Eq. 3.5.

$$S_{TA} = A_{on} - A_{off} = log\left(\frac{I_{off}}{I_{on}}\right) \qquad \text{Eq. 3.5}$$

Since the detector is set up in the direction of the probe, only Feynman diagrams contribute to the signal, which lead to a net wave vector k_S equal to k_{pr}. This means that all contributions of the pump wave vector k_{pu} must cancel out when selecting the relevant double sided Feynman diagrams. As established above, this is achieved with two interactions of the pump with the density matrix element, either on the same side, restoring the ground-state population, or on opposing sides, creating an excited-state population. In the approximation of a two-level system, coherences do not contribute to the TA signal. Figure 3.4 shows the double-sided Feynman diagrams of the three population-based contributions to the TA signal. Firstly, ground-state absorption does occur, although in reduced amount since the pump transfers some ground-state population to the excited state. This is called ground-state bleach (GSB, Figure 3.4a) and contributes negatively to the TA-signal. Secondly, stimulated emission (SE, Figure 3.4b) can occur from the excited-state population, which are de-excited by the transmitting resonant probe pulse. The additional photon is emitted at the same

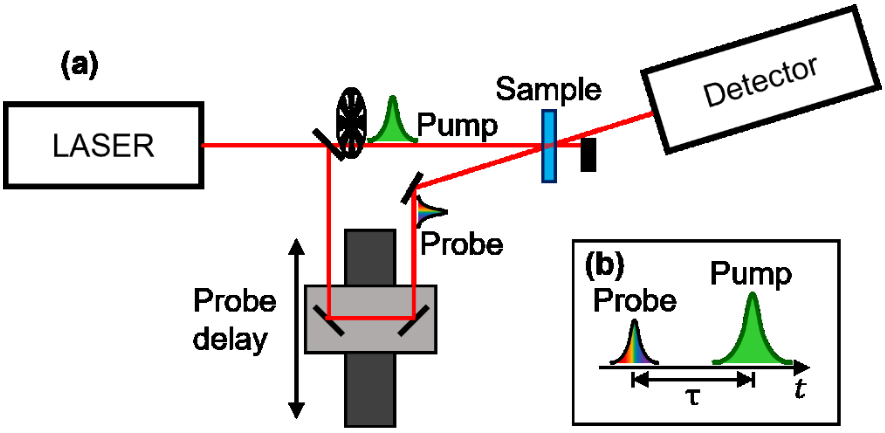

Figure 3.3: (a) Schematic setup for transient absorption spectroscopy. (b) Transient absorption pulse sequence.

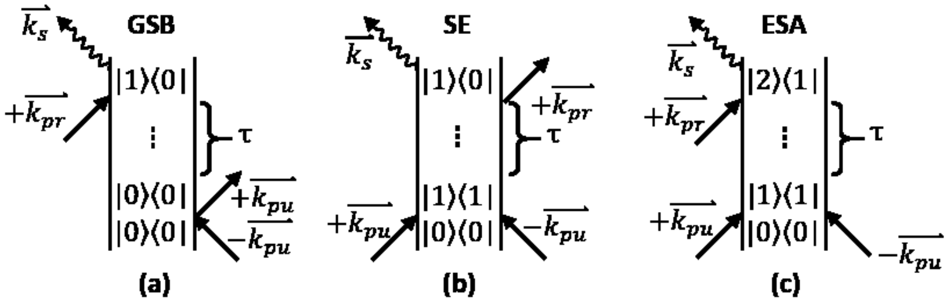

Figure 3.4: Selection of double-sided Feynman diagrams contributing to transient absorption. (a): Ground-state bleach. (b): Stimulated emission from $|1\rangle$. (c): Excited-state absorption from $|1\rangle$.

frequency and direction as the probe pulse. Lastly, the excited-state population also has characteristic absorption features (excited-state absorption, ESA, Figure 3.4c), which deplete the probe pulse intensity, contributing positively to the TA signal. Note that the sign of the double-sided Feynman diagrams for GSB and SE are the same and inverted to that for ESA. In typical applications the pump pulse is resonant with a ground-state absorption band relevant for the conducted study. Recording as many signal contributions as possible is highly desirable, since it allows to relate them to each other, which is of great benefit when interpreting the obtained data. Therefore, the probe pulse is typically a supercontinuum stretching over a relevant wavelength region. The most popular iteration of TA is the UV-VIS narrowband pump / UV-VIS broadband probe scheme, giving information about the electronically excited states involved in the samples photophysics. However, experiments using UV-VIS / IR or IR / IR pump and probe schemes are also feasible and offer information about the vibrational and hence structural changes induced by electronic or vibrational excitation. IR / UV-VIS pump probe schemes have also been reported, giving insight into the vibrational modulation of the ground-state electronic spectrum.

When employing a broadband probe, usage of a diffractive element and a series of independent detectors (such as a photodiode array (PDA)) enables collection of full transient absorption spectra. Acquiring these transient absorption spectra at several pump-probe delay yields a two-dimensional dataset, in which the transient absorption recorded by every PDA pixel evolving in time is contained. The mathematical models and computational techniques used in the analysis of such two-dimensional datasets are introduced in the next section.

3.2.1 **Analysis of TA datasets**

In the past 20 years, several reviews have been published addressing artifacts in TA and their corrections, as well as multiple general data analysis schemes.[59-63] In this section, only the applied corrections and analysis procedures are introduced.

A first artifact that can be corrected by experimental design is rotational diffusion in the liquid phase.[61] It results from linearly polarized pump and probe, as well as the molecules' capability to rotate freely in the liquid phase. Considering the linearly polarized nature of the pump pulse, it is intuitive, that molecules are preferably excited, if their transition dipole moment is oriented parallel to the polarization axis of the pump.

Similarly, the probe preferably interrogates molecules with a dipole moment parallel to its polarization axis. Therefore, a parallel orientation of pump and probe polarization results in the largest signal. However, in the liquid phase, molecules rotate freely, so that the dipole moments of the excited molecules do not stay oriented along the probe. Consequently, the signal partially decays, as the molecules lose the preferable orientation and adopt a statistical distribution. This signal decay skews the observed kinetic related to excited-state relaxation. If pump and probe are polarized orthogonal to each other, the revers process occurs: Initially, the signal is smaller than that of a randomly oriented ensemble of molecules and increases, as the excited molecules adopt this distribution. Qualitatively, from the consideration of these two fringe cases it is evident, that a relative orientation of pump and probe polarizations exists, for which the contribution of rotational diffusion vanishes. This is the case for a relative orientation of 54.7°, which is why this configuration is called "magic angle".

Usage of a broadband probe has several advantages, but one disadvantage is that pulses this spectrally broad are strongly chirped due to the different amount of dispersion they undergo when passing through optical media. This phenomenon is called group velocity dispersion and has the effect that the different wavelengths contained in the probe spectrum are not distributed equally along its duration. As a result, in the collected raw-data there is not a single time zero (τ_0), when pump and probe overlap temporally, and the excited-state dynamics are triggered. Instead, every detector pixel exhibits a distinct τ_0, leading to a characteristic curvature of the signal onset, as shown in Figure 3.5a.

Evidently, this needs to be corrected before proper data analysis can be conducted. There are several possible techniques to identify the τ_0-value for a given pixel, all of which rely on the coherent artifact as indicator for the temporal and spatial overlap of the participating laser pulses. When pump and probe overlap in space and time, interactions between them and the medium occur, that are impossible without the intense pump pulse. These include two-photon absorption, cross-phase modulation and stimulated Raman amplification.[62, 63] This causes a sharp, spike-like feature around the temporal point of pump and probe overlap, i.e., τ_0. The width of the artifact is determined by the overlap duration w_0, indicative of the temporal resolution

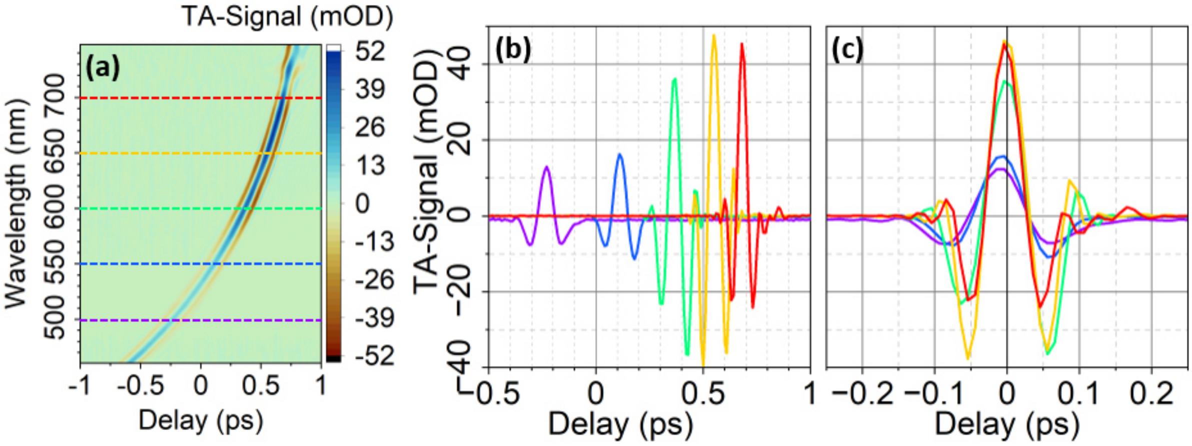

Figure 3.5: (a) Two-dimensional representation of uncorrected dispersion curve. (b) Selected kinetic traces of uncorrected dataset at 500 nm, 550 nm, 600 nm, 650 nm, and 700 nm, indicated in (a) as dashed lines. (c) The same kinetic traces after t0-correction.

achieved with the experiment. While the artifact may obscure ultrafast dynamics occurring at early delays, it is quite useful for the determination of τ_0. In practice, the experimenter deliberately records a reference measurement using only the solvent as sample, to record the pure coherent artifact without any molecular contributions. This data set is regarded as kinetic traces – i.e., the TA signal recorded for a specific wavelength pixel changing in time. Most straightforward is a fitting of the coherent artifact in the kinetic trace using a Gaussian function. Consideration of derivatives of the Gaussian function allows to also describe the more complex shapes the coherent artifact can adopt. This fitting yields τ_0 as center of the Gaussian function and its derivatives, as well as w_0 as their width. Another approach is to calculate the temporal derivative of the TA-Signal at a given wavelength pixel. In the temporal derivative, all slowly changing contributions to the TA signal, like molecular dynamics, become negligible compared to the sharp coherent artifact. This leaves only the rapidly occurring changes of the coherent artifact to be identified. Lastly, the τ_0-value for a given trace can also be handpicked after visual inspection, although this is not only laborious, but also affects reproducibility. Regardless of what method was used to determine the τ_0-value for a sufficient number of wavelength pixels, the subsequent correction is the same. A polynomial function is fitted to the determined values, yielding the time of pump-probe overlap as function of wavelength $\tau_0(\lambda)$. This function is interpolated to all the wavelength pixels detected to obtain the temporal offset for every pixel. So far, all kinetic traces had the same (experimental) delay axis. Now, every trace is assigned its own, specifically corrected delay axis, by subtracting its characteristic τ_0 from the experimental delay axis. Finally, to obtain a cohesive 2D dataset, all kinetic traces (with their corrected delays) are interpolated to a shared delay axis.

After correction for the chirp of the probe pulse, a baseline correction may be in order. This is critical when there is signal detected, even when the probe arrives at the sample before the pump (negative delays). Possible reasons for are pump-induced fluorescence or scattered pump light reaching the detector, or extremely long-lived contributions, outlasting the time between subsequent laser pulses (e.g., 1 ms for 1kHz repetition rate). These contributions are not only visible at negative delays, but also distort the data signal from actual molecular dynamics at positive delays. Therefore, a correction is crucial. To that end, a region in the negative delay is defined, where no relevant contribution is found (i.e., no onset of real signal). The TA signal measured within this region is averaged for every kinetic trace, and the average is then subtracted from the trace.

To extract as much information as possible from a TA dataset, it is crucial to properly model the data. Since almost all processes studied in TA follow first order ordinary differential equations, the exponential decay is the natural choice for fitting it. The simplest approach is to find a wavelength pixel, which is characteristic of a single band and to fit it using a single exponential decay function. This yields the decay constant, indicative of the lifetime of the species responsible for the ESA, SE or GSB band. Typical TA data also covers negative delays before the signal onset as well as the coherent artifact when pump and probe overlap temporally and spatially. The onset is considered by multiplying the exponential function with the error function and the coherent artifact is incorporated by adding a Gauss function and its derivatives (Eq. 3.6).

$$S_\lambda(t) = \frac{\operatorname{erf}\left(\frac{t}{w_0}\right)+1}{2} * A_\lambda * exp\left(\frac{-t}{\tau}\right) + \sum_{j=0} \frac{d^j}{dt^j} exp\left(\frac{-t}{w_0}\right)^2 \qquad \text{Eq. 3.6}$$

Global analysis (GA) takes this approach and expands it from a single pixel to the complete recorded spectral region.[59, 60] The goal is to reconstruct the 2D dataset using characteristic spectra multiplied by exponential decays describing the temporal evolution of them. Every kinetic trace $S_\lambda(t)$ is fitted with an individual amplitude A_λ, but the time constant τ is shared among all kinetic traces. This has two significant advantages: Firstly, the time constants obtained from a global fit are much more reliable than those from a single trace. Secondly, the amplitudes obtained in this way constitute a cohesive spectrum of differential changes associated with the given time constant. They are called decay-associated difference spectra (DADS) and their interpretation can greatly benefit the understanding of the involved processes, in ways that single, disconnected amplitudes and time-constants cannot. Evidently, in most cases a single time constant will not be sufficient to describe the complete 2D dataset satisfactorily, giving rise to multiexponential fits as given in Eq. 3.7.

$$S_\lambda(t) = \frac{\operatorname{erf}\left(\frac{t}{w_0}\right)+1}{2} * \sum_{i}^{n} A_{\lambda,i} * exp\left(\frac{-t}{\tau_i}\right) + \sum_{j=0} \frac{d^j}{dt^j} exp\left(\frac{-t}{w_0}\right)^2 \qquad \text{Eq. 3.7}$$

Global analysis therefore requires no more input than the number of time constants one expects to find in each dataset. This parameter can be predicted by singular value decomposition or simply optimized by trial and error within few minutes. In return, GA gives the relevant time constants, on which the input data evolves, as well as the corresponding DADS showing precisely what changes occur at each timescale. Due to the mathematical nature of the exponential decay function, the decay of a signal (be that signal positive or negative) is represented by the sign of the actual contribution. Bands rising during the exponential decay are represented with an opposite sign. As the name suggests, DADS show all changes associated with a given time constant, i.e., all changes that occur simultaneously. This makes them extremely powerful for the identification of relaxation pathways. If an absorption band rises to the extent that another one decays, this proofs a population transfer from one associated species to the other (see Figure 3.6b). However, the multiple contributions to a single spectrum also obscure each other. Therefore, identification of the participating species by relating experimental or calculated reference spectra to DADS can be deceptive.

Although DADS are vital to the interpretation of TA data, they do not reflect the characteristic absorption features of specific excited states. That is because the temporal evolution of the DADS are mere exponential decays. If we want to obtain physically meaningful spectra that can be related to excited states, then we need to suggest temporal evolutions that reflect how the actual populations evolve in time. When interpreted as populations, Eq. 3.7 describes the parallel decay of n independent species, which is not a realistic scenario (Figure 3.6b). Presumption of a

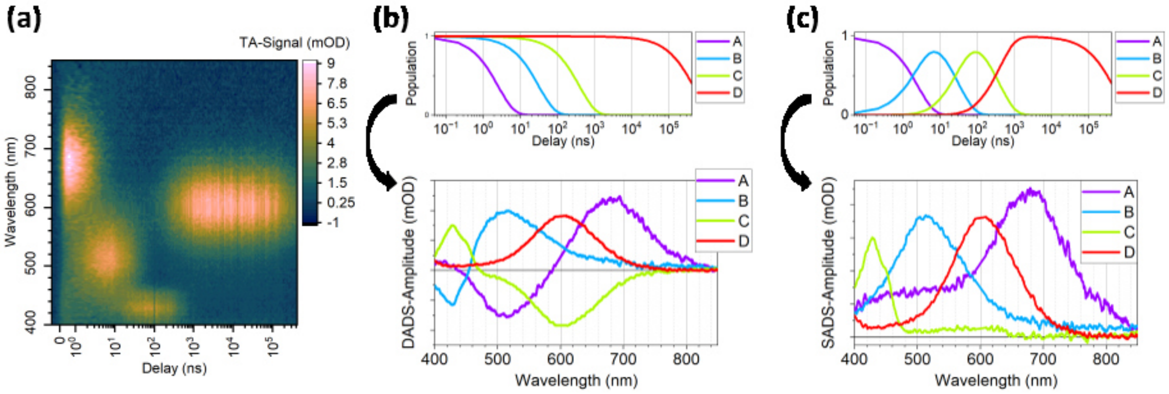

Figure 3.6: (a) Two-dimensional representation of exemplary TA-data. (b) Global analysis: Assuming the populations follow parallel exponential decays leads to DADS. (c) Numerically solved rate equations give realistic populations leading to SADS. In the shown case a sequential model was proposed.

realistic population evolution will result in spectra that can be related to individual species – such as excited states (Figure 3.6c). In other words, what is required, is a proper model of the excited-state dynamics at play. From a proposed model, rate-equations are inferred, which can be solved numerically to obtain the resulting population evolution. Note that the time constants used in this proposed model are necessarily those obtained from the global analysis, as these are the time constants on which the TA data evolves. This procedure is called global target analysis because the data is modeled to a specific target, in this case the kinetic model. Evidently, this is much more user dependent, as it requires not only an estimated number of states as input, but also their relations to each other. Proposition of a model requires careful consideration of available information about the system, such as reference spectra and possible intra- or intermolecular relaxation mechanisms. DADS can be of immense help, as they may show which bands evolve into which. Often, the testing of multiple models is necessary, to identify the most plausible SADS.

Transient absorption in the UV-VIS region is used to obtain information about the electronic state evolution after photoexcitation. The following section describes, how from the exact same experiment, vibrational and hence structural information can be derived.

3.3 Impulsive vibrational coherence spectroscopy

Impulsive vibrational coherence spectroscopy in its most simple form is equivalent to transient absorption. It is a heterodyne detected pump-probe experiment, conducted in the UV-VIS region typically associated with electronic transitions. Yet still it offers insight into vibrational and hence structural properties of electronically excited states.[64-69] To understand this, it is necessary to expand the description of the density matrix from the electronic state n $|n\rangle\langle n|$ to include the vibrational state v: $|n,v\rangle\langle n,v|$. Any molecule of more than two atoms has multiple vibrational normal modes (3N-5 for N-atomic linear molecules, 3N-6 for nonlinear molecules). However, in the following description of the density matrix $|n,v\rangle\langle n,v|$, only one of these normal modes will be considered for simplicities sake.

Electromagnetic radiation in the UV-VIS region typically drives transitions between electronic states, as the energy differences between these states are in the order of few eVs. Vibrational transitions typically are of ~10 – 300 meV, corresponding to the IR region. As established in the discussion of the Franck-Condon principle in section 2.1.3, electronic transitions are typically accompanied by vibrational transitions. Furthermore, the spectral width of laser pulses employed in time-resolved experiments can easily cover multiple vibrational sublevels within a given electronic transition. This opens the possibility of vibrational coherences within electronic populations, as displayed in Figure 3.7. If the two interactions with the pump lead to different vibrational levels within the same electronic state, the vibrational coherence can contribute to the signal. This contribution can only be of detectable magnitude if the individual molecules reaching this vibrational coherence do so collectively. However, the interactions with the electric field of the pump are random events. They occur randomly throughout the duration of the pump pulse as experienced by the sample. If molecules reach the coherent superposition of vibrational levels over a timespan exceeding the vibrational oscillation period, the individual contributions cancel out and only the shared electronic signature will be detected. It is therefore crucial, that laser pulses designated to the induction of vibrational coherences are shorter than the vibrational oscillation period in question. The coherence is then said to be generated impulsively. If this is the case, the resulting ensemble of molecules in a vibrational coherent state is often represented by a wave packet oscillating in the potential well corresponding to the vibration. The shorter the pulse is, the more synchronized the ensemble of molecules is (i.e., a narrower wave packet) and consequently, the stronger the

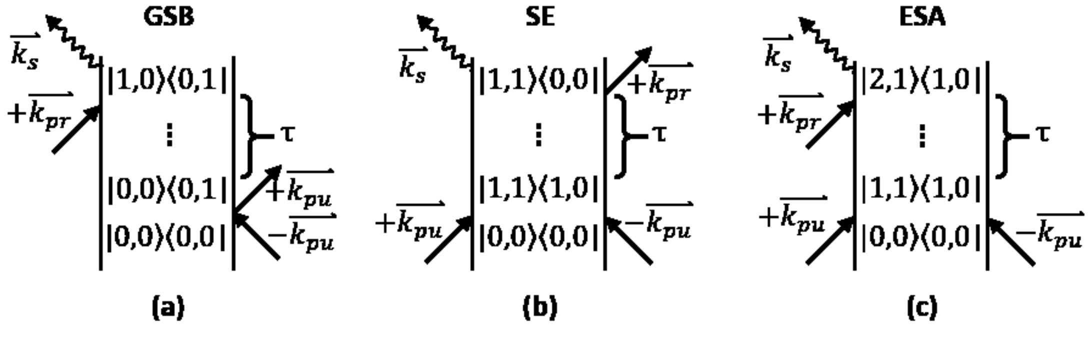

Figure 3.7: Selection of double-sided Feynman diagrams representing vibrational coherences within ground or excited-state populations, contributing to impulsive vibrational spectroscopy. (a): Ground-state bleach. (b): Stimulated emission. (c): Excited-state absorption.

detected macroscopic signal is. This raises the question about the nature of the vibrational coherence's contribution to the signal. Reconsider the wave packet oscillating in a vibrational potential well of a normal vibrational mode. Let's imagine the polarizability of the molecule changes along this normal mode, i.e., the mode is Raman active. The polarizability of the individual molecule contributes to the macroscopic susceptibility. Since we already presumed collective behavior of an ensemble of molecules in the form of the wave packet, the macroscopic susceptibility also changes as the wave packet travels along the Raman active normal coordinate. The susceptibility in turn links the external electric field (e.g., the probe) to the sample's response (i.e., the TA signal). A large susceptibility conveys a large TA signal, a small susceptibility on the other hand conveys a small TA signal. Because the wave packet oscillates along the Raman active normal mode, it modulates the polarizability and in turn the susceptibility and ultimately the detected TA signal with its characteristic vibrational frequency.

From this explanation, three limitations of IVS can be inferred: Firstly, only Raman active vibrations can manifest in the TA signal. Secondly, since wave packets inevitably diphase, especially at room temperature, the temporal window of insight into the structural properties of the excited states is limited to short delays, directly after photoexcitation. Thirdly, the modulations are significantly smaller than the amplitude of the regarded signal, as they are limited by the relative change of the overall polarizability along their respective normal mode. The first limitation is inevitably rooted in the nature of the signal generation. The second limitation could also be regarded as an additional resource since it carries information about the lifetime of the corresponding wave packet. The lifetime can give insight into the different influences limiting it, such as the damping of the solvent cage, like the linewidth in NMR spectroscopy. Furthermore, the issue of limited wave packet lifetime can be incorporated into the experimental scheme. If a given wave packet decays before the corresponding excited-state population relaxes to the ground state, an additional laser pulse can be employed to reinduce a vibrational wave packet within the excited state. Figure 3.8 shows the double-sided Feynman diagram describing this signal contribution. The additional pulse is termed push, and the resulting three-pulse technique is called pump-IVS. It resembles the original IVS scheme (impulsive induction of a wave packet and subsequent probe) with an additional pump,

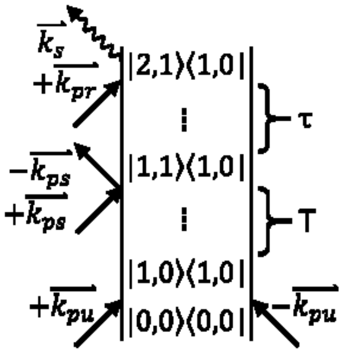

Figure 3.8: Double-sided Feynman diagram representing pump induced generation of an excited-state population. After a first delay (T), the push induces a vibrational coherences within the excited state, which is interrogated by the probe after a second delay (τ).

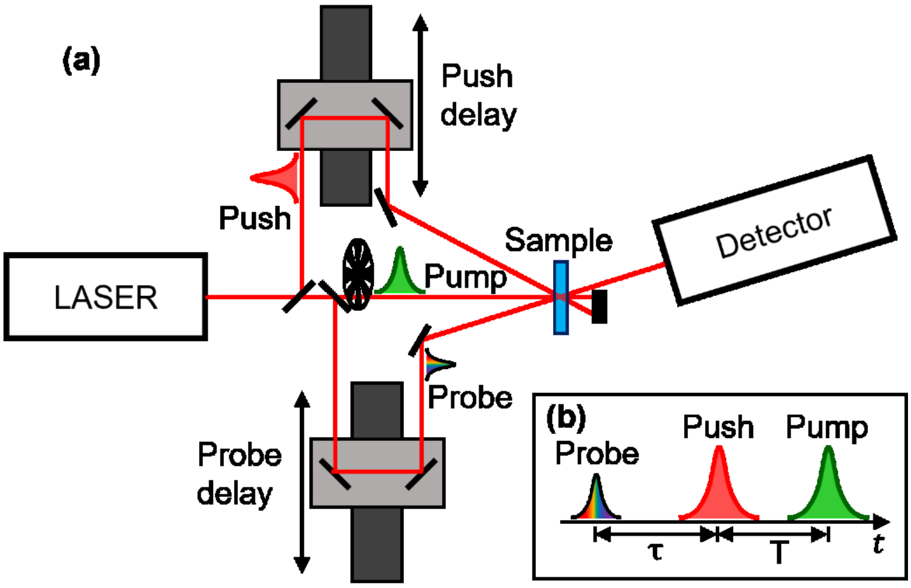

Figure 3.9: (a) Schematic setup for pump-impulsive vibrational spectroscopy. (b) Pump-impulsive vibrational spectroscopy pulse sequence.

exclusively responsible for preparing an excited-state population. The modified setup as well as the corresponding pulse-sequence are shown in Figure 3.9. The pump spectrum is tuned resonant with the ground-state absorption, while the push spectrum is tuned resonant with the absorption of the excited state of interest. Through the variable push delay T, the excited-state vibrational properties can be interrogated at any time, regardless of the dephasing of the initial wave packet. This also applies to excited states, which are formed via population transfer during the excited-state cascade and not directly from photoexcitation.

The heterodyne detection is useful to support the small signal amplitude. The homodyne detected equivalent of IVS and pump-IVS are (degenerate) four-wave-mixing (DFWM) and pump-DFWM, respectively. There the two interactions with inducing the vibrational coherence occur with two laser pulses with distinct wave vectors, called pump and Stokes. The signal is then generated not along the probe pulse, but along $\overrightarrow{k_S} = \overrightarrow{k_{pu}} - \overrightarrow{k_{St}} + \overrightarrow{k_{pr}}$. The homodyne detection allows for background free signal, but also lacks the amplification of the probe's local field, as described in section 3.1. DFWM therefore requires very sensitive detectors, such as photo multiplier tubes. The heterodyne detected (pump-)IVS signal on the other hand is intense enough that it can be split into its spectral components by the implementation of a diffractive element (such as a grating). Detection via a photodiode array (PDA) therefore enables the capturing of whole spectra. Nevertheless, both classes of methods require careful separation of the "slow" electronic population and the rapid oscillations from the vibrational wave packet contributing to the signal. This separation, as well as the subsequent analysis of the oscillating part, is described in the following section.

3.3.1 **Analysis of IVS data**

Since the IVS signal is interpreted in terms of individual kinetic traces in this work, unlike the globally interpreted TA signal, t_0-correction is not necessarily required. Similarly, to the analysis of TA data, the “slow” electronic population contribution to the signal is fitted using the model function given in Eq. 3.7. However, the focus is not on the time constants and amplitudes retrieved from this fit (Figure 3.10a), but on the residual it fails to describe: the oscillating modulations induced by the vibrational wave packet (Figure 3.10b). The singled-out oscillations can subsequently be quantified by different methods, two of which were employed and are introduced here.

The fastest method is Fourier transformation from time- to the frequency domain. It is named after the French mathematician Joseph Fourier, who stated, that any function can be expanded as a series of sine and cosine functions. Since it is possible to characterize a sine function by an amplitude, a frequency and a phase, any function can also be represented by a series of these properties. On this basis, the signal oscillations due to the wave packet can be expressed as a series of frequencies and their corresponding amplitudes – essentially a spectrum. While the phases can also be extracted, this is not relevant for the data analysis in this work and is therefore beyond the scope of this discussion. The obtained spectrum therefore shows peaks at all the frequencies, which contribute to the oscillating trace. Considering the Raman criterion of the IVS method, these spectra can be regarded as Raman spectra.

There are some aspects to consider when applying the Fourier transformation. Firstly, the density of points in the temporal domain (sampling frequency) determines the upper frequency limit in the obtained spectrum (Figure 3.11a+b). This is rooted in the fact, that at least two points must be sampled to observe the oscillation at all properly (Nyquist theorem). On the other hand, the length of the trace (not the total number of sampling points) determines the linewidth and therefore also the lower frequency limit that can reliably be interpreted in the obtained Fourier spectrum (Figure 3.11c+d). This can also easily be rationalized, since at least one period must be captured in the transformed trace, to quantify the frequency properly. Both these aspects must be considered, when designing the experiment, as they cannot be accounted for in the post-processing. In practice, a high sampling rate and a long trace length are often

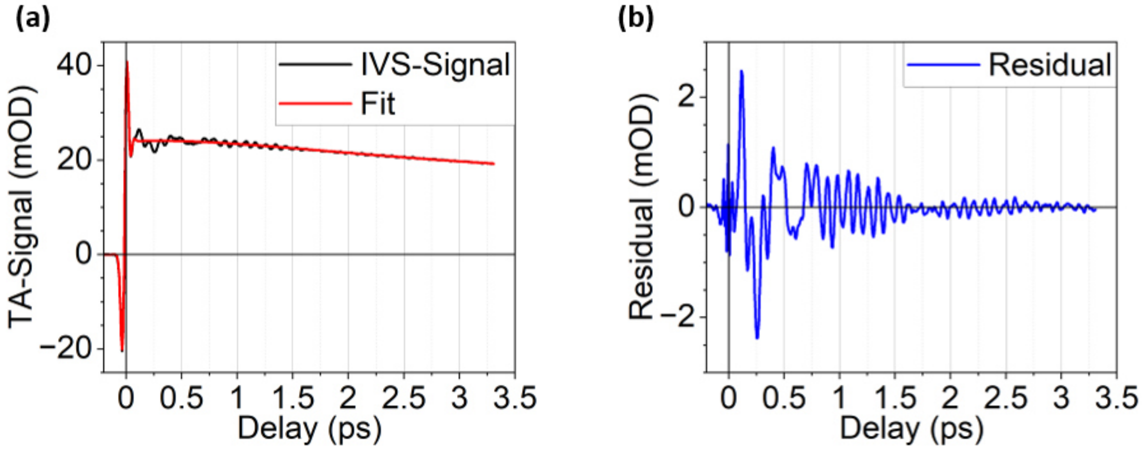

Figure 3.10: Extraction of oscillatory part of IVS signal by fitting. (a) IVS-Signal and fit according to Eq. 3.7. (b) Oscillatory part of IVS signal retrieved as residual of the fit.

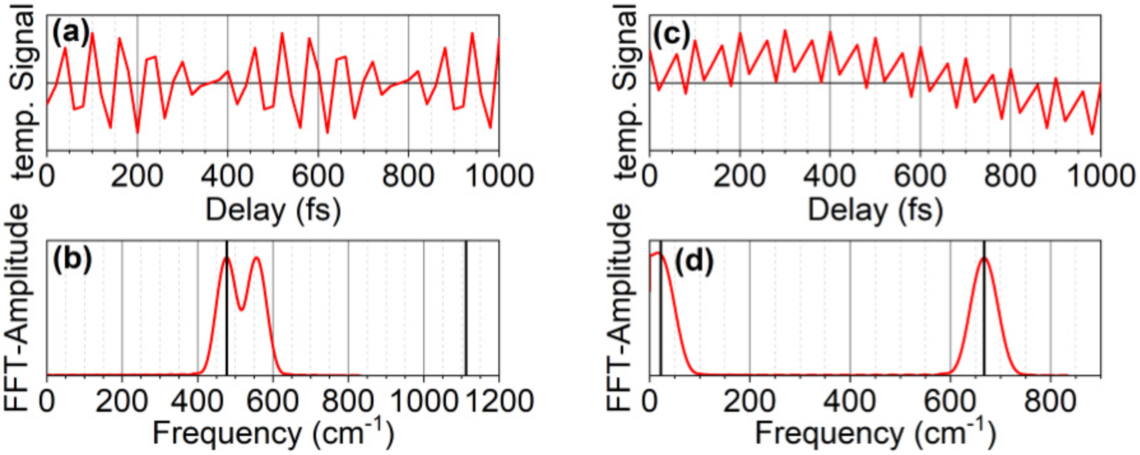

Figure 3.11 Temporal traces and FFT amplitudes thereof, demonstrating the upper and lower frequency limit. (a) Temporal trace with 30 fs (1112 cm^{-1}) and 70 fs (477 cm^{-1}) oscillations and $\frac{1}{20\,fs}$ sampling rate. (b) FFT amplitude spectrum of (a). The actual frequencies are indicated by black lines. (c) Temporal trace with 50 fs (667 cm^{-1}) and 1500 fs (22 cm^{-1}) oscillations and $\frac{1}{20\,fs}$ sampling rate. (d) FFT amplitude spectrum of (c). The actual frequencies are indicated by black lines.

conflicting goals, which lead to long data acquisition times, and the two must be balanced with the frequency region of interest in mind.

While the lowest identifiable frequency is determined by the length of the recorded trace, the density of points in the Fourier spectrum is determined by the total amount of sampling points. The obtained density of points can therefore be improved even after the experiment by expanding the recorded trace. To not falsify the obtained spectrum, this is done by appending a large number of zero value entries to the time domain signal. This technique is called zero-padding and was applied for all frequency spectra obtained by Fourier transformation in this work.

One more aspect worth considering when performing Fourier transformation, is spectral leakage. At its core, the Fourier transformation is a series expansion of a function and not a signal of finite length. This finite length introduces frequency contributions to the spectrum, which would not be present for a closed function, or a signal of infinite length. These contributions can be reduced significantly, by multiplying the signal with a window function.[70, 71] One can choose from a large variety of such window functions, all of which force a sloped onset and decay of the signal at the edges. The window functions therefore act as different envelopes, each with specific properties for the line shape and leakage suppression of the obtained spectrum. For the monitoring of vibrational coherences, the introduction of a window function is challenging, as sometimes the oscillations decay fast. The signal is therefore very susceptible to suppression at early delays, where the amplitude is largest. On the other hand, the application of a window also significantly reduces influence of the coherent artifact, which can be hard to unambiguously identify in an oscillating signal. In the thorough analysis of the (pump-)IVS data presented in this work, several windows of different slopes, especially at early delays, were considered, and the respective spectra were compared (Figure 3.12). In the unwindowed spectrum, the amplitudes of the major peaks evidently are largest. However, these are also accompanied by additional sidebands, as well as a constant background, both characteristic for spectral leakage. The Gaussian window produces the smallest

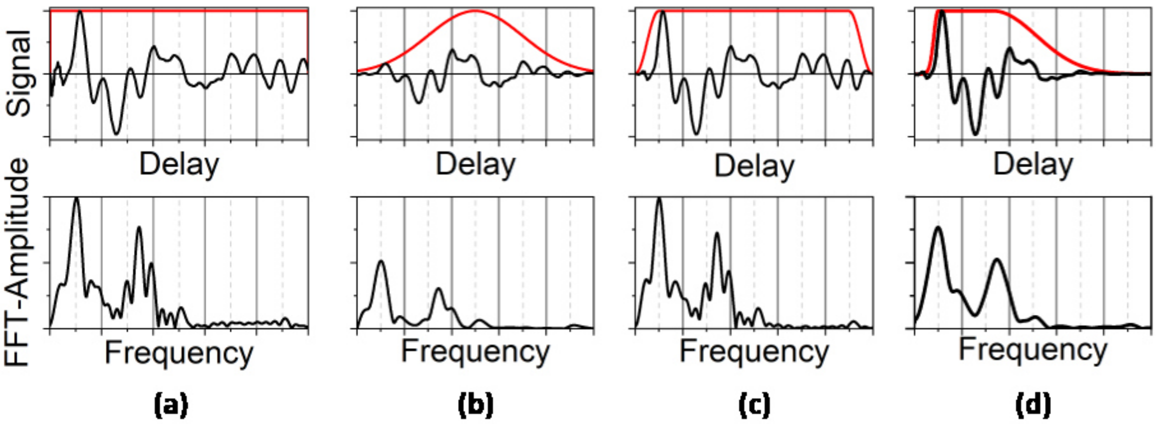

Figure 3.12: Different window functions (red) applied to the same exemplary oscillating trace (black), as well as the resulting Fourier spectra (bottom). All abscissae and ordinates are identical to allow proper comparison. (a) No window. (b) Gaussian window. (c) Cosine tapered window. (d) Custom combination of Cosine tapered rise and Gaussian decay to capture large oscillations at early delays while maintaining good suppression of spectral leakage.

amplitude, which is unsurprising, since it represents the most depleting envelope. In return, the obtained peaks are almost free of sidebands and background is absent completely. The cosine tapered window produces a spectrum similar to the unwindowed trace, although the constant background is slightly suppressed. The custom combination of the cosine tapered rise and the Gaussian decay window was designed to consider the major oscillations at early delays while suppressing spectral leakage efficiently. As indicated by the good amplitude, lack of sidebands and negligible background in the spectrum, this is achieved satisfactorily. It is worth noting, that the frequency and relative amplitude of the two main peaks are identical, regardless of the window used. To lay reliable foundations for interpretation, all spectra shown in the results section were obtained using a Gaussian window (Figure 3.12b). While the custom designed window also provides good suppression of spectral leakage, the Gaussian window is chosen to improve reproducibility of the obtained spectra. Furthermore, the double-structure of the second peak visible for the Gaussian window but not for the custom one, actually reflects real molecular oscillations in the exemplary trace, as is discussed in section 5.4. Following the same maxim of unbiased representation, amplitude spectra are shown, instead of the so-called power spectra, which distort the relative amplitudes by squaring them.

A useful temporal expansion of the Fourier transformation is sliding-window Fourier transformation, in which the regarded section of the signal in time domain is iteratively shifted. For example, a signal trace of 2 ps length can be dissected into 10 subsets of 1 ps window length, each shifted by 0.1 ps. Fourier transformation of each of the subsets yields a series of Raman spectra, reflecting the wave packets' temporal evolutions.

Another approach to quantification of oscillations in the IVS signal is to fit them using sine functions. Decay of the wave packet is accounted for by multiplication of an exponential decay, damping the individual oscillation. The complete model function used is given in Eq. 3.8.

$$S(t) = \sum_{i}^{n} A_i * sin\left(\frac{2\pi(t+\varphi_i)}{\omega_i}\right) * \exp\left(\frac{-t}{\tau_i}\right) \qquad \text{Eq. 3.8}$$

Here A_i is the amplitude, φ_i is the phase, ω_i is the frequency and τ_i the decay constant. However, the simultaneous fitting of four parameters per contribution easily exceeds the Fourier transformation as implemented in the Fast Fourier Transform algorithm (FFT). It is therefore advisable to consider the spectrum obtained by FFT for input parameters of the frequencies ω_i. An advantage, however, is that the decay time constants τ_i are directly fitted, whereas they can only be estimated qualitatively from SW-FFT.

4 Experimental Setups

In this chapter, the employed setups are shown, the physical principles of pulse generation are briefly explained, and the experimental parameters are documented.

The experiments shown in this work are conducted in two different laboratories. In section 4.1, the TA and (pump-) IVS setup used for the experiments on the iron(II)complexes is discussed. It features broadband visible pulses which are compressed down to <20 fs, allowing for excellent temporal resolution.

In section 4.2, the TA setup used on TPA and its derivate is introduced. It is characterized by a wide variety of available pump wavelengths and two different probe and probe-delay schemes, covering 10 orders of magnitude from femtoseconds to hundreds of microseconds.

4.1 Transient Absorption, (Pump-)Impulsive Vibrational Spectroscopy

4.1.1 **Setup**

A scheme of the setup is shown in Figure 4.1. The setup is powered by a regenerative Ti:Sa Laser (Libra, Coherent). The active medium is pumped by a diode laser (Evolution, Coherent) at 532 nm. The seed laser a mode locked Ti:Sa laser (Vitesse, Coherent). Opening and closing of the cavity is done via Pockels cells, triggered by a synchronization and delay generator (SDG Elite, Coherent). The spectral width (7.34 nm at 798 nm, Figure 4.2) allows for 130 fs duration of a transform-limited pulse. The CPA system emits 1.5 W at a repetition rate of 1 kHz (1.5 mJ/pulse). This

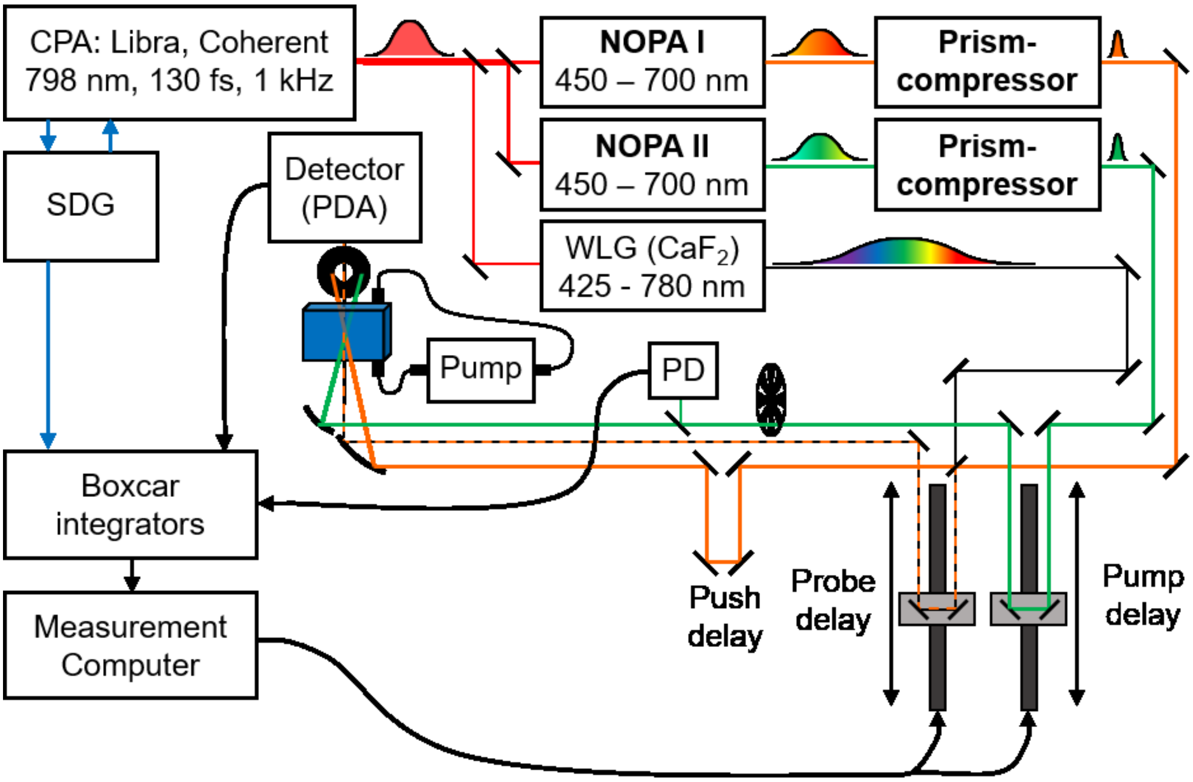

Figure 4.1: Scheme of TA- and (P-)IVS setup employed in this work. Pathways for pump (green) push (orange) and probe (black / orange) are indicated. Blue arrows represent delay reference. Black arrows represent data flow and control. CPA: Chirped pulse amplification. NOPA: Non-collinear optical parametric amplifier. SDG: Synchronization and delay generation. WLG: White light generation. PD: Photodiode. PDA: Photodiode array. Detailed description in the text.

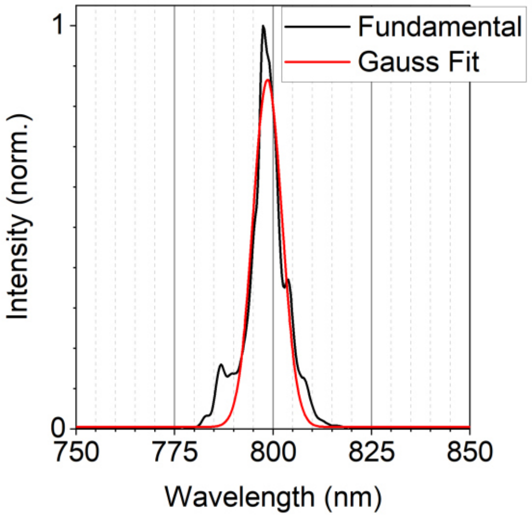

Figure 4.2: Spectrum of the fundamental output of CPA, as well as estimation of peak center and full width at half maximum (FWHM) by Gaussian fit: 798 nm, 7.34 nm, respectively.

system's power is split using beam splitters to support several pulse manipulation schemes, such as noncollinear parametric amplifiers (NOPA) and white light generation stages (WLG). For the experiments in this work, two NOPAs and WLG are required. 300 mW are coupled into each of the NOPAs, where tunable broad band pulses in the visible spectral range are generated. They are described in detail in section 4.1.3. Output power of the NOPAs is 2-5 mW. The strongly chirped output is compressed in a prism compressor, as described in section 4.1.4. 0.3 mW of the fundamental are directed into a white light generation stage. Compared to sapphire, the other common medium for white light generation, calcium fluoride is characterized by greater transparency at wavelengths below 450 nm but also a lower damage threshold. To avoid photodamage in the crystal, it is therefore constantly translated in the focus plane. After a collimation lens, the remaining fundamental is removed by passage through a calflex^{TM} filter. In the setup, it is possible to direct either a fraction of a compressed NOPA output, or the uncompressed white light into the probe pathway. Both pump and probe can be delayed separately using a computer controlled mechanical delay stage. In three pulse experiments, the push is fixed in time, but pump and probe can be delayed accordingly. The pump is directed through a chopper blocking every second pulse. Subsequently, a minor fraction of the pulse is directed onto a photodiode to indicate to the measurement computer, whether the recorded spectrum is pump on or off. Push and probe are directed onto a shared focus mirror (f = 25 cm), while the pump is directed on another focus mirror (f = 20 cm) to allow for independent control over the spot size at the sample. The sample is circulated through a flow cell (front window 0.5 mm fused silica, inner diameter d = 0.4 mm) to prevent photodamage. The front window is accounted for in the characterization of the pulse duration via autocorrelation. After collimation, an iris separates the probe from the other pulses. The probe is subsequently focused into the detector. The pulse is dispersed by a grating spectrograph (Spectrograph MS 125, LOT Oriel, 2400 lines/mm) onto a photodiode array (256 pixels). Both the PDA and the PD signal

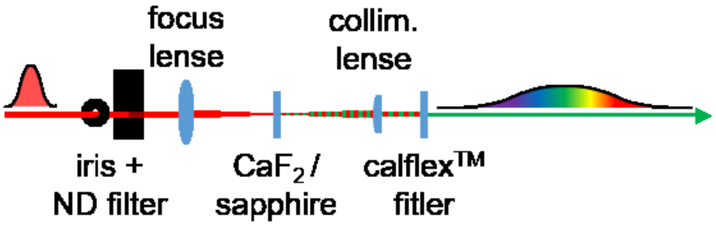

Figure 4.3: Schematic representation of a white light generation stage.

are integrated using boxcar integrators, triggered by the synchronization and delay generator.

4.1.2 **White light generation**

The generation of white light continua (WLC) is crucial for generating both broad band probe pulses covering the complete visible spectral range, as well as intense pump pulses, tunable across the same spectral region.[72, 73] A typical white light generation stage is shown in Figure 4.3. The 798 nm fundamental from the Ti:Sa CPA is coupled in through an iris and a ND-filter. This allows to spatially filter and attenuate the incoming beam. It is then directed through a focus lens into a transparent dielectric medium, typically sapphire or calcium fluoride, although more sophisticated media support repetition rates in the MHz scale.[74] Multiple nonlinear effects contribute to the spectral broadening that builds up the WLC, with the material properties governing the achievable spectral width.[75] Sapphire, e.g., is a very robust medium, but its transparency doesn't support the generation of wavelengths < 450 nm. Calcium fluoride on the other hand allows generation of WLC that stretch out to the near UV but suffers from photodamage when exposed for a few seconds. This can be compensated by constantly translating the calcium fluoride crystal in the focal plane, which requires a motorized holder stage. In the setup described in section 4.1.1, WLC generation of the broad band probe is achieved in a 2 mm thick calcium fluoride crystal, mounted on a motorized stage. Inside the two NOPAs, WLC is generated in sapphire, as the created continuum is sufficient to support the required tuning range.

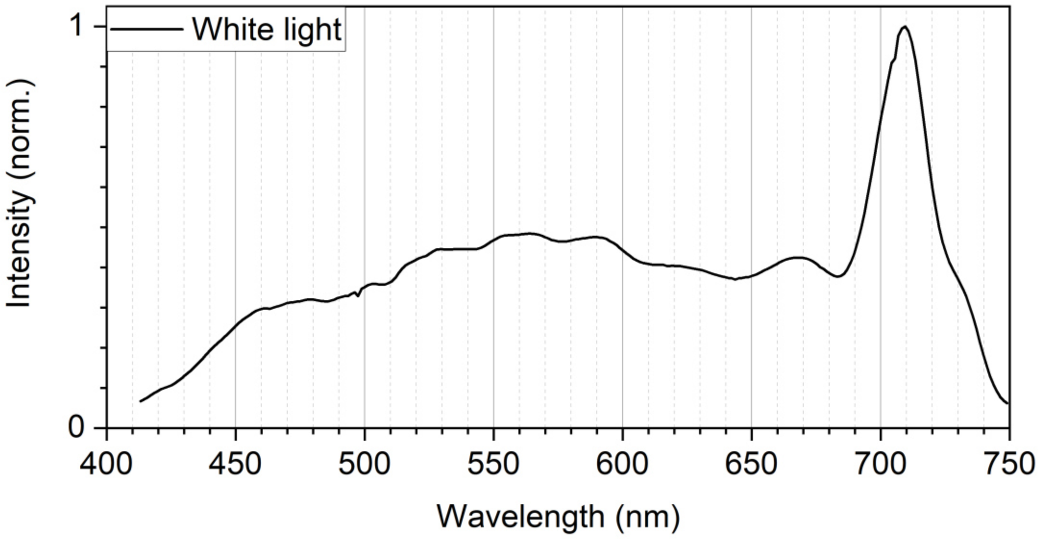

Figure 4.4: Broadband probe spectrum employed in TA experiments.

4.1.3 **VIS Pump, Push & Probe**

The pump pulse is generated in a noncollinear parametric amplifier (NOPA).[72, 76-79] From a coupled in fundamental (~300 mW) a minor fraction is split of and a white light continuum (WLC) is generated by focusing it into a sapphire crystal. The beam is collimated, the remaining fundamental is removed by passing through a calflex^{TM} filter and the white light supercontinuum is directed to a β-barium borate (BBO) crystal. From the major part of the fundamental the second harmonic (SH) is generated by focusing it into a BBO crystal (see double sided Feynman diagram in Figure 3.2a). After collimation, the remaining fundamental is removed by reflecting the second harmonic at a band specific dielectric mirror. The SH is too directed to the BBO crystal forming an angle α with the WLC. The polarization of SH and WLC are perpendicular to each other, so that the birefringence compensates for the different speeds at which they pass the crystal. To achieve optimal effective spatial and temporal overlap within the crystal, the angle α must be chosen to support the wanted spectral region within the WLC. This is called the phase matching condition, and it allows for efficient amplification of the WLC in the following way. The SH undergoes difference frequency generation (Figure 3.2c), so that from every SH photon, a photon equivalent to the amplified spectral region of the WLC is generated (signal), as well as a NIR photon (idler). The spectral region of the WLC that is amplified is thereby selected by the SH delay relative to the strongly chirped WLC, as well as the angle α (phase matching condition). The output inherits the momentum (i.e., direction) of the WLC acting as seed and therefore needs no additional collimation. Since it is an amplified subset of the WLC, the signal is also strongly chirped. It can be temporally compressed using a prism compressor (section 4.1.4).

Figure 4.5 shows an exemplary pulse characterization of the VIS pump after compression. The spectrum is centered at 516 nm with a full width at half maximum (FWHM) of 35 nm (538-503 nm). The autocorrelation can be fitted with a Gaussian of 18.5 fs. Dividing by factor $\sqrt{2}$ to account for the autocorrelation gives a pulse duration

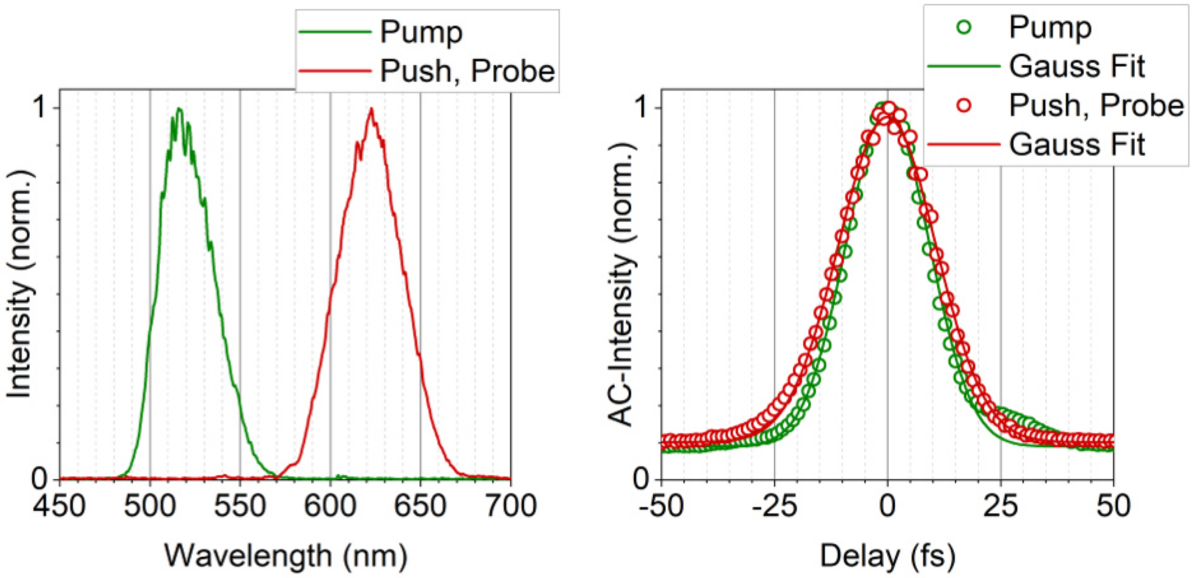

Figure 4.5: Typical Pulse characterization of the compressed NOPA outputs used as pump, push, and probe. (a) Spectral characterization. (b) Temporal characterization by auto-correlation.

of 13.1 fs. Stability of the pump power is characterized as standard deviation of a measurement over 30 seconds and typically is below 1% of the absolute power. The relative polarization of pump and probe as well as their powers are set using pairs of linear polarizers. For both TA and IVS experiments, the pump energy is set to 200 nJ/pulse, and the polarization relative to the probe is set to magic angle. For P-IVS experiments, the push energy is set to 200 nJ as well, with the polarization parallel to that of the probe. For (P-)IVS experiments, both push and probe are generated from a NOPA, and compressed in a prism compressor to allow for optimal temporal resolution. A typical pulse characterization is shown in Figure 4.5. The spectrum is centered at 623 nm with a FWHM of 43 nm (600 -643 nm). The autocorrelation curve is fitted using a Gaussian of 21.6 fs width, corresponding to a pulse duration of 15.3 fs. Typical stability of the push- / probe power is <1% of the average power.

4.1.4 **Prism compressor**

From their white light seed, the NOPA outputs inherit their significant chirp (Figure 3.5). In the visible range, dielectric media introduce positive chirp, leading to the lower frequencies in the leading edge and higher frequencies in the trailing edge of the pulse, as indicated in Figure 4.6. To compensate this, prism compressors are employed to introduce tunable quantities of negative chirp.[80] As shown in Figure 4.6, a prism compressor consists of two prisms, a variable reflector stage and a mirror. The working principle of a prism compressor is to disperse the incoming pulse in the first prism, and then to let different spectral regions travel different lengths through the second prism. Since the speed of light is reduced in media according to their refractive index, the further light travels through the prism, it is delayed more. By increasing the path length of the reflector stage, the incoming light is dispersed more, so that the distance traveled within prism 2 becomes more different for the different portions of the pulse. This allows to tune the amount of negative chirp introduced to precisely compensate the positive chirp introduced by other optics. Proper pulse compression is therefore an iterative procedure of adjusting the compressor and characterizing the pulse duration via autocorrelation. To account for all the optics passed after the prism compressor, the positive chirp inherited from the NOPAs WLC is overcorrected. The autocorrelator is set close to the sample, so that all optics leading up to the sample inside the cuvette are passed before characterization of the pulse duration. The front window of the cuvette is thereby mimicked by 0.5 mm thick glass plate. Pulse durations

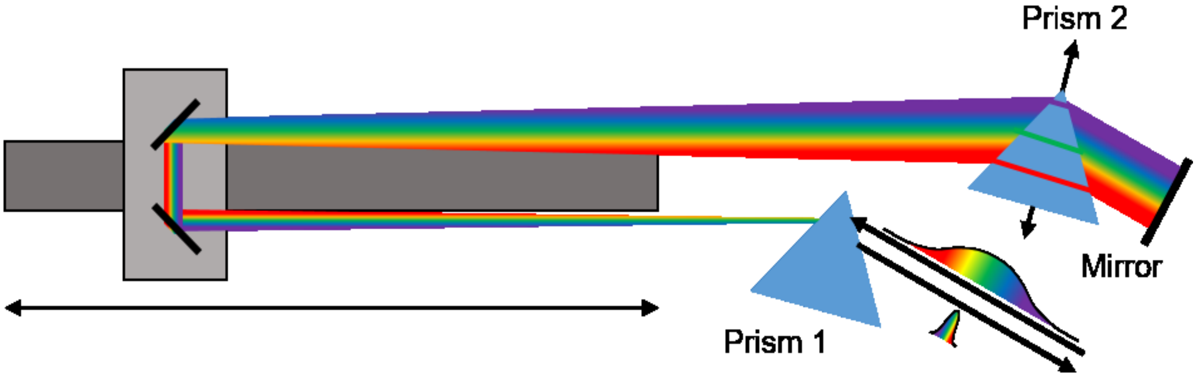

Figure 4.6: Schematic representation of a prism compressor introducing negative chirp to compensate positive chirp accumulated by passing through optics.

characterized by autocorrelation are therefore representative of the pulse duration within the sample.

4.2 Transient Absorption, UV Pump

4.2.1 **Setup**

A scheme of the TA setup used for the triphenylamine (TPA) samples is shown in Figure 4.7. The setup is powered by a regenerative Ti: Sa chirped pulse amplifier. The active medium is pumped by a laser diode at 532 nm, 30.3 W (Revolution, Coherent) and seeded by a mode locked Ti:Sa laser at 800 nm, 570 mW (Vitara, Coherent). Q-switching of the cavity is done using Pockels cells, triggered by a synchronization and delay generator (SDG Elite, Coherent). The fundamental spectrum (800 nm, 11.3 nm FWHM) is shown in Figure 4.8a and allows for 83 fs pulse duration under assumption of a transform-limited pulse with Gaussian line shape. The 6.0 W output is divided using beam splitters and powers multiple setups. A commercial optical parametric amplifier (TOPAS Prime, Light Conversion) is used to tune the center wavelength to 1200 nm. This output is coupled into two mixer stages, both driving second harmonic generation to 600 nm and subsequently 300 nm (Figure 4.8b). 40 mW output power with fluctuations of <0.5% are achieved. This output is used as pump with two commercial TA setups. Delays of up to 8 ns are scanned using the HELIOS TA spectrometer (Ultrafast systems). Here, the broad band probe pulse is generated from the 800 nm fundamental as described in section 4.1.2, with multiple optical media available to cover different spectral ranges (see section 4.2.2). The delay is set using a mechanical delay stage. The effective repetition rate of the pump is reduced to 2 kHz by a mechanical chopper (Chopper 1 in Figure 4.7). Relative polarization of pump and probe is set to magic angle to negate effects of rotational diffusion. Both pump and

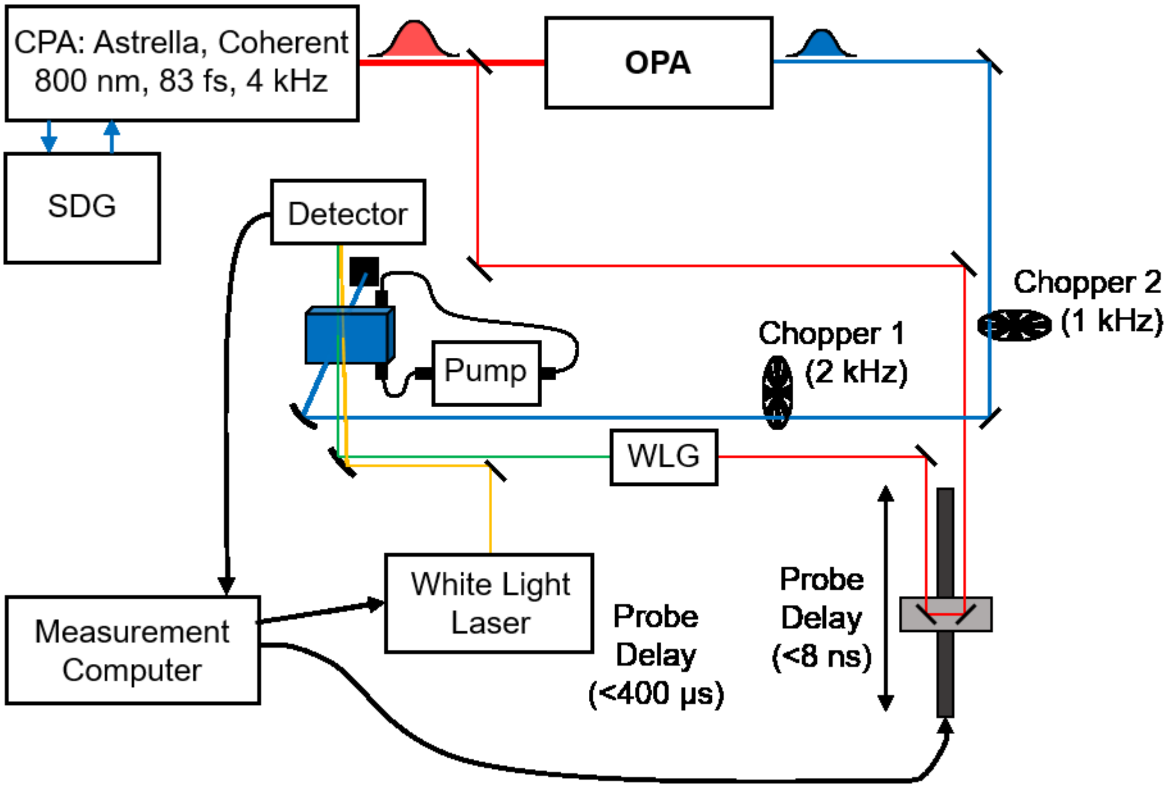

Figure 4.7: Scheme of TA setup employed for triphenylamine samples. Pathways for pump (blue) as well as short and long delay probe (green and yellow, respectively) are indicated. Black arrows represent data flow and control. CPA: Chirped pulse amplification. OPA: Optical parametric amplifier. SDG: Synchronization and delay generation. WLG: White light generation. Detailed description in the text.

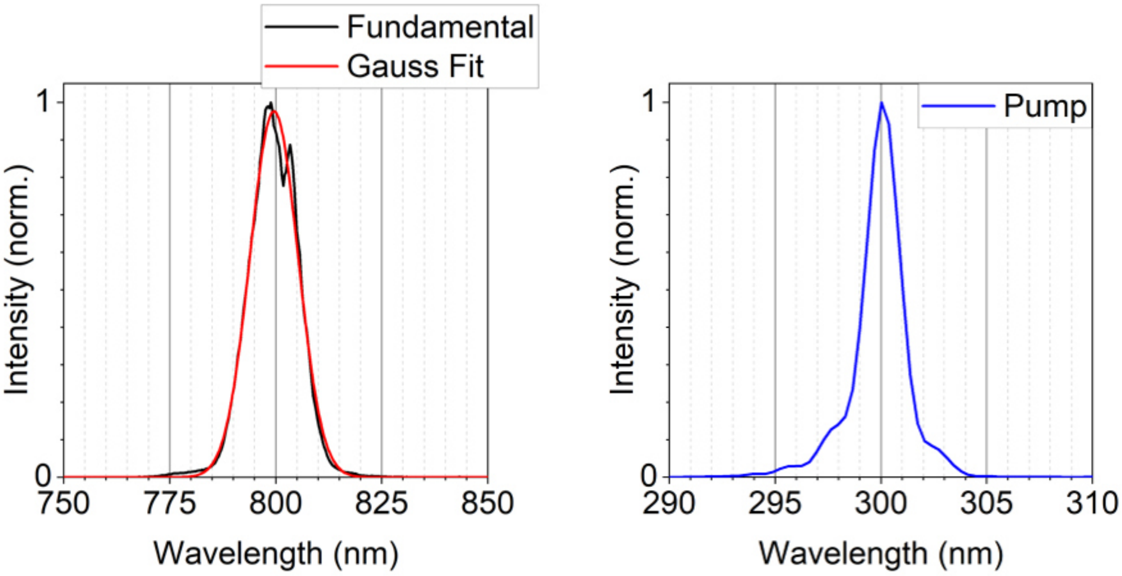

Figure 4.8: (a) Spectrum of the fundamental output of CPA, as well as estimation of peak center and full width at half maximum (FWHM) by Gaussian fit: 800 nm, 11.3 nm, respectively. (b) Spectrum of OPA output used as pump.

probe are focused into the sample using distinct focus mirrors, allowing individual adjustment of the spot diameter. Probe delays of up to 400 µs are achieved with the EOS add-on (Ultrafast Systems) by an electronically delayed white light laser. Since this laser only supports 2 kHz repetition rate, the effective repetition rate of the pump is also decreased to 1 kHz. This is achieved using an additional chopper (Chopper 2 in Figure 4.7). The chopping sequences of the short and long delay TA experiments are shown in Figure 4.9a and b, respectively. The cuvette is adjusted to the sample. All degassed samples with hexane as solvent are contained in a 2 mm fused silica cuvette with a magnetic stirrer. The respective experiments under ambient conditions are performed in the same cuvette, after the cap was opened to allow for exchange with air. Samples with chloroform as solvent are circulated through a 0.5 mm flow cell to avoid the accumulation of photoproduct.

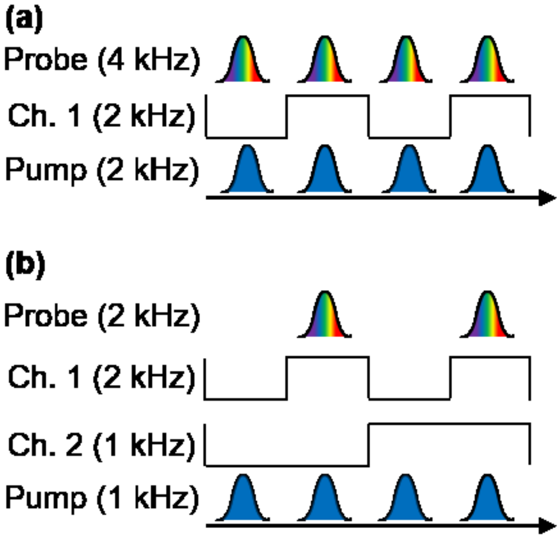

Figure 4.9: Pump chopping sequences for (a) short delay setup (4 kHz probe frequency) and (b) long delay setup (2 kHz probe frequency).

4.2.2 **White light probe spectra**

The white light probe spectra are shown in Figure 4.10. Two distinct probe spectra are employed in the short delay setup. Both are created by focusing the delayed 800 nm fundamental into a dielectric medium as documented in Figure 4.3. As discussed above for the TA- and (P-)IVS setup, the white light generated in this fashion suffers from significant chirp, which needs to be corrected in the post processing.

The first spectrum is generated in a sapphire plate and spans across the visible spectral region (460 – 770 nm) with a sharp cut-off edge at long wavelengths from the filtering of the remaining fundamental. The second probe spectrum is generated inside a calcium fluoride plate, mounted on a constantly moving motorized holder to prevent photo-damaging the medium. This spectrum extends further into the near UV region (330 – 600 nm). Consecutive measurements with the two spectral ranges enables monitoring the transient absorption over the 330 – 770 nm range. Moreover, because both spectral regions overlap significantly, the TA signal recorded there can be used to rescale the recorded signal, correcting for minor deviations in probe spot size and overlap with the pump between the measurements. After application of this correction factor, the two collected datasets can be combined to one with a wavelength axis of 330 – 770 nm. This allows for easy simultaneous fitting (global analysis) of all observed dynamics. The short probe delays are set using a computer controlled multi-pass delay stage.

The white light for long probe delays is generated by an electronically triggered photonic crystal fiber laser. Therefore, filtering of the 800 nm fundamental is not necessary, allowing to expand the spectrum to the NIR (380 – 910 nm), although it suffers from small intensities at wavelengths > 650 nm. Furthermore, both the pulse duration and the electronically controlled delay significantly limit the temporal resolution to hundreds of picoseconds.

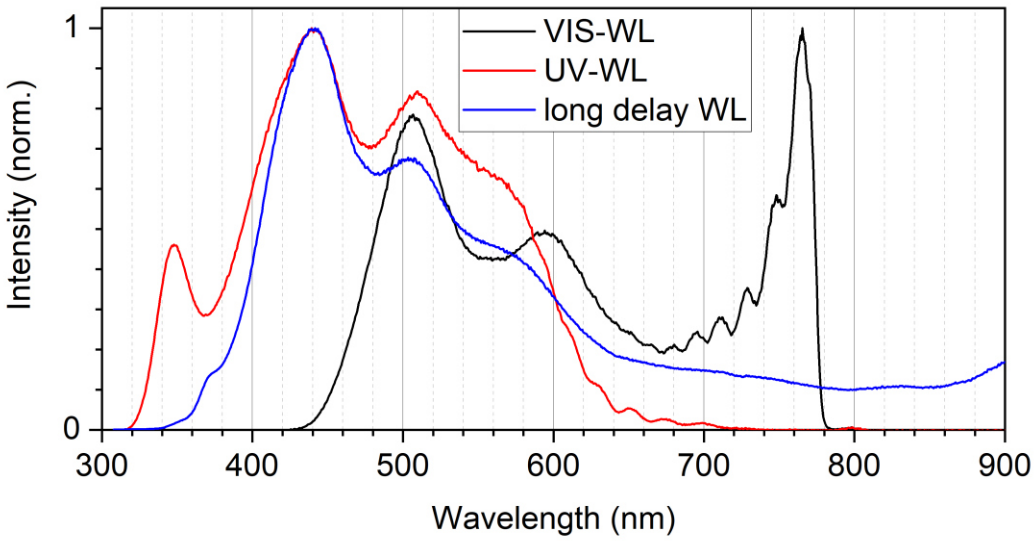

Figure 4.10: Spectra of probe pulses employed in short and long delay transient absorption.

4.3 Sample preparation

4.3.1 **General sample preparation**

All samples are obtained in solid state from cooperating groups. Without further purification, they are dissolved in the respective solvent: Acetonitrile, chloroform, DMSO, n-hexane and methanol, all in HPLC grade purity as obtained from commercial supplier. Concentrations are adjusted, to suit the cuvette thickness in the experimental setup. The iron(II)complexes are set to an absorption of 0.3 – 0.5 OD in the 0.4 mm flow cell described in section 4.1.1. TPA and DTPA concentrations are adjusted to yield 1.0 OD either in the 2 mm cuvette for (degassed) n-hexane or the 0.5 mm flow cell used for the experiments in chloroform.

Characterization of ground-state absorption, both as part of sample preparation and as control after the time-resolved experiment, is done using Shimadzu spectrophotometers UV-1800 and UV-2600.

The freeze-pump-thaw procedure for the removal of molecular oxygen from the sample solution is described below.

4.3.2 **Degassing procedure**

To characterize the influence of oxygen on the photophysics and photochemistry of a given liquid state sample, it is necessary to have reliable reference measurements without oxygen in the solution. This is achieved employing a freeze-pump-thaw procedure using a custom cuvette as shown in Figure 4.11. The dissolved sample is stored in a round flask, attached to both the cuvette and a suitable pump. The solution is frozen by submerging it in a bath of liquid nitrogen. Once frozen, the glassware is evacuated. In the setup used in this work, this is achieved by a rotary pump and a turbomolecular pump, capable of producing vacuum in the order of 10^{-5} mbar. After 5 minutes of stable vacuum, the glassware is flooded with a suitable inert gas, such as nitrogen, and the sample is allowed to thaw in a water bath. This procedure is repeated at least two more times. After the last thawing, the sample is transferred to the cuvette and the top tap is closed, sealing the degassed sample in the cuvette.

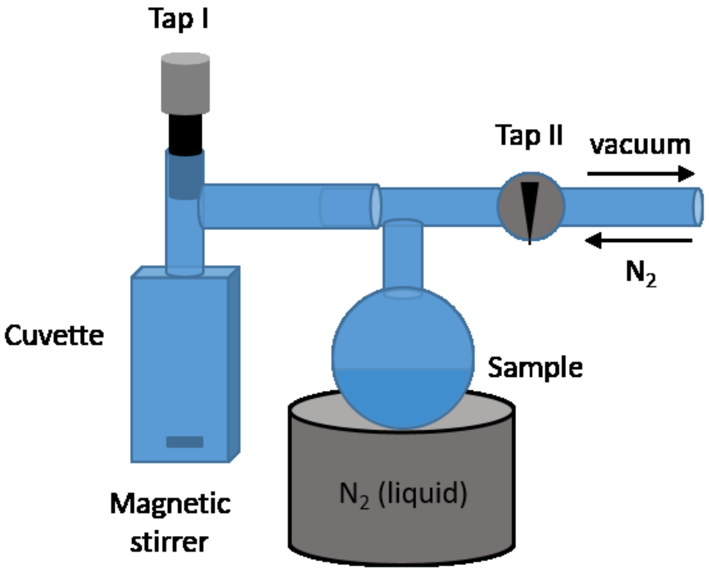

Figure 4.11: Scheme of degassable cuvette.

4.3.3 Irradiation series

Irradiation experiments were conducted to qualitatively determine rate and product of photochemical processes. Solutions of TPA and DTPA in n-hexane and chloroform (250 µM) were placed in a 2 mm fused silica cell with a magnetic stirrer under ambient and degassed conditions. They were irradiated by the unfocused pump beam (0.5 mW, 300 nm, spectrum see Figure 4.8b). Absorption spectra were recorded at several irradiation times using a Shimadzu spectrophotometer UV-2600.

5 Exploring MC and MLCT states of Fe(II) complexes

For this study, two different Iron(II)-complexes have been investigated.

Firstly, $[Fe(bpy)(CN)_4]^{2-}$ is compared to other paradigmatic Fe(II) complexes known from literature to rationalize the effect of ligand choice in this heteroleptic example. The strongly solvatochromic $[Fe(bpy)(CN)_4]^{2-}$ is then investigated using transient absorption and IVS. Its solvent dependence is probed in methanol and DMSO, establishing IVS as a suitable tool to identify MC involvement in the excited-state dynamics of Iron(II)complexes.

Secondly, the same experimental combination of time resolved electronic and vibrational spectroscopy is applied to $[Fe(cpbmi)_2]^{2+}$, to clarify the role MC states play in MLCT deactivation.

5.1 Photophysics and solvatochromism of $[Fe(bpy)(CN)_4]^{2-}$

$[Fe(bpy)(CN)_4]^{2-}$ (Figure 5.1c) consists of two types of ligands coordinated to an Fe^{2+} ion. Both ligands are chosen, and their relative composition optimized to promote a MLCT transition and stabilize the resulting MLCT population.

The necessity of both ligand types may be rationalized from comparison to two paradigmatic Fe(II)-complexes containing only one type of ligand each: $[Fe(bpy)_3]^{2+}$ and $[Fe(CN)_6]^{4-}$. Simplified energy diagrams of all three complexes are given in Figure 5.1. $[Fe(bpy)_3]^{2+}$ features three bpy ligands, known as excellent electron acceptors.[81] The optically allowed MLCT transitions result in its dark red color (λ_{max} = 537 nm).[82] However, due to their comparatively weak σ-donor strength, the exclusive use of bpy ligands results in a weak ligand field splitting of the t_{2g} and e_g manifold. Metal centered states, although optically forbidden due to the Laporte-rule, are energetically below the MLCT manifold and are easily populated from there via nonradiative pathways. As a result, the MLCT population created by photoexcitation decays to a high-spin metal

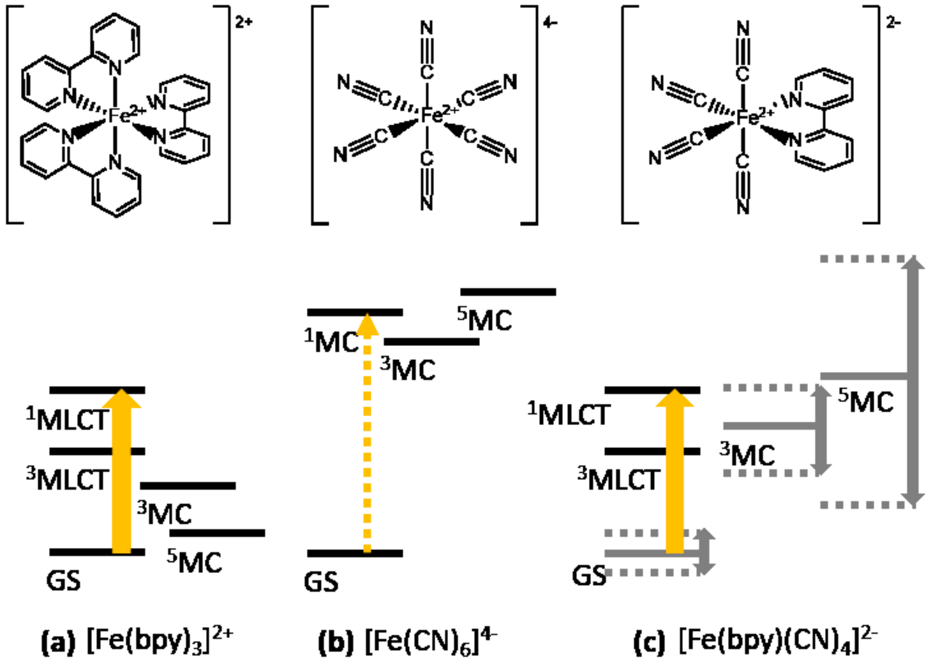

Figure 5.1: Schematic energy diagrams of paradigmatic Fe(II) complexes and $[Fe(bpy)(CN)_4]^{2-}$. Yellow arrows represent photoexcitation, grey arrows in (c) represent changes due to solvent interactions.

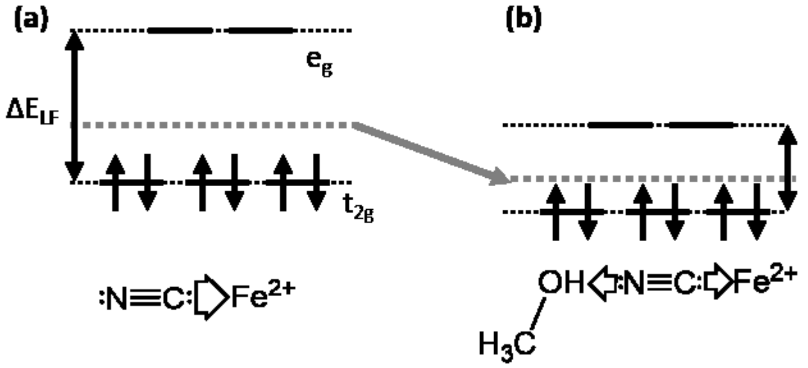

Figure 5.2: Energy diagrams of d-orbital configuration of electronic ground state when cyanide ligands (a) pose a strong ligand field and (b) when their donor capacity is diminished by solvent interaction.

centered state, the ^{5}MC, within ~130 fs.[7, 8] $[Fe(CN)_6]^{4-}$ instead is composed of an Fe^{2+} ion and six cyanide ions, posing a very strong ligand field. Consequently, high-spin metal centered states are of much higher energy than in $[Fe(bpy)_3]^{2+}$. However, in the absence of an electron accepting ligand, no optically allowed MLCT transitions are possible. Consequently, the faint yellow color of $[Fe(CN)_6]^{4-}$ is due to a Laporte-forbidden transition to a metal centered state. Note, that the strategy to shift the MC states upwards in energy by introducing strongly σ-donating ligands works: the MC state in $[Fe(bpy)_3]^{2+}$ is energetically below a transition at 537 nm, while the direct transition to a MC state in $[Fe(CN)_6]^{4-}$, lending to its faint yellow color, must be in the blue portion of the visible spectrum. The resulting iron(II)-complex is just unfit as chromophore due to the weak optical activity and the lack of MLCT states required to propagate separated charge towards an application. $[Fe(bpy)(CN)_4]^{2-}$ contains both types of ligands: bpy to provide an electron accepting ligand, enabling MLCT transitions, and cyanide ions to destabilize MC states acting as ultrafast MLCT loss channel. However, the cyanide ligands also introduce a solvent dependence into the photophysics, which is presented schematically in Figure 5.1c and explained in Figure 5.2. Cyanide ions feature two lone electron pairs at opposing ends, which are in principle capable of coordinating to metal cations: one located at the nitrogen atom and the other at the carbon atom. Since both atoms formally have 5 valence electrons but differ in nuclear charge, the nitrogen coordination site can be considered harder in terms of the hard and soft acids and bases concept (HSAB), whereas the carbon site is softer. As a result, cyanide ions coordinate to hard cations (high charge, early transition metals) via the nitrogen site (η_N) and to soft cations (low charge, later transition metals) via the carbon site (η_C). Hexacyanoferrat ($Fe(CN)_6$) is an excellent example of this. To the higher charged, harder Fe^{3+} ion in $[Fe(CN)_6]^{3-}$ cyanide coordinates η_N, whereas to the softer Fe^{2+} ions in $[Fe(CN)_6]^{4-}$ or $[Fe(bpy)(CN)_4]^{2-}$ cyanide coordinates preferably η_C. Consequently, the lone pair located at the nitrogen points outward in $[Fe(bpy)(CN)_4]^{2-}$, where it is available for interactions with Lewis acidic solvents. These electron withdrawing interactions also decrease electron density at the carbon. Hence, the actual σ-donor strength of cyanide ligands, and in turn the ligand field splitting, can be diminished by Lewis acidic solvents. This is especially true for the explicit formation of hydrogen bonds, as shown in Figure 5.2b.

The strong solvatochromism of $[Fe(bpy)(CN)_4]^{2-}$ introduced by the CN^-ligands is captured in Figure 5.3. In DMSO, the cyanide ligand's electron donating capabilities

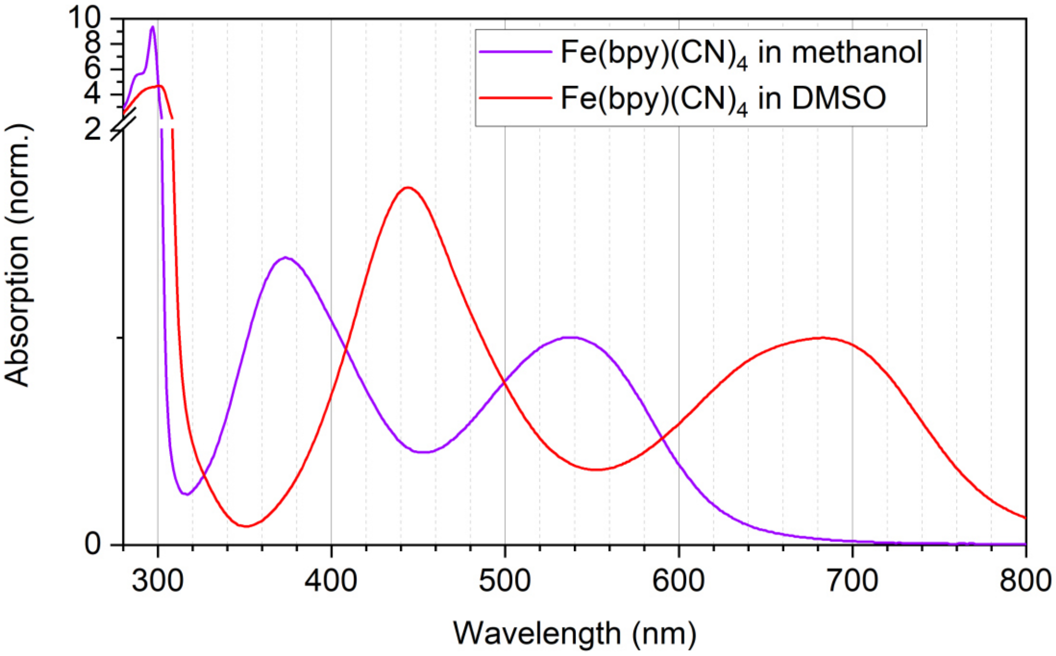

Figure 5.3: Absorption spectra of [Fe(bpy)(CN)$_4$]$^{2-}$ in methanol and DMSO.

through the lone pair located at the carbon atom are not diminished. Accordingly, the iron ion experiences a strong ligand field. Although this especially destabilizes the e_g manifold with the orbitals pointing directly towards the ligands, an overall strong ligand field affects all d-orbitals, hence destabilizing the ground state (d^6) with respect to the singlet MLCT state (d^5), see Figure 5.3a. This results in the absorption band of the optically allowed MLCT transition to be centered at 660 nm. In methanol on the other hand, a Lewis acidic solvent where explicit hydrogen bridges to the lone pair on the nitrogen atom form, the electron donor capacity of the cyanide ligands is greatly decreased. Relative to the situation in DMSO, this constitutes a stabilization of the d-orbitals and hence the ground-state energy, with respect to the singlet MLCT state, see Figure 5.2b. Consequently, the absorption band of the MLCT transition appears blue-shifted by 0.45 eV to 533 nm. A similar energy difference (0.53 eV) is found for the higher MLCT transition blue-shift (440 nm in DMSO to 370 nm in methanol). Note that the ligand centered (LC) $\pi - \pi^*$ transition at 300 nm with significantly larger ε is not affected. This proofs, that the MLCT blue-shift is exclusively due to the ground-state stabilization and not the π^* state localized on the bpy ligand.

5.2 Characterization of excited-state dynamics of $[Fe(bpy)(CN)_4]^{2-}$ in Methanol

Using methanol as solvent for $[Fe(bpy)(CN)_4]^{2-}$, the formation of hydrogen bonds between methanol molecules and the cyanide ligands decreases their donor capacity. This stabilizes the ground state as discussed above, but also all other metal centered states. To probe if high-spin MC states are stabilized sufficiently to be accessed from the bright MLCT manifold, transient absorption and impulsive vibrational spectroscopy are employed to characterize the excited-state nature and lifetimes. Figure 5.4 shows the spectral overlap between the ground and excited-state absorption spectra of $[Fe(bpy)(CN)_4]^{2-}$ in methanol and the pump and the probe pulses. Note that, while the pump was used for both TA and IVS, the probe used for broadband TA experiments is described in section 4.1.3. The probe spectrum given here only applies to the IVS experiments and was tuned to be resonant with the excited-state absorption at λ ≥ 590 nm to monitor predominantly excited-state contributions to the IVS signal.

The transient absorption of $[Fe(bpy)(CN)_4]^{2-}$ given in Figure 5.5 is comprised of three spectral contributions. Firstly, a very short lived excited-state absorption (τ ≤ 200 fs), which is clearly indicated at λ ≤ 490 nm. However, this spectral contribution may be extremely broad, stretching all over the investigated spectral range to 750 nm, although the overlapping ground-state bleach (λ ≤ 600 nm) and a second ESA band clearly dominate it. This second, longer lived (τ ≤ 20 ps), spectrally broad excited-state absorption band (600 nm – 750 nm), also seems to stretch into an overlap with the ground-state bleach. This is indicated by the noticeable blue-shift of both the excited-state absorption and the ground-state bleach. While blue-shifting excited-state absorption bands are very well known and may easily be explained considering

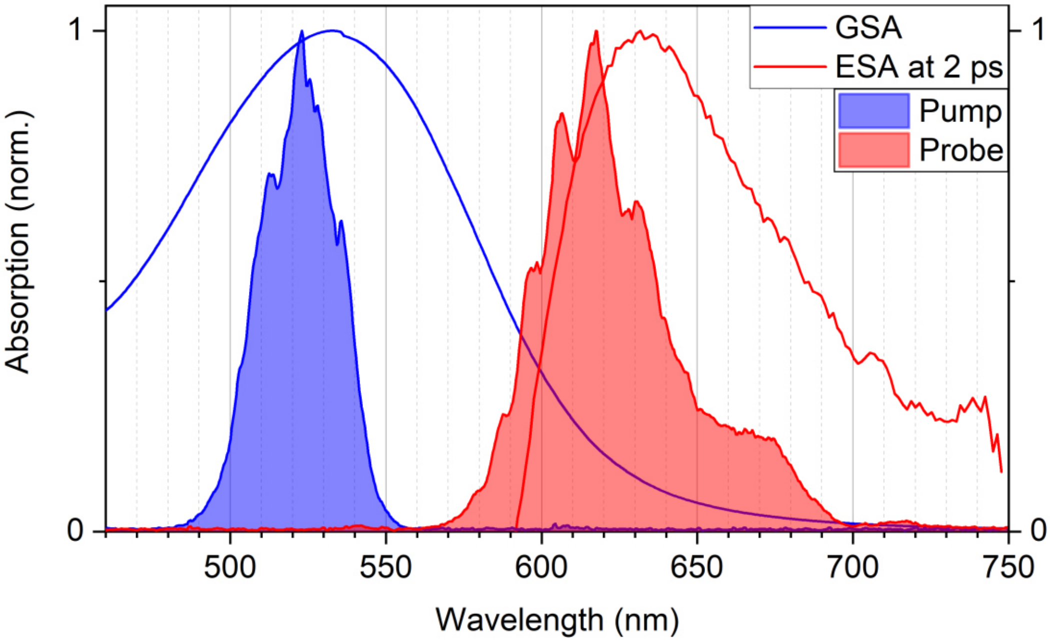

Figure 5.4: Ground- and excited-state absorption spectra of $[Fe(bpy)(CN)_4]^{2-}$ in methanol. The pump spectrum is resonant with ground-state absorption and the probe spectrum is resonant with excited-state absorption. Excited-state absorption taken from TA data. Only positive contributions are shown.

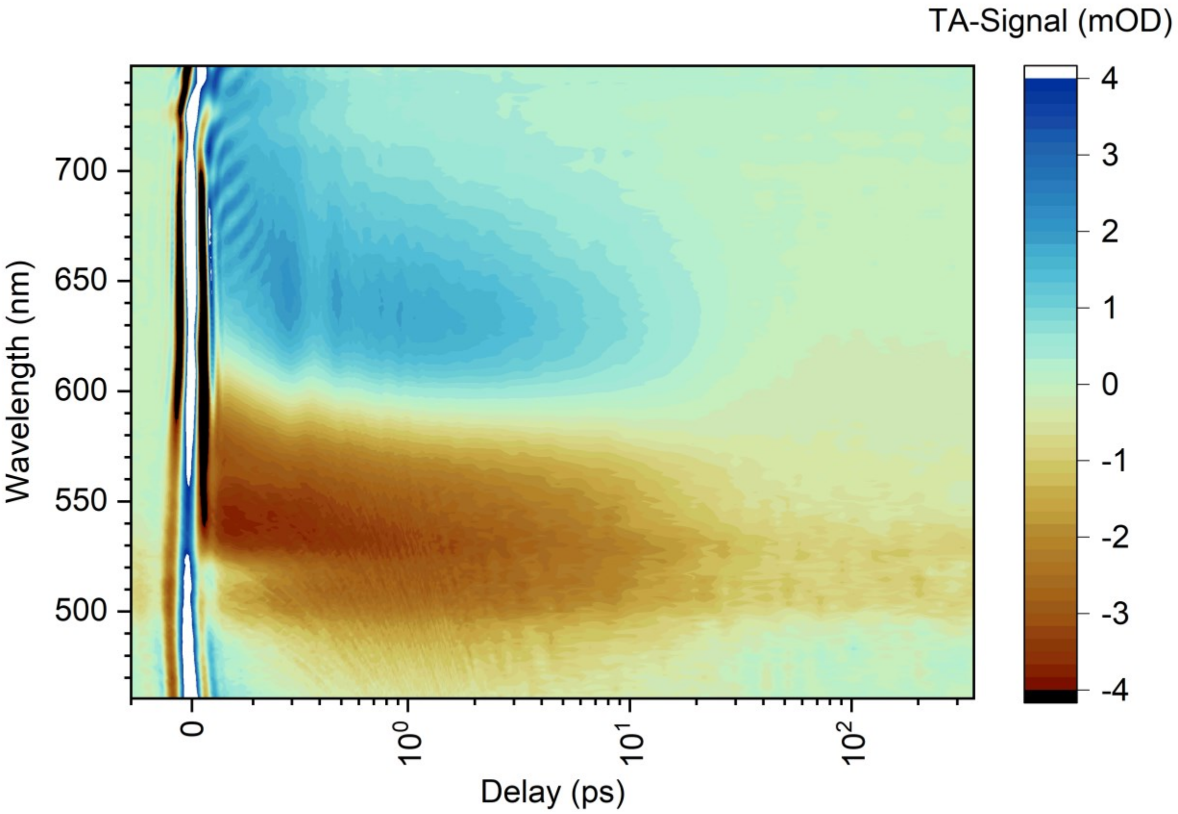

Figure 5.5 Two dimensional representation of transient absorption data of $[Fe(bpy)(CN)_4]^{2-}$ *in methanol.*

vibrational cooling within the excited state, this is not the case for the ground-state bleach. Since this bleach originates in the depleted portion of the ground-state population it can be expected to be spectrally constant. Hence, the observed dynamic spectral shift suggests a spectral overlap between the two contributions. The third contribution is the mentioned ground-state bleach, which can easily be identified as such by comparison to the absorption spectrum given in Figure 5.4. It is worth noting, that the ground-state bleach outlives all observed excited-state contributions, exceeding even the experimental observation window, suggesting that the molecular system remains in a long lived, spectrally elusive non-ground state. Quantification of the involved time constants via global analysis, under consideration of an offset to describe the lasting fraction of the ground-state bleach, yields 220 ± 20 fs and 10.3 ± 0.3 ps. The corresponding DADS and temporal cuts along characteristic wavelengths are given in Figure 5.6. The DADS associated with the shortest time constant reveals that the strong positive band indeed overlaps significantly with the ground-state bleach. Note, how the ground-state bleach forms on the femtosecond timescale in temporal cuts at both 465 and 515 nm (Figure 5.6b).

While in the unprocessed data the ground-state bleach dominates the excited-state absorption at $\lambda \geq 490$ nm, the first DADS shows, that it expands to $\lambda \leq 530$ nm. In this spectral overlap there is a maximum located at 515 nm, which will be especially relevant for identifying the nature of the initially populated state. Furthermore, there is a positive feature at $\lambda \geq 660$ nm, overlapping with the longer lived excited-state absorption band, contributing to its perceived spectral narrowing and blue-shift in the

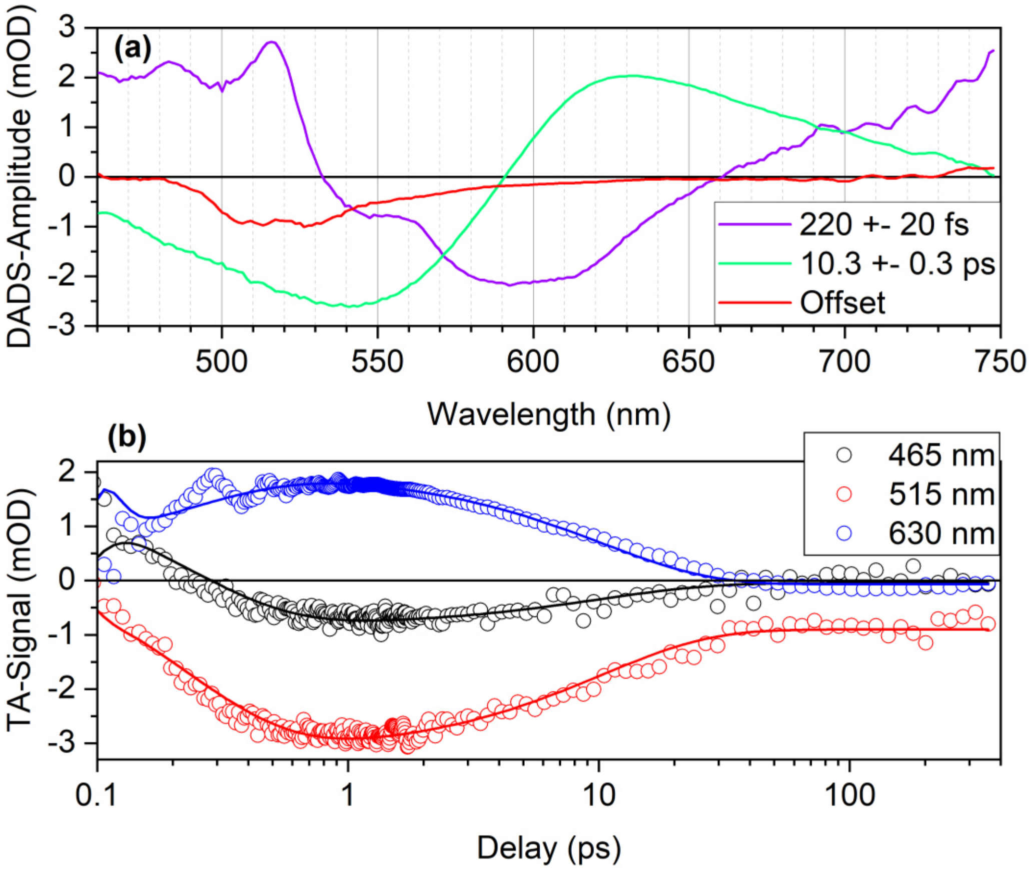

Figure 5.6: Results from global analysis of TA Data of $[Fe(bpy)(CN)_4]^{2-}$ in methanol: (a) DADS and (b) transients with fits at wavelengths characteristic of the three contributions.

unprocessed data. The negative contribution separating the two positive ones in the first DADS (530 – 660 nm) overlaps partly with the ground-state bleach. Since the overlap is only partial and a recovery of a negative contribution is not observed, it is instead due to the buildup of the longer lived excited-state absorption band (see rise at 630 nm in Figure 5.6b). The second DADS, corresponding to the 10.3 ps time constant, consists of a broad negative and a broad positive contribution bordering at $\lambda = 590$ nm. The fact, that the ground-state absorption there (Figure 5.4) is at roughly one third of its maximum at 535 nm proofs the assumed significant spectral overlap of the ESA and the GSB band. As described in the discussion of the unprocessed data (Figure 5.5), the offset can easily be identified as the mirror image of the ground-state absorption, suggesting the molecular systems do not fully relax back into the ground state on the observed time frame.

Since the first DADS (Figure 5.6a) does not indicate any premature ground-state bleach recovery but only buildup of excited-state absorption, assumption of a strictly sequential succession of involved states in a model is justified. This assumption of a sequential model leads to the SADS given in Figure 5.7a.

Due to the spectral overlap, the absorption maximum of the first species at 515 nm is only visible in the SADS as an indentation of the dominating ground-state bleach. However, this narrow absorption feature is established as a spectral signature of the bpy anion.[40, 83, 84] Additionally, the absorption band at $\lambda \geq 600$ nm has also been identified as indicative of MLCT states in iron(II)polypyridyl complexes.[29] Hence, the

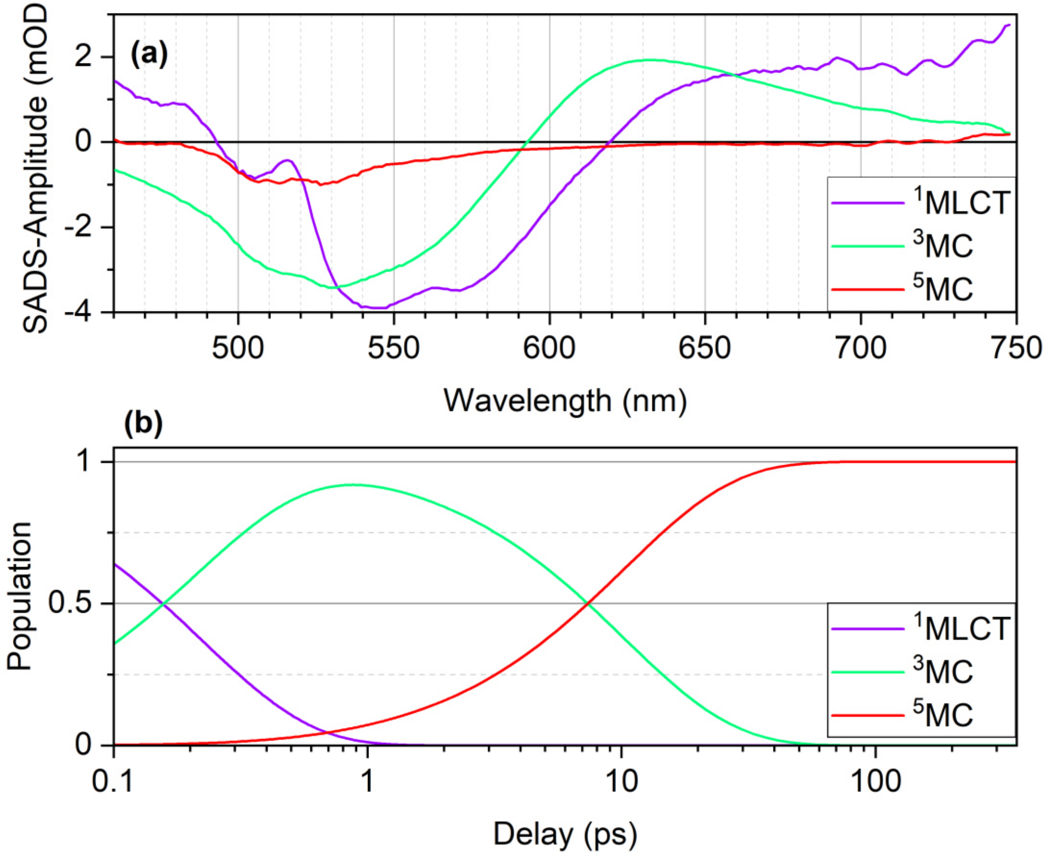

Figure 5.7: (a) SADS and (b) population traces obtained for sequential model to the TA-data of [Fe(bpy)(CN)$_4$]$^{2-}$ in methanol.

state initially populated via photoexcitation is the ^{1}MLCT state. Closer inspection of the spectral region around 515 nm in the second SADS reveals no sharp absorption feature, suggesting that the charge transfer is reversed within 220 fs, to produce a metal centered species, as is typical for iron(II)polypyridyl complexes.[7] Furthermore, the SADS is in great agreement with SADS for the ^{3}MC state of [Fe(bpy)(CN)$_4$]$^{2-}$ in water published by Kjær et al., where the situation is very similar to that in methanol.[40] Accordingly, the second SADS is assigned to the ^{3}MC state. Analogously to other iron(II)polypyridyl complexes, such as the paradigmatic [Fe(bpy)$_3$]$^{2+}$, the long-lived ground-state bleach in absence of any distinct absorption features is understood as indication of the ^{5}MC state.

Methanol, as a Lewis acidic solvent, has two distinct effects. Firstly, it stabilizes all d-orbitals at the central iron ion. This general stabilization of the ground state, with respect to the optically bright ^{1}MLCT state results in the blue-shifted ground-state absorption as discussed above. Secondly, the reduction of the cyanide ligands' donor capacity also reduces the ligand field splitting, which is the energy difference between the t_{2g} and the e_g manifold. With decreased ligand field splitting, high-spin configurations become accessible, making them available as efficient loss channel to the optically bright MLCT states. The cyanide ligands effectively become levers for the solvent's Lewis acidity to tune the excited-state surface. This is applied here to lower metal centered states into the excited-state dynamics of [Fe(bpy)(CN)$_4$]$^{2-}$ using methanol as solvent. The fact that this can indeed traced back to the influence of

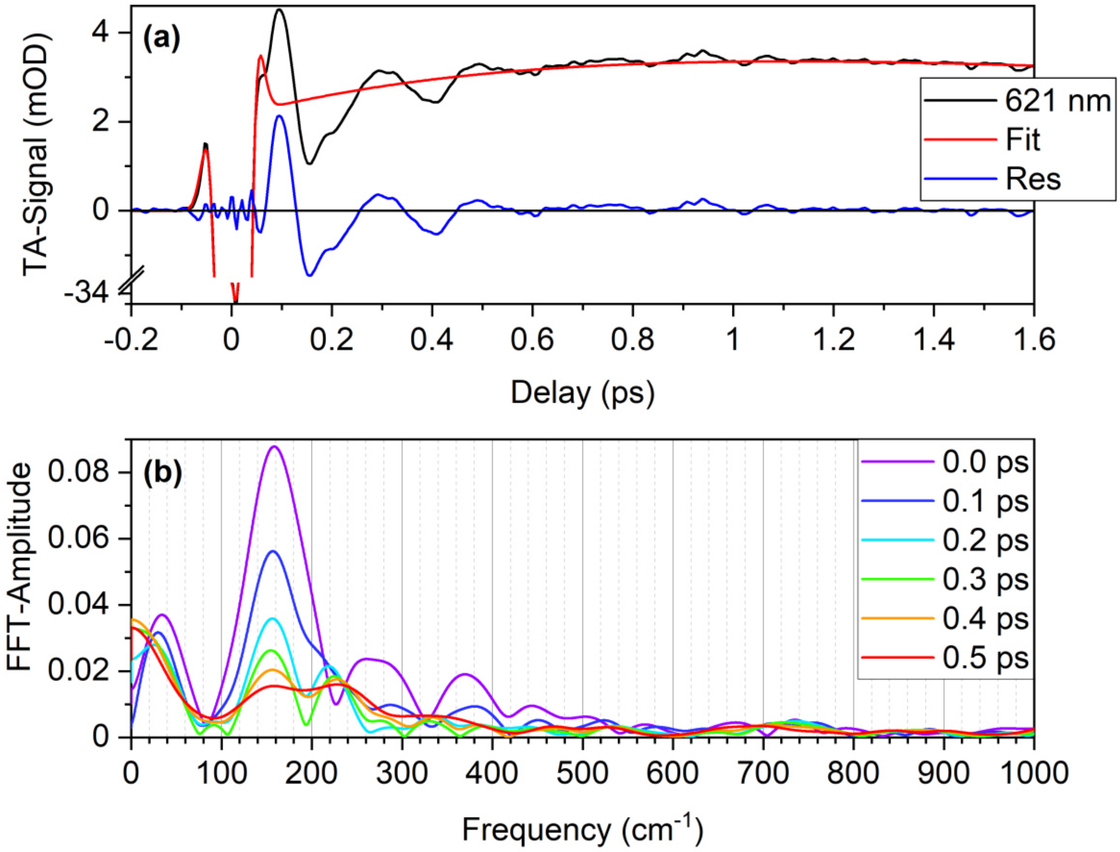

Figure 5.8: (a) IVS-Signal of [Fe(bpy)(CN)$_4$]$^{2-}$ in methanol at 621 nm, fit of coherent artifact and electronic population dynamics, as well as oscillatory residual, to which fast sliding-window fast Fourier transformation (SW-FFT) was applied. (b) Series of Raman spectra obtained by SW-FFT of the oscillatory features in the signal at 621 nm. SW-shift given in legend.

methanol will be proven in the next section when the same complex is investigated in another solvent.

Transient absorption identifies MC states as the dominant species after 220 fs in the excited-state dynamics of [Fe(bpy)(CN)$_4$]$^{2-}$ in methanol. In the following paragraphs, results from IVS on the same sample will be discussed to establish vibrational fingerprint features of these, otherwise spectrally elusive, MC states.

As depicted in Figure 5.4, the probe spectrum of the IVS experiment was tuned to be resonant with the excited-state absorption feature assigned to the ^{3}MC state. The IVS signal shown in Figure 5.8a was recorded at 621 nm, where ground-state contributions should have negligible amplitude. This enables monitoring exclusively ^{3}MC contributions. The IVS signal shows strongly damped, low-frequency oscillation with an initial amplitude of almost 4 mOD and approximately 200 fs period. This indicates a very strong oscillation, compared to the 3-4 mOD amplitude of the excited-state absorption band. Quantification of the frequency by SW-FFT yields 160 cm^{-1} (corresponding to 210 fs oscillation period), which consequentially is also the dominating feature in the obtained Raman spectra (Figure 5.8b). The series of Raman spectra also reflects the strong damping, as a sliding window shift of 0.2 ps (less than a single vibrational period) decreases the peak to a third of its initial amplitude. The obtained 160 cm^{-1} frequency is in good agreement with quantum chemical calculations provided by Thomas Penfold at the School of Natural and Environmental Sciences, Newcastle University. Using TDDFT (B3LYP*) with def2-TZVP basis set and an implicit conductor-like polarizable continuum model, he calculated a Fe-N_{bpy} breathing mode at 150 cm^{-1}. Furthermore, a significant elongation in Fe-L bond length was calculated going from the ground state or MLCT states to MC states. While the equilibrium Fe-N_{bpy} bond length in the ground state and ^{3}MLCT are 2.02 Å and 2.01 Å, respectively, they are 2.29 Å and 2.30 Å in the ^{3}MC and ^{5}MC, respectively. This results in an elongation of 0.28 Å (~14% of the initial bond length) with the ultrafast (220 fs) relaxation from the Franck-Condon region of the ^{1}MLCT to the ^{3}MC. The significant elongation can be rationalized considering the orbitals participating in the MC states. MC states, also referred to as ligand field states, are characterized by the d-orbitals of the metal center. In the given d^6 case with octahedral coordination geometry, high-spin MC states necessarily feature populated d-orbitals from the e_g manifold, pointed directly towards the ligand, which the low-spin ground state or MLCT states don’t. Accordingly, prolonged Fe-L bond lengths can be expected going from the ground or MLCT states to MC states. The ultrafast transition GS$\rightarrow$^{1}MLCT$\rightarrow$^{3}MC hence launches a wave packet along the Raman active Fe-N_{bpy} breathing mode, which modulates the transient absorption signal (Figure 5.8a) with its characteristic frequency. The strong damping may be rationalized considering the large, delocalized movement associated with the breathing vibration. As the ligands move outwards, away from the central ion, they are hindered by the solvent cage. This leads to a dephasing time much shorter than the ^{3}MC lifetime of 10.3 ps obtained from transient absorption.

Note that the explanation put forward for the wave packet launch is not specific to the investigated iron complex but should hold true for other transition metal complexes with low-spin ground and high-spin excited states as well. If the low-spin to high-spin transition is fast with respect to the breathing vibration period, such a wave packet should be launched. As the polarizability typically changes along this type of normal modes, they are generally Raman active and hence visible in IVS, making it a great tool for observing low-spin to high-spin transitions.

5.3 Characterization of excited-state dynamics of $[Fe(bpy)(CN)_4]^{2-}$ in DMSO

To demonstrate the exclusive assignment of the 160 cm^{-1} mode to the ^{3}MC state, it is necessary to attempt the counterevidence. That is, to exclude the ^{3}MC state and look for the same mode in a preferably similar system. Hence, the strong solvatochromism of $[Fe(bpy)(CN)_4]^{2-}$ is exploited to keep the molecular system identical yet exclude the ^{3}MC from the excited-state dynamics. The first half of this section is consequentially dedicated to characterizing the lifetimes and nature of the excited states of $[Fe(bpy)(CN)_4]^{2-}$ in DMSO using transient absorption. In the second half, IVS is employed to confirm the then expected absence of low-frequency breathing modes.

Figure 5.9 illustrates the spectral overlap of excitation and probe spectrum with ground and excited-state absorption, respectively. The probe spectrum given here was applied only in IVS experiments. For broadband TA experiments, the white light described in section 4.1.3 was used. The excitation spectrum was employed in both types of experiments on $[Fe(bpy)(CN)_4]^{2-}$ in DMSO.

Figure 5.10 displays the transient absorption of $[Fe(bpy)(CN)_4]^{2-}$ in DMSO. Since the ground-state absorption covers the full detected spectral range (see Figure 5.9), it is not surprising to find a corresponding ground-state bleach stretching over the complete spectral window. This bleach is only interrupted by a narrow, very intense excited-state absorption on the same timescale ($\tau \leq 40$ ps), suggesting the system relaxes from the excited state, associated with the narrow band around 525 nm, back into the ground state. Additionally, there is a strong oscillatory contribution, noticeable

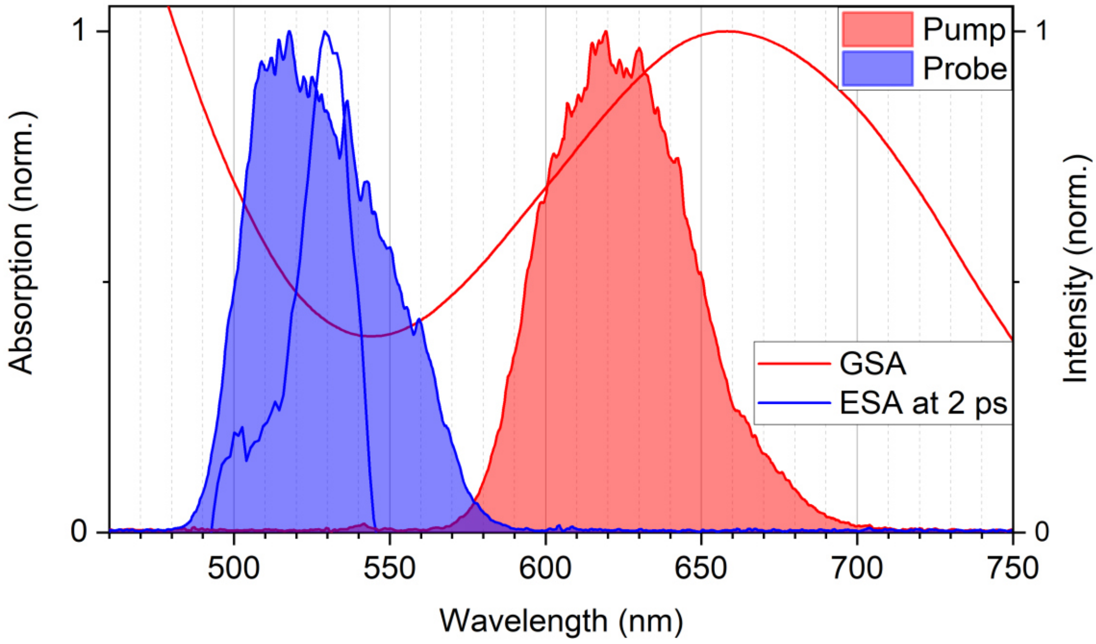

Figure 5.9: Ground and excited-state absorption spectra of $[Fe(bpy)(CN)_4]^{2-}$ in DMSO. The pump spectrum is resonant with ground-state absorption and due to spectral overlap, the probe spectrum is resonant with both ground and excited-state absorption. Excited-state absorption taken from TA data. Only positive contributions are shown.

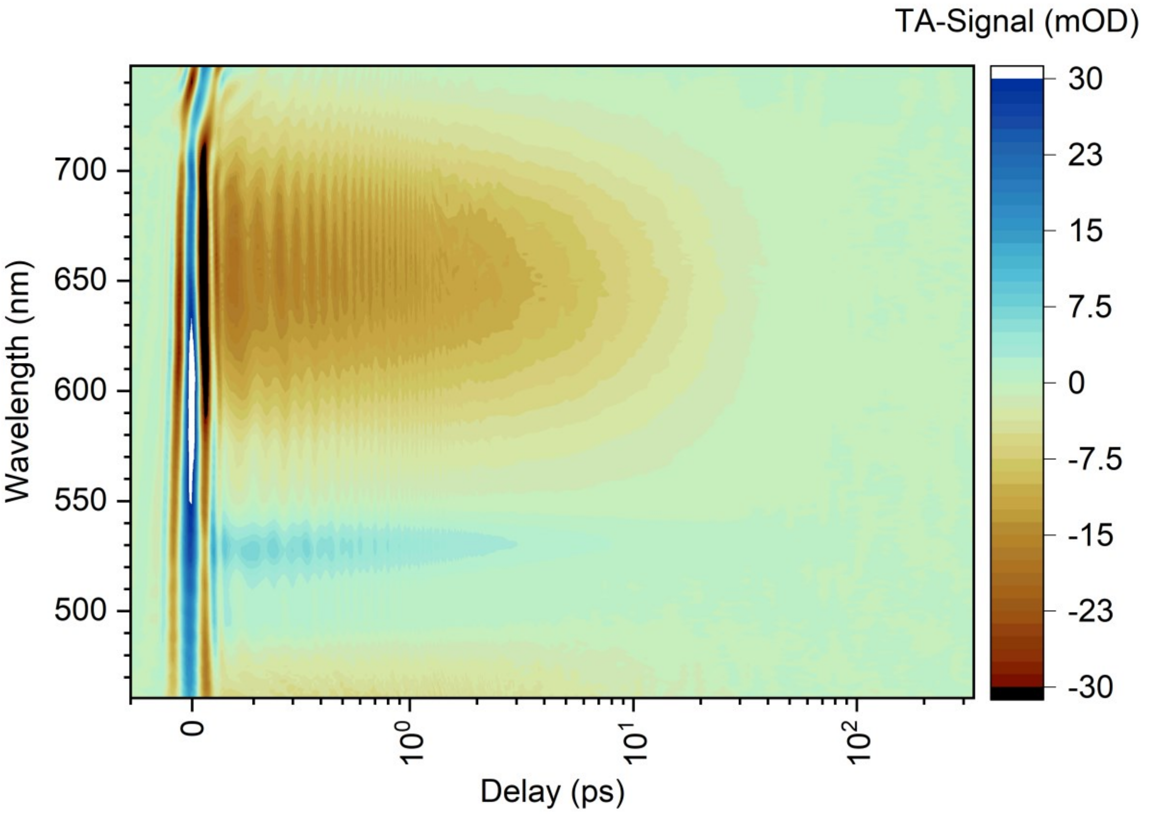

Figure 5.10: Two-dimensional representation of transient absorption data of [Fe(bpy)(CN)$_4$]$^{2-}$ in DMSO.

at all wavelengths and early delays (τ ≤ 2 ps). This feature will be addressed when discussing the IVS results.

Global analysis reveals two distinct time constants at play in the above-described transient absorption: 570 ± 30 fs and 12.5 ± 0.3 ps. While the latter can easily be identified as the shared lifetime of ground-state bleach and the main excited-state absorption, the former, shorter time constant is less obviously assigned.

Closer inspection of the characteristic traces and DADS given in Figure 5.11 reveals a two-stage decay with retention of the general spectral shape in the excited-state absorption region. However, in the spectral region of the ground-state bleach (λ ≥ 550 nm) the DADS associated with the 570 fs time constant does not resemble the ground-state bleach. This strongly hints at an initially populated, short-lived species from which the molecules do not decay into the ground state, but another excited state which shares the spectral signature at 530 nm. The DADS of the 12.5 ps component is comprised of a broad ground-state bleach contribution, overlaid with the sharp absorption band at 530 nm. This shows that ground-state absorption recovers as the excited-state absorption band at 530 nm decays, suggesting a direct relaxation between the associated states.

The two involved excited-state spectra are assigned in the following way: The initially populated species (570 fs lifetime) is necessarily of singlet character, due to the ground state's singlet state nature. Additional information about the excited state's nature may be gathered from its spectral shape. The narrow absorption feature at

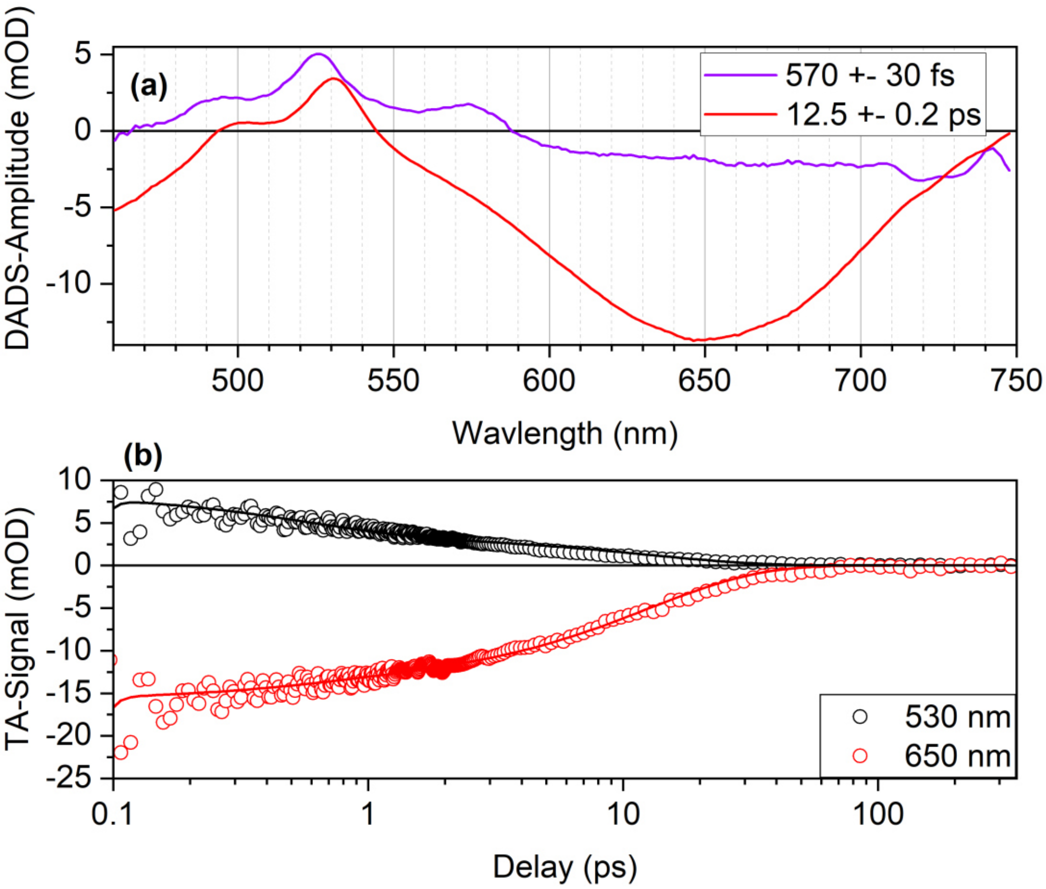

Figure 5.11: Results from global analysis of TA Data of [Fe(bpy)(CN)$_4$]$^{2-}$ in DMSO: (a) DADS and (b) transients with fits at wavelengths characteristic of the two contributions.

530 nm is established as a spectral signature of the bpy anion[83, 84]. Hence, the short-lived state populated by the photoexcitation must be the ^{1}MLCT state. It is also worth noting, that the ^{1}MLCT lifetime is more than doubled by changing the solvent from methanol (220 fs) to DMSO (570 fs). This prolongation hints at deactivation of a loss channel present in methanol, but not in DMSO. While the bpy anion feature is not found in the second species in methanol (hence the assignment to ^{3}MC), in DMSO the longer-lived state (12.5 ps) retains the bpy anion's absorption band suggesting also the MLCT nature is conserved. Due to the stark contrast in lifetime to the ^{1}MLCT, the second species is explained by an intersystem crossing to the triplet manifold, i.e., a ^{3}MLCT. The transients in Figure 5.11b clearly show that both the ground-state bleach recovery and the decay of the ESA band of the bpy anion occur on the same 12.5 ps timescale. The SADS obtained presuming a sequential decay of ^{1}MCLT and ^{3}MLCT are given in Figure 5.12a and underline the spectral similarity of the two involved species. Both are comprised of the broad ground-state bleach, interrupted by the bpy anion absorption feature at 530 nm and only differ in amplitude.

In summary, transient absorption suggests, that in DMSO the strong ligand field successfully deactivates ultrafast MLCT to MC loss channels which are typical for iron(II)polypyridyl complexes. Instead, the MLCT character is conserved, fulfilling an

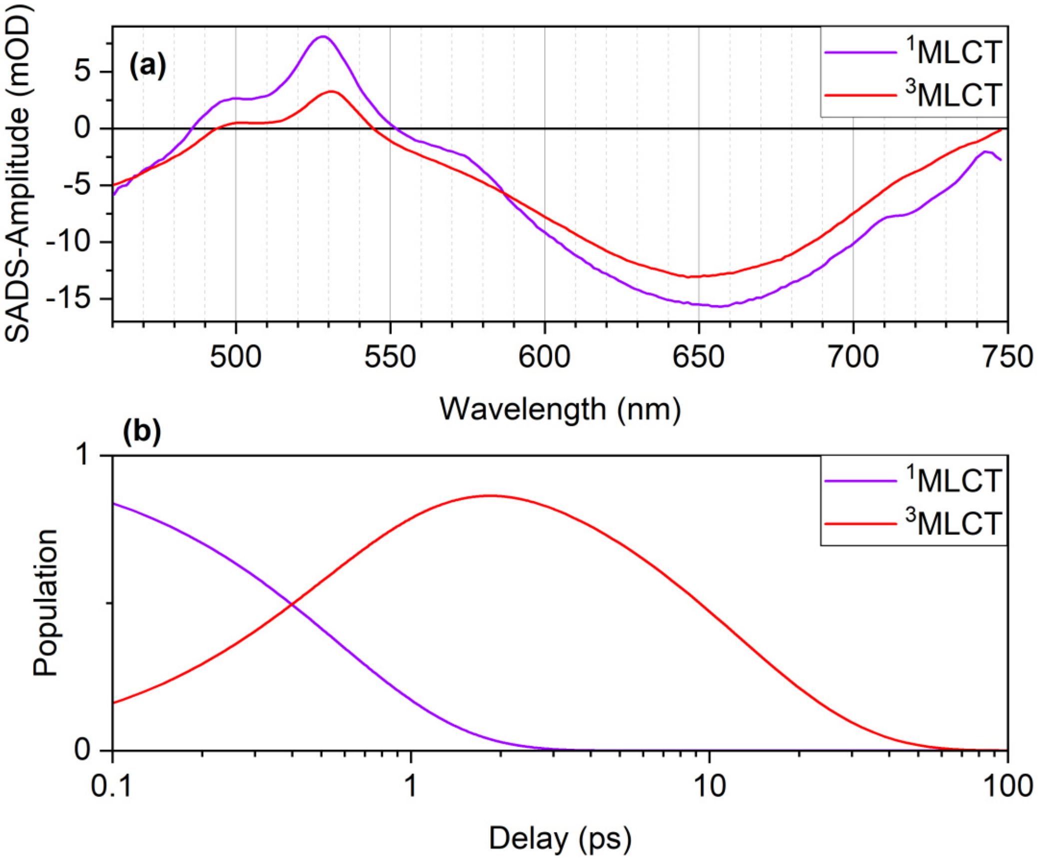

Figure 5.12: (a) SADS and (b) population traces obtained for sequential model to the TA-data of [Fe(bpy)(CN)$_4$]$^{2-}$ in DMSO.

important prerequisite for light harvesting applications. [Fe(bpy)(CN)$_4$]$^{2-}$ in DMSO hence serves as a negative sample to evaluate the MC sensitivity of IVS methods.

As Figure 5.9 demonstrates, a clear separation between ground and excited-state absorption is not possible in the present case. Yet still, the IVS experiments were conducted with the probe tuned to resonance with the excited-state absorption band of the bpy anion. This was done to favor excited-state over ground-state contributions to the IVS signal.

The obtained results are summarized in Figure 5.13. In comparison to Figure 5.8, it becomes evident, that the vibrational coherences induced are very different. While a low-frequency mode dominates the residual in methanol, in DMSO it is characterized by a single, very persistent oscillation with approximately 50 fs period (Figure 5.13a). Accordingly, the series of Raman spectra obtained by sliding-window fast Fourier transformation all exhibit a strong peak at 670 cm^{-1}, with two minor contributions around 280 – 380 cm^{-1} (Figure 5.13b). While the 670 cm^{-1} oscillation does decrease in amplitude over time, it is still visible in the residual after 3 ps (see Figure 5.13a). The appearance of this new, strong contribution raises the question about its origin. A first hint at its source can be taken from the 2D representation of the TA Data in Figure 5.10. There, the same 50 fs oscillation is visible across all wavelengths, not only in the bpy anion absorption band considered in the IVS experiment. This omnipresence

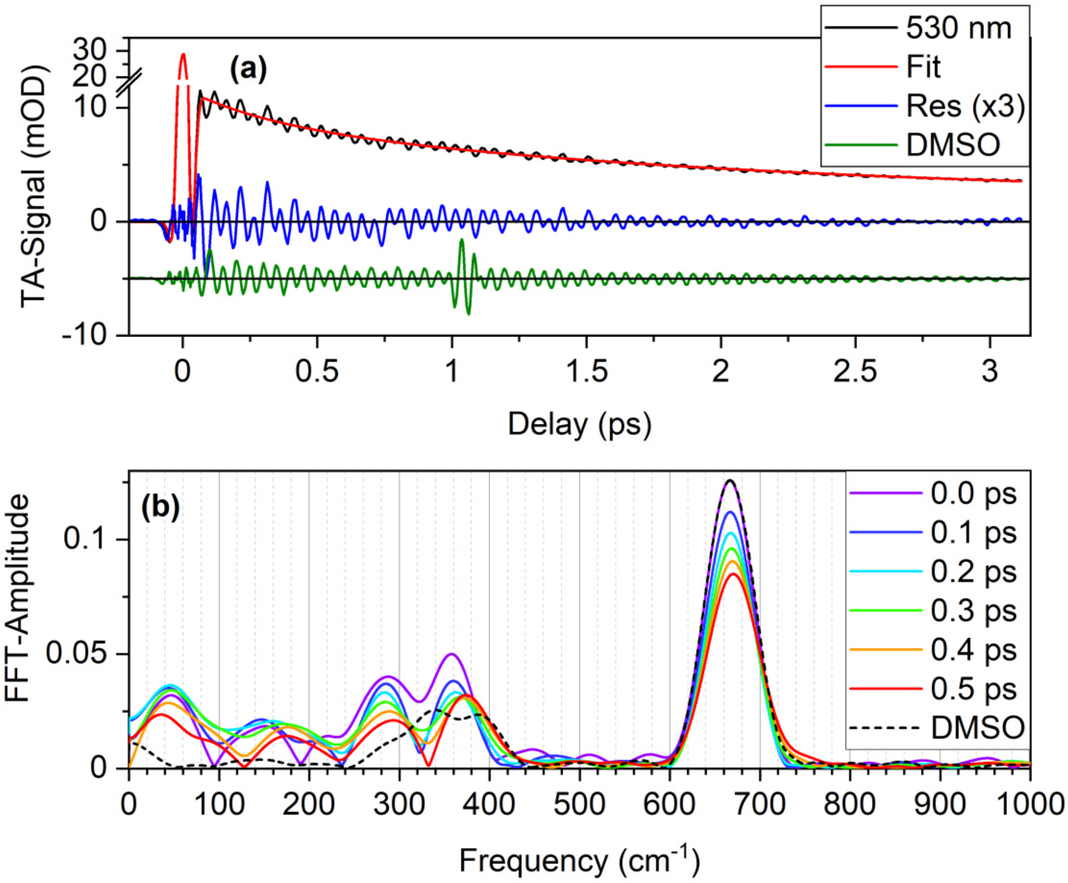

Figure 5.13: (a) IVS-Signal of [Fe(bpy)(CN)$_4$]$^{2-}$ in DMSO at 530 nm, fit of coherent artifact and electronic population dynamics, as well as oscillatory residual, to which fast SW-FFT was applied. Also, the residual of a pump-IVS trace of pure DMSO is shown, shifted by -5 mOD for clarity. There the push pulse arrives after 1 ps but does not qualitatively change the oscillations. (b) Series of Raman spectra obtained by SW-FFT of the oscillatory features in the signal at 530 nm. SW-shift given in legend.

might be explained by a ground-state contribution, regarding the ground-state absorption covering the complete experimental spectral range (Figure 5.9). In this case the oscillation should also have been present in the ground-state absorption of the methanol case, which it is not. Instead, its origin is more trivial. It appears in the DMSO and not the methanol case, because it originates directly from the solvent. DMSO has a prominent symmetric C-S-C stretch vibration at 667 cm^{-1}.[85] This assignment is further corroborated by the P-IVS experiment conducted on pure DMSO, which is also given in Figure 5.13 and reproduces all significant peaks of the Raman spectra discussed. With all relevant features of the Raman spectra assigned to the solvent, it becomes clear, that [Fe(bpy)(CN)$_4$]$^{2-}$ does not make any significant contribution. This explicitly includes the low-frequency region around 160 cm^{-1}, characteristic of the breathing mode associated with the MLCT – MC transition. Both experimental methods, TA, and IVS, confirm the involvement of MC states in the photophysics of [Fe(bpy)(CN)$_4$]$^{2-}$ in methanol and their exclusion in DMSO. The strong solvent dependence, which is indicated in its solvatochromism, hence extends to the excited-state dynamics. The solvent's interaction with the CN$^-$ ligands influences their electron donation capacity. In methanol, hydrogen bonds form to the CN$^-$ ligands, depleting their electron donating capacity. The central ion experiences a weaker ligand field, which in turn stabilizes MC states, such as the ^{3}MC and the ^{5}MC, acting as MLCT loss channels. In contrast, DMSO does not form hydrogen bonds to the CN^- ligands, which can direct their electron donation capacity to the central cation. This destabilizes the ^{3}MC and ^{5}MC and deactivates them as MLCT loss channels. The mere change of solvent goes so far to enable or disable potential functionality of $[Fe(bpy)(CN)_4]^{2-}$ in light harvesting applications. This stresses the critical necessity to understand the nature, relative positioning, and influences on the different excited states at play, when designing new materials.

In the above two sections, IVS was established as method sensitive to MLCT – MC transitions in a case, where TA could also distinguish these states. In the following section, IVS will be applied to investigate the involvement of MC states in another Fe(II)pyridyl complex, already implemented in light-harvesting applications.[48] There optically allowed MLCT contributions dominate the TA data and an involvement of the spectrally elusive MC state cannot be ruled out on this basis alone.

5.4 Photophysics of $[Fe(cpbmi)_2]^{2+}$ investigated for the role of metal centered states[86]

$[Fe(cpbmi)_2]^{2+}$ consists of two tridentate ligands (cpbmi: (carboxypyridine-2,6-diyl)bis(1-methyl-imidazol-2-ylidene)), Figure 5.14a), encapsulating an Fe^{2+} ion in an approximately octahedral geometry. The ligand-backbones are arranged linearly, resulting in the C-N-C donor atoms embracing the iron ion in a plane. The two ligands embrace the ion from opposing sides and orthogonal to one another, so that a N-Fe-N axis is formed, and the complex has C_{2v} symmetry (Figure 5.14b). In the idealized octahedron as reference polyhedron, the four carbon atoms and central iron ion would form a plane orthogonal to this N-Fe-N axis. However, the ligand backbone connecting the coordinating donor atoms is too short and the C-Fe-C angles do not add up to 360°. Like $[Fe(bpy)(CN)_4]^{2-}$, the ligands in $[Fe(cpbmi)_2]^{2+}$ are designed specifically to favor MLCT states, only here both features are integrated into a single molecular ligand. They combine pyridyl units as electron acceptors, closely related to the

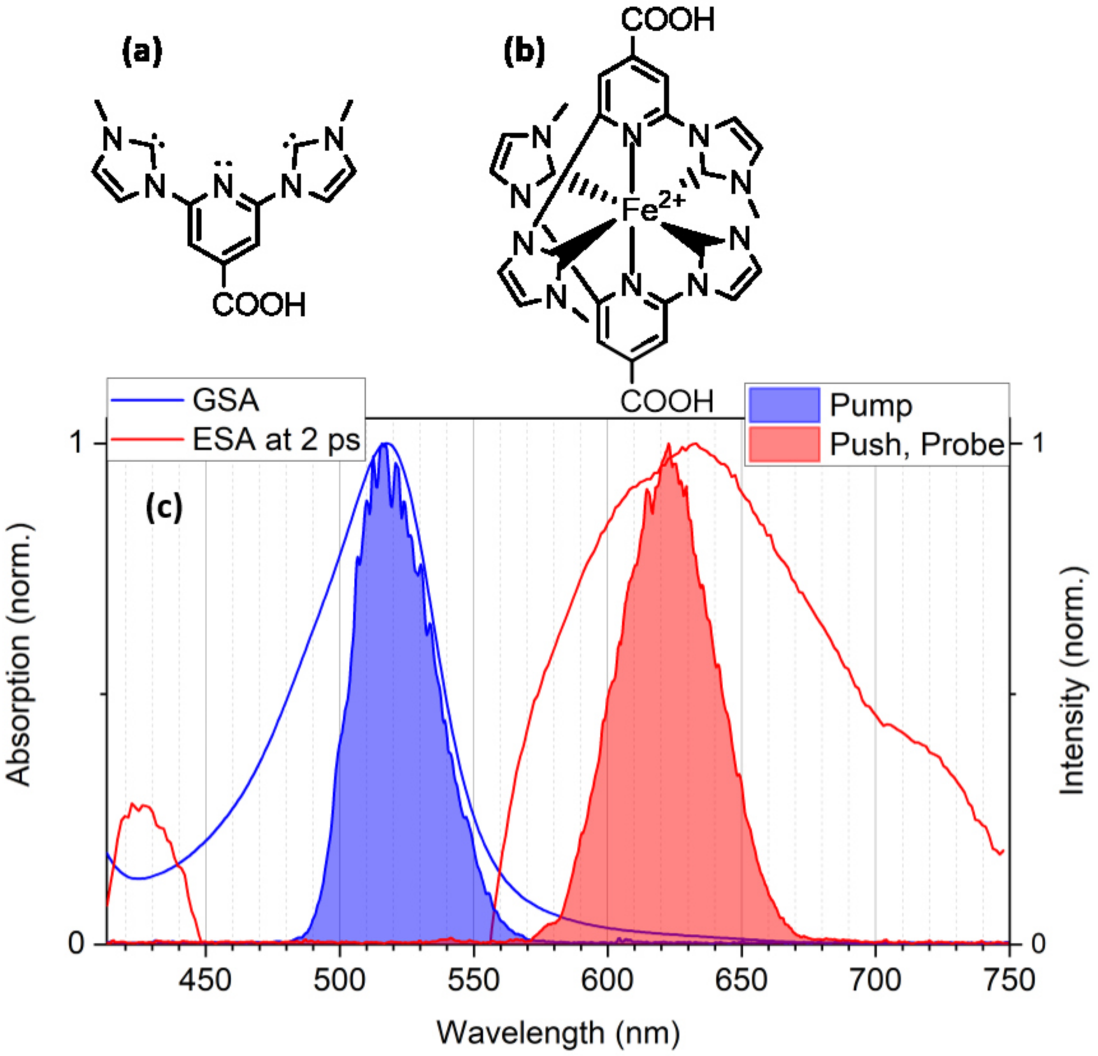

Figure 5.14:Molecular structures (a) of the cpbmi ligand, where cpbmi = (carboxypyridine-2,6-diyl) bis(1-methyl-imidazol-2-ylidene) and (b) $[Fe(cpbmi)_2]^{2+}$. (c) Ground- and excited-state absorption of $[Fe(cpbmi)_2]^{2+}$ in acetonitrile. The pump spectrum is resonant with ground-state absorption and the push / probe spectrum is almost exclusively resonant with the excited-state absorption. Excited-state absorption taken from TA data. Only positive contributions are shown.

paradigmatic bpy, and NHC units as strong σ-donors and poor π-acceptors, to destabilize MC states and in turn deactivate them as MLCT loss channels.

As displayed in Figure 5.14c, the optically allowed and hence bright MLCT transition of $[Fe(cpbmi)_2]^{2+}$ is centered at 520 nm, similar to $[Fe(bpy)_3]^{2+}$. The pump spectrum is tuned resonant to this absorption band, while push and probe spectra for the (P-)IVS experiments were tuned resonant with a broad excited-state absorption band at 630 nm. For the transient absorption experiments, the white light characterized in section 4.1.3 was employed. The resulting 2D dataset is depicted in Figure 5.15.

It consists of three different contributions. There is a weak, apparently narrow excited-state absorption band on the blue edge of the spectrum ($\lambda \leq 450$ nm, maximum at 425 nm, 5 mOD amplitude). The strong negative feature (450 nm – 550 nm, maximum at 520 nm, -28 mOD amplitude) can easily be identified as ground-state bleach with regard to the ground-state absorption given in Figure 5.14c. The third contribution is a broad excited-state absorption band, dominating the red half of the spectrum ($\lambda \geq 550$ nm, maximum at 630 nm, 9 mOD amplitude). As the overlay of ground and excited-state absorption in Figure 5.14cshows, the ground and excited-state absorption features overlap, so that the ESA bands might actually be broader, but are dominated by the intense ground-state bleach. This is especially true for the ESA feature at 425 nm. Its perceived spectral narrowness is most likely due to the minimum in the ground-state absorption and not due to its own spectral shape. Another indicator for that is, that the ESA feature's maximum corresponds exactly to the ground-state

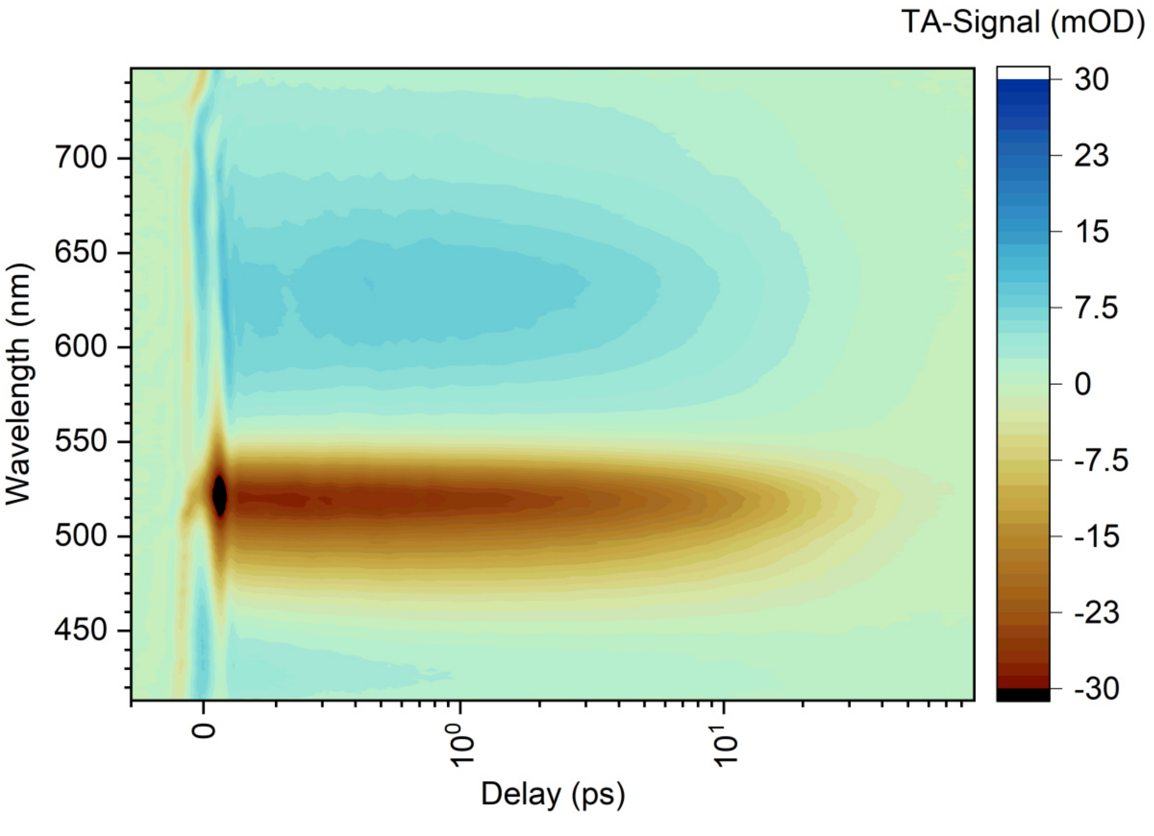

Figure 5.15: Two-dimensional representation of transient absorption data of $[Fe(cpbmi)_2]^{2+}$ in acetonitrile.

absorption minimum at 425 nm. This underlying ground-state bleach also diminishes its amplitude. By comparison of the ground-state bleach maximum (~28 mOD) and the relative absorptivity at 425 nm (~13 % of maximum) one can estimate, that the pure excited-state absorption feature at 425 nm would be ~3.6 mOD larger. Qualitatively, all three features ultimately decay on the same timescale (~ 20 ps). Quantitative analysis of the complete dataset in the form of GA reveals that in fact three distinct time constants (220 fs, 5.3 ps and 19.9 ps) are at play, of which only the last one could be identified by eye. The DADS associated with these time constants and exemplary fit curves of the global analysis are reported in Figure 5.16. The first DADS (Figure 5.16a, 220 fs) describes the simultaneous decay of a broad excited-state absorption band (λ ≤ 520 nm) and rise of the ESA band at 630 nm. This is a strong sign, that the initially populated state, absorbing at λ ≤ 520 nm, relaxes into the one associated with the broad excited-state absorption, visible at λ ≥ 550 nm. However, the absorption band at 425 nm does not fully decay within the first few hundreds of femtoseconds, but ultimately decays in parallel with the ground-state bleach and the broad excited-state absorption feature. This suggests that the supposedly narrow ESA feature originates in two different excited states: The one initially populated by the photoexcitation, and the one centered at 630 nm, which stretches through the ground-state absorption to cover the complete visible range.

This hypothesis is corroborated by the third DADS, which relates the ground-state bleach and both ESA features to a single decay on the same timescale (19.9 ps). This

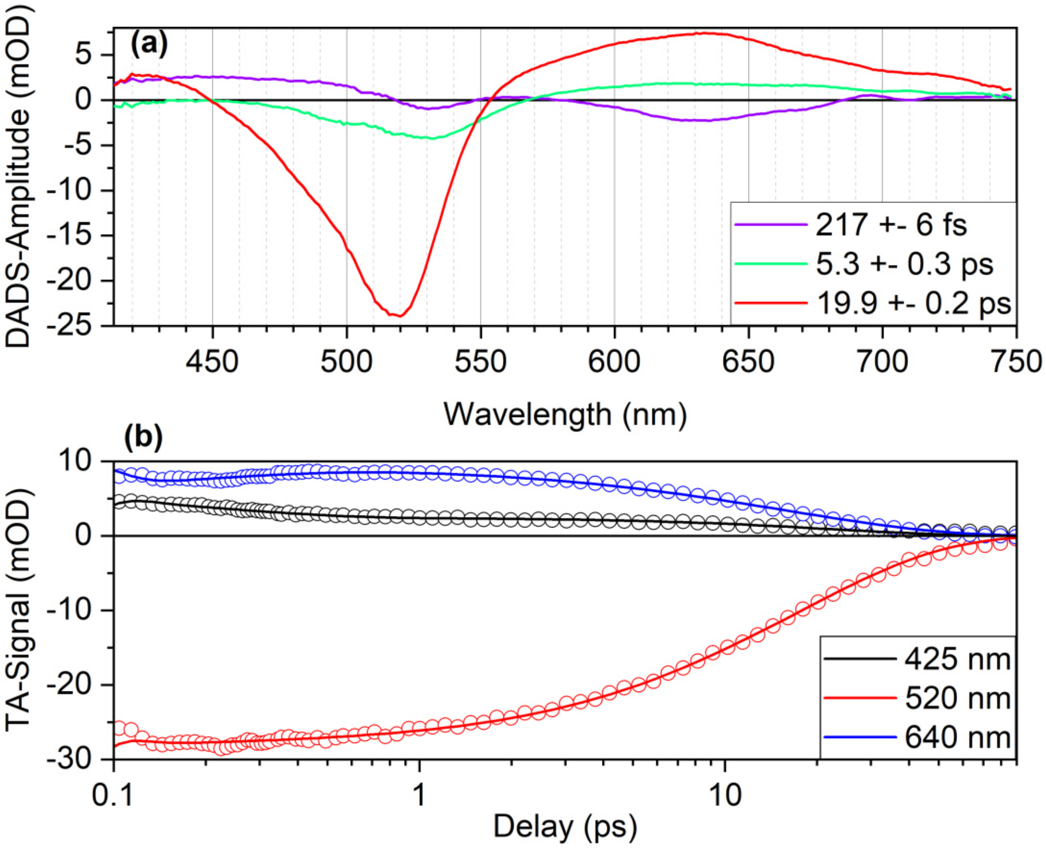

Figure 5.16: (a) DADS and (b) selected transients with fits from global analysis of TA Data of [Fe(cpbmi)$_2$]$^{2+}$ in acetonitrile.

simultaneousness again suggests, that both positive features should be considered as one extremely broad ESA band originating from the same state. In this DADS, the broad ESA band is merely overlaid with the intense ground-state bleach, showing that the corresponding state relaxes back to the ground state.

The second DADS (5.3 ps) is the most ambiguous one. Its positive feature (570 – 750 nm) could be interpreted as a partial decay of the population causing the ESA band. In this regard, the small negative feature (460 – 570 nm) would be understood as partial ground-state bleach recovery. However, this interpretation raises a lot of questions: Why is the negative feature much broader and red-shifted compared to the ground-state absorption? Why doesn't the blue side of the ESA band (λ ≤ 450 nm) also partially decay? Why does only a fraction of this excited state's population relax to the ground state quickly, while the majority still is in the excited state for almost four times that long? Hence, it is worthwhile to consider another interpretation: vibrational cooling.

Suppose an electronic state is populated via photoexcitation. Since the electronic transition occurs much faster than the atom cores can adapt to it, the molecular geometry is virtually frozen during the transition. This is the Franck-Condon-principle, and accordingly the region on the excited-state potential energy surface that corresponds to the ground-state equilibrium geometry is called the Franck-Condon region. Depending on where the Frank-Condon-region lies with respect to the next (local) minimum on the PES, the molecules often have large quantities of potential energy, which is converted to vibrational energy as they relax towards the new (excited state) equilibrium geometry. Relaxation between the different vibrational levels is typically faster than the lifetime of electronic states, resulting in thermally equilibrated excited states, sometimes referred to as Thexi states.[11, 12] The process of vibrational

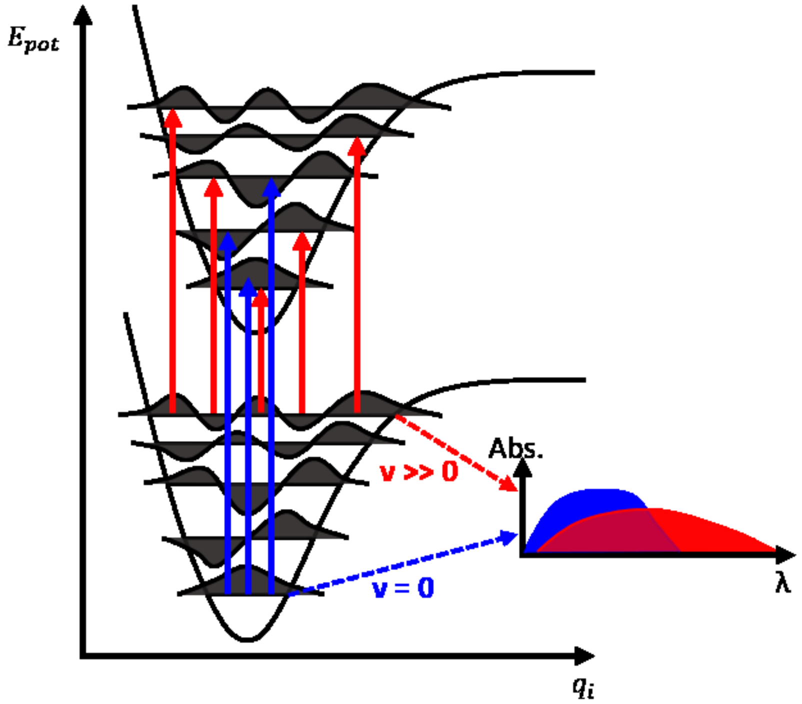

Figure 5.17: Energy diagram explaining blue-shift and spectral narrowing in vibrational cooling. Absorption spectra of vibrational levels v=0 and v>>0 resulting from respective Franck-Condon factors.

relaxation within an electronic state is called vibrational cooling and its consequences on fluorescence have been discussed in Section 2.1.3.

Let us now, regarding Figure 5.17, consider, what consequences vibrational cooling has on the absorption spectrum. Firstly, during vibrational cooling the energy difference to the above-lying electronic states increases, resulting in a blue-shift of the corresponding absorption band. Secondly, as the ensemble of molecules evolves from the vibrationally excited to the ground state, their nuclear wave functions and hence geometries become more localized (see Figure 5.17). When the molecules initially have a lot of vibrational energy, they go through many different geometries. As they vibrationally relax, their geometries converge towards the equilibrium geometry. This results in a well-defined Franck-Condon-region for optical transitions and hence a more localized energy difference to the above-lying electronic states. Consequently, during vibrational cooling the blue-shift is typically accompanied by spectral narrowing.

Let us now return to the inspection of DADS 2 in Figure 5.16a. A partial decay of the red side of the ESA band but not the blue side effectively constitutes a blue-shift and spectral narrowing, indicative of vibrational cooling. Even the small negative feature (460 – 570 nm) can be interpreted as spectral narrowing and blue-shift of the broad ESA band stretching over the complete visible range. While the red wing of the absorption band decays, the central part, obstructed by the dominant ground-state bleach, rises in amplitude.

The exemplary temporal cuts of the 2D dataset, indicative of the three signal contributions, and their equivalent fits from the global analysis in Figure 5.16b agree very well, suggesting that no additional time constants are required to satisfactorily fit the data.

The time constants and information about the spectral evolution obtained from global analysis and prior knowledge about the ligand design and similar systems published in literature[47, 48, 87] are condensed into the following interpretation of the TA data:

Photoexcitation drives the spin- and Laporte-allowed transition to the ^{1}MLCT state with an absorption band at $\lambda \leq 520$ nm. Ultrafast (220 fs) inter-system crossing with retention of the MLCT character leads to the vibrationally hot ^{3}MLCT state, whose absorption spectrum covers the full detected visible range. Vibrational cooling within this state (5.3 ps) leads to a slightly blue-shifted and more narrow absorption band, before the ^{3}MLCT relaxes back to the ground state (19.9 ps). Importantly, even after thorough examination of the TA data, it can be interpreted without consideration of MC states. To find out if this is due to them not being involved or due to their notorious spectral elusiveness, (P-)IVS methods, established as MC-sensitive earlier, are applied. The IVS results and the series of Raman spectra obtained from sliding-window Fourier transformation of the oscillatory part are given in Figure 5.18. The oscillatory component of the trace at 650 nm, isolated by fitting and subtracting of the slowly evolving part, contains contributions from different frequencies, discernable by eye (Figure 5.18a). The early delays ($\tau \leq 0.7$ ps) are dominated by a low-frequency, high amplitude oscillation with approximately 300 fs oscillation period. After the fast decay of this contribution, another, much higher frequency vibration stands out. It

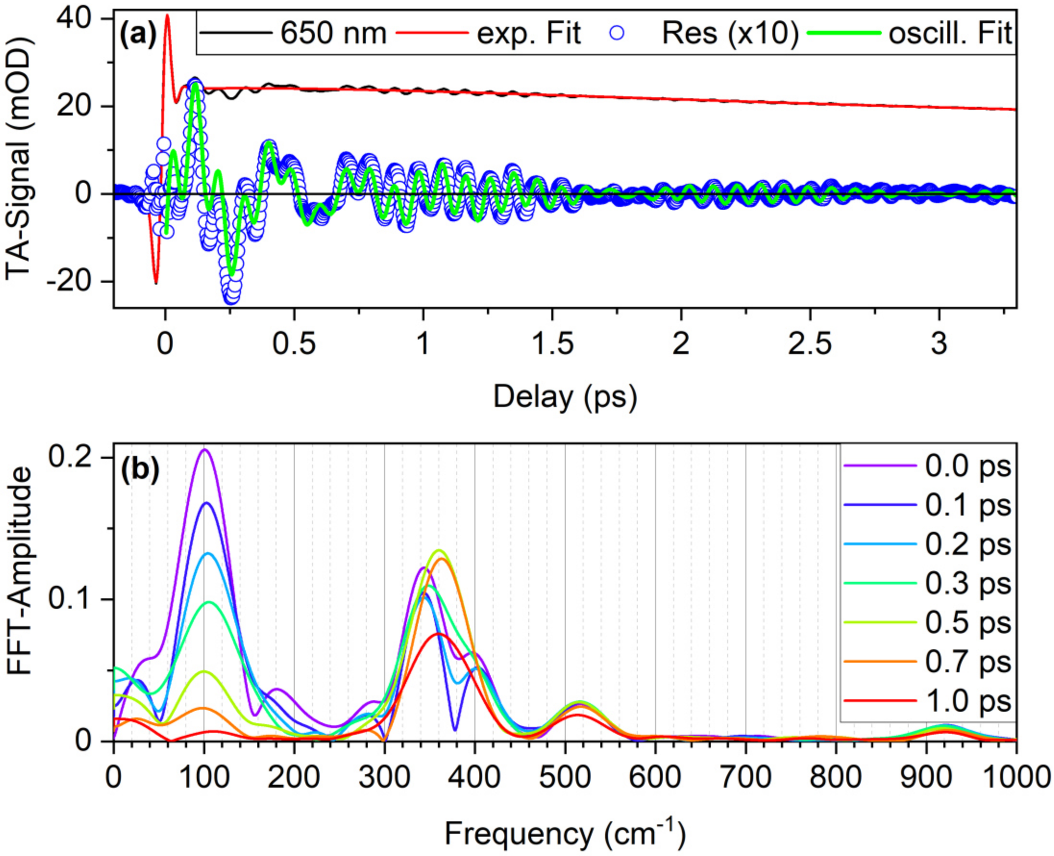

Figure 5.18: (a) IVS-Signal of [Fe(cpbmi)2]$^{2+}$ in acetonitrile at 650 nm, fit of coherent artifact and electronic population dynamics, oscillatory residual thereof, and oscillatory fit using three sine functions. (b) Series of Raman spectra obtained by SW-FFT of the oscillatory features in the signal at 650 nm. SW-shift given in legend.

oscillates with roughly 90 fs period and although the amplitude decreases, it is still visible after 3 ps. These two oscillations are consequently also the two main features in the series of Raman Spectra (Figure 5.18b): an intense band at 100 cm^{-1}, fully decaying in the first picosecond and a not fully resolved, persistent band around 350 cm^{-1}. However, fitting the oscillatory residual requires three independent, exponentially decaying sine functions to achieve satisfactory congruence. The model function is documented in Eq. 3.8 in section 3.3.1 and the results are given in Figure 5.18a and Table 5.1.

Table 5.1: Results from oscillatory fit of vibrational features in 650 nm trace.

$\tilde{\nu}$ [cm^{-1}]	A [mOD]	τ [fs]	ϕ [rad]
106	1.87	470	5.62
351	0.86	1150	6.20
379	0.36	1660	6.23

The largest amplitude is again attributed to a 106 cm^{-1} oscillation, decaying with 470 fs, which is not much longer than the oscillation frequency (316 fs). The persistent high-frequency contribution requires fitting by two sine functions of 351 cm^{-1} and 379 cm^{-1} frequency with 0.86 mOD and 0.36 mOD amplitude, respectively. Both contributions have lifetimes exceeding 1 ps. Both the data and the oscillatory fit show the 29 cm^{-1} (1.15 ps) beating they form at 0.6 ps and 1.75 ps. It is the interference of these two modes that leads to the unclear region around 375 cm^{-1} in the SW-FFT spectra. Comparison of the higher frequency modes with normal modes of $[Fe(cpbmi)_2]^{2+}$, calculated by Thomas Penfold, reveals a Fe-N stretch and ligand backbone deformation mode at 350 cm^{-1}.[86] The 379 cm^{-1} on the other hand is a well-known C-C≡N bending mode of acetonitrile. However, since none of the two higher frequency contributions are indicative of the excited-state nature, the focus is placed on the 106 cm^{-1} mode. Like $[Fe(bpy)(CN)_4]^{2-}$ in methanol, this low-frequency vibration originates in an ultrafast population transfer from the ^{1}MLCT to the ^{3}MC state. While the low-groundspin ground state and the MLCT manifold have similar iron-ligand bond lengths, the MLCT – MC transition is accompanied by a significant Fe-N bond elongation. Using TD-DFT, Fredin et al. estimated a 0.15 Å elongation for the closely related $[Fe(bmip)_2]^{2+}$ in 2014.[52] In 2020, Kunnus et al. selectively probed the ^{3}MC of $[Fe(bmip)_2]^{2+}$ using element and oxidation state specific X-ray emission spectroscopy (XES) and found a 120 cm^{-1} wave packet, launched by the ultrafast MLCT – MC transition.[47] In excellent agreement to this, the 106 cm^{-1} mode is assigned to a wave packet, launched by the MLCT – MC transition along a breathing mode on the ^{3}MC surface of $[Fe(cpbmi)_2]^{2+}$. In this regard, the 220 fs lifetime of the ^{1}MLCT obtained from global analysis should be questioned. For an impulsive population of the ^{3}MC, the transition needs to be faster, than the 316 fs oscillation period of the 106 cm^{-1} breathing mode. This suggests, that the actual ^{1}MLCT lifetime is shorter than the global analysis determined. The lifetime overestimation is most likely due to the strong oscillatory features present in the TA data at early delays, interfering with a precise identification. Indeed, fluorescence up-conversion experiments by Liu et al. suggest, that the ^{1}MLCT lifetime is actually below their 190 fs IRF.[88]

The 470 fs decay of the 106 cm^{-1} mode, characteristic of the ^{3}MC, raises the question, if this is purely due to the coherence dephasing, the vibration being damped by the solvent cage or due to a loss of ^{3}MC population. To address this question, pump-IVS was employed to investigate if this mode can be reinduced after its decay. The results of the pump-IVS experiments are shown in Figure 5.19a in the form of Raman spectra obtained by fast Fourier transformation of the oscillating residual. The respective spectra obtained from IVS (no push pulse) are given as reference.

At first glance, both the high- and low-frequency band found in the IVS Raman spectrum (Figure 5.19a) are reinduced. However, closer inspection of the low-frequency band reveals a blue-shift to 140 cm^{-1}. Both bands can be reinduced even 20 ps after initial photoexcitation. While a 34 cm^{-1} blue-shift might very well be assigned to vibrational cooling in strongly localized modes, this typically amounts to vibration in $W(CO)_6$ shifts from 1980 cm^{-1} to 1966 cm^{-1} and 1951 cm^{-1} when going from $\nu = 0 \rightarrow 1$ to $\nu = 1 \rightarrow 2$ and $\nu = 2 \rightarrow 3$, respectively.[89, 90] Hence, while the 140 cm^{-1} mode is clearly similar to the Fe-L stretch vibration on the ^{3}MC PES (106 cm^{-1}), it cannot be the identical one. Instead, consultation of the normal modes calculated by Thomas Penfold, reveals good agreement with a 27 cm^{-1} blue-shift between Fe-L few

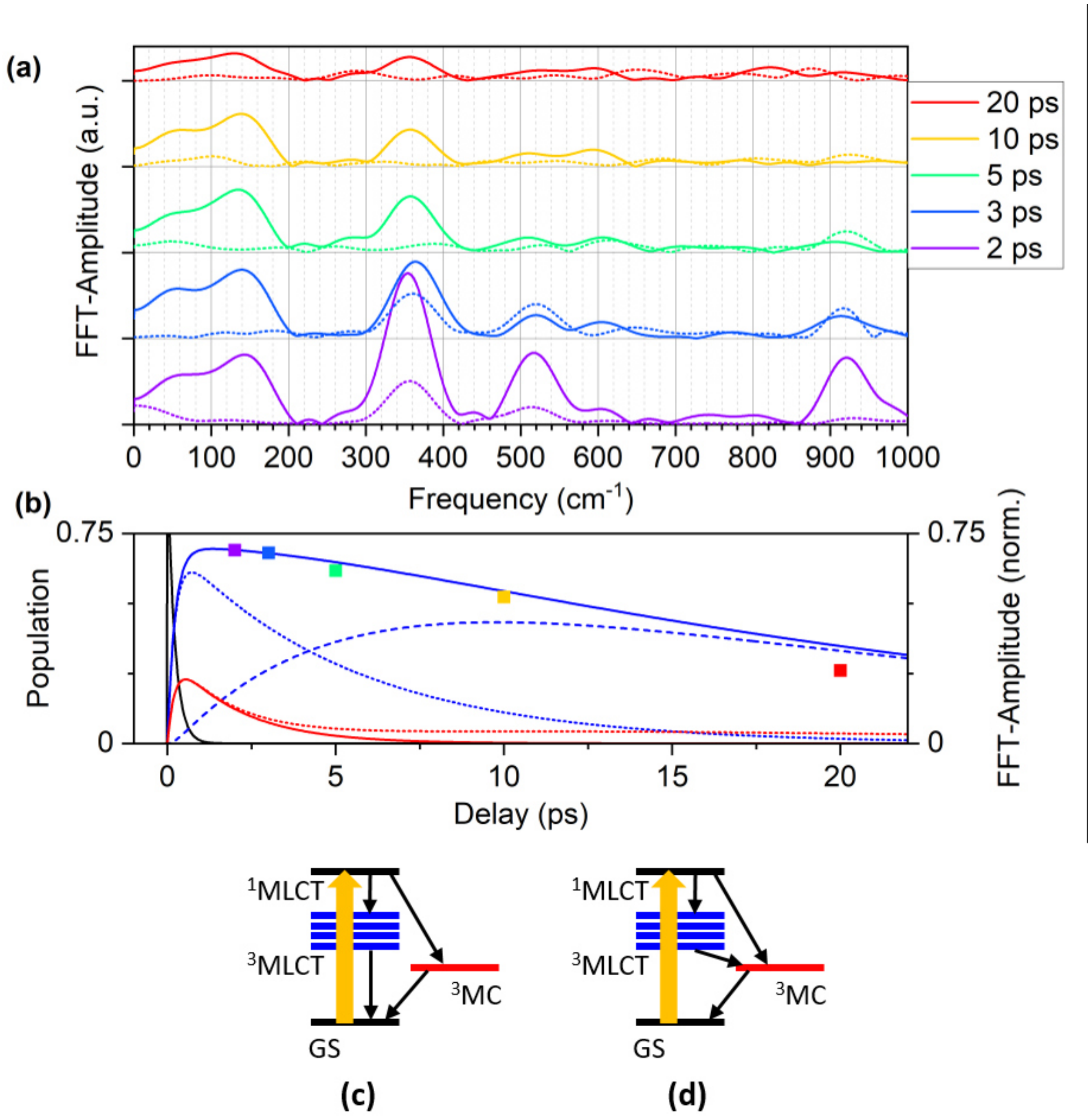

Figure 5.19: (a) Raman spectra obtained by FFT of the oscillatory features in the (pump-)IVS signal at 650 nm. Solid lines denote experiments with, dotted lines without push pulse. (b) Squares: Normalized FFT-Amplitude of pump-IVS experiment at 140 cm^{-1} and population traces of participating states: ^{1}MLCT (black); hot, cold and sum of ^{3}MLCT (blue, dotted, dashed and solid, respectively) and ^{3}MC states according to models (c) and (d) (red, solid, and dotted, respectively). For the population traces a branching of 30% of the population and 2 ps lifetime of the ^{3}MC were assumed.

percent of their original vibrational frequency. For example, the C=O stretch breathing modes on the ^{3}MC PES and the ^{3}MLCT PES (148 cm^{-1} and 175 cm^{-1}, respectively, see Table 5.2). In accordance with that, the reinducibility of the 140 cm^{-1} mode is strongly correlated with the overall ^{3}MLCT population (Figure 5.19b). Accordingly, the 140 cm^{-1} mode is assigned to a Fe-L breathing vibration within the ^{3}MLCT state.

Table 5.2: Raman activities of prominent breathing modes in ^{3}MC and ^{3}MLCT states.[86]

State	Frequency [cm^{-1}]	Raman activity (norm.)
^{3}MC	113	0.3
^{3}MC	148	0.56
^{3}MLCT	170	0.21
^{3}MLCT	175	1

The presence of this mode in the pump-IVS spectra and its absence in the IVS experiment can be rationalized in the following way: The 140 cm^{-1} mode is initiated by a Raman process within the ^{3}MLCT state. Since this state is not populated at the time of the photoexcitation, this Raman process is not possible in the IVS experiment. While this is also true for the ^{3}MC state, the ultrafast ^{1}MLCT-^{3}MC transition launches a wave packet along the Raman active Fe-L breathing mode (106 cm^{-1}), due to the notable change in Fe-L equilibrium bond length (shifted oscillators). Along the ^{1}MLCT-^{3}MLCT transition, where the excited-state nature and bond order remain constant, such an elongation is not expected (nested oscillators). Hence, no vibrational wave packet is launched along the 140 cm^{-1} breathing mode on the ^{3}MLCT PES. Only when the delayed, additional push pulse of the pump-IVS experiment arrives, there is a ^{3}MLCT population where the Raman process can occur. In principal, such a Raman process could also occur within the ^{3}MC state and the fact that even the early pump-IVS spectra (Figure 5.19a) are dominated by the 140 cm^{-1} band indicates, that the branching from the ^{1}MLCT most likely favors the ^{3}MLCT over the ^{3}MC. The absence of the 100 cm^{-1} band from the T=2 ps pump-IVS spectrum could also be explained considering a significant ^{3}MC population, relaxing extremely fast to the ground state. However, this would also be accompanied by a ground-state bleach recovery on the same timescale, which is not observed in the TA-experiment. The ^{3}MC lifetime can hence only be estimated to be larger or equal to the 470 fs dephasing time of the 106 cm^{-1} mode. It may easily be longer than the lifetime of the breathing vibration, which is most likely damped by the solvent cage. It should also be pointed out, that, according to the quantum chemical calculations, the Raman activity of the ^{3}MLCT breathing mode is 1.8 times larger than that of the ^{3}MC state. In case of the self-heterodyne detected nonlinear third order signal probed by pump-IVS this factor is squared to become >3. As a result, in direct competition, pump-IVS is significantly more sensitive to the ^{3}MLCT breathing mode, making identification of an interfering ^{3}MC mode hardly possible. The Raman process is much more likely in the ^{3}MLCT than in the ^{3}MC, but IVS's sensitivity towards the ^{3}MC does not originate in a Raman process. Instead, the impulsive population of the ^{3}MC from the MLCT states launches a wave packet along a breathing mode. During a ^{1}MLCT→^{3}MLCT transition such a wave packet cannot be launched. Therefore, the oscillations induced by the pump can be assigned to the ^{3}MC, constituting IVS's sensitivity towards the ^{3}MC state.

Furthermore, an involvement of the ^{3}MC in the deactivation of the desirable ^{3}MLCT state cannot be ruled out. If the short-lived ^{3}MC acts as loss channel for the longer lived ^{3}MLCT, this would form an "inverted kinetics" scheme, in which the ^{3}MC population is very small at all times. The population traces of both cases, a simple parallel decay of ^{3}MC and ^{3}MLCT, as well as the ^{3}MLCT decay via the ^{3}MC are given in Figure 5.19b. Although in the latter case it is steadily fed, the ^{3}MC population is exceedingly small after the initially branched portion has relaxed to the ground state, making both scenarios spectroscopically indistinguishable.

Recapitulating the results on $[Fe(cpbmi)_2]^{2+}$, IVS and pump-IVS identify breathing modes within two different states, as proof of an ultrafast branching into MLCT and MC states. IVS hence complements the sequential model obtained from transient absorption by an ultrafast branching from the ^{1}MLCT to the ^{3}MC which is in competition to the ^{3}MLCT formation. The lifetime of the ^{3}MC is expected to be ≥ 470 fs, but significantly shorter than the 19.9 ps of the ^{3}MLCT. Yet, no preliminary ground-state bleach recovery is observed in the transient absorption showing that only a very minor fraction of the ^{1}MLCT population branches into the ^{3}MC state.

The purposeful design of the cpbmi ligand successfully shifts the ^{5}MC state out of the photo-relaxation pathway through the strongly σ-donating NHC-ligands. This prevents $[Fe(cpbmi)_2]^{2+}$ from collapsing into this exceptionally long lived, metal centered state, which is doubly undesirable regarding applications as dye sensitizers: Firstly, the initially induced charge separation, a prerequisite of most applications, is abolished. Secondly, the chromophore is trapped in a long-lived dark state, acting as downtime making it less available for light absorption. At the same time, the pyridyl unit of cpbmi ensures the availability of the bright ^{1}MLCT state. However, not all MC states are successfully shifted out of the relaxation pathway. The ^{3}MC state still acts as a MLCT loss channel, although the branching significantly favors the ^{3}MLCT state, suggesting, that the vertical shift of the ^{3}MC introduces a small barrier between the Frank-Condon region of the ^{1}MLCT and its intersection with the ^{3}MC.

In summary, transient absorption and (pump-)IVS have shown to be complementary tools to investigate the excited-state dynamics of Fe(II)pyridyl complexes and how they are shaped by solvent choice and ligand design.

6 Photophysics and -chemistry of triphenylamines

The Iron(II)-complexes regarded in the previous chapter were promising candidates for dyes in DSSCs, meaning they can be employed to absorb incoming light (in the visible region) and initiate charge separation. If the energy carried by the absorbed photon is to be used, the charge separation must also be passed on, so that the charges recombine after passing through the appliance and not within the dye. To that end, the active layer, i.e. the dye in DSSCs or the preovskite in perovskite solar cells (PSCs) are sandwiched in a electron transporting material and a hole transporting material (HTM).[91] An energy diagram is shown in Figure 6.1a. The selective mobility forces the promoted electron and the hole to travel towards the anode and cathode, respectively, yielding a macroscopic voltage between them. Organic light emitting diodes (OLEDS) follow a similar structure, but work in the opposite direction (Figure 6.1b). An external voltage between anode and cathode induces excess electrons and holes, which travel towards the active (emitting) layer, where they recombine on dye molecules, forming excitons prone to radiative relaxation.

Evidently, efficient applications not only require well-designed active layers, but also suitable electron and hole transport materials. Ideally, these are characterized by suitable electrochemical properties, such as HOMO and LUMO energies, high charge mobilities, easy processability and stability towards optical and thermal degradation. Owing to their ability to stabilize positive charges via the delocalized π-system, triphenylamine (TPA) and its derivates are reversibly oxizidable and exhibit good hole mobilites.[92] Consequently, they are a class of HTM which find application in both PSCs and OLEDs.[93-97] Furthermore, they are investigated for their electronic properties with respect to different bridging motifs.[98, 99] Stable radical cations as well as charge transfer processes involving bridging side groups and the aromatic core have been reported.[100]

In this section, triphenylamine (TPA, Figure 6.2a) and a dimethylmethylene-bridged derivate thereof (DTPA, Figure 6.2b) are investigated for their photochemical reactivity. This project is a collaboration with two other groups located at the Ruprecht-Karls-Universität in Heidelberg. Angelina Jocic in the group of Milan Kivala prepared DTPA and organized nuclear magnetic resonance spectroscopy (NMR) and mass spectrometry (MS) through the organic chemistry department. Letao Huang in the

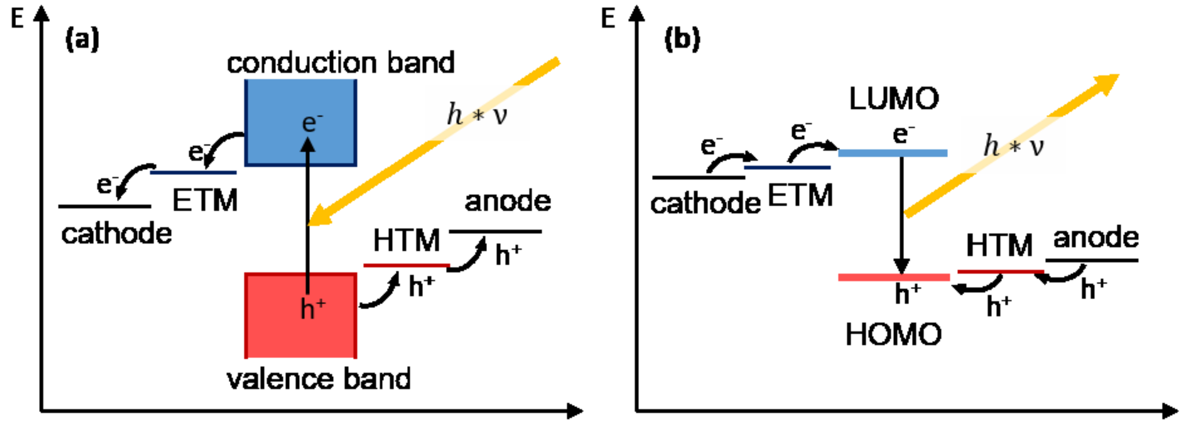

Figure 6.1: Schematic energy diagram of a perovskite solar cell (a) and an OLED (b).

group of Andreas Dreuw conducted quantum chemical studies at the Interdisciplinary Center for Scientific Computing.

The valence shell electron pair repulsion model (VSEPR) would suggest a pseudo tetrahedral geometry for TPA, where the lone electron pair corresponds to the fourth corner, like ammonia or aliphatic amines. However, basicity due to N-protonation is not found in solutions of TPA. Indeed, instead of a sp^3 hybridized lone pair and N-C bonds, the nitrogen atom is sp^2 hybridized: All N-C bonds lie within a single plane, to which the lone pair in the remaining p-orbital is perpendicular. This allows for a limited π-conjugation through which each of the phenyl rings function as an electron attracting group, inducing a small dipole between the partially positively charged nitrogen and the phenyl rings. However, the three phenyl rings cannot be regarded as a single conjugated π-system. Due to steric hindrance, they are twisted along the N-C axis which results in an overall propeller-shape. This limits the overlap with the central p-orbital at the nitrogen and negates overlap with the π-systems of neighboring phenyl moieties altogether (Figure 6.2c). The introduction of dimethylmethylene bridges

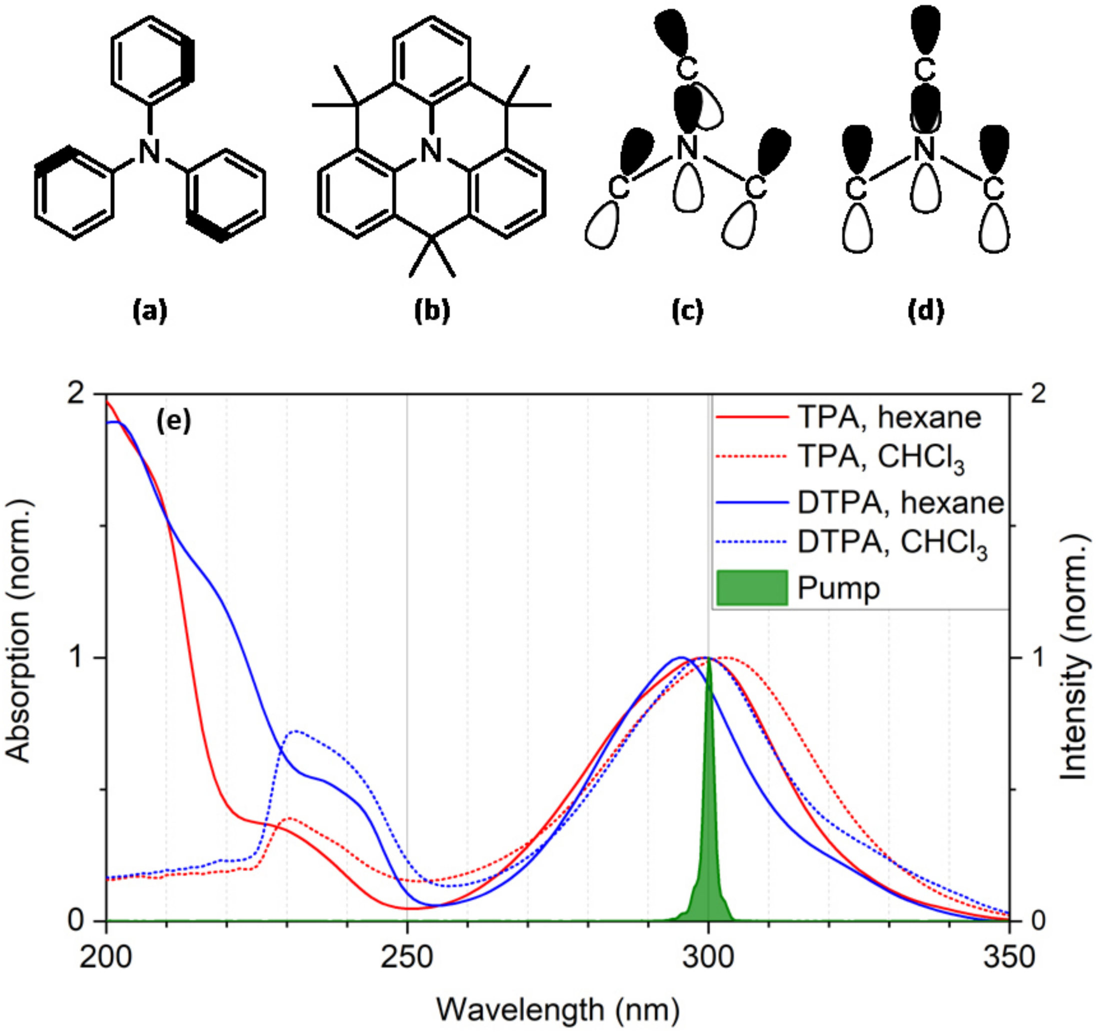

Figure 6.2: Molecular structures of triphenylamine (TPA) (a) and 4,4,8,8,12,12-hexamethyl-8,12-dihydro-4H-benzo[9,1]quinolizino[3,4,5,6,7-defg]acridin, which is referred to at dimethylmethylene-bridged TPA, DTPA for short (b). Orientation of p-orbitals in TPA (c) and DTPA (d). (e) UV-VIS absorption spectra of TPA and DTPA in hexane and chloroform, as well as the excitation spectrum used in the irradiation series and TA experiments.

forces the phenyl rings to overcome the steric barrier and reverses the propeller shape (Figure 6.2b and d). Typically, the extension of a conjugated π-system leads to a smaller gap between the π and π* MOs, resulting in a red-shifted π-π* transition. Inspection of Figure 6.2e reveals, that the planarization form TPA to DTPA is not accompanied by the expected red-shift of the absorption band. Instead, the absorption maxima around 300 nm are blue-shifted by 4 nm in both investigated solvents (see Table 6.1). Yet, the strong resemblance in position and shape of the lowest absorption band strongly suggests, that they originate in similar transitions. The absorption bands cannot result from π-π* transition purely localized on the individual phenyl rings, as they appear significantly red-shifted compared to pure benzene, which has a lowest absorption maximum at 255 nm.[101] To consider expansion of the conjugated π-system to the adjacent nitrogen, the absorption spectrum of aniline can be regarded. Its lowest absorption maximum is located at 280 nm, which is close, but not quite congruent with the 300 nm found for TPA and DTPA.[102] It can therefore be inferred, that the effective π-system in TPA and DTPA expands beyond the individual phenyl ring and the central nitrogen atom.

Comparison of the absorption spectra taken in hexane and chloroform reveals a small red-shift and a noticeable broadening of the absorption band going from the former to the latter for both TPA and DTPA. Both the red-shifts and the broadenings amount to ~0.05 eV (Table 6.1) and originate in the dipole moment increase going from hexane (0.08 D) to chloroform (1.15 D). The more polar and compact chloroform is slightly more suitable to stabilize the local dipole moments between the phenyl rings and the central nitrogen atom (+0.47 e and +0.46 e at N for TPA and DTPA, respectively, according to extended Hückel theory as implemented in Chem3D). This was noticeable, as both TPA and DTPA dissolved much more easily in chloroform, than in hexane. However, the photoexcited state appears to be slightly more polarized, so that it is stabilized more than the ground state is by the polar chloroform. This results in a marginally smaller energy difference overcome by the photoexcitation when using chloroform as solvent, rather than hexane. Furthermore, the different possible orientations of the more polar and compact chloroform have a larger variance in this stabilizing effect, resulting in the spectral broadening observed in Figure 6.2e and summarized in Table 6.1.

Table 6.1 Absorption maxima and full width at half maximum (FWHM) of both samples in both solvents.

Sample / Solvent	Absorption maximum		FWHM	
	[nm]	[eV]	[nm]	[eV]
TPA, hexane	299	4.15	277-314	0.53
TPA, $CHCl_3$	303	4.09	279-321	0.58
DTPA, hexane	295	4.20	279-309	0.43
DTPA, $CHCl_3$	299	4.15	281-315	0.48

The two investigated molecules are examined by stationary and transient absorption spectroscopy and compared to determine the influence of the planarization under different conditions of solvent and atmosphere. Since the absorption maxima vary only insignificantly around 300 nm, the excitation spectrum was kept constant as reported in Figure 6.2e for all reported TA and irradiation experiments. The probe spectra for the TA experiments are described in Sections 4.2.2.

This section is organized as follows: Section 0 focuses on TPA in hexane with and without oxygen in the solution to establish the basic photophysics and photochemical reactivity of the system. DTPA was examined under the same conditions. The results are presented and compared to the unbridged TPA to point out the influence of the bridges in section 6.2. Lastly, section 0 presents results from the investigation of both molecules dissolved in chloroform, highlighting the drastic effect electron accepting solvents can have on the excited-state dynamics.

6.1 Photochemical reactivity of TPA in hexane

After the first attempts of TA experiments on TPA in hexane showed significant sample degradation during the runtime, an irradiation series was conducted to investigate its photostability (Figure 6.3a). The series of absorption spectra shows decay of the absorption bands at λ ≤ 213 nm and the lowest absorption band at λ = 277 nm - 330 nm. Below the latter, a new, structured absorption band forms with a maximum at 291 nm and a shoulder on the red side thereof (λ ≥ 297 nm). Simultaneously, new bands form during the irradiation at λ = 213 nm - 277 nm with a maximum at 238 nm and a small one at λ ≥ 330 nm with maximum at 338 nm. These spectral regions of rising and decaying absorption bands are separated by isosbestic points at wavelengths of 213 nm, 277 nm, and 330 nm. Isosbestic points are such points in a series of spectra, at which no changes occur, even though the rest of the spectra are changing along a specific experimental parameter. In plots of differences of the spectral properties (such as Figure 6.3c and d) these isosbestic points manifest as zero values. They are a strong indicator, that the observed dynamically changing spectra result from no more than one transformation.

To rationalize this, let us consider a transformation with a single distinct characteristic spectrum for both the reactants and the products that intersect at n given wavelengths (Figure 6.4). Note, that the characteristic spectrum of the products or reactants may actually be a combination of multiple species absorbing, as is the case in Figure 6.4a and b. Regardless of the exact composition, as long as the stoichiometry of the transformation is strictly conserved, no change in the spectral property is observed at

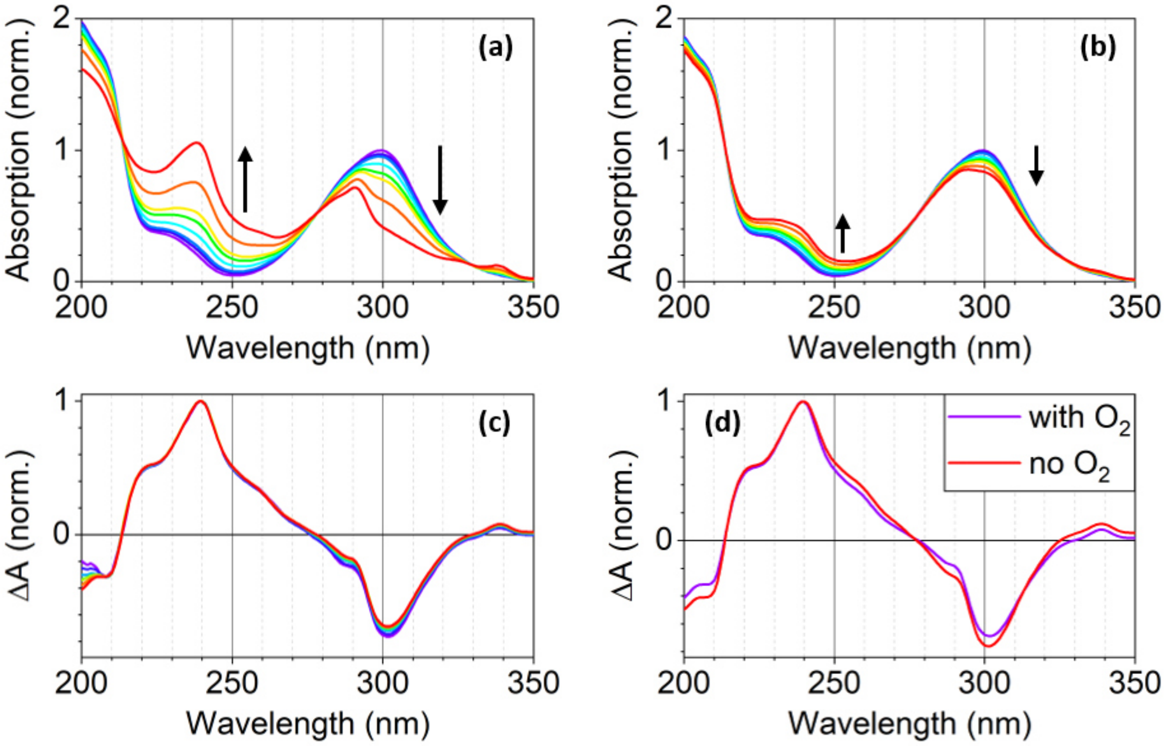

Figure 6.3: (a) and (b): Irradiation series of TPA in hexane (a) with and (b) without oxygen. Irradiation duration from purple to red: 0, 1, 2, 5, 10, 15, 30 and 60 minutes. The samples were irradiated at 0.5 mW of the 300 nm pump spectrum given in Figure 6.2e. Absorption spectra normalized to lowest maximum. (c) and (d): Normalized differences in absorption of irradiated sample and new sample. (c) Series with oxygen, irradiation duration from purple to red: 1, 2, 5, 10, 15, 30 and 60 minutes. (d) Differences with and without oxygen after 60 minutes of irradiation.

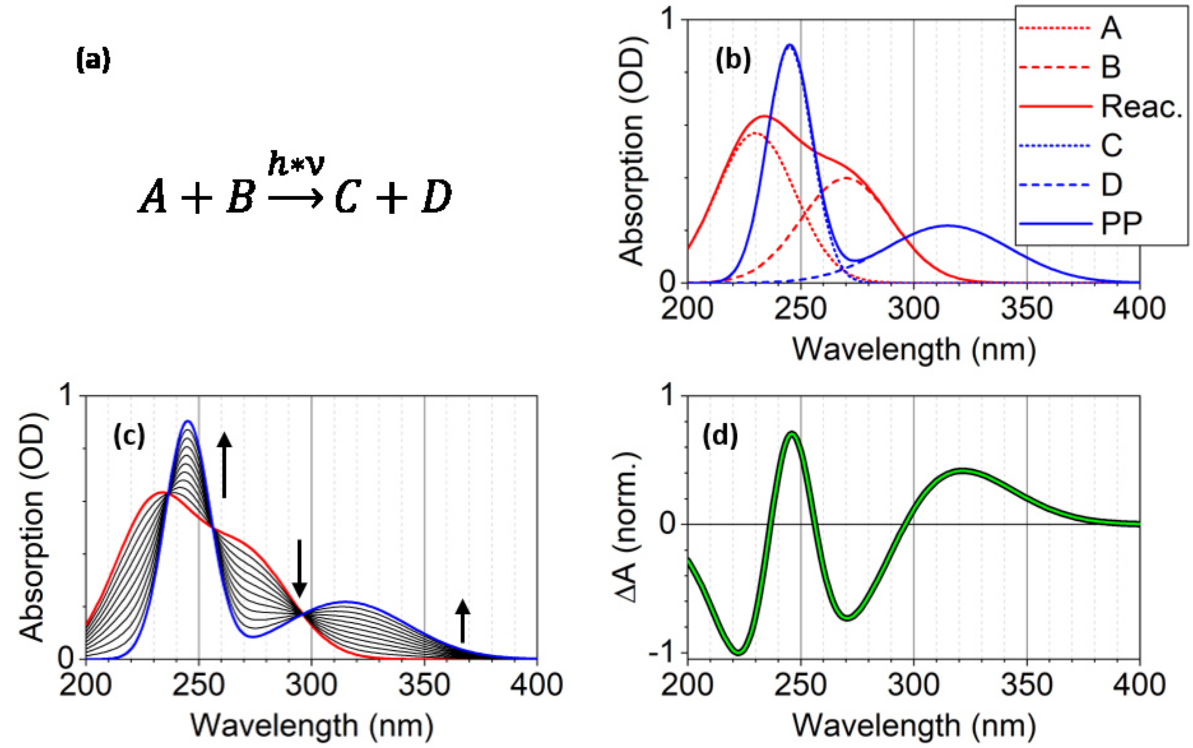

Figure 6.4: Origin of isosbestic points explained in a hypothetical case. (a) Photochemical reaction equation. (b) absorption spectra of all four components as well as characteristic spectra of reactants and photoproducts. (c) Absorption spectra going from reactants to photoproducts in 10% conversion steps. (d) Normalized difference absorption after 10 (black) and 100% conversion (green).

the intersecting wavelengths throughout the conversion (Figure 6.4c). Plotting the difference spectra between the fresh sample and any state of conversion shows regions of rising and decaying absorption bands as positive and negative features, respectively (Figure 6.4d). These are separated by the isosbestic points. If the differences are indeed due to a single transformation, the normalized difference spectra will overlap completely, regardless of the degree of conformation.

If, however, more than one transformation is at play, it is arbitrarily unlikely that all characteristic spectra intersect at the same wavelengths. Under such conditions, no isosbestic points will appear and the normalized differences will not be the same for all wavelengths and degrees of conversion. The presence of isosbestic points is therefore a strong sign that a single transformation with fixed stoichiometry composes the given series of spectra.

In the present case of an irradiation series (Figure 6.3a and c), this suggests, that a single photoproduct is formed during the irradiation of TPA in hexane in the presence of oxygen. Figure 6.3c displays the normalized absorption differences between the samples with 0 and 1, 2, 5, 10, 15, 30 and 60 minutes of irradiation. Except for small deviations at $\lambda \leq 210$ nm, all seven spectra are in good agreement with one another, furthermore, supporting the assumption of a single transformation step. This also indicates that the photoproduct itself is photostable under the present conditions. The minor deviations at $\lambda \leq 210$ nm may result from the overall large absorption in this wavelength region. The absolute value of the absorption is around 2 OD, meaning only 1% of the incident light passes the sample and reaches the detector, possibly leading to small inaccuracies.

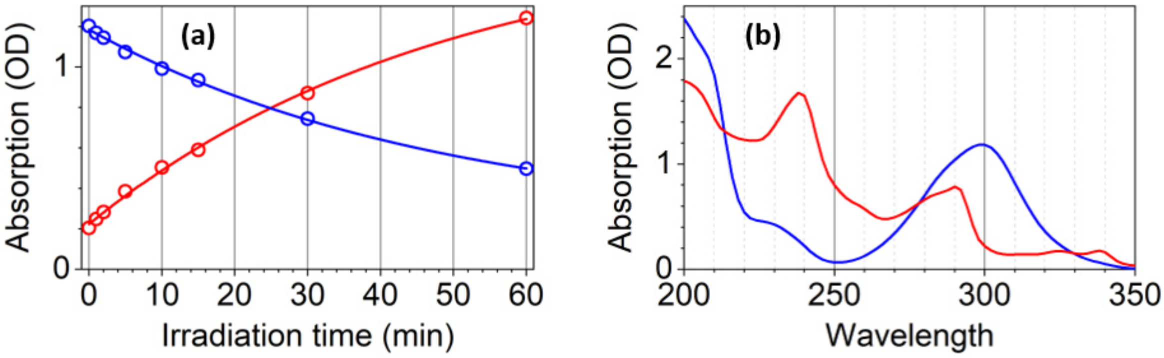

Figure 6.5: Analysis of irradiation series of TPA in hexane with oxygen (Figure 6.3a). (a): Global fitting of absorption as exponential decays at wavelengths characteristic of the photoproduct (240 nm, red) and TPA (300 nm, blue). (b): Spectra of TPA (blue) and the photoproduct (red) as extrapolated from exponential fitting as shown in (a).

To enable longer experimental TA runtimes, leading to better signal-to-noise ratios, the exclusion of oxygen from the sample was tried to circumvent the formation of the photoproduct. Figure 6.3b shows that the exclusion of oxygen indeed significantly improves the photostability of TPA in hexane, although a minor fraction of TPA is still converted to a photoproduct. Minute comparison of the irradiation series with and without oxygen reveals, that the isosbestic points at wavelengths of 213 nm, 277 nm and 330 nm are retained exactly. In addition to that, even the normalized absorption differences after 60 minutes irradiation with and without oxygen are in good agreement (Figure 6.3d). This proposes, that even though the quantum yield depends strongly on the presence of oxygen, the photoproduct being formed is not affected by it.

Almost all of the above observations are in great agreement with the literature on the photochemistry of TPA. It is well established, that diphenylamines undergo cyclization towards carbazoles.[103] Analogously, for TPA the formation of N-phenylcarbazole has been reported.[104] The UV-VIS spectrum published for the closely related N-methylcarbazole as photoproduct of N-methyl-diphenylamine has striking similarity to the spectrum of the photoproduct shown in Figure 6.5b. On this basis, the photoproduct of TPA in hexane, both with and without oxygen, is identified as N-phenylcarbazole. Furthermore, the accelerated formation of the carbazole in the presence of molecular oxygen has also been reported.[105] However, the observation of byproducts under nitrogen atmosphere as reported by Protti et al. was not reproduced in this work.[106] Instead, the excellent agreement of the difference spectra shown in Figure 6.3d proofs, that the identical photoproduct is formed under air or nitrogen atmosphere. This contradiction may be resolved considering the solvent in use. While Protti et al. conducted their experiments in acetonitrile (dipole moment 3.91 D)[107], the results given here were obtained from solution in n-hexane, which has negligible dipole moment. It is likely, that formation of the byproducts (tetrahydrocarbazoles) occurs via a polarized transition state which is stabilized in acetonitrile, but not in hexane.

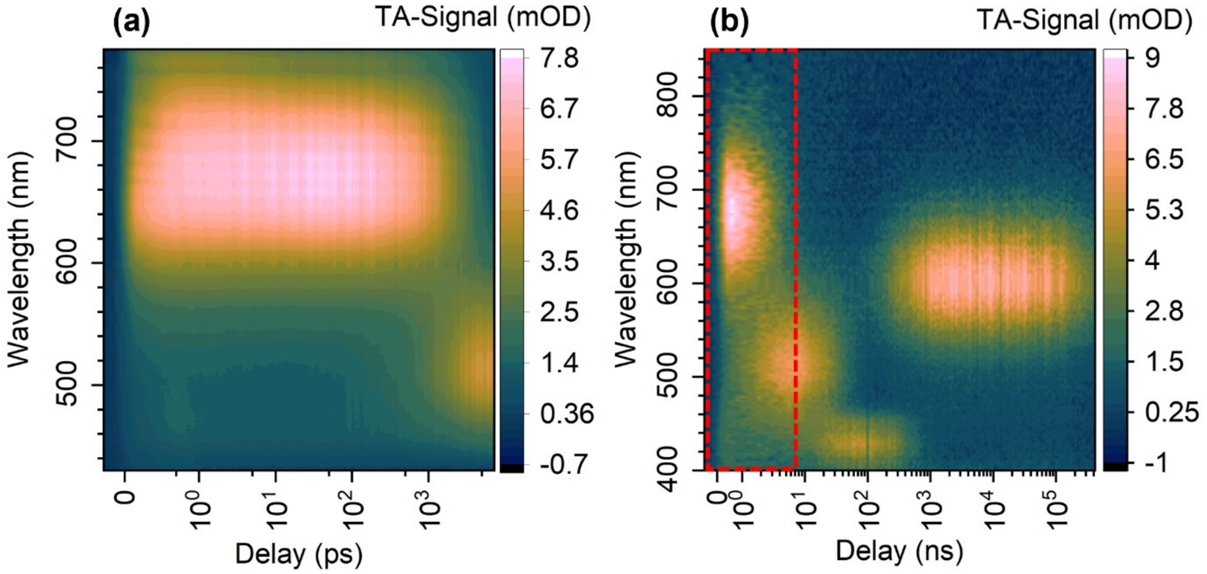

Figure 6.6: Two-dimensional representation of transient absorption data of degassed sample of TPA in hexane. (a) Short delay experiment. (b) Long delay experiment. Marked in red is the delay range covered in the short delay experiment.

Steady state absorption, as employed in the given irradiation series, gives information about the outcome of the photochemical process. However, it treats the excited-state dynamics, which are crucial to understand for a deliberate design of molecules, as a black box. To gain insight into the individual species involved in the relaxation processes, transient absorption spectroscopy was employed. The resulting 2D-datasets are given in Figure 6.6. Neither the short delay nor the long delay datasets contains negative features, which can be rationalized considering the experimental spectral range and the ground-state absorption of TPA given in Figure 6.2e. The spectral region of the ground-state bleach is not covered in the white light probe supported by the experimental setup. Instead, two distinct positive features are found in the short delay dataset and four in the long delay dataset. The short delay dataset (Figure 6.6a) is dominated by a first, broad ESA band at 580 nm – 760 nm. As this band decays after ~2 ns, another band appears at 480 nm – 580 nm. The temporal region covered by both the short and long delay experiments are in perfect agreement with one another. Expanding on the short delay data, the decay of the 500 nm ESA band is captured at ~30 ns in the long delay experiment (Figure 6.6b). On the same timescale, a third ESA band, centered at 430 nm rises. Its subsequent decay is accompanied by the rise of a fourth absorption band, centered at 600 nm, spanning the range of 560 nm – 680 nm. The onset of this very long-lived bands decay is visible in the hundreds of microseconds, yet its full decay cannot be monitored with the experimental delay range of 450 µs. The well-ordered arrangement of four consecutive absorption bands, each replacing their respective predecessor, is striking. It forces the conclusion that the molecular system cascades through four distinct excited states by mere inspection of the raw data. This conclusion is supported by the DADS obtained from simultaneous global analysis of both datasets, given in Figure 6.7. It shows seven DADS associated to five distinct time constants: 12.0 ps, 2.54 ns, 31.5 ns, 392 ns and 460 µs. While the 12.0 ps DADS is based exclusively on the short delay experiment, the 392 ns and 460 µs DADS are based on the long delay data.

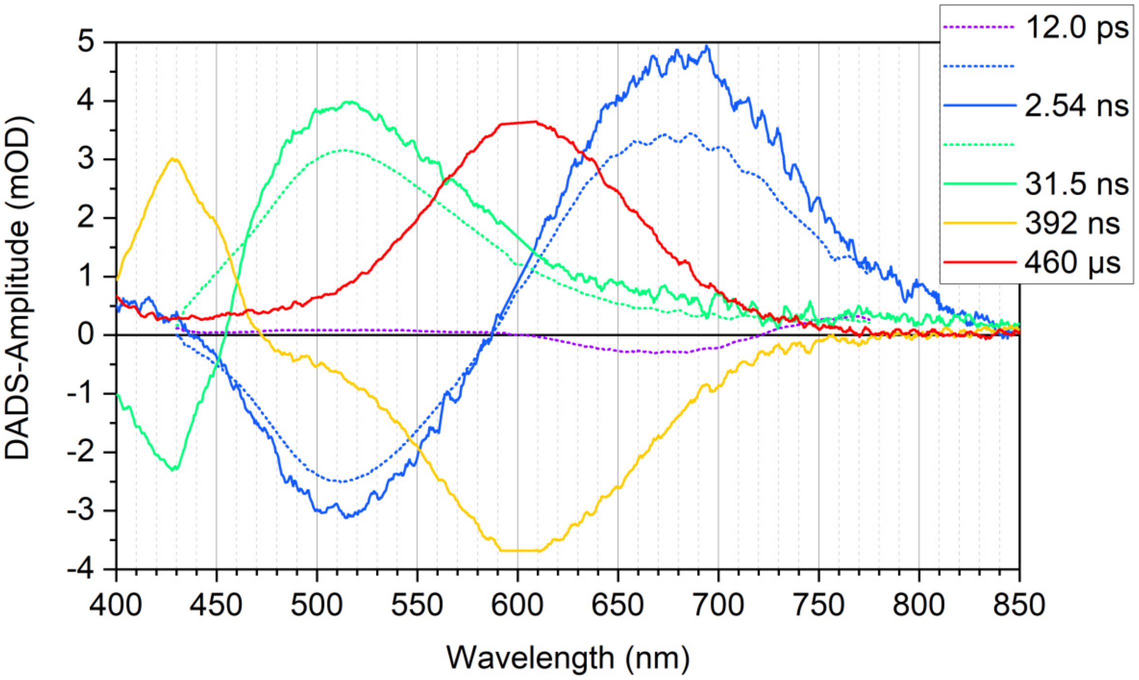

Figure 6.7: DADS obtained from simultaneous global analysis of the two TA datasets of TPA in hexane (degassed). Dotted: DADS from short delay data, solid: DADS from long delay data.

Since all contributions in the two datasets given in Figure 6.6 are positive, all negative contributions in the DADS can be regarded as rise of a positive absorption band. Regarding the DADS with 2.54 ns and 31.5 ns obtained from both the short and the long delay data, it becomes evident, that they are in excellent agreement, proving the reproducibility. Besides the small difference in amplitude and signal-to-noise ratio, due to the different white light source, the only distinction is the blue region (λ ≤ 530 nm) of the 31.5 ns DADS. This difference can easily be explained considering the different observed delay frames: In the short delay experiment, delays up to 8 ns were scanned, which allows for observation of the rise of the second absorption band. However, it does not allow for the observation of its decay and the associated rise of the third ESA band (31.5 ns). This rise of the band at 400 nm – 540 nm is therefore covered by the long delay experiment, so that it manifests as a negative contribution to the 31.5 ns DADS there, but not in the corresponding short delay DADS.

The 12.0 ps DADS is determined on the basis of the short delay data only, because of the ~100 ps temporal resolution of the long delay experiment. It is the only DADS that cannot easily be assigned a contribution in the 2D dataset in Figure 6.6a. Close inspection reveals, that its overall small amplitude is only significantly non-zero in the spectral region of the 2.54 ns DADS. It features a decay on the red side of this absorption band (λ ≥ 720 nm) and a rise on the blue side (610 nm – 720 nm). Together, this constitutes a blue-shift of the underlying ESA band, characteristic of vibrational cooling. Both DADS associated with the 2.54 ns time constant describe the decay of the first absorption band and the simultaneous rise of the second ESA band, strongly suggesting a direct population transfer in between the absorbing species. The same can be said about the 31.5 ns DADS: it consists of the decay of the second ESA band around 520 nm and the synchronous rise of the third ESA band around 430 nm. The

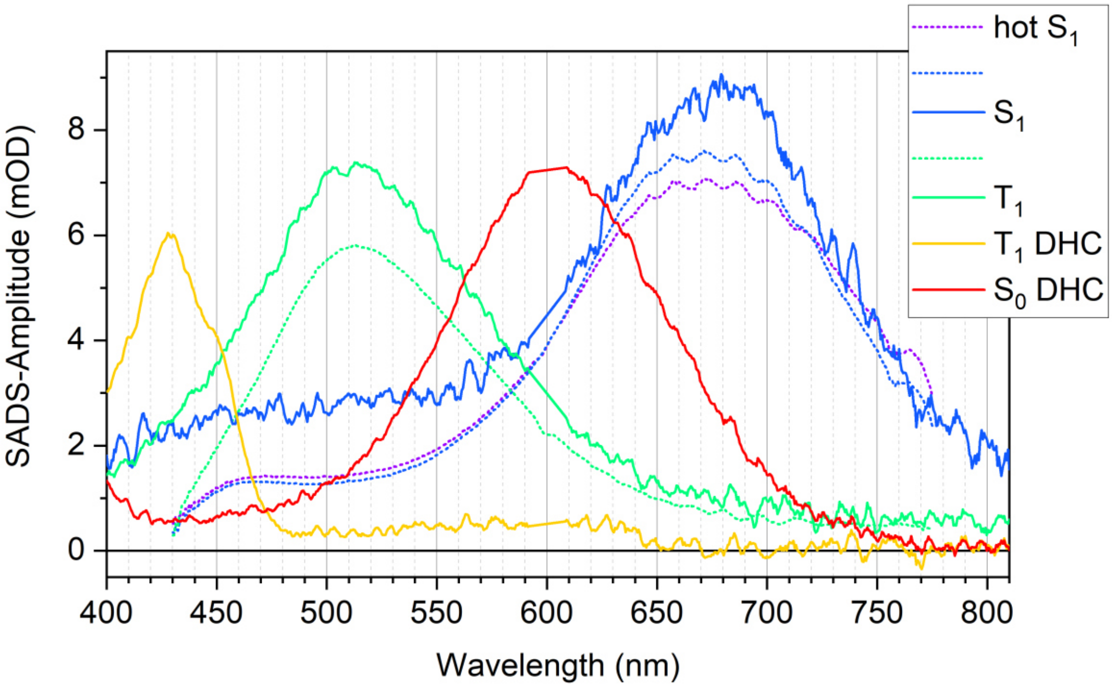

Figure 6.8: SADS obtained for sequential model to the TA-Data of TPA in hexane (degassed). Dotted: SADS from short delay data, solid: SADS from long delay data.

decay of this ESA band is in turn part of the 392 ns DADS, which also features the rise of the last observed transient species absorbing around 600 nm. The 460 µs DADS is the mirror image of this negative feature, representing the decay of this last observed ESA band. This series of decays, each accompanied by the rise of a subsequent ESA band very clearly requires a sequential excited-state cascade to model the data properly. SADS resulting from analysis presuming a sequential decay are given in Figure 6.8. The theoretical studies by Letao Huang reveal, that the bright transitions of TPA are the $S_0 \rightarrow S_2$ and $S_0 \rightarrow S_3$ transitions. Nevertheless, there is strong agreement between the first two SADS and the S_1 optical transitions calculated using TDDFT on the CAM-B3LYP level using def2-TZVP as basis set. They were predicted to be at 690 nm and a weaker transition at 460 nm, which are reflected in the peak at 690 nm and the shoulder at 450 nm of SADS 1 and 2. After optically allowed photoexcitation to the TPA S_2/S_3, the molecular systems relax ultrafast (within the ~100 fs IRF) to the lowest excited singlet state, S_1, which is experimentally not resolved. SADS 3 is in great agreement with the optical transitions calculated for the T_1 state of TPA: a strong absorption feature at 520 nm and a much weaker one at 780 nm. For the assignment of the last two transient spectra, it is necessary to consider the photoproduct formed under the irradiation of TPA as (potential) end point of the excited-state cascade. As discussed above, the photoproduct is N-phenylcarbazole. However, the last two transient absorbing species are clearly not the ground-state absorption of the N-phenylcarbazole, firstly because they are transient, not permanent, and secondly, because the N-phenylcarbazole does not show any absorption in the visible spectral range. Let us therefore contemplate the steps necessary for TPA to form N-phenylcarbazole as depicted in Figure 6.9. Formation of the five-membered ring requires breakage of the two involved aromatic systems. The

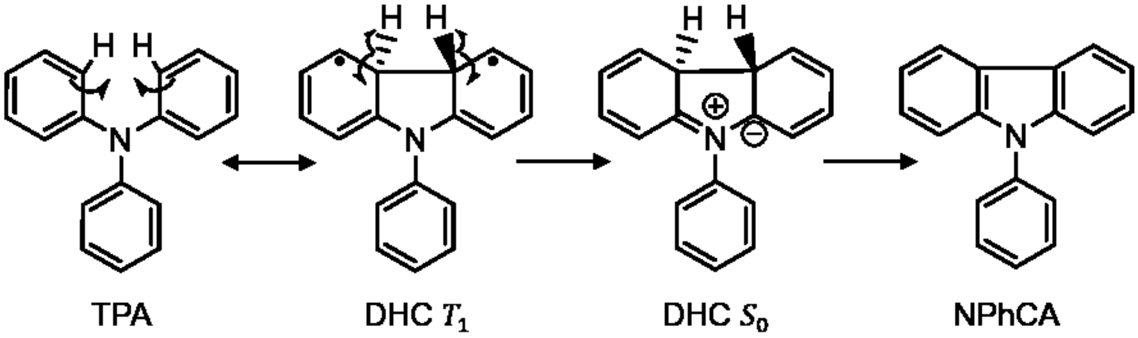

Figure 6.9: Cyclization of triphenylamine (TPA) via dihydrocarbazole (DHC) to N-phenylcarbazole (NPhCA).

sigma bond between the neighboring ortho positions is formed. This leaves behind a biradical version of the carbazole scaffold in excess of the two hydrogen atoms located at the bridge heads, termed dihydrocarbazole (DHC). To complete formation of the carbazole, recovery of the aromaticity requires abstraction of the two excessive hydrogen atoms. While in thermally activated ground-state chemistry, the simultaneous breakage of two aromatic systems seems unlikely at best, this is not only possible, but established in photochemistry.[103-106, 108] Consider the MOs involved in the formation of the five-membered ring (Figure 6.10). In a hypothetical planarized TPA, the p-orbitals building up the π-system are all perpendicular to the molecular plane. The propeller like twist of the phenyl rings manifests a preorientation of these p-orbitals towards a σ-bond like overlap. When the π-system is weakened by the π-π* transition associated with the absorption of a photon, this sigma bond is formed easily, resulting in the carbon atoms hybridization change from sp^2 to sp^3.

Supporting the idea of transient DHC are the spectra predicted by DFT calculations for the T_1 and the S_0 of it, which are in excellent agreement with SADS 4 and 5, respectively. The predicted DHC T_1 spectrum shows an absorption band at 400 nm, which is in good agreement with SADS 4 (430 nm). Similarly, absorption spectrum predicted for the zwitterionic singlet ground state of the DHC features a strong band at 540 nm which is met by the broad absorption band around 600 nm in SADS 5. In summary, the following model is proposed for the interpretation of the TA data on the

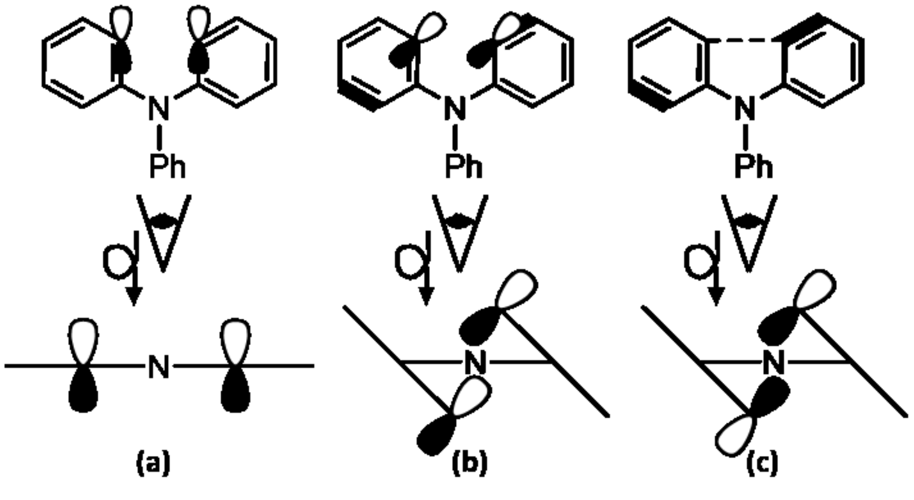

Figure 6.10 Molecular orbitals involved in formation of the carbazole five-membered ring. (a) Hypothetical planar TPA. (b) Propeller shaped TPA. (c) Photoexcited propeller shaped TPA. Bottom panel shows view along the Ph-N-axis to demonstrate the developing σ-bond.

basis of the predicted reference spectra: After photoexcitation to the bright singlet excited states (S_2, S_3) which relax within the experimental temporal resolution (~ 100 fs) to the S_1, there is vibrational thermalization within the S_1 on the 12.0 ps timescale. The equilibrated S_1 undergoes intersystem crossing (2.54 ns) to the T_1 of TPA. Within 31.5 ns a σ-bond between the ortho-positions of two neighboring phenyl moieties is formed, resulting in a five-membered ring. The obtained biradical T_1 of DHC relaxes within 392 ns via another intersystem crossing to the zwitterionic S_0 ground state of DHC. Elimination of the hydrogen atoms at the newly formed bridge heads, yields the stable photoproduct, NPhCA. Since this process is extremely unlikely in the absence of molecular oxygen, the quantum yield for photoproduct formation is small in the degassed sample (Figure 6.3b).

From the irradiation experiments, which consider the involved photophysics as a black box system, it was inferred, that formation of NPhCA is greatly accelerated in the presence of molecular oxygen (Figure 6.3a). It is therefore most interesting to open this black box using TA spectroscopy and compare the inner proceedings to those of the degassed sample discussed above. The 2D datasets for short and long delays are shown in Figure 6.11a and b, respectively. Comparison to the datasets obtained from the degassed sample (Figure 6.6) yields a clear similarity and a stark contrast. Firstly, all four main contributions from the degassed sample also appear under ambient conditions: The first species absorbing at 580 nm - 760 nm, the second one at 480 nm – 580 nm, the third at ~430 nm and the fourth one at 560 nm – 680 nm. However, it is at least as apparent, that the amplitude of all ESA bands after the first one are significantly diminished compared to the degassed datasets. This is especially true for ESA bands assigned to the DHC T_1 and S_0, which are hardly visible in the 2D representation given in Figure 6.11b. This is also reflected in the respective DADS in Figure 6.12. Again, DADS 2 and 3, which could be obtained from both short and long delay data are in excellent agreement to one another. Furthermore, the quantitative analysis also reveals, that the time constants associated with the four primary features

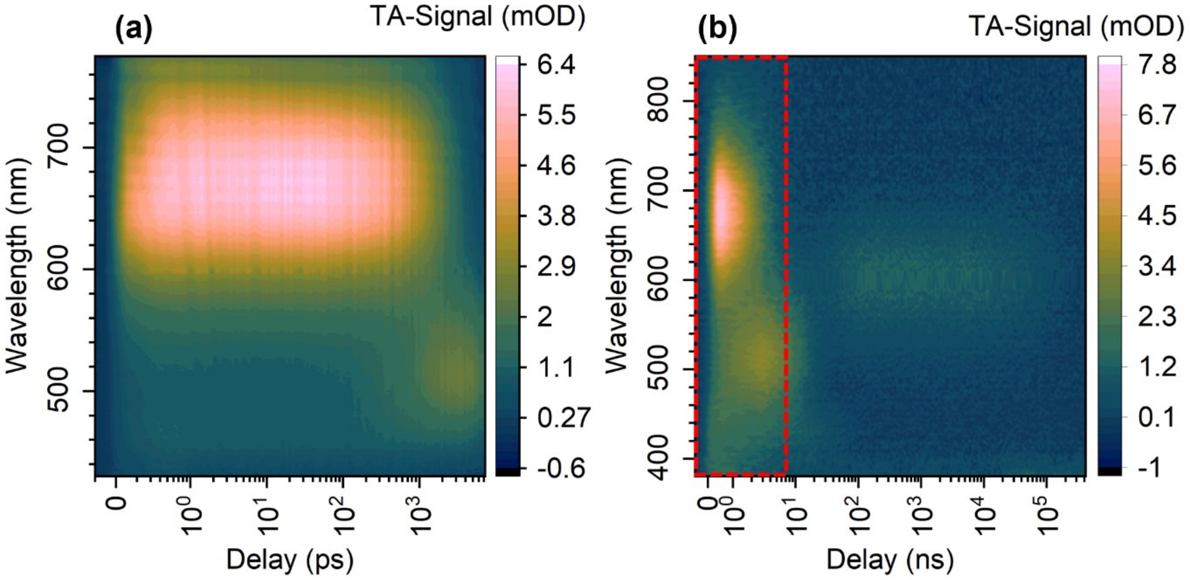

Figure 6.11: Two-dimensional representation of transient absorption data of TPA in hexane under ambient conditions. (a) Short delay experiment. (b) Long delay experiment. Marked in red is the delay range covered in the short delay experiment.

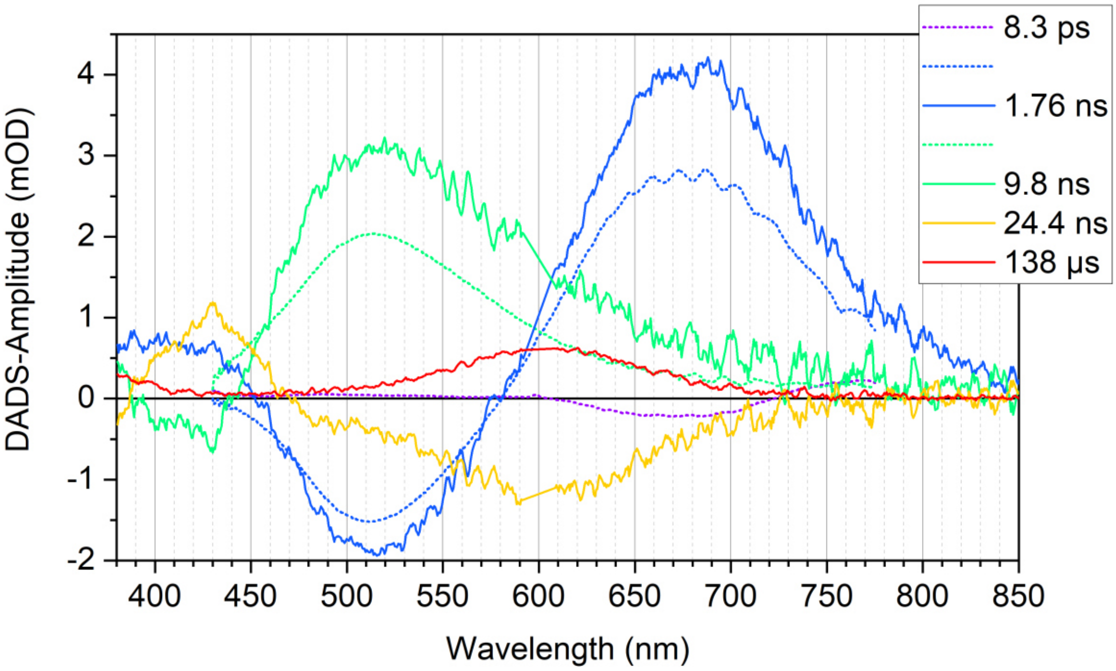

Figure 6.12: DADS obtained from simultaneous global analysis of the two TA datasets of TPA in hexane under ambient conditions. Dotted: DADS from short delay data, solid: DADS from long delay data.

are significantly shortened: the second time constant, which was associated with the TPA S_1 lifetime is now quantified at 1.76 ns instead of 2.54 ns. The TPA T_1 lifetime was 31.5 ns in the degassed sample and is reduced to 9.8 ns, which is less than a third of the original value. The DHC T_1 lifetime is reduced most drastically from 293 ns to 24.4 ns and the DHC S_0 lifetime is greatly decreased from 460 µs to 138 µs, too. Even though the amplitudes and lifetimes are affected greatly by the presence of molecular oxygen in the solution, qualitatively, the sequence of one DADS leading to the next one is conserved exactly. This behavior therefore requires an explanation, which covers both the smaller ESA amplitudes and their reduced lifetimes while maintaining the established excited-state framework. This is achieved considering loss channels as addition to the photophysics and photochemistry discussed for degassed conditions. In order to understand the nature of these additional loss channels, it is useful, to note, that the two excited-state lifetimes affected most are those of the triplet states: the TPA T_1 lifetime is decreased to approximately one third, the DHC T_1 lifetime even to one twelfth of its original lifetime. This brings both to the same order of magnitude (~factor 2.5) when there originally was factor 10 between them. It is intuitive, that triplet states are most vulnerable towards oxygen, a reactive triplet ground-state species since they are not shielded by spin state mismatch. Additionally, the harmonization in lifetimes strongly suggests a similar mechanism behind the newly formed, oxygen related loss channels. Since no additional photoproducts were observed comparing the degassed and ambient irradiation series (Figure 6.3d), oxidation in the sense of incorporation of (molecular) oxygen into the TPA molecule can be disregarded. Triplet fusion (TF) on the other hand can explain the greatly decreased triplet lifetimes. TF is a process on the basis of Dexter electron exchange.[109] It is shown in Figure 6.13 and Eq. 6.1. As the name suggests, Dexter

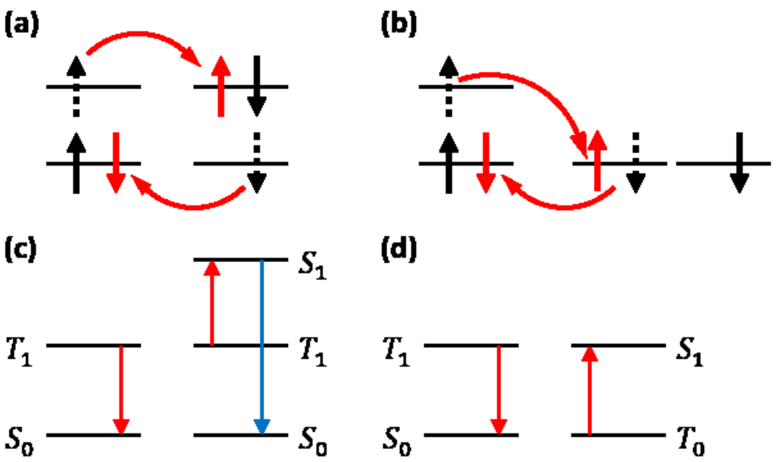

Figure 6.13: (a) and (b): Triplet fusion shown in MO representation. Dashed arrows denote electrons before their exchange; red arrows denote electron exchange. (c) and (d): TF shown in state representation (Jablonski diagrams). Red arrows denote electron exchange; blue arrow represents fluorescence. (a) and (c) show case for two singlet ground-state molecules. (b) and (d) show special case with oxygen as emitter.

electron exchange means, that molecules in close proximity can exchange electrons, given that their wave functions overlap, and that energy is conserved. TF is a specific case of this electron exchange between two molecules, each in a (excited) triplet state (T_1). The result of this exchange is that both molecules reach a singlet state (Figure 6.13a). Due to the conservation of energy, one molecule (the sensitizer) returns to the S_0, while the other (emitter) reaches the S_1 (Eq. 6.1).

$$T_1 + T_1 \rightarrow S_0 + S_1 \qquad \text{Eq. 6.1}$$

Evidently, this is only possible, if the energy of the singlet states is no larger than the energy of the two triplet states, as shown for a homo-fusion in Eq. 6.2 .

$$2E(T_1) \geq E(S_1) \qquad \text{Eq. 6.2}$$

TF is harnessed in photon upconversion, as two triplet excitons of smaller energy are converted to a singlet exciton of higher energy which is susceptible to fluorescence (Figure 6.13c). While this typically requires outstanding excited-state lifetimes or high exciton densities, neither is required when molecular oxygen takes the role of the emitter (Eq. 6.3).

$$T_1^{TPA} + T_0^{O_2} \rightarrow S_0^{TPA} + S_1^{O_2} \qquad \text{Eq. 6.3}$$

Since O2 is of a triplet ground state (T_0), it is freely available as exchange partner for both the TPA and DHC T_1. The exothermicity criterion is stated for the hetero fusion of T_1 of TPA and T_0 of O2 in Eq. 6.4. Note that $E_{O_2}(T_0) = 0$ by definition.

$$E_{TPA}(T_1) \geq E_{O_2}(S_1) \qquad \text{Eq. 6.4}$$

The energy required for generation of singlet oxygen ($E_{O_2}(S_1)$) is 0.97 eV.[110, 111] The electron exchange is shown in Figure 6.13b. Note that spin pairing energy cannot be represented in this MO diagram. The clearer representation for this case is the Jablonski diagram in Figure 6.13d. The fact that oxygen is of triplet ground state not only makes it widely available in solution, but also means that it can only function as emitter, but not as sensitizer in the Dexter-electron exchange. It is therefore an ideal quencher for the occurring T_1 states of TPA and DHC, bringing them both to their respective S_0 ground states. Furthermore, TF with molecular oxygen not only explains the shortened lifetimes of the two triplet species, but also the change of the relative amplitudes.

To elaborate this, first note that the similarities of the four spectral signatures is proof, that the molecules go through the exact same excited states with their characteristic spectral features. The amplitude of ESA bands in the TA signal is determined by the respective characteristic absorption spectrum (the SADS) and the concentration of the absorbing species. The absolute amplitude may also vary with pulse energy, spot-size and the overlap of pump and probe. However, all these parameters were kept as similar as experimentally possible (see similar amplitude of unaffected DADS mainly associated with TPA S_1 in Figure 6.7 and Figure 6.12). Furthermore, none of these parameters should affect the relative SADS amplitude, i.e., the ratios of the SADS of TPA T_1:TPA S_1, DHC T_1:TPA T_1 etc. Changes in these ratios therefore reflect changes in the concentration of the absorbing species – not its characteristic spectrum. Observe, that the amplitudes of the four main DADS for the degassed sample in Figure 6.7 are widely different than those of the ambient experiment (Figure 6.12). If a strictly sequential model was presumed for the ambient sample, as was done for the degassed sample, this would lead to similar distortions of the relative amplitude of the obtained SADS. However, as discussed above, SADS are a characteristic property of the partaking states and should not change significantly upon the mere inclusion of oxygen in the sample. Instead, the model needs to be changed, so that it presumes correct population traces, which give the same relative SADS amplitude as in the

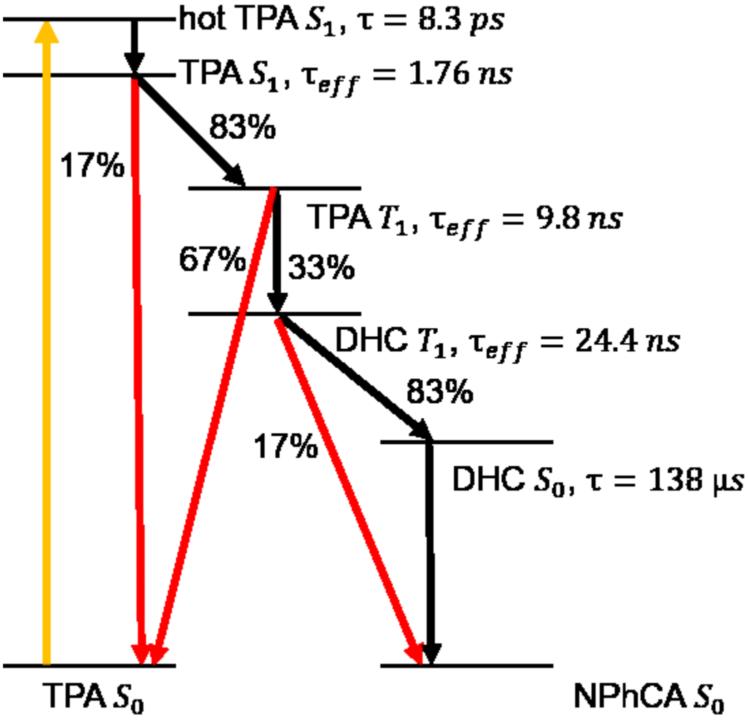

Figure 6.14: Model used in GTA on TPA in hexane (ambient). Yellow: Photoexcitation. Black: Sequential core model from degassed sample. Red: loss channels introduced to compensate for relative SADS amplitude. Since both TPA $S_0$and NPhCA S_0 are not observable within the experimental spectral range, decay to either of them is indistinguishable in the given experiment.

degassed case. To achieve this, branching parameters were introduced where necessary to compensate relative SADS amplitude. The resulting model with highlighted additional loss channels is depicted in Figure 6.14. The obtained SADS are given in Figure 6.15 and are in excellent agreement with those of the degassed sample shown in Figure 6.8. Note that the signal to noise ratio suffers from the small amplitude of the detected signal, which is amplified in the amplitude corrected SADS. All relaxation pathways identified in the following discussion are summarized at the end of it in Figure 6.16.

It is worthwhile to point out, that the largest branching parameter is introduced at the TPA T_1. While the ISC from the TPA S_1 to its T_1 is almost quantitative (83%), only a third of the TPA T_1 population undergoes cyclization towards the DHC T_1. This is in good qualitative agreement with the observed shortening of the TPA S_1 and T_1 lifetimes (2.54 ns to 1.76 ns and 31.5 ns to 9.8 ns, respectively). Following the assumption of an additional loss channels, the effective lifetime (τ_{eff}) observed under ambient conditions is a result of a combined decay of the unperturbed decay in the degassed sample (τ_{deg}) and an oxygen-related decay (τ_{O_2}). The three time constants of the parallel decay are in the relation given in Eq. 6.5.

$$\frac{1}{\tau_{eff}} = \frac{1}{\tau_{deg}} + \frac{1}{\tau_{O_2}} \qquad \text{Eq. } 6.5$$

Eq. 6.5 can be rearranged to determine the time constant of the oxygen-related decay:

$$\tau_{O_2} = \frac{\tau_{eff}\tau_{deg}}{\tau_{deg} - \tau_{eff}} \qquad \text{Eq. } 6.6$$

Using the time constants assigned to the individual processes, their respective yields Φ_i can be concluded, as given in Eq. 6.7.

$$\Phi_i = \frac{\frac{1}{\tau_i}}{\sum \frac{1}{\tau_i}} \qquad \text{Eq. } 6.7$$

The oxygen-related quenching time constant for the TPA S_1 and its yield are 5.73 ns and 31%, respectively. This is in small contrast to the 17% yield loss estimated from the SADS compensation and will be discussed later. The quenching of the TPA T_1 however, is much more drastic. The quenching time constant is 14.2 ns, yielding 69%, leaving 31% for the DHC T_1 formation. This is in excellent agreement with the 33% determined from the SADS amplitude compensation. The compensation of the DHC S_0 SADS requires introduction of a 17% branching from the DHC T_1. This suggests, fewer molecules form the zwitterionic DHC S_0 from the biradical DHC T_1. However, analyzing the time constants of this process, one might expect a much larger effect: From the reduction from 392 ns to 24.4 ns, one can infer a 26 ns time constant for the oxygen-related decay, resulting in merely 6% yield for the unperturbed decay. The fact that from the SADS amplitudes, 83% yield is obtained can therefore only be explained if there are two distinct interactions of the DHC T_1 with molecular oxygen. One of the interactions yields a species with no absorption signature in the detected wavelength range, possibly an adduct with oxygen on the route towards NPhCA – the observed

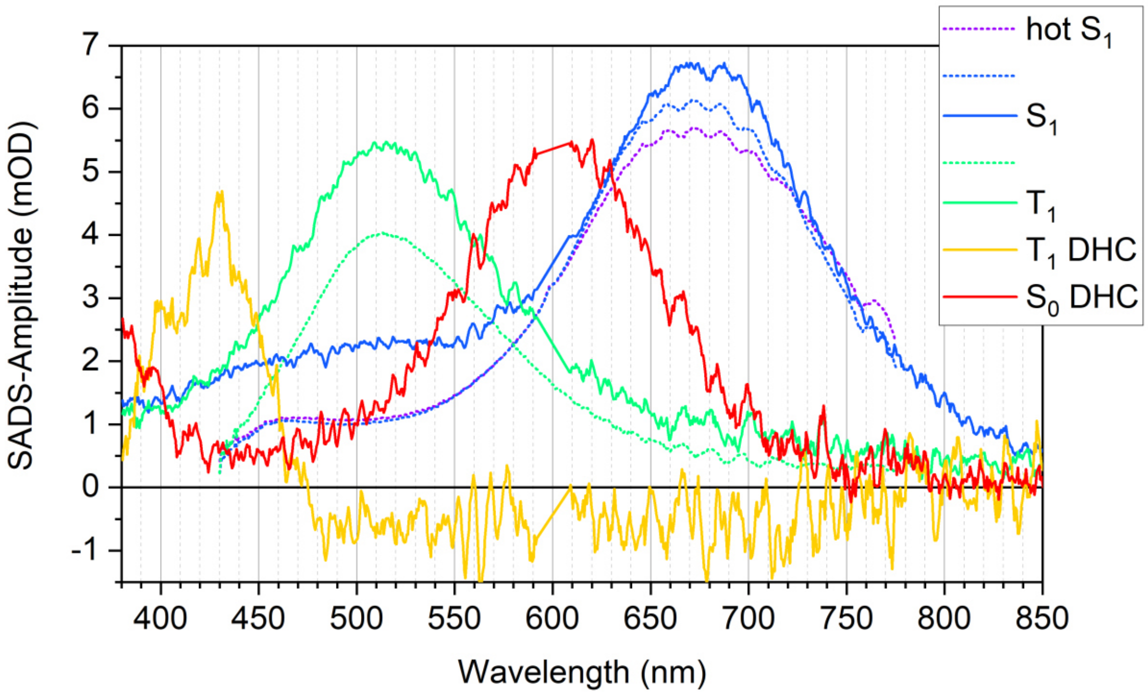

Figure 6.15: SADS obtained for sequential model to the TA-Data of TPA in hexane (ambient). Dotted: SADS from short delay data, solid: SADS from long delay data. Model (Figure 6.14) designed to replicate relative SADS amplitudes from Figure 6.8.

photoproduct. In effect, DHC requires elimination of the hydrogen atoms at the newly formed bridge heads (see Figure 6.9) to form the final photoproduct. It is likely that molecular oxygen in the solution can assist this reaction by hydrogen abstraction. This may contribute to the significantly more efficient formation of NPhCA in the presence of oxygen. The other interaction must yield DHC in its zwitterionic ground state DHC S_0 – precisely as is expected for TF from the DHC T_1. To separate these two distinct oxygen-related decay channels (τ_{add} and τ_{TTA}) using Eq. 6.7, two assumptions must be made: The first assumption is, that the total DHC S_0 yield via τ_{deg} and τ_{TTA} is 83%, as estimated from the SADS amplitudes. The second assumption is, that the effective oxygen-related decay time constant is the 26 ns determined from the lifetime shortening $\left(\frac{1}{\tau_{O_2}} = \frac{1}{\tau_{add}} + \frac{1}{\tau_{TTA}}\right)$. Based on these assumptions from Eq. 6.7 follows the Ansatz in Eq. 6.8.

$$\Phi_{deg} + \Phi_{TF} = 0.83 = \frac{\frac{1}{\tau_{deg}} + \frac{1}{\tau_{TTA}}}{\frac{1}{\tau_{deg}} + \frac{1}{\tau_{O_2}}} \qquad \text{Eq. 6.8}$$

Eq. 6.8 can be rearranged to determine the TF associated time constant (τ_{TF}, Eq. 6.9). Subsequently τ_{add} can be inferred from τ_{O_2} similar to Eq. 6.5 and Eq. 6.6.

$$\tau_{TF} = \frac{100\tau_{deg}\tau_{O_2}}{83\tau_{deg} - 17\tau_{O_2}} \qquad \text{Eq. 6.9}$$

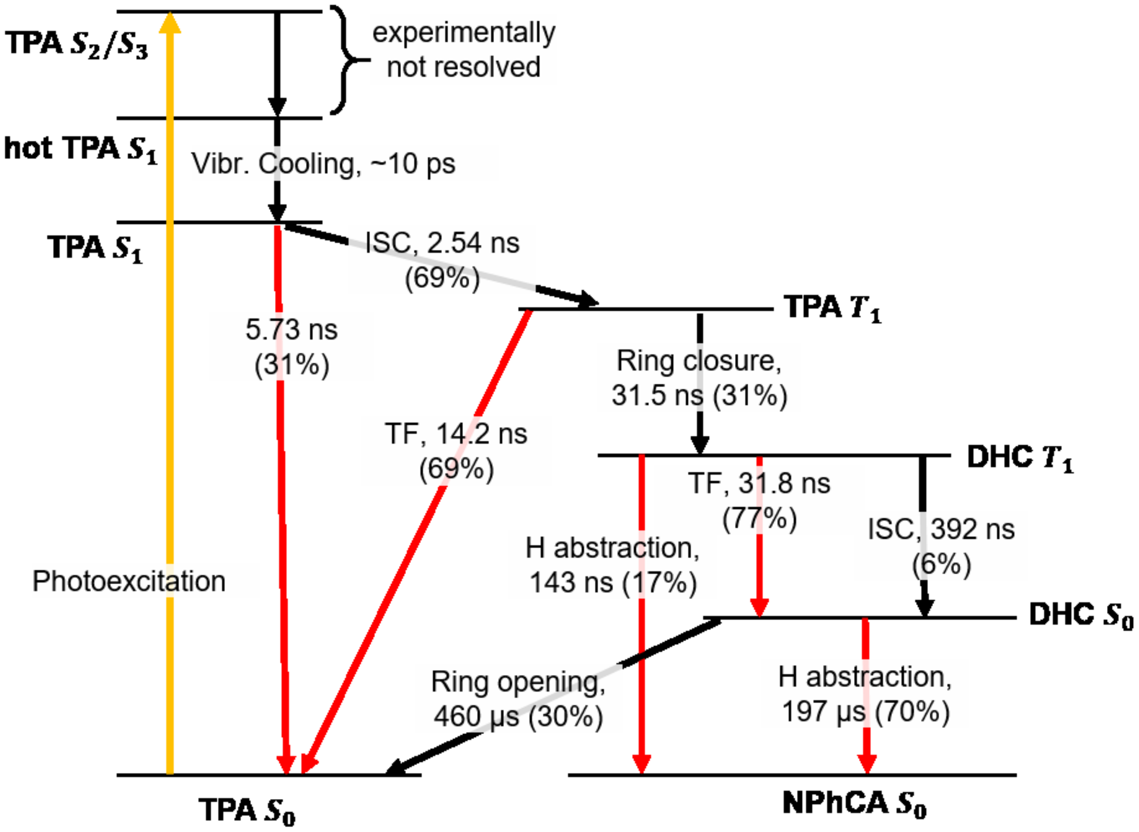

Figure 6.16: Jablonski diagram displaying the photophysics and photochemistry of TPA in hexane as identified by TA experiments under degassed and ambient conditions. Yellow: Photoexcitation. Black: Sequential model sufficient for degassed sample. Red: Oxygen-related decay channels.

The two time constants are quantified at 31.8 ns for TF and 143 ns for adduct formation and their respective yields are 77% and 17% as defined by the chosen Ansatz. TF with molecular oxygen is therefore the major loss channel of both triplet species: TF in the TPA T_1 returns it back to its S_0 ground state, effectively cutting the excited-state cascade short, while TF with the DHC T_1 significantly accelerates the formation of DHC S_0, which is also formed in the absence of O_2, but much more slowly.

Regarding DHC S_0, the effective lifetime of 138 µs is also drastically shorter than the unperturbed 460 µs decay. The oxygen-related decay can be quantified according to Eq. 6.6 at 197 µs. Considering the vanishing quantum yield of the NPhCA formation in the degassed sample, it is eligible to assume that the 460 µs decay leads to TPA S_0 almost quantitatively. In the ambient sample, this unproductive channel only accounts for 30% of the yield. Considering the greatly improved quantum yield of the NPhCA formation under ambient conditions, it is likely, that the remaining 70% of molecules decaying via an oxygen-related path, follow a productive channel. While the experimentally available delay range didn't allow observation of possible species following the DHC S_0 in the degassed sample, the accelerated decay principally enables this. However, Figure 6.6b clearly shows no absorption feature following the DHC S_0 band centered at 600 nm. There are two possible reasons for that: either the oxygen adduct shows no absorption within the observed spectral range, or it is short-lived and produces NPhCA via hydrogen abstraction faster than it is formed itself. Since NPhCA itself also has no absorption within the covered spectral range, both cases are indistinguishable given the recorded data. In summary, a quantum yield of

16% can be estimated for the NPhCA formation from the comparison of relative ESA amplitudes and time constants in the degassed and ambient sample. Remember, that the quantum yield in the degassed sample was considered to be zero, although the irradiation series did show minor conversion (Figure 6.3b). Even after one hour of irradiation the yield was approximately that of 10 minutes of irradiation of the ambient sample. This suggests roughly a factor of six between the overall quantum yield, in the ambient sample (16%) and that in the degassed sample (~2-3%). This is within the signal-to-noise ratio of the obtained TA data and can therefore be disregarded. Molecular oxygen in the solution therefore plays a fascinating double role: Firstly, it significantly hinders the formation of DHC as a key step for NPhCA formation. It does so mainly by TF with the TPA T_1, prematurely returning 69% of molecules back to their TPA S_0 ground state. Secondly, it greatly facilitates abstraction of the hydrogen atoms at the DHC bridge heads. As a result, instead of 2-3%, 75% of molecules that complete cyclization to DHC T_1 do go on to yield NPhCA. This second role outweighs the quenching significantly, leading to the improved quantum yield observed for the photoproduct in the irradiation series.

The results described above support the findings of Helmut Görner and Sergio Bonesi.[105, 106, 112] They identify molecular oxygen in the above mentioned double role as strong quencher of the TPA T_1 and as hydrogen abstraction agent, resulting in a significantly improved product formation with oxygen in the solution. To the best of our knowledge, the characteristic spectrum of the TPA S_1 has been measured for the first time in the present work. The spectra shown in the publications of Görner and Bonesi for TPA T_1, DHC T_1 and DHC S_0 are in excellent agreement with those shown above, supporting the given assignment. The absence of side products in the degassed sample has been attributed to the changed solvent (hexane instead of acetonitrile). However, there are some minor discrepancies with the reports of Bonesi et al. regarding the interaction of molecular oxygen with the DHC T_1. In their publication from 2014 they argue on the basis of DFT calculations, that only the TPA T_1 - TPA S_0 gap is sufficient to support TF with molecular oxygen.[112] According to the calculations shown there, the DHC T_1 - DHC S_0 gap is insufficient to support formation of singlet oxygen. Nevertheless, the 24.4 ns DADS in the ambient sample (Figure 6.12) very clearly shows direct transition from DHC T_1 to DHC S_0, as was observed in the degassed sample, but accelerated by more than factor 10. While the transition is not complete (17% lost, most likely forming NPhCA via an oxygen-adduct) it is still by far the dominating DHC T_1 loss-channel. This is experimental proof of an oxygen-based DHC T_1 - DHC S_0 transfer mechanism which is more than tenfold more efficient than regular ISC (31.8 ns vs 392 ns, Figure 6.16). Hypothetically speaking, oxygen might catalyze this transition by adduct formation and subsequent elimination of the added oxygen. However, these processes would need to occur faster than the observed 24.4 ns DHC T_1 decay, otherwise they should be reflected in the TA data. TF is therefore considered the most likely explanation for the oxygen-based acceleration of the DHC T_1 - DHC S_0 transition.

Furthermore, 2014 Bonesi et al. put forward a mechanism in which molecular oxygen adds to the diradical DHC T_1, leading to subsequent elimination of hydrogen peroxide and formation of NPhCA.[112] In 2021, however, addition of O_2 is proposed in the zwitterionic DHC S_0.[106] In the present work, both DHC T_1 and S_0 show accelerated decay rates in the presence of oxygen forming species that show no absorption features in the detected spectral range (17% from DHC T_1 and 70% from DHC S_0). These are most likely the oxygen adducts formulated by Bonesi at al., suggesting that routes towards hydrogen abstraction are available from both states. As the spectrum, and in turn nature and lifetime of the oxygen adduct species could not be recorded in the given spectral range, they are omitted in Figure 6.16. Both DHC T_1 and S_0 are shown to directly yield NPhCA as final photoproduct.

Finally, the accelerated decay of the TPA S_1 in the ambient sample is regarded (1.76 ns instead of 2.54 ns). The 17% yield loss from the SADS compensation suggest a quenching mechanism returning the TPA S_1 to its S_0 ground state. This does not fully explain the 31% accelerated S_1 decay, suggesting also the S_1-T_1-transition is enhanced by molecular oxygen. For a possible explanation reconsider, that triplet fusion (TF) with molecular oxygen poses an efficient loss channel for the TPA T_1 state, because it is both spin-allowed and energetically feasible. As elaborated above, TF is characterized by the consumption of two independent triplet excitons and the generation of one singlet exciton. Obviously, the TPA S_1 state cannot fall victim to TF, but the reverse process, called singlet fission (SF). As the reverse process of TF, singlet fission is the spin-allowed generation of two triplet excitons, from one singlet exciton (Eq. 6.10).[113-115]

$$S_0 + S_1 \rightarrow T_1 + T_1 \qquad \text{Eq. 6.10}$$

Accordingly, the exothermicity criterion for triplet fusion is reversed for singlet fission (Eq. 6.11).

$$E(S_1) \geq 2E(T_1) \qquad \text{Eq. 6.11}$$

Singlet fission is typically observed between chromophores fixed in close proximity, either in films or in as chromophore dimers or oligomers in solution.[116-118] Neither of these conditions are fulfilled in the presented experiments. In solution, diffusion controlled singlet fission has also been observed, although typically at very high concentrations.[119-121] In dilute solutions the S_1 lifetime τ_{S_1} is shorter than the diffusion time $\tau_{SF,diff}$, so that the singlet state decays more efficiently by other processes. To demonstrate that the experimental TPA concentration of 210 µM is insufficient to support diffusion-controlled singlet fission, let us estimate the diffusion time and compare it to the S_1 lifetimes reported above. Assuming that every TPA S_1-TPA S_0 encounter leads to singlet fission, and approximating that the concentration of TPA S_0 is not changed by the pump, the diffusion-controlled rate of singlet fission ($k_{SF,diff}$) is given by Eq. 6.12:

$$k_{SF,diff} = k_{diff} * [TPA] \qquad \text{Eq. 6.12}$$

Here k_{diff} is the diffusion constant, which for equally sized particles is determined by the temperature T and the solvent's viscosity η, only (Eq. 6.13)[122].

$$k_{diff} = \frac{8RT}{3\eta} \qquad \text{Eq. 6.13}$$

With the viscosity of n-hexane (0.3 mPa*s) and 294 K temperature, we find $k_{diff} = 2.17 * 10^{10} M^{-1} s^{-1}$. Considering the experimental TPA concentration of 210 µM, this yields a diffusion time constant $\tau_{SF,diff} = k_{SF,diff}^{-1}$ of 220 ns. Even using most beneficial assumptions, the TPA S_1 lifetimes (degassed 2.54 ns and ambient 1.76 ns) do not allow for effective diffusion-controlled singlet fission.

However, Wollscheid et al. recently reported oxygen-catalyzed sequential singlet fission.[123] There, the singlet exciton on acene derivates promoted triplet ground state oxygen to its singlet excited state while falling back to its own T_1 state (Eq. 6.14). Subsequently, the singlet oxygen promoted another chromophore from the S_0 ground state to its T_1 state, completing the singlet fission process (Eq. 6.15).

$$S_1^{acene} + T_0^{O_2} \rightarrow T_1^{acene} + S_1^{O_2} \qquad \text{Eq. 6.14}$$

$$S_0^{acene} + S_1^{O_2} \rightarrow T_1^{acene} + T_0^{O_2} \qquad \text{Eq. 6.15}$$

This raises the question, if similar processes may be behind the accelerated S_1 decay under ambient conditions. To contemplate this, let us consider the energetic requirements. Since oxygen-catalyzed singlet fission is a two-step process, the energy criterion formulated for the one-step process also becomes two distinct criteria (Eq. 6.16 and Eq. 6.17).

$$E_{TPA}(S_1) - E_{TPA}(T_1) \geq E_{O_2}(S_1) \qquad \text{Eq. 6.16}$$

$$E_{O_2}(S_1) \geq E_{TPA}(T_1) \qquad \text{Eq. 6.17}$$

Since the molecules have time to adopt the equilibrium geometry within the TPA S_1, $E_{TPA}(S_1)$ and $E_{TPA}(T_1)$ in Eq. 6.16 are with respect to the TPA S_0 at the equilibrium geometry of the TPA S_1. Unfortunately, these exact numbers are not available at the time of publishing. However, the vertical energy difference between the TPA S_0 minimum and the S_1 PES is 4.2 eV, according to the calculations of Letao Huang. This will serve as rough (over-)estimate for $E_{TPA}(S_1)$. For clarification of the difference see Figure 6.17. With $E_{O_2}(S_1)$=0.97 eV, it follows, that the exothermicity criterion for the

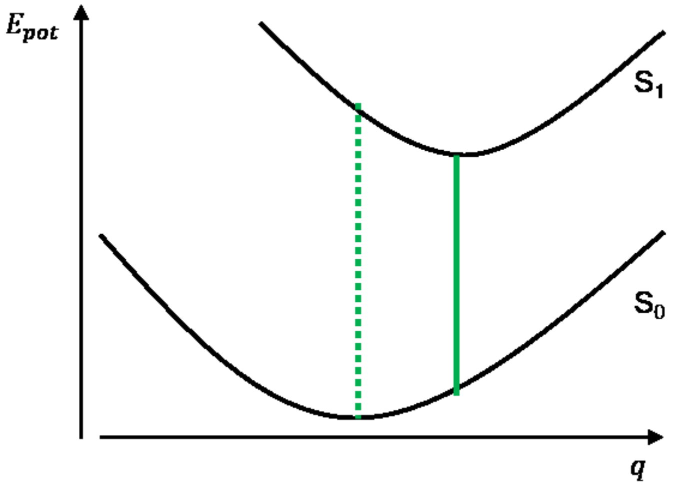

Figure 6.17: Schematic representation of potential energy surfaces of TPA S_0 and S_1 to illustrate the discussed energies. Green dotted line: 4.2 eV form S_0 minimum to S_1 PES. Green solid line: Energy available to drive initial step of oxygen catalyzed singlet fission.

TPA T_1 at the S_1 equilibrium energy is $E_{TPA}(T_1)$<3.23 eV. From the efficient TPA T_1 quenching via TF with molecular oxygen, we can infer, that $E(T_1)$≥0.97eV (see Eq. 6.4).[110] This lower boundary for the TPA T_1 energy does not contradict the exothermicity criterion in Eq. 6.16, but suggests, that the first step of oxygen-catalyzed singlet fission indeed accelerates the TPA S_1-T_1 transition.

Regarding Eq. 6.17, it is evident, that this is the inverse argument for triplet fusion with molecular oxygen (Eq. 6.4). As triplet fusion occurs efficiently, $E_{O_2}(S_1)$ must be smaller than $E_{TPA}(T_1)$, making the generation of TPA T_1 from singlet oxygen impossible. Completion of the oxygen-catalyzed singlet fission is therefore not feasible, which agrees with the 17% decreased S_1-T_1 yield observed in the ambient sample.

With a thorough understanding of the photophysics and photochemistry of the paradigmatic TPA in hexane, the next section will focus on its dimethylmethylene bridged derivate: DTPA.

6.2 Photophysics of DTPA in hexane

In the last section the photoinduced cyclization of TPA to NPhCA was investigated in depth. In this section, a similar sample is investigated, with the key difference, that the ortho positions, between which the carbazole-5-ring is formed are already connected via dimethylmethylene (DMM) bridges. These bridges enforce planarity of all phenyl rings in the resulting DTPA, which has strong implications for the photostability, as the irradiation series in Figure 6.18 show. All spectra recorded after irradiation time of up to one hour are perfectly congruent. Unlike TPA, there is no formation of a distinct photoproduct observable, even after one hour of irradiation. Neither is any depletion of the absorption found as result of unspecific photobleaching, both under ambient and degassed conditions. There are many possible reasons, why the DMM bridges circumvent formation of a carbazole-like photoproduct. Firstly, the three-membered ring that would result from the C-C σ-bond would be very strained. This puts not only a thermodynamic penalty on the final product, but also constitutes a major kinetic barrier, since molecule need to deform against this strain to form the σ-bond. Secondly, since H-abstraction is not possible at the bridge heads, they would remain sp^3-hybridized, meaning recovery of the adjacent aromatic systems is not possible. Thirdly, the planarization negates the preorientation of the p-orbitals towards a σ-bond between neighboring phenyl rings, as is the case for TPA (see Figure 6.10a).

In order to find out how the planarization affects the excited-state dynamics and at what point the excited-state dynamics of TPA and DTPA diverge, transient absorption spectroscopy was employed. The two datasets of the short and long delay experiments are shown in Figure 6.19a and b, respectively. Both are comprised of two positive features. A first, extremely broad ESA band covers virtually the complete observed spectral range with a maximum just on or outside the red end of the spectra at 850 nm. It stretches all across the visible range with decreasing amplitude and decaying around 5 ns close to the delay limit of the short delay experiment. The simultaneous rise of the second band is therefore just visible in the short delay data (Figure 6.19a). It shows an ESA band in the range of 440 – 560 nm, with maximum at 510 nm. In the long delay dataset, the decay of this band is found at approximately 10 µs. Importantly, there is no transition to another species absorbing in the detected spectral range, suggesting the DTPA molecules return to the ground state. These observations are also reflected in the DADS (Figure 6.19c) obtained by simultaneous

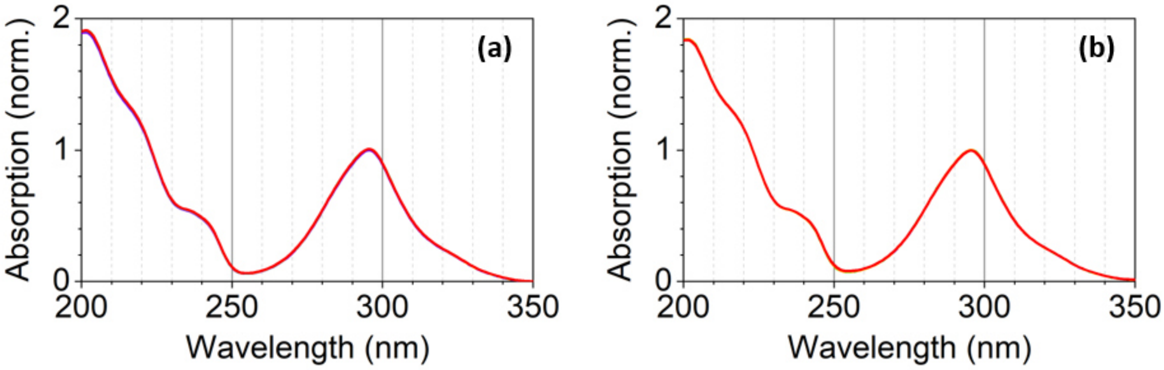

Figure 6.18: (a) and (b): Absorption spectra normalized to lowest maximum. Irradiation series of DTPA in hexane (a) under ambient and (b) degassed conditions. Irradiation duration from purple to red: 0, 1, 2, 5, 10, 15, 30 and 60 minutes. The samples were irradiated at 0.5 mW of the 300 nm pump spectrum given in Figure 6.2e.

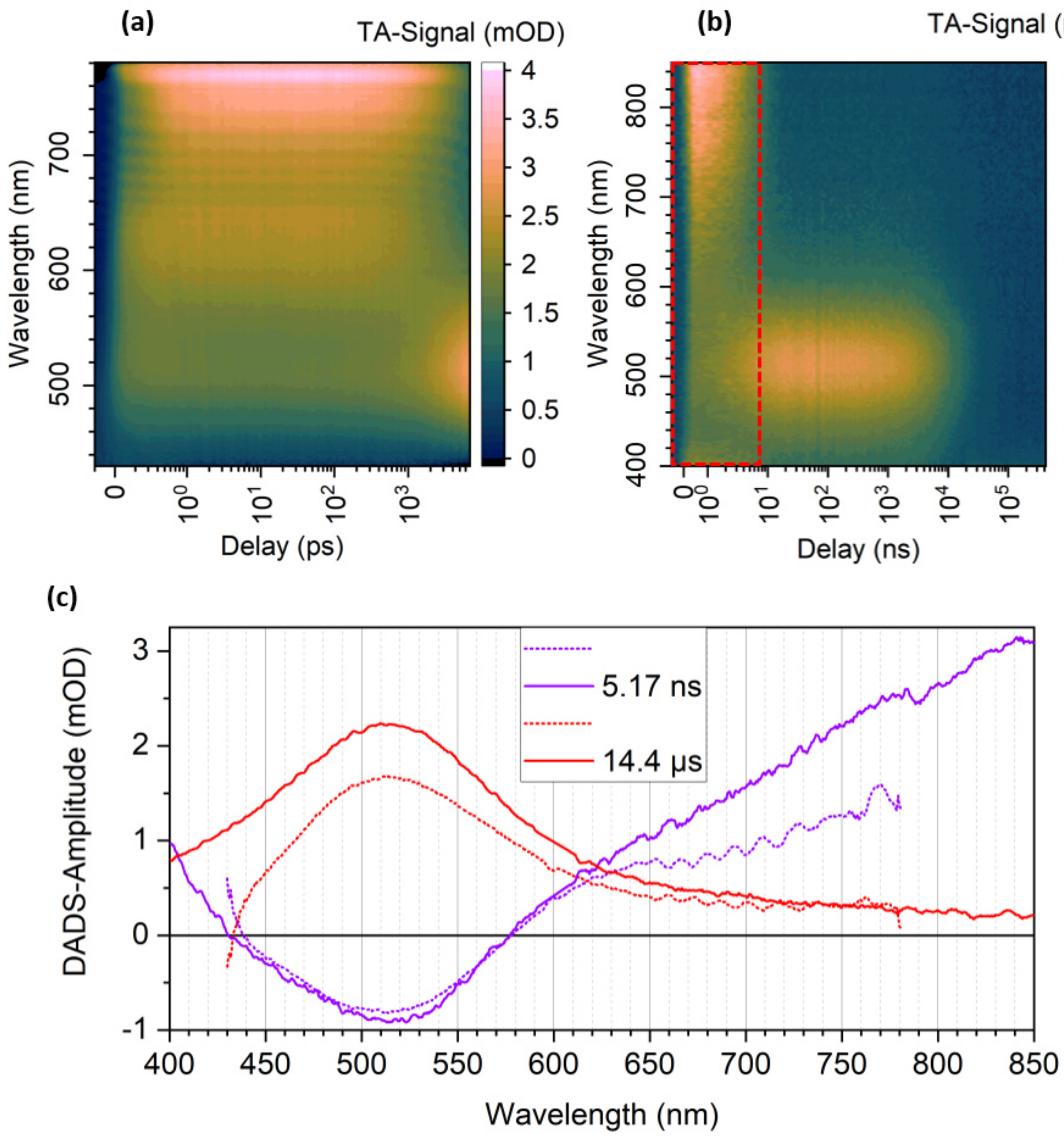

Figure 6.19: (a) and (b): Two-dimensional representation of transient absorption data of degassed sample of DTPA in hexane. (a) Short delay experiment. (b) Long delay experiment. Marked in red is the delay range covered in the short delay experiment. (c): DADS obtained from simultaneous global analysis of the two TA datasets. Dotted: DADS from short delay data, solid: DADS from long delay data.

global analysis of the two datasets. The DADS of the short and long delay data are in excellent agreement. Minor deviations across the spectral dimension may result from spatial inhomogeneities in the white light probe pulses. The first DADS (time constant 5.17 ns) includes the decay of the extremely broad first transient absorption band as well as the rise of the narrower band around 510 nm. The second DADS with 14.4 µs time constant describes the uniform decay of this excited-state absorption band and reveals a tail on the red side of its maximum stretching to 800 nm, which isn't discernable in the 2D-representation. A first comparison to the excited-state dynamics in the propeller shaped TPA makes two distinctions obvious. Firstly, the dynamics of DTPA include only two distinct species, unlike the four observable for TPA. Secondly, the decay times of the ESA bands are significantly longer for DTPA than the first two species of TPA. The simultaneous decay of the first and rise of the second ESA band

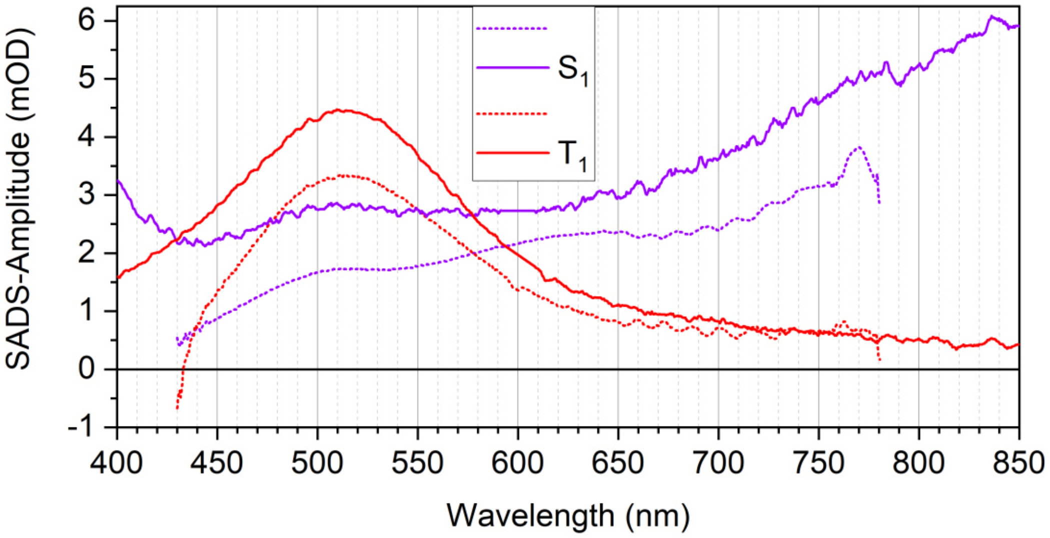

Figure 6.20: SADS obtained for sequential model to the TA-Data of DTPA in hexane (degassed). Dotted: SADS from short delay data, solid: SADS from long delay data.

included in the 5.17 ns DADS clearly requires a sequential model for proper identification of the individual SADS. These SADS are depicted in Figure 6.20. Comparison with the first two SADS obtained for TPA (Figure 6.8) shows striking similarities, especially for the second SADS. Like for the TPA S_1, the first SADS is extremely broad with a long tail in the blue spectral region. Unlike the TPA S_1, the absorption maximum is red-shifted to 850 nm or above. Such a red-shift may be expected considering the improved π-conjugation and consequently delocalization of the MOs participating in the π-π*-transition. The second SADS however is in excellent agreement with that of the TPA T_1: both have an absorption maximum at 510 nm and feature a long tail on the red side, stretching to 800 nm. These parallels suggest an assignment analogously to TPA of SADS 1 and 2 to the DTPA S_1 and T_1, respectively. This assignment is corroborated by the quantum chemical calculations of Letao Huang. His TDDFT calculations (for details please refer to section 0) predict multiple transitions in the visible range for the DTPA S_1 at 445 nm, 550 nm, 620 nm and 740 nm, of which the first is the least intense, and the last is the most intense. This agrees with the observed, very broad ESA band, although individual bands cannot be discerned in the SADS. However, similar to TPA, the transitions of significant oscillator strength from S_0 ground state of DTPA are not to the S_1, but rather S_3 and S_4. It is therefore inferred that the photoexcitation to the TPA S_3/S_4 is followed by ultrafast relaxation to the lowest singlet excited state – the TPA S_1. Since there is no evidence of this process in the TA data, it must occur within the ~100 fs IRF of the short delay experiment. For the DTPA T_1, theory predicts two weak but close transitions at 500 nm and 540 nm, matching the second SADS very well. Furthermore, the lowest ground-state absorption maximum is due to optically bright transitions to the S_2 and S_3, as is the case for TPA. It can therefore be inferred that the optically bright transition to the S_2 and S_3 are followed by ultrafast relaxation (within experimental IRF) to the S_1. Subsequent ISC (5.17 ns) yields the T_1, which lives for 14.4 µs, before the molecular system returns to the ground state.

Let us now recapitulate, what changes the introduction of the DMM bridges constitute for the excited-state dynamics. The forced planarization results in a red-shifted S_1 absorption, as well as significantly prolonged lifetime: 5.17 ns instead of 2.54 ns. Possibly, the rigidity introduced by the crosslinks between the phenyl groups impedes distortions towards the geometry required for the ISC. Although the spectral signature of the TPA and DTPA T_1 are remarkably similar, their lifetime and decay channel are hugely different. The DMM-bridges increase the T_1 lifetime from 31.5 ns to 14.4µs by factor 450 and from the lack of subsequent ESA signals, it can be concluded, that cyclization similar to TPA does not occur. The fact that not even transient cyclization is observed (DHC from TPA) and instead, the lifetime of the T_1 is increased, suggests, that there is a significant barrier towards σ-bond formation introduced by the DMM bridges. This barrier results from two distinct effects: firstly, the increased rigidity puts a big strain especially on deformations that include the approach of ortho positions of

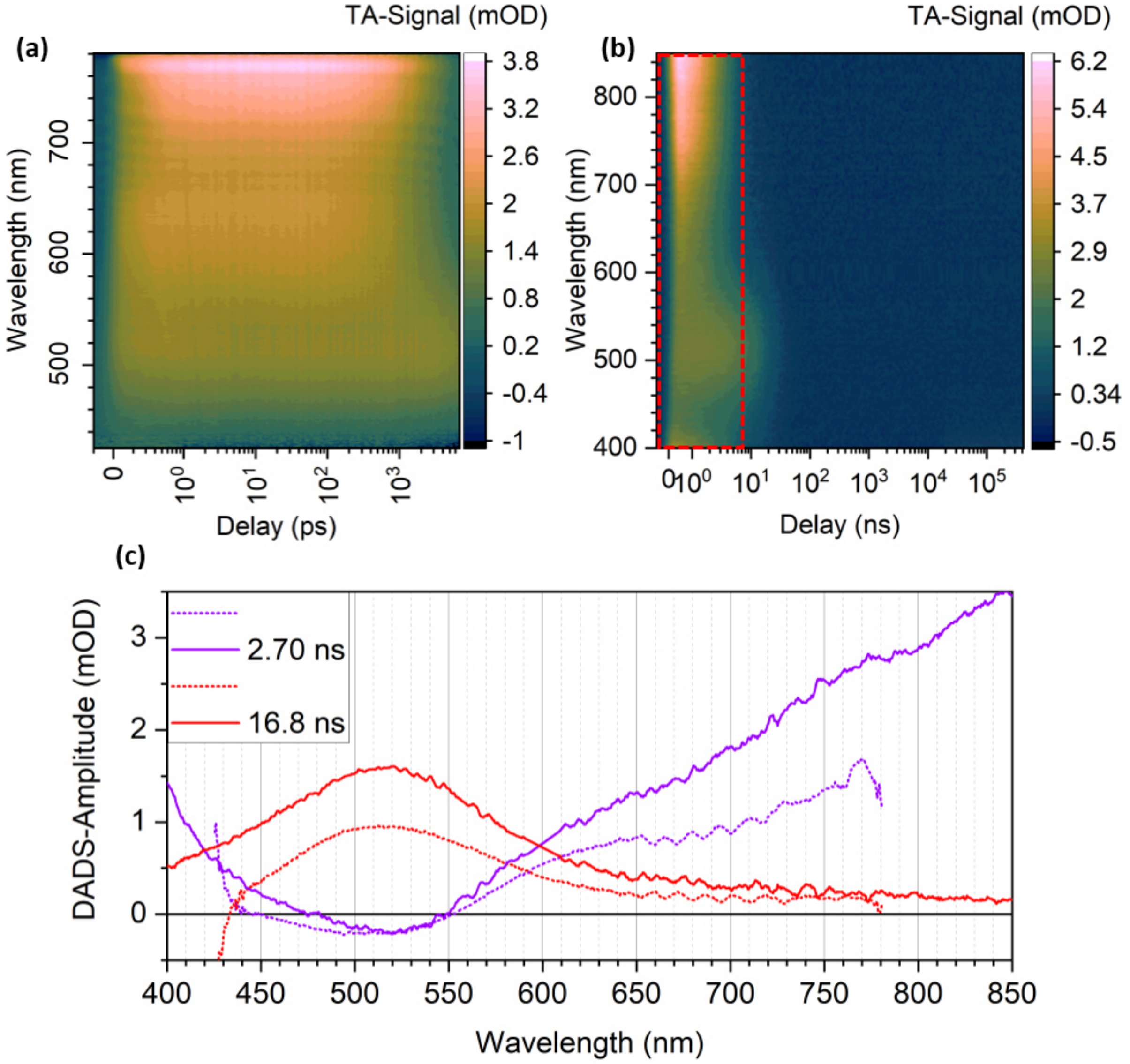

Figure 6.21: (a) and (b): Two-dimensional representation of transient absorption data of ambient sample of DTPA in hexane. (a) Short delay experiment. (b) Long delay experiment. Marked in red is the delay range covered in the short delay experiment. (c): DADS obtained from simultaneous global analysis of the two TA datasets. Dotted: DADS from short delay data, solid: DADS from long delay data.

neighboring phenyl rings. Secondly, the planarity enforced by the DMM bridges leads to parallelized p-orbitals at all phenyl rings. Preorientation of the p-orbitals towards formation of a new σ-bond is therefore circumvented. The combination of these two effects results in the complete obstruction of cyclization. The greatly improved rigidity may also contribute to the significantly increased T_1 lifetime, as it impedes structural flexibility which may be required to enable ISC back to the S_0.

As is shown in Figure 6.18a, the presence of oxygen does not enable photoinduced cyclization. In order to investigate, if oxygen affects the excited-state dynamics at all, TA experiments were also conducted under ambient sample conditions. The results are shown in Figure 6.21a and b. At first glance, the similarities of the degassed and ambient sample, especially in the short delay data are striking (Figure 6.19a and Figure 6.21a). There is the same first ESA band with its maximum at or beyond 850 nm and the extensive shoulder on the blue side, across all the visible region. Furthermore, its decay around three nanoseconds and the associated rise of another ESA band, centered around 500 nm is congruent with the degassed sample data. Consistently, the short delay region in the long delay dataset agrees with the degassed sample data (Figure 6.21b, $\tau \leq 10$ ns). However, there is a stark contrast in the temporal behavior of the second species. While it stretches far into the microsecond range under degassed conditions, it fully decays within 50 ns under ambient conditions. Both the similarities and the accelerated decay are also corroborated by the global analysis results (Figure 6.21c). The DADS are in excellent agreement with those shown in Figure 6.19c, except for the relative amplitude of the first and the second DADS and the determined time constants. While the first DADS's amplitude is reproduced within the experimental precision, the second DADS is approximately one fourth smaller than under degassed conditions. Together with the significantly shortened first time constant (5.17 ns to 2.70 ns) this suggests an additional decay channel for the first species. While the decay associated to the first DADS occurs approximately twice as

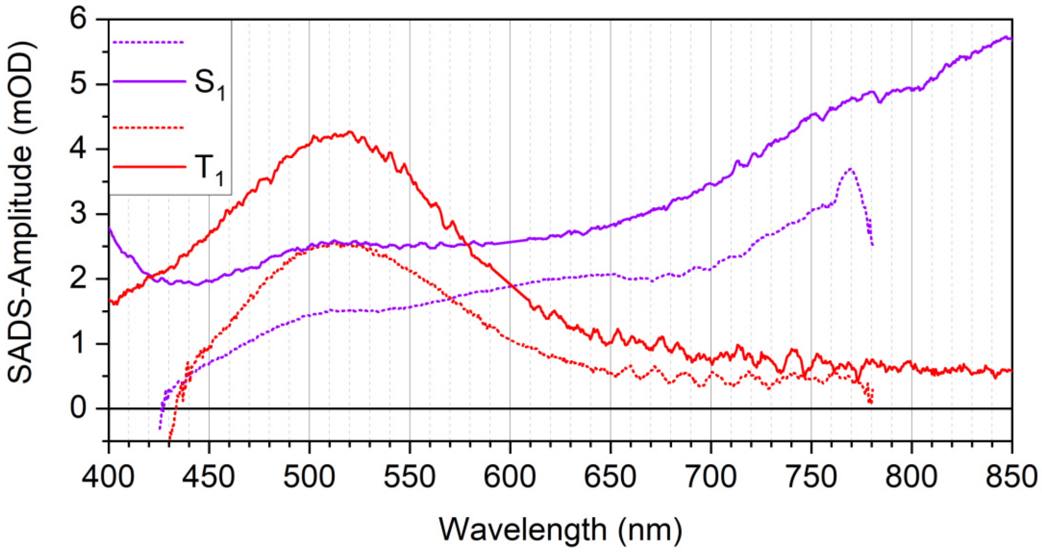

Figure 6.22: SADS obtained for sequential model to the TA-Data of DTPA in hexane (ambient). Dotted: SADS from short delay data, solid: SADS from long delay data. Model is sequential with additional loss-channel for S_1 to replicate relative SADS amplitudes from Figure 6.20.

fast, the acceleration of the second decay is even more significant. The 14.4 μs time constant under degassed conditions is depleted to one over 850 to just 16.8 ns.

Based on the excellent agreement of the DADS under degassed and ambient conditions, the two ESA bands are assigned to the DTPA S_1 and T_1, analogously. Presumption of the same sequential base model with additional loss channel (37%) for the S_1 to compensate the relative T_1 amplitude yields the SADS shown in Figure 6.22. Retrieval of the time-constants and yields of the oxygen-related loss channels following Eq. 6.6 and Eq. 6.7 gives 5.65 ns (48%) for the S_1 and 16.8 ns (quantitative) for the T_1 loss channels. Note that the T_1 loss channel acts on the same time scale as the TF observed in TPA and DHC (14.2 ns and 31.8 ns, respectively). This suggests that diffusion limited TF is also the main loss channel of the DTPA T_1. The resulting model is shown in Figure 6.23.

In summary, the increased rigidity through introduction of DMM bridges hinders structural fluctuations which convey radiationless transitions like ISC, thereby greatly increasing the excited-state lifetimes of DTPA with respect to those of TPA. Furthermore, it prevents the photoinduced cyclization to carbazole-like products, thereby greatly improving the photostability. Unlike with TPA, no transient cyclization is observed in the TA experiments. It can therefore be inferred that a kinetic barrier, rather than the energetically unsuitable hypothetical product (loss of aromaticity, strained three-membered ring) circumvents the photochemistry. This barrier is achieved by enforcing planarity, which circumvents preorientation of the partaking p-orbitals at neighboring phenyl rings. Furthermore, deformation of the molecular backbone towards formation of the new C-C σ-bond is hindered through the strain of

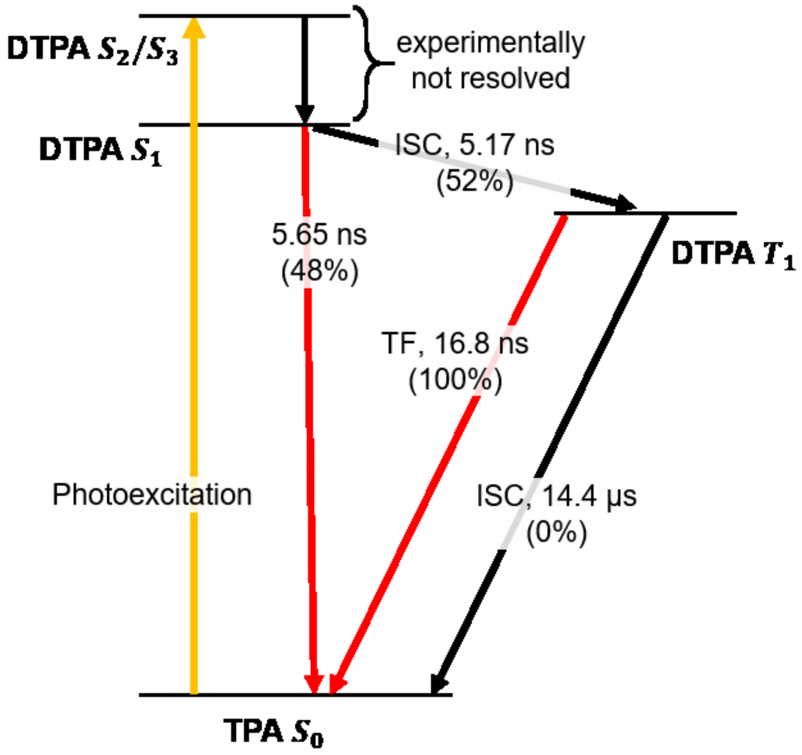

Figure 6.23: Jablonski diagram displaying the photophysics and photochemistry of DTPA in hexane as identified by TA experiments under degassed and ambient conditions. Yellow: Photoexcitation. Black: Sequential model sufficient for degassed sample. Red: Oxygen-related decay channels.

the C_{Ph}-C_{DMM}-C_{Ph} angle. The obstruction of the ring formation increases the DTPA T_1 lifetime by factor 450 from 31.5 ns to 14.4 µs, with respect to TPA. However, molecular oxygen in the solution plays a remarkably similar role for DTPA as for TPA. While hydrogen abstraction does not take place, TF drastically quenches the triplet state, reducing its lifetime from 14.4 µs to 16.8 ns.

The paradigmatic TPA and the derived DTPA were investigated in hexane to examine, how their inherent photophysical and –chemical properties are tuned by the propeller shape, the introduction of the dimethylmethylene bridges and the presence of oxygen. In the next section, one more dimension will be added to this experimental coordinate system: the solvent.

6.3 Photochemical reactivity of TPA and DTPA in chloroform

The photophysics and –chemistry of TPA and DTPA were examined separately in the previous two sections, because there were significant differences introduced by the dimethylmethylene bridges. Since the photoinduced processes of TPA and DTPA in chloroform are qualitatively identical and there are merely small quantitative differences, they will be regarded together in this section.

Chloroform is not only significantly more polar than hexane (1.15 D and 0.08 D, respectively), but also reportedly able to accept electrons after photoexcitation of TPA, which hexane is not.[124, 125] A first drastic consequence of the solvent change is apparent in Figure 6.24, showing the irradiation series of TPA and DTPA in chloroform under degassed and ambient conditions. Note that absorption spectra cannot be interpreted reliably at wavelengths smaller than 250 nm, due to the onset of the solvent's absorption. Both molecules form significant amounts of a photoproduct, which is indicated by the decay of the original absorption band at 300 nm and the simultaneous rise of another absorption band at longer wavelengths. As shown by the closely spaced orange and red spectra, the conversion is almost complete after 30 minutes of irradiation, already. This means the quantum yield for this photochemical reaction is significantly higher than the cyclization towards the carbazole in hexane. The red-shifted absorption band is indicative of an expanded π-system. For TPA (Figure 6.24a and b), the additional absorption band rises at 360 nm, for DTPA it is more red-shifted to 390 nm. This suggests, that both molecules form similar photoproducts with an expanded π-system and that the expansion is larger for

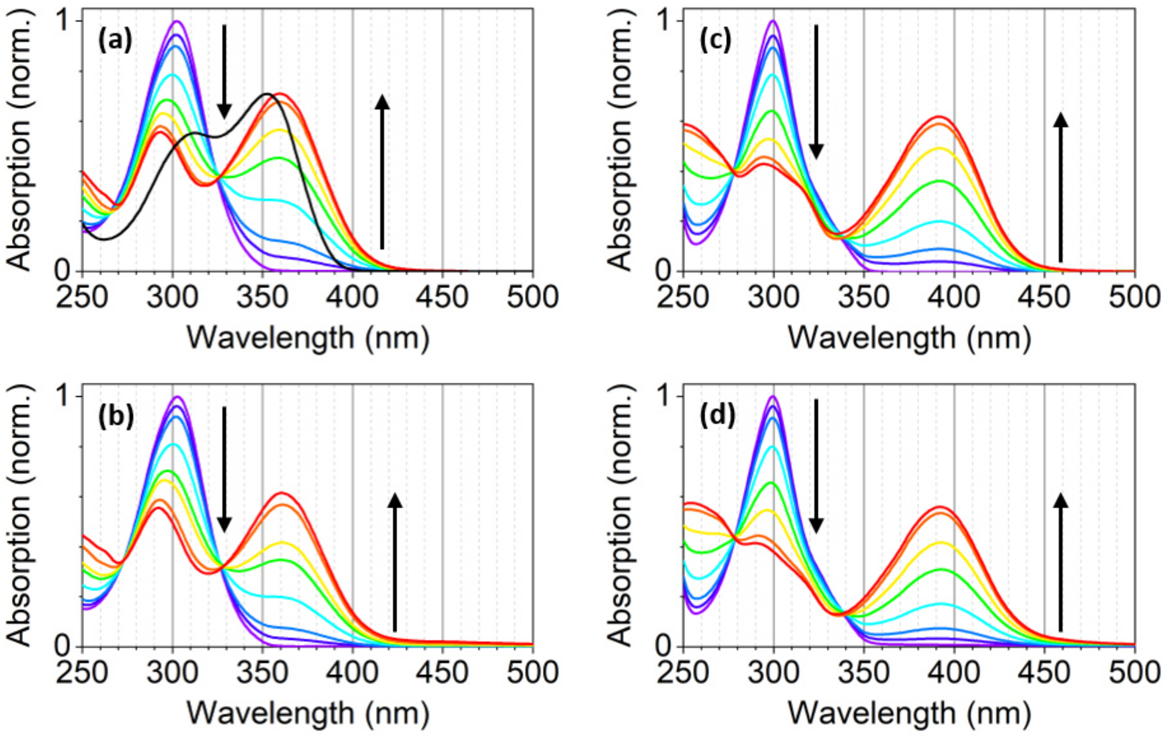

Figure 6.24: Irradiation series of TPA (left) and DTPA (right) in chloroform under degassed (top) and ambient (bottom) conditions. Irradiation duration from purple to red: 0, 1, 2, 5, 10, 15, 30 and 60 minutes. The samples were irradiated at 0.5 mW of the 300 nm pump spectrum given in Figure 6.2e. Absorption spectra normalized to lowest maximum. Black line in (a) is the absorption spectrum of the TPA dimer tetraphenylbenzidine (TPB).

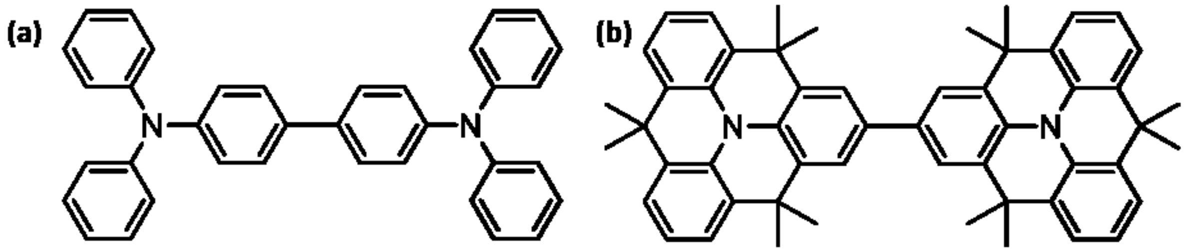

Figure 6.25: Dimers as photoproducts of TPA and DTPA in chloroform: (a) N,N,N',N'-Tetraphenylbenzidine (TPB) (b) 4,4,4',4',8,8,8',8',12,12,12',12'-dodecamethyl-8,8',12,12'-tetrahydro-4H,4'H-2,2'-bibenz[9,1]quinolizino[3,4,5,6,7-defg]acridine. For simplicities sake, (b) will be referred to as DTPA-dimer.

DTPA than for TPA. All these observations can be explained considering dimer formation, as will be elaborate in the following paragraph.

Supposing formation of a C-C σ-bond between the para positions of two TPA / DTPA monomers yields benzidine-like dimers (Figure 6.25). Although a σ-bond separates the monomer units, the neighboring carbon atoms are both sp^2 hybridized, resulting in an expanded π-system. The enforced planarity of DTPA improves conjugation of all six phenyl rings, leading to an even larger π-system and therefore explaining the larger red-shift. This explanation is supported by both experimental and theoretical determination of the respective dimer absorption spectrum. For the commercially unavailable DTPA-dimer, TD-DFT calculations conducted by Letao Huang also predict a double peak at 276 nm and 324 nm. While the absolute band position is significantly red-shifted in the spectra of the photoproduct, the predicted difference of 0.66 eV is close to the experimentally observed 0.95 eV. The absorption spectrum of N,N,N',N'-tetraphenylbenzidine (TPB), the TPA dimer, is given as reference in Figure 6.24a. It consists of a double band at 310 nm and 350 nm, similar to that of the photoproduct obtained by the irradiation series. Although the general position and shape of the spectra agree very well, the double peak of the photoproduct are clearly more separated. This broadening is attributed to further chemical modifications occurring after the initial electron transfer. The photo-oxidation mechanism in chloroform under ambient conditions proposed by Richtol et al. involves several radical species, including $CHCl_2^{\bullet}$, $CHCl_2O_2^{\bullet}$, $ClO^{\bullet}$ and $Cl^{\bullet}$. Given the formation of these reactive species alongside the dimer within the volume of the pump laser focus point, side products can be expected, leading to the broadened absorption bands. Indeed, indication for an involvement of oxygen in this mechanism can be found when comparing the irradiation series in degassed and ambient samples. Both the absorption spectra of the irradiated TPA and DTPA show small, yet significant tails on the red side of the newly formed absorption band. In the degassed sample series, there are no such tails, suggesting oxygen contributes to a larger variety of photoproducts being formed. Furthermore, the close, but distinct missing of isosbestic points (TPA: 272 nm, 328 nm; DTPA: 278 nm, 338 nm) supports the interpretation of a dominant, but not quite quantitative photoproduct, even under degassed conditions.

In order to understand the steps involved in the formation of the photoproduct, TA experiments were conducted on TPA and DTPA in chloroform. Due to the much higher conversion rate, experiments had to be conducted using a flow cell, instead of a simple closed cell, preventing measurements in degassed conditions. The transient absorption of TPA in chloroform is shown in Figure 6.26. At first glance, it becomes

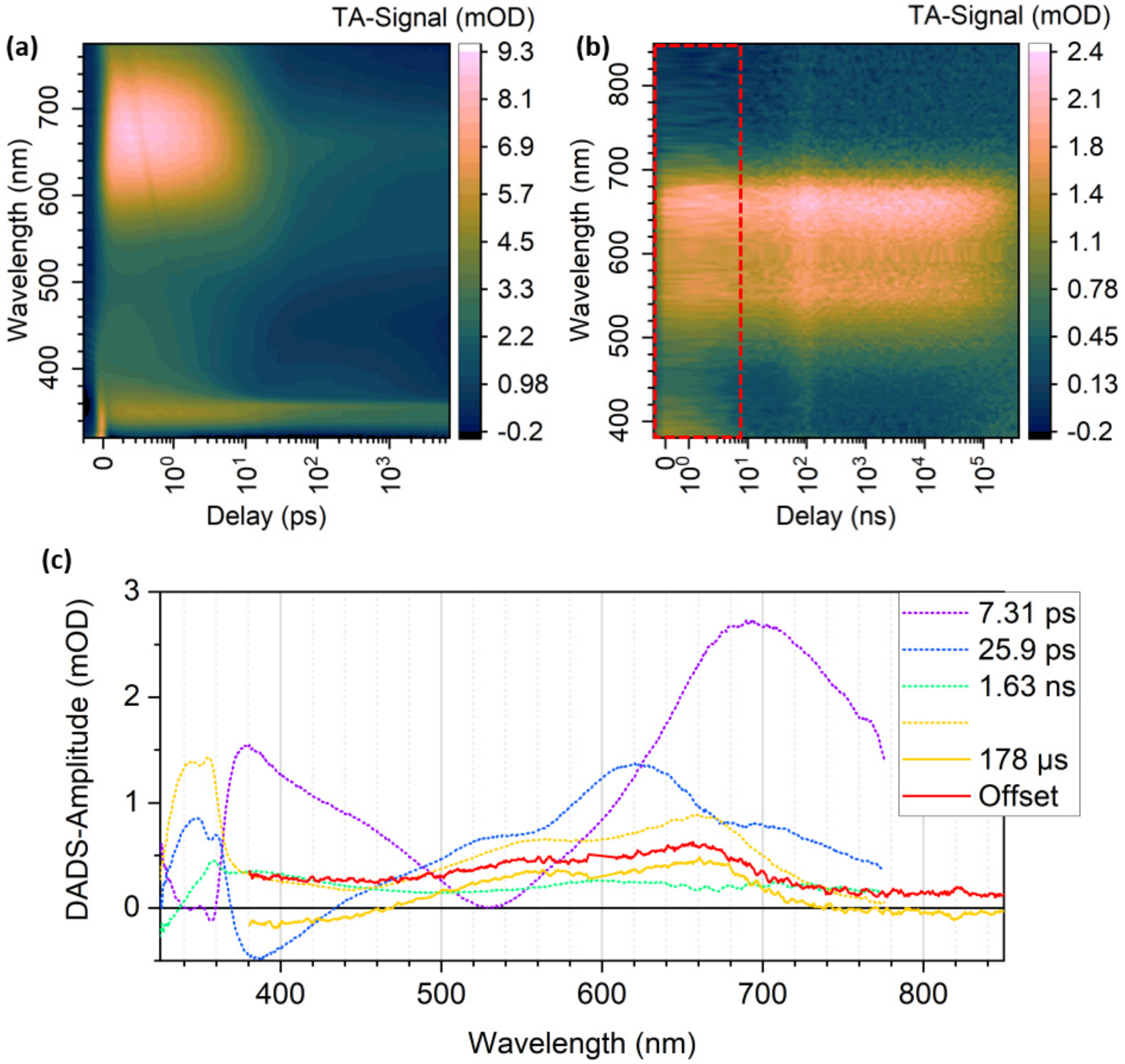

Figure 6.26: (a) and (b): Two-dimensional representation of transient absorption data of TPA in chloroform. (a) Short delay experiment. (b) Long delay experiment. Marked in red is the delay range covered in the short delay experiment. (c): DADS obtained from simultaneous global analysis of the two TA datasets. Dotted: DADS from short delay data, solid: DADS from long delay data.

clear that it is significantly more complex than that in hexane. The short delay data starts with a strong, broad ESA band covering the region of 600 – 750 nm. This is accompanied by a narrow ESA band centered at 340 nm. While the former decays after ~10 ps, the latter remains during the complete short delay range, although the exact shape changes and amplitude decreases. After the decay of the band at 600 – 750 nm, a weak but broad absorption band at wavelengths 520 – 700 nm becomes visible, which does not decay on the observed delay range. The persistent, narrow ESA band has an underlying ESA band with much smaller amplitude, which decays after ~5 ns. It is the red-sided wing of this band, which is visible in the long delay data (Figure 6.26b) at λ≤420 nm. The rest of the long delay dataset is dominated by a broad double-peak structure at 550 nm and 660 nm, which just begins to decay at the end of the 350 µs delay range. As can be expected from the intricate 2D-data, DADS from global analysis of the two datasets (Figure 6.26c) are not easily interpreted. The 7.31 ps DADS reflects the partial decay and narrowing of the strong ESA band with maximum at ~700 nm, as well the red-sided wing of the narrow ESA band at 350 nm. The second DADS (25.9 ps) covers the further decay over the complete visible range with a clear structure including maxima at 530 nm and 620 nm, and the partial decay of the narrow ESA band at 350 nm. These two positive bands are separated by a negative feature, describing the rise of a broader, weaker ESA band lying under the strong narrow one at 350 nm. The DADS assigned to the 1.63 ns time constant describes the decay of said band, as well as the decay of a small ESA band stretching across the complete visible region. The two last DADS (178 µs and offset, respectively) describe the same absorption features with maxima at 550 nm and 660 nm, whose decay is only partly covered by the experimental delay range. The intense absorption band at 500 nm – 750 nm and early delays is in good agreement with the spectrum obtained for the TPA S_1 in hexane. It follows a double exponential decay (7.31 ps, 25.9 ps) as indicated by the contributions in the corresponding DADS. At first the ESA band is extremely broad, intense, and mostly featureless. After the first decay, covering mostly the red side of the ESA band, distinct maxima at 620 nm and 520 nm stand out. These observations agree with a significant vibrational cooling, as they form a blue-shift and a spectral narrowing of the band. This structured band decays into one very weakly absorbing over the complete visible range. This is characterized by a significant rise around 400 nm, reflected by the negative amplitude in the 25.9 ps DADS. The last two DADS are in good agreement with the spectra the quantum chemical calculations of Letao Huang predict for the radical cation TPA$^{\bullet+}$. According to his calculations, the absorption spectrum of the radical cation consists of two bands at 500 nm and 550 nm, both with small amplitude compared to the TPA S_1, with the latter being the more intense one. In none of the first three DADS, the formation of the spectrum of the TPA$^{\bullet+}$ is indicated, suggesting, it is formed instantaneously with respect to the experimental temporal resolution of ~100 fs. Reiterating that photoexcitation occurs to the optically bright S_2/S_3, an ultrafast decay into the vibrationally hot S_1 and competing electron transfer to the solvent forming TPA$^{\bullet+}$ can be envisioned. With this interpretation of the first and last two time constants and DADS, the remaining third DADS (1.63 ns) comes into focus. As stated above,

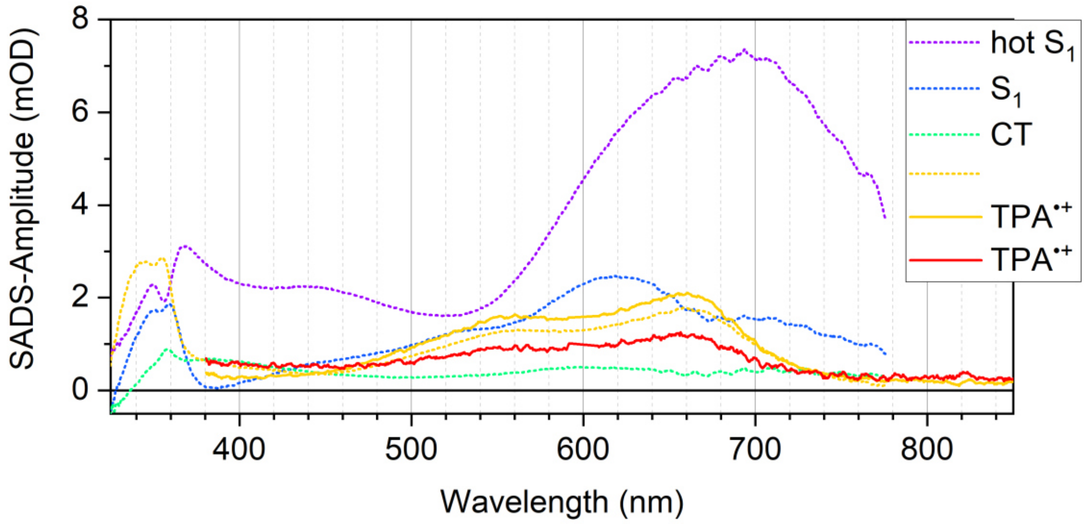

Figure 6.27: SADS obtained for parallel decay of S_1 and TPA$^{\bullet+}$ in the TA-Data of TPA in chloroform. Dotted: SADS from short delay data, solid: SADS from long delay data.

the associated species is formed with the decay of the vibrationally cool S_1, see the negative contribution in the 25.9 ps DADS at 400 nm. Comparison to the time constant of the ISC and spectrum of the T_1 obtained from the measurement in hexane clarifies, that a different process must be occurring. Based on the 0.622 eV electron affinity of chloroform, a charge transfer process can be expected.[126] While the spectrum of the free TPA$^{\bullet+}$. However, the DADS does not resemble the spectrum of the free TPA$^{\bullet+}$. Furthermore, at this point of the kinetics, photoexcited TPA molecules underwent radiationless relaxation from bright S_2/S_3 to the S_1, followed by vibrational relaxation within the S_1. They therefore caries significantly less excess energy than immediately after photoexcitation, when formation of the free radical cation occurs. Instead, the charge transfer process results in a complex, in which TPA$^{\bullet+}$ and CHCl$_3^{\bullet-}$ remain closely coordinated. This state is labeled as CT. Unable to escape this complex, the radical ions remain prone to electron back-transfer. Consequently, the lifetime of the

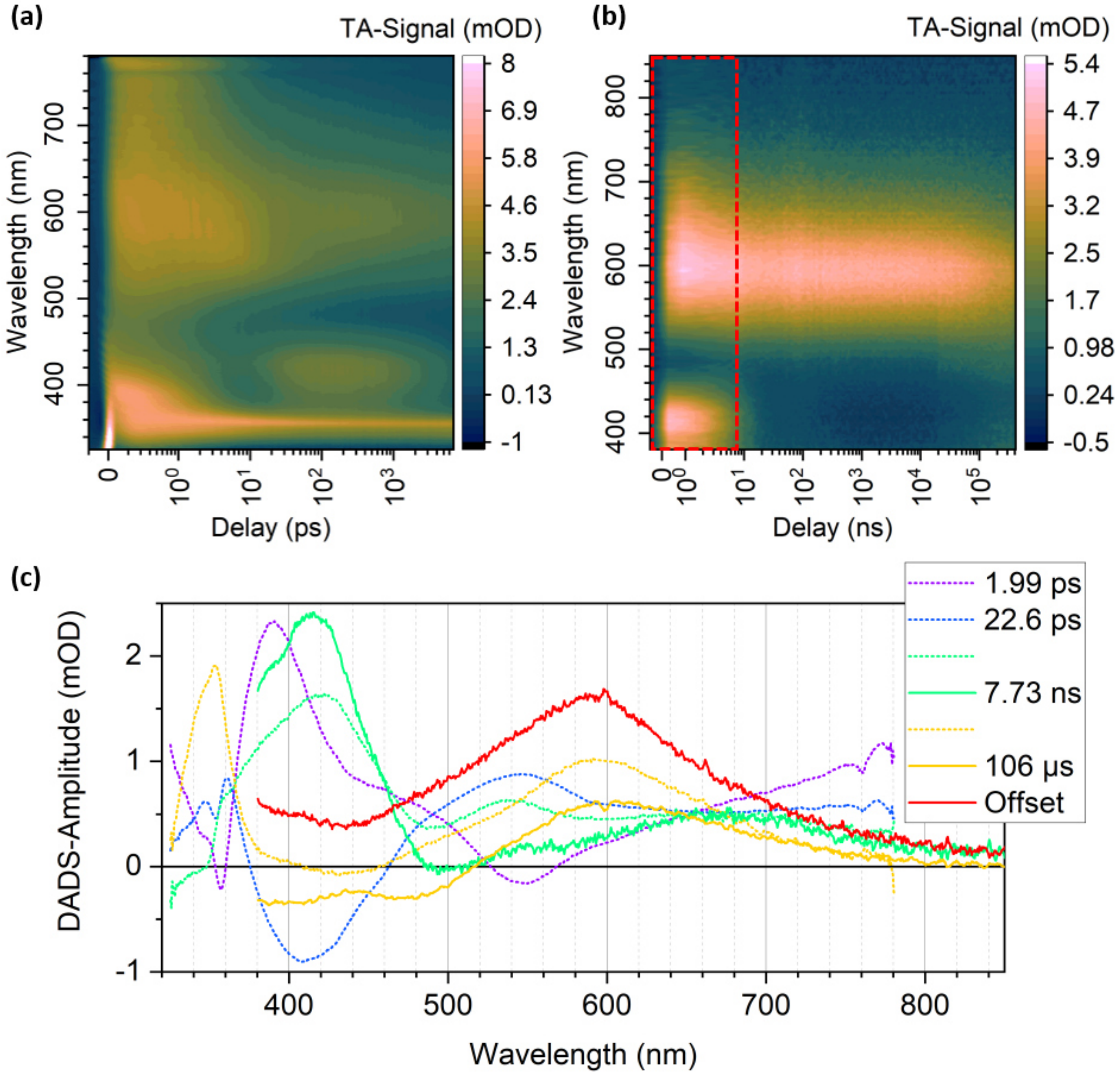

Figure 6.28: (a) and (b): Two-dimensional representation of transient absorption data of DTPA in chloroform. (a) Short delay experiment. (b) Long delay experiment. Marked in red is the delay range covered in the short delay experiment. (c): DADS obtained from simultaneous global analysis of the two TA datasets. Dotted: DADS from short delay data, solid: DADS from long delay data.

charge transfer state is much shorter than that of the free radical cation (1.63 ns and >350 µs, respectively). Figure 6.27 shows the SADS resulting from the sequential decay of hot S_1, S_1 and CT[TPA$^{\bullet+}$•CHCl$_3^{\bullet-}$] and the (partial) decay of TPA$^{\bullet+}$ parallel to that.

Let us now turn to DTPA to identify the influence of planarization to the photochemical processes established for TPA. Figure 6.28 shows the TA data of DTPA in chloroform along with the DADS retrieved from global analysis. Similarly, to TPA, the first DADS describes a decay of the red side (λ≥600 nm) and small rise of the blue side of the first absorption band covering the complete visible range, constituting its blue-shift. The band is accompanied by another strong ESA at λ≤400 nm. The second DADS (22.6 ps) reflects the decay of the broad ESA stretching across the complete visible range, as well as the rise of a distinct ESA band at 400 nm. The decay of this band is covered in the third DADS (7.73 ps). The same was observed for TPA, although the absorption band was blue-shifted and overlapped significantly with the sharp absorption feature at 350 nm. For DTPA, the absorption band is distinctly visible in both the short and long delay dataset. After the band at 400 nm decays, the transient absorption is dominated by a single broad ESA band with maximum at 600 nm. The start of its decay is barely covered in the 350 µs range of the long delay experiment, leading to a partial decay being reflected by DADS 4 (106 µs) and a non-decaying offset.

SADS obtained applying the same model as for TPA are shown in Figure 6.29 and a Jablonski diagram summarizing the discussed photoinduced processes for TPA and DTPA in chloroform is shown in Figure 6.30.

Analogously to TPA, the three groups of distinct spectra are assigned to the S_1, a solute-solvent charge transfer complex (CT) and the free radical cation DTPA$^{\bullet+}$. Quantum chemical calculations identify S_3/S_4 as final states of the optically bright transitions from the ground state. However, agreement of the observed first spectrum (very broad, across the visible region) and the one calculated for the S_1 (transitions at

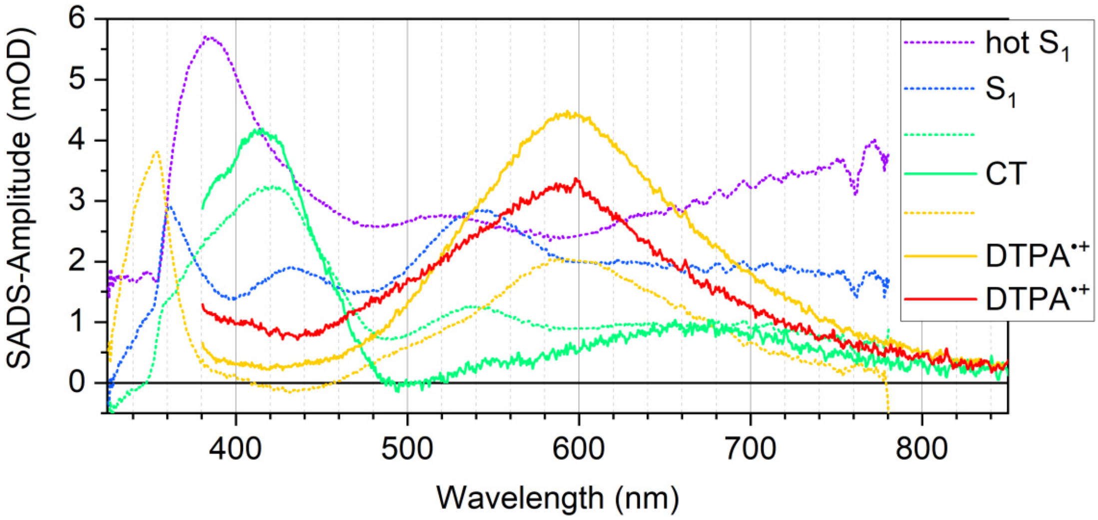

Figure 6.29: SADS obtained for parallel decay of S_1 and DTPA$^{\bullet+}$ in the TA-Data of DTPA in chloroform. Dotted: SADS from short delay data, solid: SADS from long delay data.

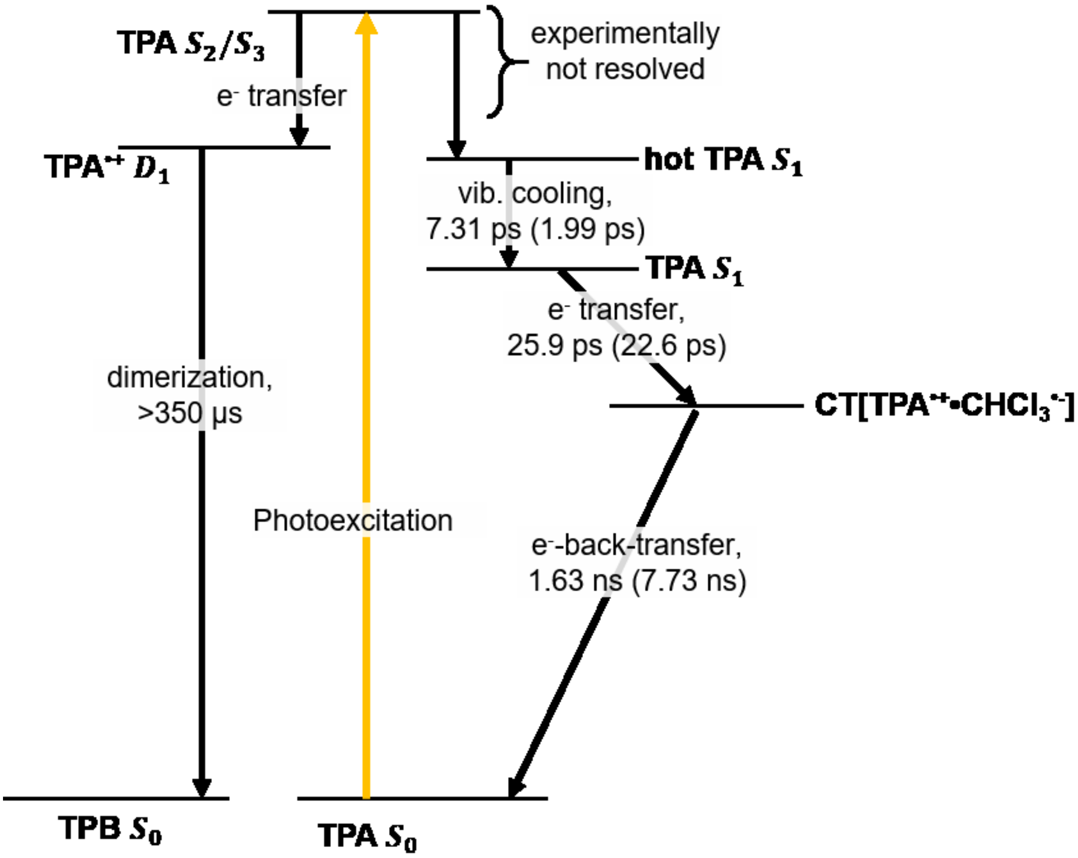

Figure 6.30: Jablonski diagram summarizing the photophysics and photochemistry of TPA (DTPA) in chloroform. Time constants in brackets apply to DTPA.

440 nm, 550 nm, 620 nm, and 730 nm) is good. This suggests effective, ultrafast radiationless relaxation of the higher excited singlet states into the S_1 occurs faster than the ~100 fs experimental temporal resolution, as was argued in the experiments using hexane as solvent. Similar to TPA in chloroform and DTPA in hexane, the strong broad ESA band in the visible range at early delays (τ≤20 ps) is therefore assigned to the S_1. The effective blue-shift on the 1.99 ps timescale is accordingly interpreted as vibrational cooling within this state, before it relaxes on the 22.6 ps timescale. While the vibrational cooling occurs significantly faster in DTPA than in TPA (1.99 ps vs 7.31 ps) this is not the case for the S_1 lifetime (22.6 ps vs 25.9 ps). Most likely, the structural rigidity introduced by the dimethylmethylene bridges prevents larger geometrical rearrangement, without affecting the probability for the charge-transfer process.

The separated double band structure (intense at 420 nm, weak at 660 nm) is assigned to the solute-solvent charge transfer complex. Compared to the broader 350 nm band in TPA which lies beneath a more intense, narrow one, the red-shift of the corresponding band in DTPA (420 nm) makes it distinctly visible, both in the 2D data and in the third DADS. Since the rate of the charge transfer process leading to the CT complex is slightly accelerated, one might expect similar for the back electron transfer, limiting the CT complex's lifetime. However, it is prolonged notably, compared to the one in TPA (7.73 ns vs 1.63 ns). Since the structural rigidity does not impede the first electron transfer, it cannot serve as explanation for the decelerated rate of the back-electron transfer. Instead, let us consider, what effect the improved π-conjugation has on both processes. In DTPA, the expanded π-conjugation allows distribution of the radical cation's positive charge and unpaired electron over all three phenyl rings and the nitrogen atom, effectively stabilizing both. In TPA, this delocalization is hindered by the propeller like shape. It can therefore be inferred that the radical cation is stabilized more in DTPA than in TPA. This contributes to both the shortened S_1 lifetime by making the initial CT process more exothermic, and the prolonged lifetime of the CT complex, by slowing down the rate of the back-electron transfer.

The last group of distinct spectra, the extremely long lived, broad band peaking at 600 nm, is assigned to the free radical cation $DTPA^{\bullet+}$. The band position and lifetime are remarkably similar to the ones found for $TPA^{\bullet+}$. Furthermore, this assignment is corroborated by quantum chemical calculations by Letao Huang, predicting a single absorption band in the visible region at 575 nm. As the rise of this absorption band is not indicated in any of the previously discussed DADS, it is assumed, that electron transfer forming $DTPA^{\bullet+}$ occurs from the bright S_3/S_4. From the radical cation $DTPA^{\bullet+}$ electrophilic attack on the most exposed para-position of another chromophore molecule is plausible and eventually leads to formation of a benzidine-like DTPA-dimer, the photoproduct observed in the irradiation experiments. Unlike the electron transfer to the omnipresent solvent, this process is diffusion-limited, leading to lifetimes that cannot be reliably estimated on the experimental 350 μs delay range. Note, that this long time constant for the dimerization confirms, that the bound CT complex (lifetime 7.73 ns) does not contribute to the photoproduct formation.

On the factual level, the Jablonski diagrams in Figure 6.16, Figure 6.23 and Figure 6.30 display the rich photophysics and photochemistry of TPA and DTPA, featuring ISC, TF, intramolecular formation of σ-bonds, electron transfer and dimerization. On the methodological level, they demonstrate how powerful transient absorption in conjunction with predicted ESA spectra from theory is at exploring excited-state dynamics. Careful design of multiple measurements under deliberately varied conditions allows for identification of the influence of solvent, atmosphere, and chromophore design on the intricate excited-state dynamics, which remain hidden to the eye and stationary spectroscopy.

7 Conclusion & Outlook

In this work, time-resolved spectroscopy was applied to rationalize the effects of different excited-state tuning approaches in iron(II) complexes and triphenylamines. Investigated tuning vectors were chemical modification as well as oxygen content and choice of choice of solvent.

Impulsive vibrational spectroscopy was established as sensitive of ultrafast MLCT – MC transitions, sensing wave packet motions in low-frequency breathing modes. The method was then applied to a promising sensitizer dye and finds an ultrafast branching to a spectrally elusive MC state, acting as loss-channel to the desired MLCT manifold. This is a significant simplification for the testing procedures of transition metal-based dye sensitizers, where MC states could only be identified reliably using time-resolved X-ray methods, requiring large scale synchrotron facilities.

The photochemistry of TPA was mapped out in great detail, expanding on the known carbazole formation by characterization of the TPA S_1 spectrum, and the solvent dependence of side products in absence of oxygen. An entirely different photochemistry was found in chloroform, where electron transfer from TPA to the solvent occurs, subsequently leading to the formation of dimers. Furthermore, the effect of forced planarization on the photophysics was investigated with the dimethylmethylene bridged DTPA. It was found to prohibit carbazole formation by obstructing preorientation of the p-orbitals in hexane, whereas the photochemistry in chloroform is analogue to that of the propeller-shaped parent molecule.

7.1 Identification of elusive MLCT-loss channels in Fe(II) complexes

The solvent dependent donor strength of cyanide ligands was exploited to toggle between MLCT and MC excited states in the photophysics of $[Fe(bpy)(CN)_4]^{2-}$. This was confirmed using transient absorption spectroscopy to identify characteristic MLCT bands in DMSO, and a long-lived ground-state bleach in the absence of any excited-state absorption in methanol. Impulsive vibrational spectroscopy was then applied to $[Fe(bpy)(CN)_4]^{2-}$ in both solvents. In methanol, low-frequency breathing modes are identified as fingerprints of a wave packet launched along a breathing mode with the ultrafast MLCT-MC transition. This is corroborated by Thomas Penfold's quantum chemical excited-state geometry optimizations, predicting a significant elongation of the Fe-L bonds going from the ground and MLCT states to the MC manifold. The elongation can be rationalized by the partial population of the antibonding e_g orbitals, directed precisely along the Fe-L axis. In DMSO, where MC states are destabilized and do not partake in the excited-state dynamics, these low-frequency breathing modes are not induced by the photoexcitation. This allows the identification of ultrafast populated MC states by ultrashort visible pulses, which previously required time-resolved X-ray methods.[47, 127] While they allow for real-time monitoring of the metal center's oxidation state, they require large scale facilities with limited beam time. The newly established method was applied to $[Fe(cpbmi)_2]^{2+}$, a promising sensitizer dye. With standard transient absorption spectroscopy, MLCT states are found with lifetimes of up to 19.9 ps. However, IVS finds a pump-induced 100 cm^{-1} breathing mode indicative of an ultrafast MLCT-MC transition, which is not indicated in the TA data, due to the MC's elusive nature. From this, an ultrafast branching from the initially populated ^{1}MLCT to the ^{3}MLCT and the ^{3}MC is inferred, ultimately limiting every light harvesting application relying on initial charge separation. Another breathing vibration is identified by a delayed push pulse at 140 cm^{-1}. Correlation with the population obtained from TA and quantum chemical calculations by Thomas Penfold allow the assignment to a similar breathing mode, but on the ^{3}MLCT potential energy surface.

In this work, a direct cause-and-effect relation between MLCT-MC transitions and low-frequency modes in the excited-state Raman spectra of iron(II) complexes was shown and rationalized. This sets up IVS as powerful, yet widely available tool for the identification of MC-related loss channels to the desired MLCT states in dye-sensitizers. This can contribute to an accelerated and more efficient search for suitable iron-based substitutes to the paradigmatic ruthenium-based dyes applied in Grätzel cells today.

In the past three years, iron(III) N-heterocyclic carbene complexes have emerged as potent light-harvesting complexes for solar cells and photocatalysis as well.[128-132] Due to the higher oxidation state of the iron center, the desired charge transfer states result from ligand-to-metal electron transfers in these complexes. Yet still, IVS may be of similar use in this area of the field, identifying MC-related loss channels, from the desired CT-manifold.

7.2 Manipulation of TPA photophysics and –chemistry by oxygen and solvent choice

The photophysics and –chemistry of TPA and the planarized derivate DTPA was investigated as function of oxygen content and electron affinity of the solvent. In hexane, TPA largely adopted the same behavior as reported in the literature for acetonitrile as solvent.[105, 106, 112, 125] After intersystem crossing to TPA T_1, the preoriented p-orbitals of neighboring phenyl rings form a sigma bond, leading to transient dihydrocarbazole (DHC). In the absence of oxygen, the cyclization is reversed almost completely and only a minor fraction undergoes hydrogen abstraction to form N-phenyl-carbazole as stable photoproduct. Molecular oxygen in the solution adopts a conflicting double role: On one hand, it reduces the quantum yield for the cyclization to DHC by quenching the excited states of TPA. On the other hand, it facilitates hydrogen abstraction drastically, so that the overall quantum yield of the carbazole formation is increased. This reported behavior is reproduced and expanded in this work by two major aspects.

Firstly, no side product formation was observed in hexane in the absence of oxygen, suggesting a charged transition state to the tetrahydrocarbazoles observed in acetonitrile. This opens up quantitative photosynthetic routes to carbazole derivates with di- or triphenylamine precursors susceptible to oxygen.

Secondly, monitoring the dynamics completely from femto- to microseconds allowed for detailed characterization of all partaking transient species, and the intricate role of oxygen in the solution. While its effect on yield and lifetime of DHC S_0 have been addressed by flash photolysis, the data presented here allows quantification of the loss channels at every intermediate state. It could be shown that oxygen not only quenches the TPA T_1, but also the triplet state of the transient DHC. While it reduces its lifetime by more than factor 10, the yield of DHC S_0 is hardly affected (>80%). Additionally, the femtosecond temporal resolution at early delays allowed the first-time reporting of the TPA S_1 spectrum, which served as reference for the interpretation of transient absorption in chloroform.

The investigation of DTPA under the same conditions showed, that the structural rigidity introduced by the dimethylmethylene bridges impedes transitions between electronic states. The initial intersystem crossing DTPA $S_1 \rightarrow T_1$ is delayed by factor two. Formation of the sigma bond (as in TPA) is obstructed completely, by the rigid planarization, which circumvents preorientation of p-orbitals at neighboring phenyl rings. This expands the T_1 lifetime from 31.5 ns to 14.4 µs and causes the outstanding photostability of DTPA over other di- or triphenylamines.

In chloroform, a decidedly electron affine solvent, both TPA and DTPA were shown to adopt remarkably similar photochemistry. From the optically bright S_2 / S_3, an ultrafast branching occurs. One share decays via electron transfer to the solvent forming the radical cation of the respective chromophore. The other share relaxes into the S_1, who's spectrum was identified by comparison to the hexane measurements. However, the S_1 lifetime is cut short to few picoseconds by another charge transfer process. Due to the smaller energy difference, the resulting chromophore cation and solvent anion remain coordinated by Coulomb attraction, resulting in relaxation to the ground state by electron back transfer. The unbound radical cation goes on to produce a stable photoproduct with an additional red-shifted absorption band, closely resembling the absorption spectrum of tetraphenylbenzidine (TPB). This suggests dimerization via the para-position, expanding the effective π-system. To further investigate this point two approaches are feasible.

The seemingly simplest is to characterize the photoproduct via standard techniques, such as nuclear magnetic resonance spectroscopy (NMR) and mass spectrometry (MS). Neither of the two techniques so far yielded reliable results. At concentration required for NMR, irradiation leads to unspecific products. This can possibly be avoided by irradiating a diluted sample and increase the concentration after the stable photoproduct has formed by evaporation of the solvent. MS using electrospray ionization (ESI) suffered from unclear results, even for pure TPA, likely due to its tendency to form aggregates.[133, 134] Electron ionization (EI) has proven capable of producing results for pure TPA. This motivates to produce the photoproduct by irradiation in solution and subsequently collect the solid sample by complete removal of the solvent, as EI does not support liquid samples.

The other approach is to examine not the outcome, but the photochemical process itself. If the chromophore radical cations decay via dimerization, then their lifetime should show a dependence on the chromophore concentration: An increased concentration should result in shorter diffusion times and consequently decreased lifetimes of the radical cation, observable by its characteristic absorption band. The presented experiments on TPA in chloroform were conducted with 830 µmol/l and the decay of the radical cation absorption band is only partially covered in the 350 µs time frame. A doubling of the TPA concentration should therefore lead to a significantly reduced lifetime of the radical cation.

8 References

1. Arora, K.; Herroon, M.; Al-Afyouni, M. H.; Toupin, N. P.; Rohrabaugh, T. N.; Loftus, L. M.; Podgorski, I.; Turro, C.; Kodanko, J. J., Catch and Release Photosensitizers: Combining Dual-Action Ruthenium Complexes with Protease Inactivation for Targeting Invasive Cancers. *J Am Chem Soc* **2018,** *140* (43), 14367-14380.
2. Oregan, B.; Gratzel, M., A Low-Cost, High-Efficiency Solar-Cell Based on Dye-Sensitized Colloidal Tio2 Films. *Nature* **1991,** *353* (6346), 737-740.
3. Nazeeruddin, M. K.; Kay, A.; Rodicio, I.; Humphrybaker, R.; Muller, E.; Liska, P.; Vlachopoulos, N.; Gratzel, M., Conversion of Light to Electricity by Cis-X2bis(2,2'-Bipyridyl-4,4'-Dicarboxylate)Ruthenium(Ii) Charge-Transfer Sensitizers (X = Cl-, Br-, I-, Cn-, and Scn-) on Nanocrystalline Tio2 Electrodes. *J Am Chem Soc* **1993,** *115* (14), 6382-6390.
4. Knoll, J. D.; Albani, B. A.; Turro, C., New Ru(II) Complexes for Dual Photoreactivity: Ligand Exchange and O-1(2) Generation. *Accounts Chem Res* **2015,** *48* (8), 2280-2287.
5. Al-Afyouni, M. H.; Rohrabaugh, T. N.; Al-Afyouni, K. F.; Turro, C., New Ru(II) photocages operative with near-IR light: new platform for drug delivery in the PDT window. *Chem Sci* **2018,** *9* (32), 6711-6720.
6. Wezenberg, S. J.; Chen, K. Y.; Feringa, B. L., Visible-Light-Driven Photoisomerization and Increased Rotation Speed of a Molecular Motor Acting as a Ligand in a Ruthenium(II) Complex. *Angew Chem Int Edit* **2015,** *54* (39), 11457-11461.
7. Gawelda, W.; Cannizzo, A.; Pham, V. T.; van Mourik, F.; Bressler, C.; Chergui, M., Ultrafast nonadiabatic dynamics of [Fe-II(bpy)(3)](2+) in solution. *J Am Chem Soc* **2007,** *129* (26), 8199-8206.
8. Consani, C.; Premont-Schwarz, M.; ElNahhas, A.; Bressler, C.; van Mourik, F.; Cannizzo, A.; Chergui, M., Vibrational Coherences and Relaxation in the High-Spin State of Aqueous [Fe-II(bpy)(3)](2+). *Angew Chem Int Edit* **2009,** *48* (39), 7184-7187.
9. Franck, J., Elementary processes of photochemical reactions. *T Faraday Soc* **1926,** *21* (3), 0536-0542.
10. Condon, E., A theory of intensity distribution in band systems. *Phys Rev* **1926,** *28* (6), 1182-1201.
11. King, R. B.; American Chemical Society. Division of Inorganic Chemistry., *Inorganic compounds with unusual properties : a symposium sponsored by the Division of Inorganic Chemistry of the American Chemical Society, held at the University of Georgia, Athens, Ga., Jan. 6-8, 1975*. The Society: Washington, 1976; p ix, 437 p.
12. Henry, W.; Coates, C. G.; Brady, C.; Ronayne, K. L.; Matousek, P.; Towrie, M.; Botchway, S. W.; Parker, A. W.; Vos, J. G.; Browne, W. R.; McGarvey, J. J., The early picosecond photophysics of Ru(II) polypyridyl complexes: A tale of two timescales. *J Phys Chem A* **2008,** *112* (20), 4537-4544.
13. Terenin, A.; Ermolaev, V., Sensitized Phosphorescence in Organic Solutions at Low Temperature - Energy Transfer between Triplet States. *T Faraday Soc* **1956,** *52* (8), 1042-1052.
14. DeRosa, M. C.; Crutchley, R. J., Photosensitized singlet oxygen and its applications. *Coordin Chem Rev* **2002,** *233*, 351-371.
15. Gade, L., H.;, Photochemie von Koordinationsverbindungen. In *Koordinationschemie*, 1998; pp 480-501.

16. Gutlich, P.; Gaspar, A. B.; Garcia, Y., Spin state switching in iron coordination compounds. *Beilstein J Org Chem* **2013,** *9*, 342-391.
17. Nakaya, M.; Ohtani, R.; Lindoy, L. F.; Hayami, S., Light-induced excited spin state trapping in iron(III) complexes. *Inorg Chem Front* **2021,** *8* (2), 484-498.
18. Oppermann, M.; Zinna, F.; Lacour, J.; Chergui, M., Chiral control of spin-crossover dynamics in Fe (II) complexes. *Nat Chem* **2022,** *14* (7), 739-+.
19. Vogler, A.; Kunkely, H., Excited state properties of organometallic compounds of rhenium in high and low oxidation states. *Coordin Chem Rev* **2000,** *200*, 991-1008.
20. Vlcek, A., Mechanistic roles of metal-to-ligand charge-transfer excited states in organometallic photochemistry. *Coordin Chem Rev* **1998,** *177*, 219-256.
21. Julia, F., Ligand-to-Metal Charge Transfer (LMCT) Photochemistry at 3d-Metal Complexes: An Emerging Tool for Sustainable Organic Synthesis. *Chemcatchem* **2022,** *14* (19).
22. Vogler, A.; Kunkely, H., Ligand-to-ligand and intraligand charge transfer and their relation to charge transfer interactions in organic zwitterions. *Coordin Chem Rev* **2007,** *251* (3-4), 577-583.
23. Mathoniere, C., Metal-to-Metal Electron Transfer: A Powerful Tool for the Design of Switchable Coordination Compounds. *Eur J Inorg Chem* **2018,** (3-4), 248-258.
24. Karges, J.; Kuang, S.; Maschietto, F.; Blacque, O.; Ciofini, I.; Chao, H.; Gasser, G., Rationally designed ruthenium complexes for 1-and 2-photon photodynamic therapy. *Nat Commun* **2020,** *11* (1).
25. Duan, L. L.; Bozoglian, F.; Mandal, S.; Stewart, B.; Privalov, T.; Llobet, A.; Sun, L. C., A molecular ruthenium catalyst with water-oxidation activity comparable to that of photosystem II. *Nat Chem* **2012,** *4* (5), 418-423.
26. Concepcion, J. J.; Jurss, J. W.; Brennaman, M. K.; Hoertz, P. G.; Patrocinio, A. O. T.; Iha, N. Y. M.; Templeton, J. L.; Meyer, T. J., Making Oxygen with Ruthenium Complexes. *Accounts Chem Res* **2009,** *42* (12), 1954-1965.
27. Frances-Monerris, A.; Gros, P. C.; Assfeld, X.; Monari, A.; Pastore, M., Toward Luminescent Iron Complexes: Unravelling the Photophysics by Computing Potential Energy Surfaces. *Chemphotochem* **2019,** *3* (9), 666-683.
28. Housecroft, C. E.; Constable, E. C., Solar energy conversion using first row d-block metal coordination compound sensitizers and redox mediators. *Chem Sci* **2022,** *13* (5), 1225-1262.
29. Monat, J. E.; McCusker, J. K., Femtosecond excited-state dynamics of an iron(II) polypyridyl solar cell sensitizer model. *J Am Chem Soc* **2000,** *122* (17), 4092-4097.
30. Bowman, D. N.; Jakubikova, E., Low-Spin versus High-Spin Ground State in Pseudo-Octahedral Iron Complexes. *Inorg Chem* **2012,** *51* (11), 6011-6019.
31. Sandroni, M.; Favereau, L.; Planchat, A.; Akdas-Kilig, H.; Szuwarski, N.; Pellegrin, Y.; Blart, E.; Le Bozec, H.; Boujtita, M.; Odobel, F., Heteroleptic copper(I)-polypyridine complexes as efficient sensitizers for dye sensitized solar cells. *J Mater Chem A* **2014,** *2* (26), 9944-9947.
32. Buldt, L. A.; Wenger, O. S., Chromium complexes for luminescence, solar cells, photoredox catalysis, upconversion, and phototriggered NO release. *Chem Sci* **2017,** *8* (11), 7359-7367.
33. Lindh, L.; Chabera, P.; Rosemann, N. W.; Uhlig, J.; Warnmark, K.; Yartsev, A.; Sundstrom, V.; Persson, P., Photophysics and Photochemistry of Iron Carbene Complexes for Solar Energy Conversion and Photocatalysis. *Catalysts* **2020,** *10* (3).

34. Lindh, L.; Gordivska, O.; Persson, S.; Michaels, H.; Fan, H.; Chabera, P.; Rosemann, N. W.; Gupta, A. K.; Benesperi, I.; Uhlig, J.; Prakash, O.; Sheibani, E.; Kjaer, K. S.; Boschloo, G.; Yartsev, A.; Freitag, M.; Lomoth, R.; Persson, P.; Warnmark, K., Dye-sensitized solar cells based on Fe N-heterocyclic carbene photosensitizers with improved rod-like push-pull functionality. *Chem Sci* **2021,** *12* (48), 16035-16053.

35. Magra, K.; Frances-Monerris, A.; Cebrian, C.; Monari, A.; Haacke, S.; Gros, P. C., Bidentate Pyridyl-NHC Ligands: Synthesis, Ground and Excited State Properties of Their Iron(II) Complexes and the Role of the fac/mer Isomerism. *Eur J Inorg Chem* **2022,** *2022* (7).

36. Marri, A. R.; Marekha, B.; Penfold, T.; Haacke, S.; Gros, P. C., Towards panchromatic Fe(ii) NHC sensitizers via HOMO inversion. *Inorg Chem Front* **2022,** *10* (1), 118-126.

37. Gade, L., H.;, Grundlagen der Kristall-/Ligandenfeldtheorie. In *Koordinationschemie*, 1998; pp 183-241.

38. Carey, M. C.; Adelman, S. L.; McCusker, J. K., Insights into the excited state dynamics of Fe(II) polypyridyl complexes from variable- temperature ultrafast spectroscopy. *Chem Sci* **2019,** *10* (1), 134-144.

39. Zhang, W. K.; Kjaer, K. S.; Alonso-Mori, R.; Bergmann, U.; Chollet, M.; Fredin, L. A.; Hadt, R. G.; Hartsock, R. W.; Harlang, T.; Kroll, T.; Kubicek, K.; Lemke, H. T.; Liang, H. W.; Liu, Y. Z.; Nielsen, M. M.; Persson, P.; Robinson, J. S.; Solomon, E. I.; Sun, Z.; Sokaras, D.; van Driel, T. B.; Weng, T. C.; Zhu, D. L.; Warnmark, K.; Sundstromb, V.; Gaffney, K. J., Manipulating charge transfer excited state relaxation and spin crossover in iron coordination complexes with ligand substitution. *Chem Sci* **2017,** *8* (1), 515-523.

40. Kjaer, K. S.; Kunnus, K.; Harlang, T. C. B.; Van Driel, T. B.; Ledbetter, K.; Hartsock, R. W.; Reinhard, M. E.; Koroidov, S.; Li, L.; Laursen, M. G.; Biasin, E.; Hansen, F. B.; Vester, P.; Christensen, M.; Haldrup, K.; Nielsen, M. M.; Chabera, P.; Liu, Y. Z.; Tatsuno, H.; Timm, C.; Uhlig, J.; Sundstom, V.; Nemeth, Z.; Szemes, D. S.; Bajnoczi, E.; Vanko, G.; Alonso-Mori, R.; Glownia, J. M.; Nelson, S.; Sikorski, M.; Sokaras, D.; Lemke, H. T.; Canton, S. E.; Warnmark, K.; Persson, P.; Cordones, A. A.; Gaffney, K. J., Solvent control of charge transfer excited state relaxation pathways in [Fe(2,2 '-bipyridine)(CN)(4)](2-). *Phys Chem Chem Phys* **2018,** *20* (6), 4238-4249.

41. Winkler, J. R.; Sutin, N., Lifetimes and Spectra of the Excited-States of Cis-Dicyanobis(2,2'-Bipyridine)Iron(Ii) and Cis-Dicyanobis(2,2'-Bipyridine)Ruthenium(Ii) in Solution. *Inorg Chem* **1987,** *26* (2), 220-221.

42. Winkler, J. R.; Creutz, C.; Sutin, N., Solvent Tuning of the Excited-State Properties of (2,2'-Bipyridine)Tetracyanoferrate(Ii) - Direct Observation of a Metal-to-Ligand Charge-Transfer Excited-State of Iron(Ii). *J Am Chem Soc* **1987,** *109* (11), 3470-3471.

43. Arduengo, A. J.; Harlow, R. L.; Kline, M., A Stable Crystalline Carbene. *J Am Chem Soc* **1991,** *113* (1), 361-363.

44. Arduengo, A. J.; Dias, H. V. R.; Harlow, R. L.; Kline, M., Electronic Stabilization of Nucleophilic Carbenes. *J Am Chem Soc* **1992,** *114* (14), 5530-5534.

45. Arduengo, A. J.; Bock, H.; Chen, H.; Denk, M.; Dixon, D. A.; Green, J. C.; Herrmann, W. A.; Jones, N. L.; Wagner, M.; West, R., Photoelectron-Spectroscopy of a Carbene/Silylene/Germylene Series. *J Am Chem Soc* **1994,** *116* (15), 6641-6649.

46. Jacobsen, H.; Correa, A.; Poater, A.; Costabile, C.; Cavallo, L., Understanding the M-(NHC) (NHC = N-heterocyclic carbene) bond. *Coordin Chem Rev* **2009,** *253* (5-6), 687-703.

47. Kunnus, K.; Vacher, M.; Harlang, T. C. B.; Kjaer, K. S.; Haldrup, K.; Biasin, E.; van Driel, T. B.; Papai, M.; Chabera, P.; Liu, Y. Z.; Tatsuno, H.; Timm, C.; Kallman, E.; Delcey, M.; Hartsock, R. W.; Reinhard, M. E.; Koroidov, S.; Laursen, M. G.; Hansen, F. B.; Vester, P.; Christensen, M.; Sandberg, L.; Nemeth, Z.; Szemes, D. S.; Bajnoczi, E.; Alonso-Mori, R.; Glownia, J. M.; Nelson, S.; Sikorski, M.; Sokaras, D.; Lemke, H. T.; Canton, S.; Moller, K. B.; Nielsen, M. M.; Vank, G.; Warnmark, K.; Sundstrom, V.; Persson, P.; Lundberg, M.; Uhlig, J.; Gaffney, K. J., Vibrational wavepacket dynamics in Fe carbene photosensitizer determined with femtosecond X-ray emission and scattering. *Nat Commun* **2020,** *11* (1).

48. Harlang, T. C. B.; Liu, Y. Z.; Gordivska, O.; Fredin, L. A.; Ponseca, C. S.; Huang, P.; Chabera, P.; Kjaer, K. S.; Mateos, H.; Uhlig, J.; Lomoth, R.; Wallenberg, R.; Styring, S.; Persson, P.; Sundstrom, V.; Warnmark, K., Iron sensitizer converts light to electrons with 92% yield. *Nat Chem* **2015,** *7* (11), 883-889.

49. Papai, M.; Vanko, G.; Rozgony, T.; Penfold, T. J., High-Efficiency Iron Photosensitizer Explained with Quantum Wavepacket Dynamics. *J Phys Chem Lett* **2016,** *7* (11), 2009-2014.

50. Magra, K.; Domenichini, E.; Frances-Monerris, A.; Cebrian, C.; Beley, M.; Darari, M.; Pastore, M.; Monari, A.; Assfeld, X.; Haacke, S.; Gros, P. C., Impact of the fac/mer Isomerism on the Excited-State Dynamics of Pyridyl-carbene Fe(II) Complexes. *Inorg Chem* **2019,** *58* (8), 5069-5081.

51. Magra, K.; Darari, M.; Domenichini, E.; Frances-Monerris, A.; Cebrian, C.; Beley, M.; Pastore, M.; Monari, A.; Assfeld, X.; Haacke, S.; Gros, P. C., Photophysical Investigation of Iron(II) Complexes Bearing Bidentate Annulated Isomeric Pyridine-NHC Ligands. *J Phys Chem C* **2020,** *124* (34), 18379-18389.

52. Fredin, L. A.; Papai, M.; Rozsalyi, E.; Vanko, G.; Warnmark, K.; Sundstrom, V.; Persson, P., Exceptional Excited-State Lifetime of an Iron(II)-N-Heterocyclic Carbene Complex Explained. *J Phys Chem Lett* **2014,** *5* (12), 2066-2071.

53. Liu, Y. Z.; Harlang, T.; Canton, S. E.; Chabera, P.; Suarez-Alcantara, K.; Fleckhaus, A.; Vithanage, D. A.; Goransson, E.; Corani, A.; Lomoth, R.; Sundstrom, V.; Warnmark, K., Towards longer-lived metal-to-ligand charge transfer states of iron(II) complexes: an N-heterocyclic carbene approach. *Chem Commun* **2013,** *49* (57), 6412-6414.

54. Brown, A. M.; McCusker, C. E.; McCusker, J. K., Spectroelectrochemical identification of charge-transfer excited states in transition metal-based polypyridyl complexes. *Dalton T* **2014,** *43* (47), 17635-17646.

55. Dierks, P.; Kruse, A.; Bokareva, O. S.; Al-Marri, M. J.; Kalmbach, J.; Baltrun, M.; Neuba, A.; Schoch, R.; Hohloch, S.; Heinze, K.; Seitz, M.; Kuhn, O.; Lochbrunner, S.; Bauer, M., Distinct photodynamics of kappa-N and kappa-C pseudoisomeric iron(ii) complexes. *Chem Commun* **2021,** *57* (54), 6640-6643.

56. Shen, Y. R., *The principles of nonlinear optics*. p xii, 563 pages.

57. Mukamel, S., *Principles of nonlinear optical spectroscopy*. Oxford University Press: New York, 1995; p xviii, 543 p.

58. Berera, R.; van Grondelle, R.; Kennis, J. T. M., Ultrafast transient absorption spectroscopy: principles and application to photosynthetic systems. *Photosynth Res* **2009,** *101* (2-3), 105-118.

59. van Stokkum, I. H. M.; Larsen, D. S.; van Grondelle, R., Global and target analysis of time-resolved spectra. *Bba-Bioenergetics* **2004,** *1657* (2-3), 82-104.

60. Ruckebusch, C.; Sliwa, M.; Pernot, P.; de Juan, A.; Tauler, R., Comprehensive data analysis of femtosecond transient absorption spectra: A review. *J Photoch Photobio C* **2012,** *13* (1), 1-27.

61. Lessing, H. E.; Jena, A. V., Separation of Rotational Diffusion and Level Kinetics in Transient Absorption Spectroscopy. *Chem Phys Lett* **1976,** *42* (2), 213-217.

62. Ekvall, K.; van der Meulen, P.; Dhollande, C.; Berg, L. E.; Pommeret, S.; Naskrecki, R.; Mialocq, J. C., Cross phase modulation artifact in liquid phase transient absorption spectroscopy. *J Appl Phys* **2000,** *87* (5), 2340-2352.

63. Lorenc, M.; Ziolek, M.; Naskrecki, R.; Karolczak, J.; Kubicki, J.; Maciejewski, A., Artifacts in femtosecond transient absorption spectroscopy. *Appl Phys B-Lasers O* **2002,** *74* (1), 19-27.

64. Dhar, L.; Rogers, J. A.; Nelson, K. A., Time-Resolved Vibrational Spectroscopy in the Impulsive Limit. *Chem Rev* **1994,** *94* (1), 157-193.

65. Liebel, M.; Kukura, P., Broad-Band Impulsive Vibrational Spectroscopy of Excited Electronic States in the Time Domain. *J Phys Chem Lett* **2013,** *4* (8), 1358-1364.

66. Kraack, J. P.; Wand, A.; Buckup, T.; Motzkus, M.; Ruhman, S., Mapping multidimensional excited state dynamics using pump-impulsive-vibrational-spectroscopy and pump-degenerate-four-wave-mixing. *Phys Chem Chem Phys* **2013,** *15* (34), 14487-14501.

67. Wende, T.; Liebel, M.; Schnedermann, C.; Pethick, R. J.; Kukura, P., Population-Controlled Impulsive Vibrational Spectroscopy: Background- and Baseline-Free Raman Spectroscopy of Excited Electronic States. *J Phys Chem A* **2014,** *118* (43), 9976-9984.

68. Liebel, M.; Schnedermann, C.; Wende, T.; Kukura, P., Principles and Applications of Broadband Impulsive Vibrational Spectroscopy. *J Phys Chem A* **2015,** *119* (36), 9506-9517.

69. Ernsting, N. P.; Kovalenko, S. A.; Senyushkina, T.; Saam, J.; Farztdinov, V., Wave-packet-assisted decomposition of femtosecond transient ultraviolet-visible absorption spectra: Application to excited-state intramolecular proton transfer in solution. *J Phys Chem A* **2001,** *105* (14), 3443-3453.

70. Harris, F. J., Use of Windows for Harmonic-Analysis with Discrete Fourier-Transform. *P Ieee* **1978,** *66* (1), 51-83.

71. Nuttall, A. H., Some Windows with Very Good Sidelobe Behavior. *Ieee T Acoust Speech* **1981,** *29* (1), 84-91.

72. Reed, M. K.; Steinershepard, M. K.; Armas, M. S.; Negus, D. K., Microjoule-Energy Ultrafast Optical Parametric-Amplifiers. *J Opt Soc Am B* **1995,** *12* (11), 2229-2236.

73. Huber, R.; Satzger, H.; Zinth, W.; Wachtveitl, J., Noncollinear optical parametric amplifiers with output parameters improved by the application of a white light continuum generated in CaF2. *Opt Commun* **2001,** *194* (4-6), 443-448.

74. Bradler, M.; Baum, P.; Riedle, E., Femtosecond continuum generation in bulk laser host materials with sub-mu J pump pulses. *Appl Phys B-Lasers O* **2009,** *97* (3), 561-574.

75. Gaeta, A. L., Catastrophic collapse of ultrashort pulses. *Phys Rev Lett* **2000,** *84* (16), 3582-3585.

76. Shirakawa, A.; Sakane, I.; Takasaka, M.; Kobayashi, T., Sub-5-fs visible pulse generation by pulse-front-matched noncollinear optical parametric amplification. *Appl Phys Lett* **1999,** *74* (16), 2268-2270.

77. Cerullo, G.; De Silvestri, S., Ultrafast optical parametric amplifiers. *Rev Sci Instrum* **2003,** *74* (1), 1-18.

78. Manzoni, C.; Cerullo, G., Design criteria for ultrafast optical parametric amplifiers. *J Optics-Uk* **2016,** *18* (10).

79. Megerle, U.; Pugliesi, I.; Schriever, C.; Sailer, C. F.; Riedle, E., Sub-50 fs broadband absorption spectroscopy with tunable excitation: putting the analysis of ultrafast molecular dynamics on solid ground. *Appl Phys B-Lasers O* **2009,** *96* (2-3), 215-231.

80. Martinez, O. E.; Gordon, J. P.; Fork, R. L., Negative Group-Velocity Dispersion Using Refraction. *J Opt Soc Am A* **1984,** *1* (10), 1003-1006.

81. Bradley, P. G.; Kress, N.; Hornberger, B. A.; Dallinger, R. F.; Woodruff, W. H., Vibrational Spectroscopy of the Electronically Excited-State .5. Time-Resolved Resonance Raman-Study of Tris(Bipyridine)Ruthenium(Ii) and Related Complexes - Definitive Evidence for the Localized Mlct State. *J Am Chem Soc* **1981,** *103* (25), 7441-7446.

82. Decurtins, S.; Felix, F.; Ferguson, J.; Gudel, H. U.; Ludi, A., The Electronic-Spectrum of Fe(Bpy)32+ and Os(Bpy)32+. *J Am Chem Soc* **1980,** *102* (12), 4102-4106.

83. Liu, Y. Z.; Kjaer, K. S.; Fredin, L. A.; Chabera, P.; Harlang, T.; Canton, S. E.; Lidin, S.; Zhang, J. X.; Lomoth, R.; Bergquist, K. E.; Persson, P.; Warnmark, K.; Sundstrom, V., A Heteroleptic Ferrous Complex with Mesoionic Bis(1,2,3-triazol-5-ylidene) Ligands: Taming the MLCT Excited State of Iron(II). *Chem-Eur J* **2015,** *21* (9), 3628-3639.

84. Braterman, P. S.; Song, J. I.; Peacock, R. D., Electronic Absorption-Spectra of the Iron(Ii) Complexes of 2,2'-Bipyridine, 2,2'-Bipyrimidine, 1,10-Phenanthroline, and 2,2'-6',2''-Terpyridine and Their Reduction Products. *Inorg Chem* **1992,** *31* (4), 555-559.

85. Martens, W. N.; Frost, R. L.; Kristof, J.; Kloprogge, J. T., Raman spectroscopy of dimethyl sulphoxide and deuterated dimethyl sulphoxide at 298 and 77 K. *J Raman Spectrosc* **2002,** *33* (2), 84-91.

86. Hainer, F.; Alagna, N.; Marri, A. R.; Penfold, T. J.; Gros, P. C.; Haacke, S.; Buckup, T., Vibrational Coherence Spectroscopy Identifies Ultrafast Branching in an Iron(II) Sensitizer. *J Phys Chem Lett* **2021,** *12* (35), 8560-8565.

87. Duchanois, T.; Etienne, T.; Cebrian, C.; Liu, L.; Monari, A.; Beley, M.; Assfeld, X.; Haacke, S.; Gros, P. C., An Iron-Based Photosensitizer with Extended Excited-State Lifetime: Photophysical and Photovoltaic Properties. *Eur J Inorg Chem* **2015,** (14), 2469-2477.

88. Liu, L.; Agathangelou, D.; Roland, T.; Crégut, O.; Duchanois, T.; Beley, M.; Léonard, J.; Gros, P.; Haacke, S., High sensitivity fluorescence up-conversion spectroscopy of 3MLCT emission of metal-organic complexes. *EPJ Web Conf.* **2019,** *205*, Art. No. 09009.

89. Witte, T.; Yeston, J. S.; Motzkus, M.; Heilweil, E. J.; Kompa, K. L., Femtosecond infrared coherent excitation of liquid phase vibrational population distributions (v > 5). *Chem Phys Lett* **2004,** *392* (1-3), 156-161.

90. Strasfeld, D. B.; Shim, S. H.; Zanni, M. T., Controlling vibrational excitation with shaped mid-IR pulses. *Phys Rev Lett* **2007,** *99* (3).

91. Burschka, J.; Pellet, N.; Moon, S. J.; Humphry-Baker, R.; Gao, P.; Nazeeruddin, M. K.; Gratzel, M., Sequential deposition as a route to high-performance perovskite-sensitized solar cells. *Nature* **2013,** *499* (7458), 316-+.

---

92. Schaub, T. A.; Padberg, K.; Kivala, M., Bridged triarylboranes, -silanes, -amines, and -phosphines as minimalistic heteroatom-containing polycyclic aromatic hydrocarbons: Progress and challenges. *J Phys Org Chem* **2020,** *33* (2).

93. Zhao, X. J.; Wang, M. K., Organic hole-transporting materials for efficient perovskite solar cells. *Mater Today Energy* **2018,** *7*, 208-220.

94. Urieta-Mora, J.; Garcia-Benito, I.; Molina-Ontoria, A.; Martin, N., Hole transporting materials for perovskite solar cells: a chemical approach. *Chem Soc Rev* **2018,** *47* (23).

95. Shahnawaz; Swayamprabha, S. S.; Nagar, M. R.; Yadav, R. A. K.; Gull, S.; Dubey, D. K.; Jou, J. H., Hole-transporting materials for organic light-emitting diodes: an overview. *J Mater Chem C* **2019,** *7* (24), 7144-7158.

96. Jhulki, S.; Moorthy, J. N., Small molecular hole-transporting materials (HTMs) in organic light-emitting diodes (OLEDs): structural diversity and classification. *J Mater Chem C* **2018,** *6* (31), 8280-8325.

97. Agarwala, P.; Kabra, D., A review on triphenylamine (TPA) based organic hole transport materials (HTMs) for dye sensitized solar cells (DSSCs) and perovskite solar cells (PSCs): evolution and molecular engineering. *J Mater Chem A* **2017,** *5* (4), 1348-1373.

98. Ajdari, M.; Pappenberger, R.; Walla, C.; Hoffmann, M.; Michalsky, I.; Kivala, M.; Dreuw, A.; Tegeder, P., Impact of Connectivity on the Electronic Structure of N-Heterotriangulenes. *J Phys Chem C* **2022**.

99. Michalsky, I.; Gensch, V.; Walla, C.; Hoffmann, M.; Rominger, F.; Oeser, T.; Tegeder, P.; Dreuw, A.; Kivala, M., Fully Bridged Triphenylamines Comprising Five- and Seven-Membered Rings. *Chem-Eur J* **2022,** *28* (34).

100. Schaub, T. A.; Mekelburg, T.; Dral, P. O.; Miehlich, M.; Hampel, F.; Meyer, K.; Kivala, M., A Spherically Shielded Triphenylamine and Its Persistent Radical Cation. *Chem-Eur J* **2020,** *26* (15), 3264-3269.

101. Inagaki, T., Absorption-Spectra of Pure Liquid Benzene in Ultraviolet Region. *J Chem Phys* **1972,** *57* (6), 2526-&.

102. Kumler, W. D.; Strait, L. A., The ultraviolet absorption spectra and resonance in benzene derivatives - Sulfanilamide, metanilamide, p-aminobenzoic acid, benzenesulfonamide, benzoic acid aniline. *J Am Chem Soc* **1943,** *65*, 2349-2354.

103. Grellmann, K. H.; Linschitz, H.; Sherman, G. M., Photo-Conversion of Diphenylamines to Carbazoles, and Accompanying Transient Species. *J Am Chem Soc* **1963,** *85* (12), 1881-&.

104. Linschitz, H.; Grellmann, K. H., Reaction Pathways in Photochemical Conversion of Diphenylamines to Carbazoles. *J Am Chem Soc* **1964,** *86* (2), 303-&.

105. Gorner, H., Photoinduced oxygen uptake of diphenylamines in solution and their ring closure revisited. *J Phys Chem A* **2008,** *112* (6), 1245-1250.

106. Protti, S.; Mella, M.; Bonesi, S. M., Photochemistry of triphenylamine (TPA) in homogeneous solution and the role of transient N-phenyl-4a,4b-dihydrocarbazole. A steady-state and time-resolved investigation. *New J Chem* **2021,** *45* (36), 16581-16593.

107. Steiner, P. A.; Gordy, W., Precision Measurement of Dipole Moments and Other Spectral Constants of Normal and Deuterated Methyl Fluoride and Methyl Cyanide. *J Mol Spectrosc* **1966,** *21* (3), 291-&.

108. Forster, E. W.; Gellmann, K. H., Light-Induced Conversion of Triphenylamine to Excited Triplet-State of 11,12-Dihydrocarbazole. *Chem Phys Lett* **1972,** *14* (4), 536-&.

---

109. Dexter, D. L., A Theory of Sensitized Luminescence in Solids. *J Chem Phys* **1953,** *21* (5), 836-850.

110. Schweitzer, C.; Schmidt, R., Physical mechanisms of generation and deactivation of singlet oxygen. *Chem Rev* **2003,** *103* (5), 1685-1757.

111. Darmanyan, A. P.; Lee, W.; Jenks, W. S., Charge transfer interactions in the generation of singlet oxygen O-2((1)Delta(g)) by strong electron donors. *J Phys Chem A* **1999,** *103* (15), 2705-2711.

112. Bonesi, S. M.; Dondi, D.; Protti, S.; Fagnoni, M.; Albini, A., (Co)oxidation/cyclization processes upon irradiation of triphenylamine. *Tetrahedron Lett* **2014,** *55* (18), 2932-2935.

113. Smith, M. B.; Michl, J., Singlet Fission. *Chem Rev* **2010,** *110* (11), 6891-6936.

114. Smith, M. B.; Michl, J., Recent Advances in Singlet Fission. *Annu Rev Phys Chem* **2013,** *64*, 361-386.

115. Havlas, Z.; Michl, J., Singlet Fission. *Chem Listy* **2018,** *112* (10), 669-677.

116. Wollscheid, N.; Gunther, B.; Rao, V. J.; Berger, F. J.; Lustres, J. L. P.; Motzkus, M.; Zaumseil, J.; Gade, L. H.; Hofener, S.; Buckup, T., Ultrafast Singlet Fission and Intersystem Crossing in Halogenated Tetraazaperopyrenes. *J Phys Chem A* **2020,** *124* (39), 7857-7868.

117. Herz, J.; Buckup, T.; Paulus, F.; Engelhart, J.; Bunz, U. H. F.; Motzkus, M., Acceleration of Singlet Fission in an Aza-Derivative of TIPS-Pentacene. *J Phys Chem Lett* **2014,** *5* (14), 2425-2430.

118. Alagna, N.; Lustres, J. L. P.; Roozbeh, A.; Han, J.; Hahn, S.; Berger, F. J.; Zaumseil, J.; Dreuw, A.; Bunz, U. H. F.; Buckup, T., Ultrafast Singlet Fission in Rigid Azaarene Dimers with Negligible Orbital Overlap. *J Phys Chem B* **2020,** *124* (41), 9163-9174.

119. Wollscheid, N.; Lustres, J. L. P.; Brosius, V.; Motzkus, M.; Bunz, U. H. F.; Buckup, T., Diffusion-Controlled Singlet Fission in a Chlorinated Phenazinothiadiazole by Broadband Femtosecond Transient Absorption. *J Phys Chem B* **2020,** *124* (45), 10186-10194.

120. Walker, B. J.; Musser, A. J.; Beljonne, D.; Friend, R. H., Singlet exciton fission in solution. *Nat Chem* **2013,** *5* (12), 1019-1024.

121. Stern, H. L.; Musser, A. J.; Gelinas, S.; Parkinson, P.; Herz, L. M.; Bruzek, M. J.; Anthony, J.; Friend, R. H.; Walker, B. J., Identification of a triplet pair intermediate in singlet exciton fission in solution. *P Natl Acad Sci USA* **2015,** *112* (25), 7656-7661.

122. Berg, O. G.; Vonhippel, P. H., Diffusion-Controlled Macromolecular Interactions. *Annu Rev Biophys Bio* **1985,** *14*, 131-160.

123. Wollscheid, N.; Lustres, J. L. P.; Kefer, O.; Hahn, S.; Brosius, V.; Bunz, U. H. F.; Motzkus, M.; Buckup, T., Oxygen-catalysed sequential singlet fission. *Nat Commun* **2019,** *10*.

124. Fitzgerald, E. A.; Wuelfing, P.; Richtol, H. H., Photochemical Oxidation of Some Substituted Aromatic Amines in Chloroform. *J Phys Chem-Us* **1971,** *75* (18), 2737-+.

125. Chen, F. Q.; Yu, Q.; Guo, Y.; Fan, M. G., Photophysical Studies on Organic-Compounds - Time-Resolved Transient Absorption-Spectra Studies on Triphenylamine in Various Solvents. *Sci China Ser B* **1991,** *34* (2), 135-140.

126. Kauppila, T. J.; Kotiaho, T.; Kostiainen, R.; Bruins, A. P., Negative ion-atmospheric pressure photoionization-mass spectrometry. *J Am Soc Mass Spectr* **2004,** *15* (2), 203-211.

127. Tatsuno, H.; Kjaer, K. S.; Kunnus, K.; Harlang, T. C. B.; Timm, C.; Guo, M. Y.; Chabera, P.; Fredin, L. A.; Hartsock, R. W.; Reinhard, M. E.; Koroidov, S.; Li,

L.; Cordones, A. A.; Gordivska, O.; Prakash, O.; Liu, Y. Z.; Laursen, M. G.; Biasin, E.; Hansen, F. B.; Vester, P.; Christensen, M.; Haldrup, K.; Nemeth, Z.; Szemes, D. S.; Bajnoczi, E.; Vanko, G.; Van Driel, T. B.; Alonso-Mori, R.; Glownia, J. M.; Nelson, S.; Sikorski, M.; Lemke, H. T.; Sokaras, D.; Canton, S. E.; Dohn, A. O.; Moller, K. B.; Nielsen, M. M.; Gaffney, K. J.; Warnmark, K.; Sundstrom, V.; Persson, P.; Uhlig, J., Hot Branching Dynamics in a Light-Harvesting Iron Carbene Complex Revealed by Ultrafast X-ray Emission Spectroscopy. *Angew Chem Int Edit* **2020,** *59* (1), 364-372.

128. Rosemann, N. W.; Chabera, P.; Prakash, O.; Kaufhold, S.; Warnmark, K.; Yartsev, A.; Persson, P., Tracing the Full Bimolecular Photocycle of Iron(III)-Carbene Light Harvesters in Electron-Donating Solvents. *J Am Chem Soc* **2020,** *142* (19), 8565-8569.

129. Chabera, P.; Lindh, L.; Rosemann, N. W.; Prakash, O.; Uhlig, J.; Yartsev, A.; Warnmark, K.; Sundstrom, V.; Persson, P., Photofunctionality of iron(III) N-heterocyclic carbenes and related d(5) transition metal complexes. *Coordin Chem Rev* **2021,** *426*.

130. Prakash, O.; Lindh, L.; Kaul, N.; Rosemann, N. W.; Losada, I. B.; Johnson, C.; Chabera, P.; Ilic, A.; Schwarz, J.; Gupta, A. K.; Uhlig, J.; Ericsson, T.; Haggstrom, L.; Huang, P.; Bendix, J.; Strand, D.; Yartsev, A.; Lomoth, R.; Persson, P.; Warnmark, K., Photophysical Integrity of the Iron(III) Scorpionate Framework in Iron(III)-NHC Complexes with Long-Lived 2LMCT Excited States. *Inorg Chem* **2022**.

131. Ilic, A.; Schwarz, J.; Johnson, C.; De Groot, L. H. M.; Kaufhold, S.; Lomoth, R.; Warnmark, K., Photoredox catalysis via consecutive (LMCT)-L-2- and (MLCT)-M-3-excitation of an Fe(iii/ii)-N-heterocyclic carbene complex. *Chem Sci* **2022,** *13* (32), 9165-9175.

132. Schwarz, J.; Ilic, A.; Johnson, C.; Lomoth, R.; Warnmark, K., High turnover photocatalytic hydrogen formation with an Fe(iii) N-heterocyclic carbene photosensitiser. *Chem Commun* **2022,** *58* (35), 5351-5354.

133. Moulin, E.; Niess, F.; Maaloum, M.; Buhler, E.; Nyrkova, I.; Giuseppone, N., The Hierarchical Self-Assembly of Charge Nanocarriers: A Highly Cooperative Process Promoted by Visible Light. *Angew Chem Int Edit* **2010,** *49* (39), 6974-6978.

134. Krug, M.; Wagner, M.; Schaub, T. A.; Zhang, W. S.; Schusslbauer, C. M.; Ascherl, J. D. R.; Munich, P. W.; Schroder, R. R.; Grohn, F.; Dral, P. O.; Barbatti, M.; Guldi, D. M.; Kivala, M., The Impact of Aggregation on the Photophysics of Spiro-Bridged Heterotriangulenes. *Angew Chem Int Edit* **2020,** *59* (37), 16233-16240.

9 Acknowledgements

If I have seen further, it is by standing on the shoulders of giants. If this was true for Sir Isaac Newton, then it positively applies to me and evidently his shoulders are among the many on which I get to stand today.

The last, and to me personally most significant pair of shoulders in this series are those of my supervisor, Dr. Tiago Buckup. Through his advice, his support, and his teaching on the blackboard, on paper sketches, on the experimental setups and on my own data, he elevated me to submitting this work. I thank you for passion for science and your patience with me.

I thank Prof. Dr. Robert Volpp for his enthusiastic discussions and his ability to make safety instructions entertaining.

I thank Prof. Dr. Andreas Dreuw for the willingness to share his expertise both in the TPA project meetings and in his report on this work.

I also thank Prof. Felix Deschler for his generous support of my work after adopting my colleagues and me into his group.

I would like to thank my many colleagues, past and present. The references given in Chapter 8 are the context of this work. They are the necessary framework, without which, this work would not be possible, interesting, relevant or make any sense. In this exact way, you were the context of my labor. Thank you.

I thank Dr. Nicolò Alagna for his patient introduction to the experimental setup and Dr. Klaus Wollscheid for his Matlab-scripts which are so well-documented, they pass as educational. I thank Dr. Pavel Kolesnichenko for his sharing his practical and theoretical expertise on the field of time-resolved spectroscopy with me. I thank Florian Nicolai for his support and honest exchange as we share these last steps of our PhD journey. I thank Oskar Kefer for his help in the laboratory and his excellent global analysis toolset. I thank Danyellen Galindo for her imperturbable positivity in the face of frustration and Hendrik Brockmann for his motivating collaboration on the TPA project.

It has been a great privilege to work on projects with collaborators providing not only samples, but insight, advice, and help, so that we could stimulate the respective parts of our shared research.

In the context of the iron(II) complex project, I thank Prof. Stefan Haacke for the provided samples and his experienced advice as well as Prof. Thomas Penfold for his quantum chemical calculations and the insight he provided with them.

With regard to the TPA project I thank Prof. Milan Kivala for sharing his expertise in our meetings. I thank Angelina Jocic for providing the samples and NMR and MS analysis and Letao Huang for his quantum chemical calculations.

I also thank Marina Sommer for her invaluable support in all things administrative and her little gifts which go a long way in creating a positive atmosphere.

Finally, I want to thank my family. You are the context of *me*. *I* would not be possible, interesting, relevant, or make any sense, and I would certainly not be standing on anyone’s shoulders, if it weren’t for you.

I thank my parents. For a long time, I was convinced, that, if ever something good would come of me, it would be thanks to your love and support. In recent years I started learning, that it is also thanks to your hard work and patience.

I thank my wonderful wife. It is not good, that I should be alone. You truly are my help fit for me. You are my connector to this world, my support, my ally, my love, and my home.

Lastly, I thank my daughter and her sibling, whom I cannot wait to meet in person. No matter what else might be troubling me, you ground me. You are the great joy in my life and all the outlook I could wish for.

GESAMTFAKULTÄT FÜR MATHEMATIK, INGENIEUR- UND NATURWISSENSCHAFTEN

COMBINED FACULTY OF MATHEMATICS, ENGINEERING AND NATURAL SCIENCES

RUPRECHT-KARLS-
UNIVERSITÄT
HEIDELBERG

Eidesstattliche Versicherung gemäß § 8 der Promotionsordnung für die Gesamtfakultät für Mathematik, Ingenieur- und Naturwissenschaften der Universität Heidelberg / Sworn Affidavit according to § 8 of the doctoral degree regulations of the Combined Faculty of Mathematics, Engineering and Natural Sciences at Heidelberg University

1. Bei der eingereichten Dissertation zu dem Thema / The thesis I have submitted entitled

   ……………………………………………………………………………………………………

   …………………………………………………………………………………………………….

   handelt es sich um meine eigenständig erbrachte Leistung / is my own work.

2. Ich habe nur die angegebenen Quellen und Hilfsmittel benutzt und mich keiner unzulässigen Hilfe Dritter bedient. Insbesondere habe ich wörtlich oder sinngemäß aus anderen Werken übernommene Inhalte als solche kenntlich gemacht. / I have only used the sources indicated and have not made unauthorised use of services of a third party. Where the work of others has been quoted or reproduced, the source is always given.

3. Die Arbeit oder Teile davon habe ich wie folgt/bislang nicht[1)] an einer Hochschule des In- oder Auslands als Bestandteil einer Prüfungs- oder Qualifikationsleistung vorgelegt. / I have not yet/have already[1)] presented this thesis or parts thereof to a university as part of an examination or degree.

   Titel der Arbeit / Title of the thesis: ……………………………………………………………………………

   Hochschule und Jahr / University and year: …………………..…………………………………………......

   Art der Prüfungs- oder Qualifikationsleistung / Type of examination or degree: …………………………

4. Die Richtigkeit der vorstehenden Erklärungen bestätige ich. / I confirm that the declarations made above are correct.

5. Die Bedeutung der eidesstattlichen Versicherung und die strafrechtlichen Folgen einer unrichtigen oder unvollständigen eidesstattlichen Versicherung sind mir bekannt. / I am aware of the importance of a sworn affidavit and the criminal prosecution in case of a false or incomplete affidavit.

Ich versichere an Eides statt, dass ich nach bestem Wissen die reine Wahrheit erklärt und nichts verschwiegen habe. / I affirm that the above is the absolute truth to the best of my knowledge and that I have not concealed anything.

……………………………………….. ……………………….…………………………..

Ort und Datum / Place and date Unterschrift / Signature

---

1) Nicht Zutreffendes streichen. Bei Bejahung sind anzugeben: der Titel der andernorts vorgelegten Arbeit, die Hochschule, das Jahr der Vorlage und die Art der Prüfungs- oder Qualifikationsleistung. / Please cross out what is not applicable. If applicable, please provide: the title of the thesis that was presented elsewhere, the name of the university, the year of presentation and the type of examination or degree.

The German text is legally binding.